

**RAMAN MICROSPECTROSCOPIC IMAGING AND MULTIVARIATE  
ANALYSIS TO INVESTIGATE THE CHEMICAL PROPERTIES OF NOVEL  
GEOLOGICAL AND PLANETARY MATERIALS**

by

Joseph P. Smith

A dissertation submitted to the Faculty of the University of Delaware in partial fulfillment of the requirements for the degree of Doctor of Philosophy in Chemistry and Biochemistry

Spring 2017

© 2017 Joseph P. Smith  
All Rights Reserved

**RAMAN MICROSPECTROSCOPIC IMAGING AND MULTIVARIATE  
ANALYSIS TO INVESTIGATE THE CHEMICAL PROPERTIES OF NOVEL  
GEOLOGICAL AND PLANETARY MATERIALS**

by

Joseph P. Smith

Approved: \_\_\_\_\_  
Murray V. Johnston, Ph.D.  
Chair of the Department of Chemistry and Biochemistry

Approved: \_\_\_\_\_  
George H. Watson, Ph.D.  
Dean of the College of Arts and Sciences

Approved: \_\_\_\_\_  
Ann L. Ardis, Ph.D.  
Senior Vice Provost for Graduate and Professional Education

I certify that I have read this dissertation and that in my opinion it meets the academic and professional standard required by the University as a dissertation for the degree of Doctor of Philosophy.

Signed:

---

Karl S. Booksh, Ph.D.  
Professor in charge of dissertation

I certify that I have read this dissertation and that in my opinion it meets the academic and professional standard required by the University as a dissertation for the degree of Doctor of Philosophy.

Signed:

---

John T. Newberg, Ph.D.  
Member of dissertation committee

I certify that I have read this dissertation and that in my opinion it meets the academic and professional standard required by the University as a dissertation for the degree of Doctor of Philosophy.

Signed:

---

Lars Gundlach, Ph.D.  
Member of dissertation committee

I certify that I have read this dissertation and that in my opinion it meets the academic and professional standard required by the University as a dissertation for the degree of Doctor of Philosophy.

Signed:

---

Louis A. Obando, Ph.D.  
Member of dissertation committee

## ACKNOWLEDGMENTS

The research presented in this dissertation was accomplished with the support of many people. I first and foremost would like to acknowledge and deeply thank my research advisor, Dr. Karl S. Booksh, for his guidance and mentorship. Furthermore, the research accomplished in this dissertation would not have been possible without Dr. Booksh's support, and I sincerely thank him for allowing me to perform chemical research under his advisement. Additionally, I would like to thank the members of my dissertation committee—Dr. John T. Newberg, Dr. Lars Gundlach, and Dr. Louis A. Obando—for all of their tremendous help and advice with my research. I would also like to thank Dr. Steven Brown for his guidance with my research. In addition, I would like to thank Dr. Billy P. Glass and Dr. Frank C. Smith for their help and geological expertise on the research presented within this dissertation. Finally, I would like to acknowledge the numerous collaborators that I have been lucky enough to work with during my time at the University of Delaware, including Dr. Tsu-Wei Chou, Dr. Raul F. Lobo, Dr. Dionisios G. Vlachos, Dr. Alexandra E. Krull-Davatzes, Dr. Bruce M. Simonson, Dr. Peter B. Leavens, and Dr. Brian J. Bahnson.

Funding of the research accomplished throughout this dissertation is also immensely appreciated. Specifically, support of this research by both the National Science Foundation (Chem312184) and the Delaware Space Grant College and Fellowship Program (NASA Grant NNX15A119H) is gratefully acknowledged. Moreover, I would like to specifically thank the NASA Delaware Space Grant College and Fellowship Program for awarding me their graduate fellowship in 2016-2017 to

perform chemical research. Additionally, I would like to thank both Dr. Karl S. Booksh and Dr. Sharon Rozovsky for allowing me to be a mentor and research assistant for the Science and Engineering Leadership Experience Research Experience for Undergraduates (SELI-REU) Program, which is funded by the National Science Foundation. I would also like to acknowledge the Society for Applied Spectroscopy (SAS) for both allowing me to be the President of the University of Delaware's Student Chapter and for the Bruce R. Kowalski Award given to outstanding young researchers in the field of chemometrics. In addition, I would like to recognize the Eastern Analytical Symposium (EAS) for their Graduate Student Award sponsored by Merck & Co., Inc. for research in analytical chemistry. I would like to additionally thank the University of Delaware for the Excellence in Teaching Award. Finally, I would like to thank the Department of Chemistry and Biochemistry at the University of Delaware for the Elizabeth Dyer Award for excellence in teaching and for the Glenn S. Skinner Memorial Award for distinction in scholarship, research, and service. Overall, I am deeply appreciative of the remarkable support I have received throughout my time at the University of Delaware.

Finally, the research presented in this dissertation was accomplished with the support of many friends and family throughout my career at the University of Delaware. Specifically, the members of Dr. Karl S. Booksh's research group, both past and present, are gratefully acknowledged. I am also utmost thankful for the support from Mackenzie L. Lauro, who has not only taught me about research given her expertise, but has truly inspired me and fostered my personal growth enormously. I would also like to thank Christopher Arble for his support as well as the members of the analytical and physical chemistry divisions for their help. Finally, I would like to

thank my family members, especially my mother Deborah Smith, my father Raymond J. Smith, my brother Raymond P. Smith, my sister Jennifer Loria, and my brother-in-law Louis Loria for all of their support during my time at the University of Delaware. Overall, without the support of a myriad of people, the work accomplished in this dissertation would not be possible, and I want to deeply thank everyone who has helped throughout my time at the University of Delaware.

## TABLE OF CONTENTS

LIST OF TABLES .....	xi
LIST OF FIGURES .....	xii
ABSTRACT .....	xix

### Chapter

1	INTRODUCTION .....	1
1.1	Raman Spectroscopy .....	1
1.2	Raman Microspectroscopic Imaging .....	5
1.3	Multivariate Analysis Methods and Chemometrics .....	9
1.4	Multivariate Curve Resolution-Alternating Least Squares (MCR-ALS) .....	13
1.5	Combining Multivariate Analysis with Raman Microspectroscopic Imaging.....	15
2	RAMAN MICROSPECTROSCOPIC IMAGING WITH MULTIVARIATE CURVE RESOLUTION-ALTERNATING LEAST SQUARES (MCR-ALS) APPLIED TO THE HIGH-PRESSURE POLYMORPH OF TITANIUM DIOXIDE, TiO <sub>2</sub> -II.....	19
2.1	Abstract.....	19
2.2	Introduction .....	20
2.3	Materials and Methods .....	25
2.3.1	Sample Preparation.....	25
2.3.2	Scanning Electron Microscopy (SEM).....	26
2.3.3	Raman Microspectroscopic Imaging.....	26
2.3.4	Multivariate Data Analysis.....	28
2.3.4.1	Principal Component Analysis (PCA).....	28
2.3.4.2	Multivariate Curve Resolution-Alternating Least Squares (MCR-ALS).....	30
2.4	Results and Discussion .....	33
2.4.1	Raman Microspectroscopy .....	33

2.4.2	Principal Component Analysis (PCA) and Scanning Electron Microscopy (SEM) .....	38
2.4.3	Multivariate Curve Resolution-Alternating Least Squares (MCR-ALS) Applied to Raman Microspectroscopic Imaging ...	44
2.4.4	Evaluation of Component Selection for MCR-ALS .....	60
2.4.5	Spatial Resolution Enhancements .....	66
2.4.6	Estimated Raman Spectrum of Pure TiO <sub>2</sub> -II .....	70
2.4.7	Geologic Importance of Characterizing the TiO <sub>2</sub> -II-Bearing Grains using MCR-ALS Applied to Raman Microspectroscopic Imaging .....	74
2.5	Conclusions .....	76
3	HIGH SPECTRAL AND HIGH SPATIAL RESOLUTION RAMAN MICROSCOPIC IMAGING OF THE HIGH-PRESSURE POLYMORPH, TiO <sub>2</sub> -II: PROVIDING DATA SETS FOR MULTIVARIATE AND CHEMOMETRIC ANALYSIS .....	79
3.1	Abstract.....	79
3.2	Introduction .....	80
3.3	Materials and Methods .....	81
3.3.1	Sample Preparation.....	81
3.3.2	Scanning Electron Microscopy (SEM).....	82
3.3.3	Raman Microspectroscopic Imaging.....	82
3.3.4	Multivariate Curve Resolution-Alternating Least Squares (MCR-ALS).....	84
3.4	Results and Discussion .....	86
3.4.1	Raman Microspectroscopy with High Spectral and High Spatial Resolution.....	86
3.4.2	High Spectral Resolution Raman Microspectroscopic Imaging with Multivariate Curve Resolution-Alternating Least Squares (MCR-ALS).....	87
3.4.3	High Spatial Resolution Raman Microspectroscopic Imaging with MCR-ALS .....	90
3.4.4	Value of High Spectral and High Spatial Resolution Raman Microspectroscopic Imaging Data Sets to the Scientific Community .....	93
3.5	Conclusions .....	95

4	SPATIAL AND SPECTRAL RESOLUTION OF CARBONACEOUS MATERIAL FROM HEMATITE ( $\alpha$ -Fe <sub>2</sub> O <sub>3</sub> ) USING MULTIVARIATE CURVE RESOLUTION-ALTERNATING LEAST SQUARES (MCR-ALS) WITH RAMAN MICROSPECTROSCOPIC IMAGING: IMPLICATIONS FOR THE SEARCH FOR LIFE ON MARS .....	97
4.1	Abstract.....	97
4.2	Introduction .....	98
4.3	Materials and Methods .....	105
4.3.1	Materials and Sample Preparation.....	105
4.3.2	Raman Microspectroscopic Imaging.....	106
4.3.3	Multivariate Data Analysis.....	108
4.3.3.1	Principal Component Analysis (PCA).....	109
4.3.3.2	Multivariate Curve Resolution-Alternating Least Squares (MCR-ALS).....	110
4.3.4	Combinatorial Data Sets.....	112
4.4	Results and Discussion .....	113
4.4.1	Raman Spectra of Hematite and Carbonaceous Material.....	113
4.4.2	Spectral Overlap of Chemical Species .....	117
4.4.3	Principal Component Analysis (PCA) of Raman Microspectroscopic Imaging Data.....	121
4.4.4	Multivariate Curve Resolution-Alternating Least Squares (MCR-ALS) Applied to Raman Microspectroscopic Imaging .	123
4.4.5	Multivariate Curve Resolution-Alternating Least Squares Applied to Combinatorial Data Sets.....	131
4.4.6	Implications for Planetary Science, Geochemistry, and Geology .....	140
4.5	Conclusions .....	143
5	MULTIVARIATE CURVE RESOLUTION-ALTERNATING LEAST SQUARES (MCR-ALS) WITH RAMAN MICROSPECTROSCOPIC IMAGING APPLIED TO LUNAR METEORITES.....	146
5.1	Abstract.....	146
5.2	Introduction .....	147
5.3	Materials and Methods .....	155
5.3.1	Materials and Sample Preparation.....	155

5.3.2	Polarized Light Microscopy .....	156
5.3.3	Raman Microspectroscopic Imaging.....	156
5.3.4	Multivariate Curve Resolution-Alternating Least Squares (MCR-ALS).....	158
5.4	Results and Discussion .....	160
5.4.1	Polarized Light Microscopy of Lunar Meteorites LAP 02205 and LAP 04841 .....	160
5.4.2	Multivariate Curve Resolution-Alternating Least Squares (MCR-ALS) with Raman Microspectroscopic Imaging of Lunar Meteorite LAP 02205 .....	162
5.4.3	Multivariate Curve Resolution-Alternating Least Squares (MCR-ALS) with Raman Microspectroscopic Imaging of Lunar Meteorite LAP 04841 .....	172
5.5	Conclusions .....	185
6	CONCLUSIONS AND FUTURE DIRECTIONS .....	188
6.1	Conclusions of the Investigation of the High-Pressure, $\alpha$ -PbO <sub>2</sub> - Structured Polymorph of Titanium Dioxide, TiO <sub>2</sub> -II.....	189
6.2	Conclusions of High Spectral and High Spatial Resolution Raman Microspectroscopic Imaging Data and its Analysis by Multivariate Methods.....	191
6.3	Conclusions of the Spatial and Spectral Resolution of Carbonaceous Material from Hematite ( $\alpha$ -Fe <sub>2</sub> O <sub>3</sub> ) using Raman Microspectroscopic Imaging and Multivariate Analysis .....	193
6.4	Conclusions of the Investigation of Lunar Meteorites Using Raman Microspectroscopic Imaging and Multivariate Analysis.....	195
6.5	Future Directions .....	197
	REFERENCES .....	203
	Appendix	
A	REPRINT PERMISSIONS .....	227

## LIST OF TABLES

- Table 2.1: Assignment of the Raman bands observed in TiO<sub>2</sub>-II-bearing grains from the four spherule layers based on literature.[114, 115, 117, 118, 121] Rutile (R), anatase (A), TiO<sub>2</sub>-II (T), and quartz (Q) are shown..... 35
- Table 4.1: Assignment of the Raman bands observed in hematite (H) and carbonaceous material (CM) under 532 nm and 785 nm excitation. Band assignments are from the literature.[164-172] ..... 116

## LIST OF FIGURES

- Figure 1.1: Scattering events at the molecular level. Inelastic scattering (Raman scattering) and elastic scattering (Rayleigh scattering) are depicted. After excitation of sample with monochromatic radiation of frequency  $\nu_{\text{ex}}$ , scattering with the same frequency  $\nu_{\text{ex}}$  can be observed, termed Rayleigh scattering. Inelastic scattering with either a lower-frequency of  $\nu_{\text{ex}} - \nu_{\text{v}}$ , termed Stokes scattering, or inelastic scattering with a higher-frequency of  $\nu_{\text{ex}} + \nu_{\text{v}}$  termed anti-Stokes scattering are generated. .... 3
- Figure 1.2: Schematic of a typical Raman microscope used to perform Raman microspectroscopy and Raman microspectroscopic imaging. .... 7
- Figure 1.3: Using Raman microspectroscopy at defined spatial locations, termed Raman microspectroscopic imaging, to investigate the chemical and molecular properties of the sample. Raman microspectroscopic imaging generates extensive data sets containing spatial (x and y) with spectral information ( $\nu$ ) about the sample, encompassed within the three-dimensional experimental data matrix. .... 9
- Figure 1.4: The analysis of Raman microspectroscopic imaging data by univariate analysis methods. Using univariate analysis methods, the integration of a particular band, in this case the  $440 \text{ cm}^{-1}$  band of rutile (red), generates a chemical image. If spectral overlap is present within this spectral region—such as the  $464 \text{ cm}^{-1}$  of quartz (black) and the  $426 \text{ cm}^{-1}$  band of  $\text{TiO}_2\text{-II}$  (pink)—univariate analysis methods fail to provide a representative distribution of the analyte of interest—rutile (red). .... 12

Figure 1.5: Multivariate curve resolution-alternating least squares (MCR-ALS) applied to Raman microspectroscopic imaging. The experimental data generated from Raman microspectroscopic imaging contains three-dimensional (3-D) information—spatial information (x and y) and spectral information (v). This 3-D experimental data is unfolded into a two-dimensional (2-D) experimental matrix, D, with spatial information (both x and y together) and spectral information (v). Using MCR-ALS, the concentration profile matrix, C, and the resolved spectra matrix, $S^T$ , can be resolved. These matrices ultimately allow for the generation of spatially-resolved chemical images and corresponding resolved Raman spectra for each individual, pure chemical species within a sample. ....	14
Figure 1.5: The number of peer-reviewed publication per year for Raman & Chemical Imaging (A) and multivariate curve resolution (B) per year. Data of the publications for each year are from Web of Science ( <a href="https://webofknowledge.com/">https://webofknowledge.com/</a> ).....	17
Figure 2.1: Raman spectra of quartz (a), rutile (b), anatase (c), and synthetic TiO <sub>2</sub> -II (d), with an overlay of each Raman spectrum (e). TiO <sub>2</sub> -II was synthesized from rutile powder in a static high-pressure hydrothermal environment[78] at a pressure of 10 GPa and a temperature of 500 °C..	34
Figure 2.2: Raman spectra showing the presence of the high-pressure, $\alpha$ -PbO <sub>2</sub> -structured polymorph TiO <sub>2</sub> -II within four grains recovered from the Carawine spherule layer (CSL, grey), Jeerinah spherule layer (JSL, brown), Bee Gorge spherule layer (BGSL, green), and Monteville spherule layer (MSL, black). Raman spectra of anatase (blue), rutile (red), synthetic TiO <sub>2</sub> -II formed under dry, shock-induced conditions[84, 102] (Synthetic TiO <sub>2</sub> -II <sup>A</sup> , purple), and synthetic TiO <sub>2</sub> -II formed under hydrothermal, static conditions[78] (Synthetic TiO <sub>2</sub> -II <sup>B</sup> , pink) are also shown. Raman spectrum labeled “Synthetic TiO <sub>2</sub> -II <sup>A</sup> ” is from El Goresy et al.[84].....	37
Figure 2.3: Principal component analysis (PCA) plot of the scores on the first principal component (PC 1; 53.60%) and the second principal component (PC 2; 40.23%). ....	39
Figure 2.4: Backscattered electron (BSE) images of grains (a/b) from the Monteville spherule layer (MSL). Both grains contain polycrystalline micrometer- and submicrometer-sized particles of polydispersed sizes and shapes. Secondary electron (SE) image of the MSL grain is shown in the inset of (a).....	42

Figure 2.5: Spatially-resolved chemical maps with corresponding resolved Raman spectra for a grain from the Bee Gorge spherule layer. The optical images, with the probed area outlined in green (a), red (c), and yellow (e), and mean spectrum (black)  $\pm$  one standard deviation (+ in red, - in blue) are shown for each series of maps. Rutile, TiO<sub>2</sub>-II, and substrate-adhesive epoxy were resolved for each of the three areas outlined in green (a), red (c), and yellow (e). The maps in (a) and corresponding resolved spectra in (b) were generated using 20x magnification, whereas the maps in (c) with corresponding resolved spectra in (d) and the maps in (e) with corresponding resolved spectra in (f) were both generated using 100x magnification. Each Raman microspectroscopic imaging measurement was generated using a 20 x 20 spectral grid. The results in (a/b, c/d, and e/f) were obtained using a four component MCR-ALS model, and were generated using 532 nm excitation with 10 mW of laser power. .... 46

Figure 2.6: Spatially-resolved chemical maps and resolved Raman spectra generated using MCR-ALS applied to Raman microspectroscopic imaging of grains from the BGSL (a/b) and MSL (c/d). The optical images, with locations of spectral grids outlined in green, and mean spectrum (black)  $\pm$  the standard deviation (+ in red, - in blue) are shown for each series of maps. Rutile, TiO<sub>2</sub>-II, anatase, and substrate-adhesive epoxy were resolved, in which the maps in (a) and corresponding resolved spectra in (b) were generated using 50x magnification, and maps in (c) with corresponding resolved spectra in (d) were generated using 20x magnification. Each of the Raman microspectroscopic imaging results was generated using a 15 x 15 spectral grid. The results in (a/b) and (c/d) were obtained using five and twelve component MCR-ALS models, respectively, and they were generated using 532 nm excitation with 5 mW of laser power. .... 51

Figure 2.7: Spatially-resolved chemical maps and corresponding resolved Raman spectra were generated using MCR-ALS methods applied to Raman microspectroscopic imaging of a grain from the CSL (a/b). The optical image, with the spectral grid location outlined in green, and mean spectrum (black)  $\pm$  the standard deviation (+ in red, - in blue) are shown for the series of maps. Rutile, TiO<sub>2</sub>-II, anatase, quartz and substrate-adhesive epoxy were resolved, in which the maps in (a) and corresponding resolved spectra in (b) were generated using 50x magnification and a 20 x 20 spectral grid. The results were obtained using 532 nm excitation, 10 mW of laser power, and a twenty component MCR-ALS model. .... 55

- Figure 2.8: Spatially-resolved chemical maps and corresponding resolved Raman spectra were generated using MCR-ALS methods applied to Raman microspectroscopic imaging of a grain from the MSL (a/b). The optical image, with the spectral grid location outlined in green, and mean spectrum (black) +/- the standard deviation (+ in red, - in blue) are shown. Rutile, TiO<sub>2</sub>-II, anatase, quartz and substrate-adhesive epoxy were resolved, in which the maps in (a) with corresponding resolved spectra in (b) were both generated using 50x magnification. The Raman microspectroscopic imaging measurements were generated using a 20 x 20 spectral grid. The results were generated using 532 nm excitation with 5 mW of laser power, and they were obtained using a twenty component MCR-ALS model. .... 59
- Figure 2.9: Resolved spectra resulting from MCR-ALS applied to Raman microspectroscopic imaging of a MSL grain. The MCR-ALS model was built with four components. .... 61
- Figure 2.10: Resolved spectra resulting from MCR-ALS applied to Raman microspectroscopic imaging of a MSL grain. The MCR-ALS model was built with eight components. .... 63
- Figure 2.11: Resolved spectra resulting from MCR-ALS applied to Raman microspectroscopic imaging of a MSL grain. The MCR-ALS model was built with twelve components. .... 65
- Figure 2.12: Spatially-resolved chemical maps and resulting Raman spectra of TiO<sub>2</sub>-II generated using MCR-ALS applied to Raman microspectroscopic imaging of a grain from the MSL. The chemical maps and resolved spectrum shown in (a) were generated using 400 spectra (20 x 20 grid) obtained with 15 seconds of integration time and one co-average, termed “high spectral”. The chemical maps and resolved spectrum shown in (b) were generated using 10,000 spectra (100 x 100 grid) obtained using 1 second of integration time and no co-averages, termed “high spatial”. The results shown in (a) and (b) were both obtained using 50x magnification, 532 nm excitation, and a twenty component MCR-ALS model..... 67
- Figure 2.13: Raman spectra from synthetic TiO<sub>2</sub>-II using 785 nm excitation with a laser power of 1 to 100 mW (a) and 532 nm excitation with a laser power of 0.2 to 20 mW (b). In (c), an estimated Raman spectrum (in black) for pure TiO<sub>2</sub>-II is compared with a Raman spectrum (in pink) for synthetic TiO<sub>2</sub>-II. .... 72

- Figure 3.1: Backscattered electron (BSE) image (A) of a selected MSL grain. Raman spectra acquired with high spectral resolution (B) were collected at the corresponding numbered locations shown in blue (A). Raman spectra acquired with high spatial resolution (C) were collected at the corresponding numbered locations shown in red (A). ... 87
- Figure 3.2: Spatially-resolved chemical maps, spatially-resolved pixel-by-pixel chemical images, and resolved Raman spectra of rutile (B), TiO<sub>2</sub>-II (C), anatase (D), quartz (E), and substrate-adhesive epoxy (F) generated using MCR-ALS applied to Raman microspectroscopic imaging. The backscattered electron (BSE) image (A), optical image (A), and mean spectrum (black, A) +/- the standard deviation (+ in red, - in blue; A) are shown. Raman microspectroscopic imaging results were generated using 532 nm excitation and a 20 by 20 spectral grid. .... 90
- Figure 3.3: Spatially-resolved chemical maps, spatially-resolved pixel-by-pixel chemical images, and resolved Raman spectra of rutile (A), TiO<sub>2</sub>-II (B), anatase (C), quartz (D), and substrate-adhesive epoxy (E) generated using MCR-ALS applied to Raman microspectroscopic imaging. Raman microspectroscopic imaging results were generated using 532 nm excitation and a 100 by 100 spectral grid. .... 93
- Figure 4.1: Raman spectra of hematite (A) and carbonaceous material (C) using 532 nm excitation and Raman spectra of hematite (B) and carbonaceous material (D) using 785 nm excitation. .... 115
- Figure 4.2: Overlay of Raman spectra (A) of hematite (green), carbonaceous material (blue), and substrate-adhesive epoxy (grey) using 532 nm excitation. Overlay of Raman spectra (B) of hematite (green), carbonaceous material (blue), and substrate-adhesive epoxy (grey) using 785 nm excitation. .... 119
- Figure 4.3: Principal component analysis (PCA) plot (A) of the scores on the first principal component (PC 1; 66.42%) and the second principal component (PC 2; 14.65%) using 532 nm excitation. PCA plot (B) of the scores on PC1 (80.13%) and PC2 (11.69%) using 785 nm excitation. .... 122

- Figure 4.4: Spatially-resolved chemical maps and resolved Raman spectra of carbonaceous material (B), substrate-adhesive epoxy (C), and hematite (D) generated using MCR-ALS applied to Raman microspectroscopic imaging using 532 nm excitation. The optical image (A) and mean spectrum (black, A) +/- the standard deviation (+ in red, - in blue; A) are shown. A five-component MCR-ALS model was employed. .... 126
- Figure 4.5: Spatially-resolved chemical maps and resolved Raman spectra of carbonaceous material (B), substrate-adhesive epoxy (C), and hematite (D) generated using MCR-ALS applied to Raman microspectroscopic imaging using 785 nm excitation. The optical image (A) and mean spectrum (black, A) +/- the standard deviation (+ in red, - in blue; A) are shown. A five-component MCR-ALS model was employed. .... 129
- Figure 4.6: Spatially-resolved chemical maps and resolved Raman spectra of carbonaceous material (A), substrate-adhesive epoxy (B), and hematite (C) generated using MCR-ALS applied to the 532 nm excitation combinatorial data set. A five-component MCR-ALS model was employed. .... 134
- Figure 4.7: Spatially-resolved chemical maps and resolved Raman spectra of carbonaceous material (A), substrate-adhesive epoxy (B), and hematite (C) generated using MCR-ALS applied to the 785 nm excitation combinatorial data set. A five-component MCR-ALS model was employed. .... 137
- Figure 5.1: Polarized light microscopy images of LAP 02205 (a/b) and LAP 04841 (c/d). .... 161
- Figure 5.2: Results of MCR-ALS applied to Raman microspectroscopic imaging using 532 nm excitation of LAP 02205. Spatially-resolved chemical images and corresponding resolved Raman spectra of diamond-polish (b), pyroxene (c), and substrate-adhesive epoxy (d) are shown. The optical image (a) and mean spectrum (black, a) +/- the standard deviation (+ in red, - in blue; a) are shown. A five-component MCR-ALS model was employed. .... 169

- Figure 5.3: Results of MCR-ALS applied to Raman microspectroscopic imaging using 785 nm excitation of LAP 02205. Spatially-resolved chemical images and corresponding resolved Raman spectra of ilmenite (b), pyroxene (c), and substrate-adhesive epoxy (d) are shown. The optical image (a) and mean spectrum (black, a) +/- the standard deviation (+ in red, - in blue; a) are shown. A three-component MCR-ALS model was employed. .... 172
- Figure 5.4: Results of MCR-ALS applied to Raman microspectroscopic imaging using 532 nm excitation of LAP 04841. Spatially-resolved chemical images and corresponding resolved Raman spectra of pyroxene (b), pyroxene (c), pyroxene (d), troilite (e), and substrate-adhesive epoxy (f). The optical image (a) and mean spectrum (black, a) +/- the standard deviation (+ in red, - in blue; a) are shown. A five-component MCR-ALS model was employed. .... 178
- Figure 5.5: Results of MCR-ALS applied to Raman microspectroscopic imaging using 532 nm excitation of LAP 04841. Spatially-resolved chemical images and corresponding resolved Raman spectra of diamond-polish (b), pyroxene (c), substrate-adhesive epoxy (d), pyroxene (e), pyroxene (f) and high-temperature polymorphic anorthite (g). The optical image (a) and mean spectrum (black, a) +/- the standard deviation (+ in red, - in blue; a) are shown. A six-component MCR-ALS model was employed. .... 181

## ABSTRACT

Developing and applying analytical methodology, including the collection and subsequent analysis of chemical data, is critical for the scientific community at large. In this dissertation, innovative analytical methods, including microspectroscopy and microspectroscopic imaging, in conjunction with multivariate analysis methods and chemometric techniques are employed to fundamentally study the chemical properties of diverse, novel materials. Specifically, this dissertation will focus on three collaborative, multidisciplinary studies. First, the high-pressure,  $\alpha$ -PbO<sub>2</sub>-structured polymorph of titanium dioxide, termed TiO<sub>2</sub>-II, was investigated to understand ancient impact events on Earth. Raman microspectroscopy was used to identify, for the *first* time, TiO<sub>2</sub>-II in grains recovered from four Neoproterozoic (~2.5 billion years old) spherule layers—a discovery that has eluded researchers for nearly 30 years until now. By further investigating these grains using Raman microspectroscopic imaging with multivariate analysis methods, spatially-resolved chemical images and resolved Raman spectra of the individual chemical species within these complex grains were generated. The spatial resolution of the chemical images was increased using a pioneering strategy, and a Raman spectrum for pure TiO<sub>2</sub>-II was estimated for the *first* time. Second, a novel analytical methodology was utilized to enhance the search for life on Mars. In 2020, both the National Aeronautics and Space Administration (NASA) and the European Space Agency (ESA) have planned rover missions to Mars. The primary objective for both missions is the search for evidence of extant or past life. Using multivariate analysis methods with Raman microspectroscopic imaging, the

identification, differentiation, and resolution of chemical species relevant to Martian exploration was achieved. For the *first* time, organic carbon was spatially and spectrally resolved from hematite ( $\alpha$ -Fe<sub>2</sub>O<sub>3</sub>), a chemical species abundant on Mars and highly relevant for Martian exploration and discovery. Third, innovative analytical methodology was used to study extraterrestrial materials. The chemical properties of lunar meteorites, provided by the NASA Johnson Space Center, were elucidated using microspectroscopic imaging techniques with multivariate analysis. Spatially-resolved chemical maps with resolved Raman spectra of the pure chemical species within these heterogeneous meteorites were produced. Overall, this dissertation aims to move analytical chemistry in a transformative and innovative direction in ways that can benefit and interest the broader scientific community.

## Chapter 1

### INTRODUCTION

#### 1.1 Raman Spectroscopy

Spectroscopy, a pillar of analytical chemistry, concerns the interaction of electromagnetic radiation with matter. Typically, spectroscopic methods measure intensity of electromagnetic radiation as a function of wavelength or wavenumber to ultimately produce a spectrum for a given analyte of interest. Spectroscopic methods are commonly based on emission, absorption, fluorescence, or scattering phenomena. One of the principal spectroscopic methods based on scattering is Raman spectroscopy. Raman spectroscopy was established after a discovery by C.V. Raman in 1928 documenting that molecularly scattered radiation can differ from incident radiation, and this difference is dependent upon the molecular and chemical structure of the given analyte.[1] This discovery led to the Nobel Prize in physics being awarded to C.V. Raman in 1931. Since its initial discovery, Raman spectroscopy has revolutionized both the analytical chemistry and scientific community at large.

Raman spectroscopy fundamentally centers on the detection of inelastically scattered radiation of an analyte. Specifically, exposure of a sample using monochromatic radiation (**Figure 1.1**), typically from a laser source, produces both elastic scattering, termed Rayleigh scattering and inelastic scattering, termed Raman scattering. Subsequent to exposure of a sample with a laser of frequency  $\nu_{\text{ex}}$ , excitation to a virtual energy level and reemission of a photon with a different frequency and

energy is produced.[2-4] This photon can be emitted with a lower-frequency (and lower energy) of  $\nu_{\text{ex}} - \nu_{\text{v}}$ , termed Stokes scattering, the same frequency (and the same energy) of  $\nu_{\text{ex}}$  termed Rayleigh scattering, or with a higher-frequency (and higher energy) of  $\nu_{\text{ex}} + \nu_{\text{v}}$  termed anti-Stokes scattering (**Figure 1.1**).[2-4] At ambient conditions, Stokes scattering is more intense than anti-Stokes scattering because the ground vibrational energy level is more populated than the excited vibrational energy levels, in which at room temperature, Stokes and anti-Stokes scattering typically differ by an order of magnitude.[5, 6] Rayleigh scattering, which involves collisions between the molecule and photon with no energy loss, is more probable to occur than Raman scattering.[2-4] This is due to the energy transfer of molecules in the ground vibrational energy level to higher vibrational energy levels, followed by reemission to return to the ground vibrational energy level, is most likely.[2-4]

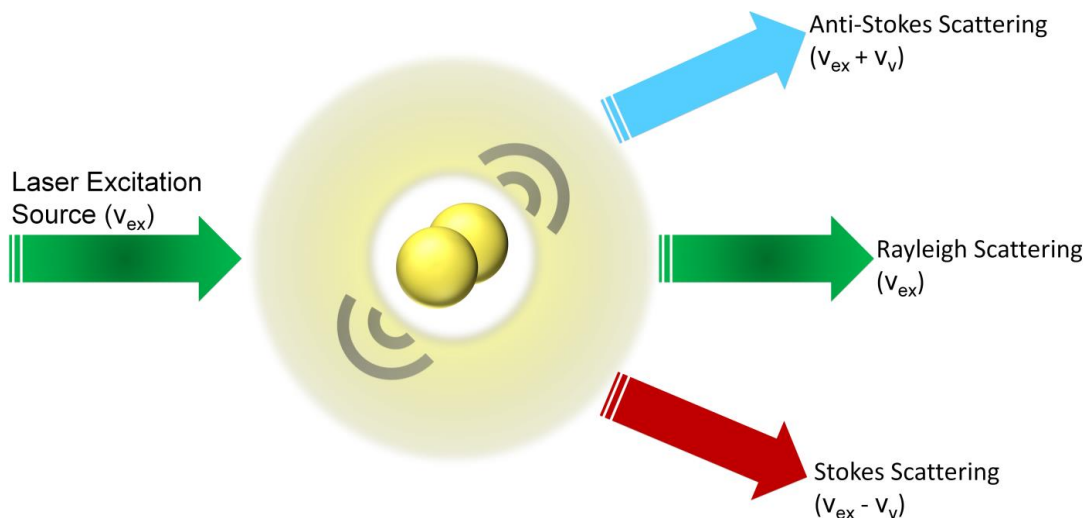


Figure 1.1: Scattering events at the molecular level. Inelastic scattering (Raman scattering) and elastic scattering (Rayleigh scattering) are depicted. After excitation of sample with monochromatic radiation of frequency  $\nu_{ex}$ , scattering with the same frequency  $\nu_{ex}$  can be observed, termed Rayleigh scattering. Inelastic scattering with either a lower-frequency of  $\nu_{ex} - \nu_v$ , termed Stokes scattering, or inelastic scattering with a higher-frequency of  $\nu_{ex} + \nu_v$  termed anti-Stokes scattering are generated.

Raman scattering is dependent upon several factors—the intensity of the incident radiation, the derivative of the polarizability of the analyte, and the frequency of the resulting scattered radiation.[5] The dependence upon the intensity of the incident radiation displays a dramatic increase with decreasing wavelength of excitation, yet this dependence often goes unused due to the common photodecomposition observed with ultraviolet excitation.[2-4] This results in the incident radiation for Raman scattering typically being in the visible or near-infrared regions. Additionally, the intensity of Raman scattering displays a fourth-power dependence on the frequency of the resulting scattered radiation.[5] However, this dependence is invalid if the excitation frequency,  $\nu_{ex}$ , is close to the frequency of an

electron transition.[5] In this case, significantly more intense scattering events are observed, termed resonance Raman scattering events.[5] Finally, for Raman scattering to occur, a change in the polarizability of the molecule during vibration is required. Unlike infrared spectroscopy, which requires a change in dipole moment or charge distribution of a molecule, Raman scattering involves the distortion of electrons located around a particular bond and scattering of radiation as during the return to its normal state.[2-4] Therefore, for Raman scattering, the molecule is polarized during this distortion, allowing for the inelastic scattering to occur.[2-4] Overall, the phenomenon of Raman scattering, which is dependent upon incident radiation intensity, polarizability of the analyte, and the frequency of the scattered radiation, can be harnessed for spectroscopic purposes.

Raman spectroscopy is widely used in a myriad of disciplines, including catalysis[7, 8], materials science[9-12], pharmaceuticals[13-15], biology and biomedicine[4, 16-18], cancer diagnosis[19, 20], engineering[21-23], food and drug analysis[24, 25], geological science[26, 27], environmental science[28, 29], and planetary science[30, 31]. The wide ranging applications of Raman spectroscopy stem from the unique advantages offered by this analytical technique. Specifically, Raman spectroscopy is a non-destructive, non-ionizing, and non-contact analytical technique that requires little to no sample preparation.[32] Raman spectroscopy can be performed on samples <1  $\mu\text{m}$  in size, and limits of detection in the picogram regime have been demonstrated using Raman spectroscopy with surface enhancements.[33] Due to the use of visible and near-infrared laser excitation sources for Raman spectroscopy, glass and quartz sample cells can be utilized. This allows for samples to be contained within transparent cells, including high-temperature and high-pressure

cells, to retain chemical information during *in situ* reactions or processes.[34] Raman spectroscopy can analyze gaseous, liquid, and solid samples. Aqueous solutions containing water can be analyzed using Raman spectroscopy due to water being Raman-inactive, allowing for biological or other aqueous samples to be analyzed without any additional sample preparation.[35] Finally, a main advantage of Raman spectroscopy is its high sensitivity to chemical and molecular structure, in which samples with the same elemental and chemical compositions with different molecular structure can be efficiently analyzed.[33] This allows for Raman spectroscopy to be employed to gain chemical, molecular, and structural information about an analyte of interest, including the differentiation and investigation of polymorphs of the same chemical composition.[36, 37] Almost all materials display Raman scattering, except pure metals, allowing for a variety of materials or analytes of interest to be investigated.[2-4]

## **1.2 Raman Microspectroscopic Imaging**

The advantages of Raman spectroscopy have led to recent advantages in the application of Raman spectroscopy on the micrometer-scale, termed Raman microspectroscopy.[38, 39] One of the primary uses of Raman microspectroscopy is in the application of chemical imaging.[5, 39-41] Performing chemical imaging using Raman microspectroscopy, termed Raman microspectroscopic imaging, has recently gained momentum throughout the scientific community, including for applications in chemical imaging of novel carbonaceous materials[42, 43], imaging of extraterrestrial materials[44], label-free, non-invasive imaging of biological materials[45], cell imaging for drug targeting[46], *in vivo* biomarker detection[47], and pharmacokinetics

for cancer detection in living cells[48]. Raman microspectroscopic imaging is typically employed using a Raman microscope (**Figure 1.2**). A Raman microscope is commonly equipped with a laser excitation source, which directs monochromatic radiation onto a sample using a series of scanning mirrors and an objective lens. The use of an objective lens allows for micrometer-sized probing areas to be produced onto a sample. After excitation of a sample with a probing area in the micrometer-regime, the resulting scattered radiation is dispersed back through the objective lens, filtered through a notch filter and a slit or confocal pinhole aperture, dispersed onto a grating-based spectrometer, and finally detected using a charge coupled device (CCD) detector. A Raman microscope also has a movable sample stage, in which this sample stage can be controllably posited on specific locations on a sample with micrometer precision to collect Raman spectra with a defined, independent spatial location. Using this instrumental design, Raman microspectroscopic imaging can be performed with ease, and ultimately, a Raman microscope can provide extensive analysis of the locations about a sample with micrometer-sized, spatially-resolved probing regions.

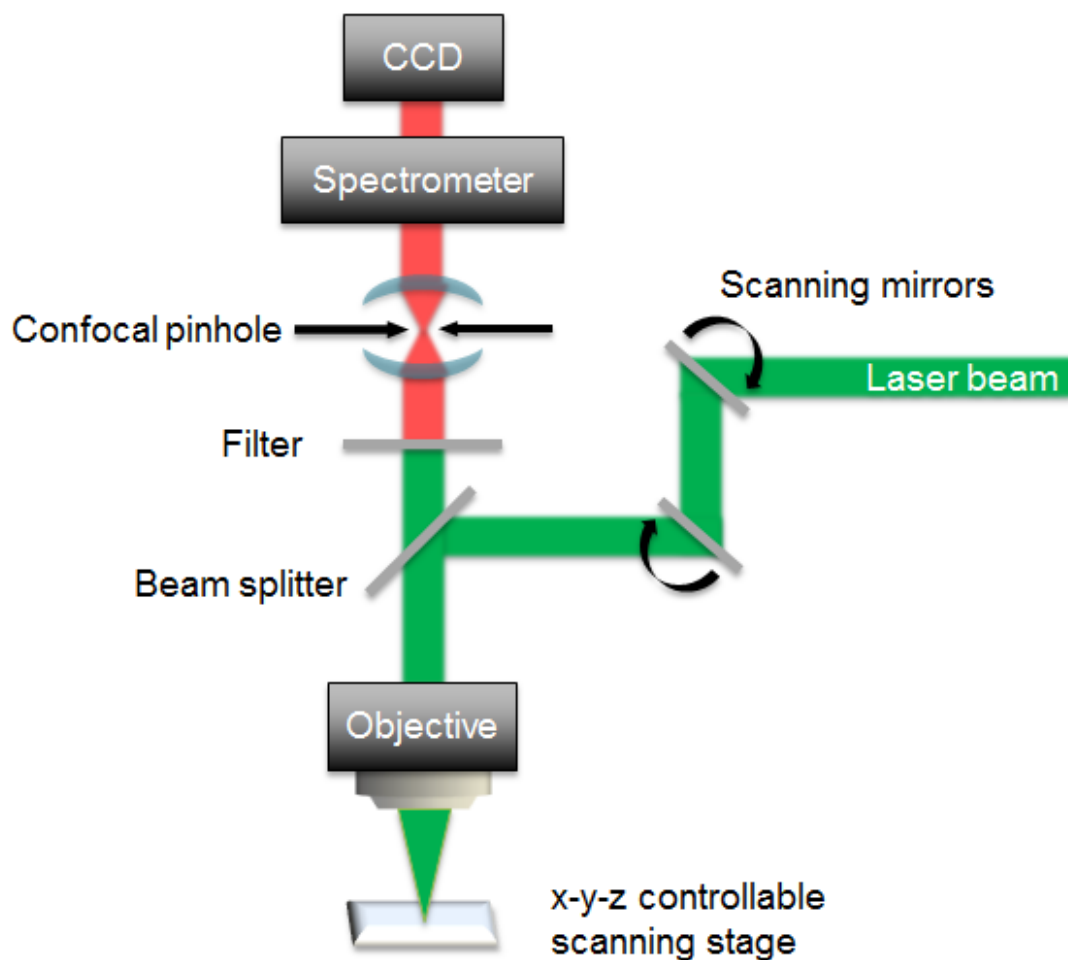


Figure 1.2: Schematic of a typical Raman microscope used to perform Raman microspectroscopy and Raman microspectroscopic imaging.

The basis of Raman microspectroscopic imaging entails defining specific locations on a sample to collect Raman spectra. Typically, this is accomplished by employing spectral grids that contain hundreds, thousands, or even millions of independent Raman spectra (**Figure 1.3**). Moreover, analysis of the Raman microspectroscopic imaging data that contain these Raman spectra results in the formation of chemical and molecular images concerning the chemical species within

the probing area. The primary use of Raman microspectroscopic imaging is therefore for the collection of spatially-resolved chemical information about a sample. Since Raman microspectroscopic imaging produces multidimensional analytical information, including x and y spatial information with  $\nu$  ( $\text{cm}^{-1}$ ) spectral information, samples can be spatially and spectrally characterized given the unique advantages of Raman microspectroscopy. Furthermore, the advantages of Raman microspectroscopic imaging include characterizing chemical composition and molecular structure, high-specificity, high sensitivity, non-destructive, non-ionizing, non-contacting, limited sample preparation, low sensitivity to water, small probing area, low limits of detection, utilizing with quartz and glass cells, and high materials availability for analyses.[5, 40, 49] Overall, Raman microspectroscopic imaging generates extensive spatial and spectral data about a sample, and through analysis of this collected data, visualization of chemical, molecular, and structural information about the sample can be obtained.

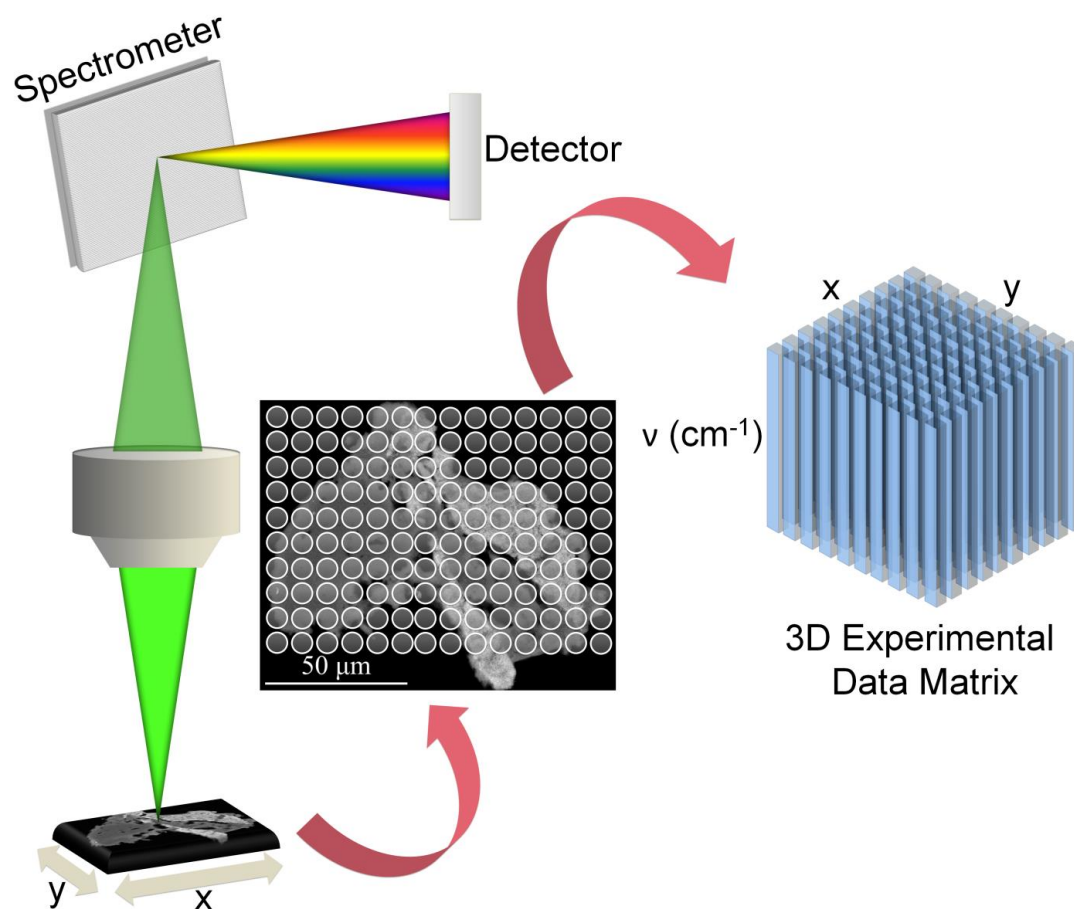


Figure 1.3: Using Raman microspectroscopy at defined spatial locations, termed Raman microspectroscopic imaging, to investigate the chemical and molecular properties of the sample. Raman microspectroscopic imaging generates extensive data sets containing spatial (x and y) with spectral information ( $\nu$ ) about the sample, encompassed within the three-dimensional experimental data matrix.

### 1.3 Multivariate Analysis Methods and Chemometrics

The analysis of the collected spectroscopic data is essential for providing spatially-resolved chemical and molecular information about a sample. Traditionally, Raman microspectroscopic imaging is performed using univariate analysis methods.

Univariate analysis methods generate “heat” or intensity maps based on the integration or amplitude of a characteristic Raman band of a known analyte of interest within a sample. However, by using univariate analysis methods, interference effects can significantly influence the data.[50-52] For example, if a mixed sample contains chemical species with overlapping spectral features or contains potentially unknown chemical species, univariate analysis methods can provide a limited or inaccurate analysis.[50-52] Spectral overlap being present amongst chemical species is a common occurrence when performing Raman microspectroscopic imaging and the inadequacy of univariate analysis methods is demonstrated (**Figure 1.4**). If the three-dimensional experimental data matrix, containing spatial (x and y) and spectral (v) information about a sample, has spectral overlapping species and is analyzed using univariate analysis methods (**Figure 1.4**), the integration of one particular wavenumber region for the analyte of interest is inaccurate. This is due to the fact that if spectral overlap is present, the integration of these overlapping bands will not produce a chemical image for the analyte of interest. Rather, the resulting chemical image will represent the distribution of the analyte of interest along with the other chemical species that display overlapping spectral features. For example, if Raman microspectroscopic imaging data is generated on a sample containing the three chemical species of rutile ( $\text{TiO}_2$ ), quartz ( $\text{SiO}_2$ ), and  $\text{TiO}_2$ -II ( $\text{TiO}_2$ ), which display spectral overlap, and univariate analysis methods are employed (**Figure 1.4**) to generate a chemical image for the distribution of rutile—by integrating the  $440\text{ cm}^{-1}$  Raman band of rutile—the resulting distribution will not only be characteristic of rutile, but also be heavily influenced by quartz (from the  $464\text{ cm}^{-1}$  band) and  $\text{TiO}_2$ -II (from the  $426\text{ cm}^{-1}$  band). Therefore, univariate analysis of Raman microspectroscopic

imaging data containing chemical species that display spectral overlap produces chemical images that are not entirely representative of the analyte of interest.

Univariate analysis methods can also allow for critical chemical information to go unnoticed and unused.[50-52] This is the result of the interference effects commonly observed in Raman microspectroscopic imaging data that univariate analysis methods fail to compensate for, including background interference, fluorescence, laser power fluctuations, loss of focus, sample roughness, sample opacity, and optical alignment.[50-52] Multivariate analysis methods and chemometric analysis, however, can address these common interference effects, and provide increased sensitivity and selectivity, enhanced visualization, and significant data reduction when used in conjunction with Raman microspectroscopic imaging.[50-52] Thus, multivariate analysis methods applied to Raman microspectroscopic imaging data can be used to both identify the chemical species present within an unknown sample and discern a representative distribution of the chemical species.[50, 53-55]

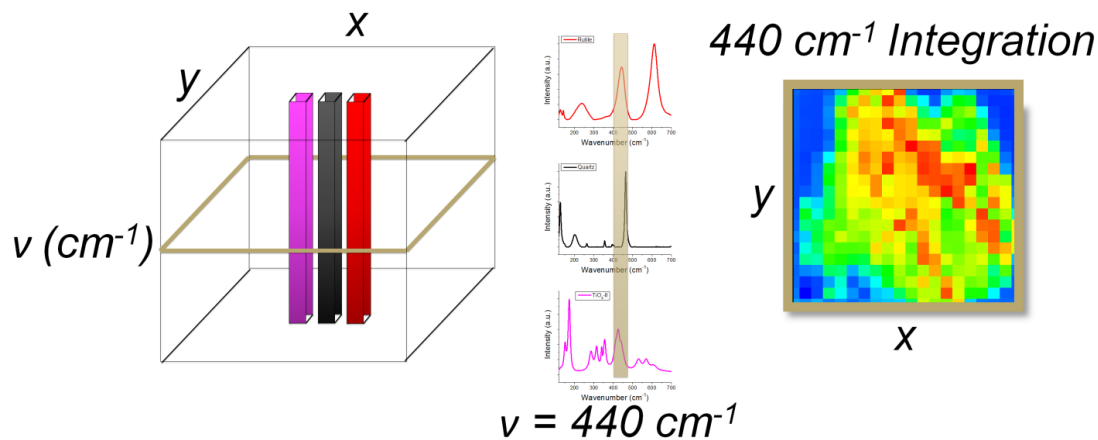


Figure 1.4: The analysis of Raman microspectroscopic imaging data by univariate analysis methods. Using univariate analysis methods, the integration of a particular band, in this case the  $440 \text{ cm}^{-1}$  band of rutile (red), generates a chemical image. If spectral overlap is present within this spectral region—such as the  $464 \text{ cm}^{-1}$  of quartz (black) and the  $426 \text{ cm}^{-1}$  band of  $\text{TiO}_2\text{-II}$  (pink)—univariate analysis methods fail to provide a representative distribution of the analyte of interest—rutile (red).

The application of mathematical and statistical analysis to spectroscopic data in order to most effectively extract chemical information is termed multivariate analysis or chemometrics. The field of multivariate analysis and chemometrics has an underlying goal of determining the best analytical methodology to study chemical problems. This centers around establishing the most appropriate strategy for collecting chemical data and subsequently analyzing the collected chemical data. Moreover, multivariate analysis and chemometrics play a role in both optimizing current analytical methodology and leading in the development of new analytical methodology. In this dissertation, the application of multivariate analysis and chemometrics to spectroscopic data, especially Raman microspectroscopic imaging

data, to most effectively solve and understand complex chemical systems will be explored.

#### **1.4 Multivariate Curve Resolution-Alternating Least Squares (MCR-ALS)**

A variety of multivariate analysis methods have been used to evaluate Raman microspectroscopic imaging data, including multivariate curve resolution-alternating least squares (MCR-ALS), principal component analysis (PCA), cluster analysis, neural networks, partial least squares (PLS), and direct classical least squares (DCLS).[50, 56-58] Specifically, multivariate curve resolution (MCR) is a class of multivariate analysis methods commonly used to solve mixture analysis. Multivariate curve resolution specifically provides a bilinear description of raw, experimental data of a mixture into meaningful profiles of the pure chemical species. Multivariate curve resolution was first described in chemical applications by Lawton and Sylvester for the resolution of the ultraviolet-visible spectra of two dye molecules.[59] After its initial use in chemistry, MCR was coupled with iterative methods, such as alternating least squares (ALS), to resolve mixed chemical information.[60] Using MCR-ALS in conjunction with physically meaningful constraints, including non-negative concentration and non-negative spectral features, this multivariate analysis method gained traction in the scientific community and was able to efficiently resolve complex, heterogeneous chemical systems.[51, 52, 55, 61, 62]

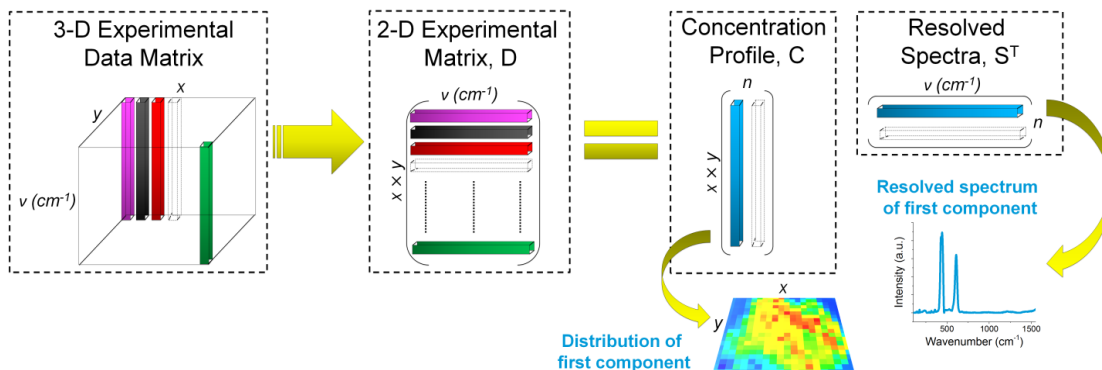


Figure 1.5: Multivariate curve resolution-alternating least squares (MCR-ALS) applied to Raman microspectroscopic imaging. The experimental data generated from Raman microspectroscopic imaging contains three-dimensional (3-D) information—spatial information ( $x$  and  $y$ ) and spectral information ( $\nu$ ). This 3-D experimental data is unfolded into a two-dimensional (2-D) experimental matrix,  $D$ , with spatial information (both  $x$  and  $y$  together) and spectral information ( $\nu$ ). Using MCR-ALS, the concentration profile matrix,  $C$ , and the resolved spectra matrix,  $S^T$ , can be resolved. These matrices ultimately allow for the generation of spatially-resolved chemical images and corresponding resolved Raman spectra for each individual, pure chemical species within a sample.

Multivariate curve resolution-alternating least squares has recently gained momentum in the scientific community for its use with Raman microspectroscopic imaging.[54, 55, 62-66] Specifically, MCR-ALS provides spatially and spectrally resolved chemical information from Raman microspectroscopic imaging data using a simple, additive bilinear model of pure contributions.[55, 61, 65] Multivariate curve resolution-alternating least squares applied to Raman microspectroscopic imaging can ultimately provide the distribution and resolved spectra for each individual, pure chemical species within a given system (**Figure 1.5**). Specifically, MCR-ALS with Raman microspectroscopic imaging begins with the generation of three-dimensional (3-D) experimental data from Raman microspectroscopic imaging.[51, 52, 55, 61, 62]

This 3-D experimental data matrix contains chemical information of both spatial (x and y) and spectral ( $\nu$ ) origin. By unfolding the 3-D experimental data matrix into a two-dimensional (2-D) experimental matrix containing the spatial information in one direction (both x and y) and the spectral information ( $\nu$ ) in the other direction, the bilinear MCR-ALS model can be employed.[51, 52, 55, 61, 62] Moreover, physically meaningful constraints, such as non-negativity of concentrations and spectra, can be applied during the MCR-ALS process to resolve both the concentration profile matrix and the resolved spectra matrix.[51, 52, 55, 61, 62] Subsequent refolding of the concentration profile matrix into its distinct spatial information (x and y separately) produces spatially-resolved chemical images displaying the distribution of the individual chemical species present within the experimental data.[51, 52, 55, 61, 62] Moreover, the resolved spectra matrix contains each corresponding resolved Raman spectra for the individual, pure chemical species present within the experimental data.[51, 52, 55, 61, 62] Overall, using the multivariate analysis method MCR-ALS in conjunction with Raman microspectroscopic imaging, spatially-resolved chemical images and corresponding resolved Raman spectra of the individual, pure chemical species within a heterogeneous, complex mixture can be deduced.

### **1.5 Combining Multivariate Analysis with Raman Microspectroscopic Imaging**

In this dissertation, the development and application of analytical methodology centering around both multivariate analysis methods, namely MCR-ALS, and Raman microspectroscopic imaging was accomplished for the investigation of diverse, novel materials. Both Raman microspectroscopic imaging and multivariate methods have recently gained tremendous momentum in the scientific community (**Figure 1.6**),

culminating into an exponential rate of growth since ~1990 for both analytical techniques. Specifically, the combination of multivariate analysis methods with Raman microspectroscopic imaging and Raman microspectroscopy will be utilized in this dissertation to fundamentally study the chemical properties of diverse materials.

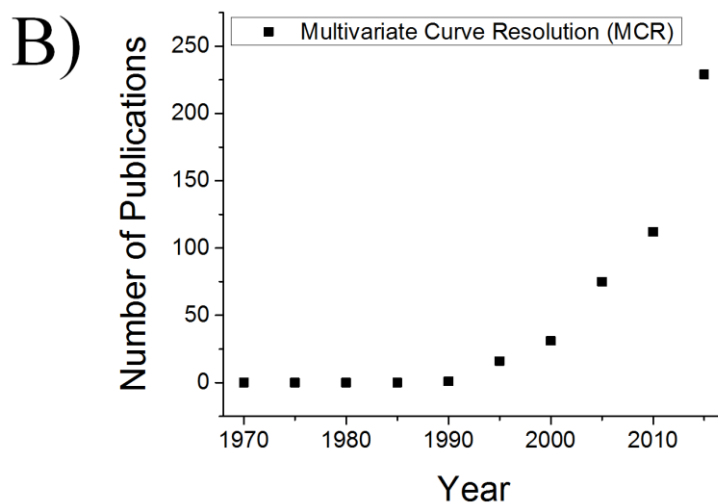
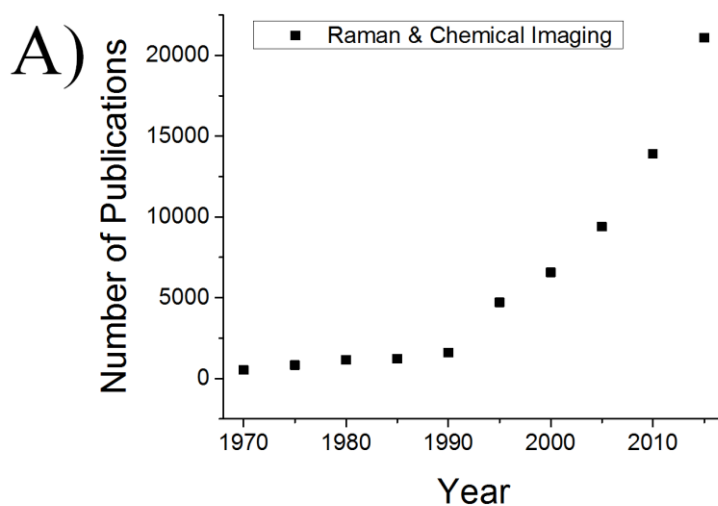


Figure 1.5: The number of peer-reviewed publication per year for Raman & Chemical Imaging (A) and multivariate curve resolution (B) per year. Data of the publications for each year are from Web of Science (<https://webofknowledge.com/>).

Overall, this dissertation aspires to move analytical chemistry in a transformative and innovative direction in ways that can benefit the broader scientific community. A wide range of complex chemical systems will be fundamentally studied

for the *first* time using Raman microspectroscopic imaging with multivariate analysis. Specifically, this dissertation will focus on the three primary research topics and studies. In chapter two, the investigation of a high-pressure polymorph of titanium dioxide, termed TiO<sub>2</sub>-II, using microscopic, spectroscopic, and chemical imaging techniques with multivariate analysis are presented. In chapter three, Raman microspectroscopic imaging data containing both high spectral and high spatial resolution are evaluated using MCR-ALS, including the presentation of the importance of this Raman microspectroscopic imaging data to the scientific community. In chapter four, the spatial and spectral resolution of carbonaceous material from hematite ( $\alpha$ -Fe<sub>2</sub>O<sub>3</sub>) using multivariate analysis with Raman microspectroscopic imaging is accomplished. The implications of this analytical methodology for the search for life on Mars are also offered in chapter four. In chapter five, two lunar meteorites are investigated using Raman microspectroscopic imaging with multivariate analysis methods, in which the chemical properties of these lunar meteorites are elucidated. Finally, in chapter six, the conclusions and future directions of the research presented in this dissertation are described.

## Chapter 2

### **RAMAN MICROSPECTROSCOPIC IMAGING WITH MULTIVARIATE CURVE RESOLUTION-ALTERNATING LEAST SQUARES (MCR-ALS) APPLIED TO THE HIGH-PRESSURE POLYMORPH OF TITANIUM DIOXIDE, TiO<sub>2</sub>-II**

#### **2.1 Abstract**

The high-pressure,  $\alpha$ -PbO<sub>2</sub>-structured polymorph of titanium dioxide (TiO<sub>2</sub>-II) was recently identified in micrometer-sized grains recovered from four Neoproterozoic spherule layers deposited between ~2.65 and ~2.54 billion years ago. Several lines of evidence support the interpretation that these layers represent distal impact ejecta layers. The presence of shock-induced TiO<sub>2</sub>-II provides physical evidence to further support an impact origin of these spherule layers. Detailed characterization of the distribution of TiO<sub>2</sub>-II in these grains may be useful for correlating the layers, estimating the paleodistances of the layers from their source craters, and providing insight into the formation of the TiO<sub>2</sub>-II. In this chapter, we report the investigation of TiO<sub>2</sub>-II-bearing grains from these four spherule layers using multivariate curve resolution-alternating least squares (MCR-ALS) applied to Raman microspectroscopic imaging. Raman spectra provide evidence of grains consisting primarily of rutile (TiO<sub>2</sub>) and TiO<sub>2</sub>-II, as shown by Raman bands at 174 cm<sup>-1</sup> (TiO<sub>2</sub>-II), 426 cm<sup>-1</sup> (TiO<sub>2</sub>-II), 443 cm<sup>-1</sup> (rutile), and 610 cm<sup>-1</sup> (rutile). Principal component analysis (PCA) yielded a predominantly three phase system comprised of rutile, TiO<sub>2</sub>-II, and substrate-adhesive epoxy. Scanning electron microscopy (SEM) suggests heterogeneous grains containing polydispersed micrometer- and submicrometer-sized

particles. MCR-ALS applied to the Raman microspectroscopic imaging yielded up to five distinct chemical components—three phases of  $\text{TiO}_2$  (rutile,  $\text{TiO}_2$ -II, and anatase), quartz ( $\text{SiO}_2$ ), and substrate-adhesive epoxy. Spectral profiles and spatially-resolved chemical maps of the pure chemical components were generated using MCR-ALS applied to the Raman microspectroscopic maps. The spatial resolution of the Raman microspectroscopic maps was enhanced in comparable, cost-effective analysis times by limiting spectral resolution and optimizing spectral acquisition parameters. Using the resolved spectra of  $\text{TiO}_2$ -II generated from MCR-ALS analysis, a Raman spectrum for pure  $\text{TiO}_2$ -II was estimated to further facilitate its identification.

## 2.2 Introduction

Titanium dioxide ( $\text{TiO}_2$ ) is an extensively studied semiconductor oxide due to its proven capability with respect to environmental purification processes, water-splitting reactions, pigments, ultraviolet filtration and protection, photovoltaic solar cells, and photocatalysis.[67-70]  $\text{TiO}_2$  has a wide range of uses because of its optical and photocatalytic properties, inexpensive cost, and widespread natural availability. There are three main polymorphs of natural  $\text{TiO}_2$ : rutile (tetragonal), anatase (tetragonal), and brookite (orthorhombic), with rutile being the most abundant polymorph.[71] Anatase and the relatively rare brookite are generally the low-temperature and low-pressure  $\text{TiO}_2$  polymorphs.[72] At ambient pressure, anatase and brookite are stable up to 600 °C and 700 °C, respectively.[72] The transformation of bulk anatase to rutile is thermodynamically favorable at temperatures between 0 and 1300 K, and rutile is the stable polymorph of bulk  $\text{TiO}_2$  over a wide temperature range at ambient pressure.[72] When these polymorphs are subjected to temperatures and

pressures in the 400-1500 °C and 4-12 GPa regime, high-pressure polymorphs of TiO<sub>2</sub> can be produced.[73-75]

Five high-pressure polymorphs of TiO<sub>2</sub> are presently known: (1) an orthorhombic  $\alpha$ -PbO<sub>2</sub>-structured polymorph (TiO<sub>2</sub>-II, space group *Pbcn*); (2) a monoclinic baddeleyite-structured polymorph (MI, space group *P2<sub>1</sub>/c*); (3) an orthorhombic polymorph (TiO<sub>2</sub>-OI, space group *Pbca*); (4) a cubic polymorph (space group *Fm3m* & *Pa3*); and (5) an orthorhombic cotunnite-structured polymorph (TiO<sub>2</sub>-OII, space group *Pnma*).[76, 77] Among the high-pressure polymorphs, TiO<sub>2</sub>-II is especially important due to its relative stability at both ambient pressure and temperature.[78] With recent advances in its synthesis, TiO<sub>2</sub>-II has shown initial promise with respect to its photocatalytic and optical activity and has shown increasing promise for applied uses in catalytic and photovoltaic processes.[78, 79]

In nature, TiO<sub>2</sub>-II has been found as a minor phase in ultrahigh-pressure (UHP) metamorphic rocks[80, 81] and minerals [82, 83], and in shock-metamorphosed rocks and grains associated with three confirmed impact structures[84-86] and a confirmed distal impact ejecta layer.[87] The precursor phases for the shock-induced TiO<sub>2</sub>-II associated with the impact structures appear to have been rutile [84-86] and possibly anatase [85]. Recently, grains (~100  $\mu$ m in size) containing rutile and TiO<sub>2</sub>-II have been documented from four Neoproterozoic spherule layers deposited between ~2.65 and ~2.54 billion years ago (Ga).[88] These grains, which comprise the samples for the present study, represent a new geological context for TiO<sub>2</sub>-II.

These four layers are part of a larger set of ~17 spherule layers, deposited between ~3.47 and ~2.49 Ga, that have been documented within stratigraphic successions in South Africa and Western Australia.[89, 90] The layers contain varying

amounts of mostly spheroidal, millimeter-sized and smaller spherules, many of which show internal textures indicative of formation by rapid cooling or quenching of a melt.[89-91] The spherules are interpreted as having formed from melt ejecta and/or by condensation of rock vapor clouds produced by large impact events.[89-92] In addition to the spherules, several lines of geologic, petrologic, geochemical and isotopic evidence strongly support the interpretation that these early Precambrian spherule layers represent distal impact ejecta layers.[89-91, 93-95]

A long-standing conundrum for the impact origin of the early Precambrian spherule layers has been the near absence of documented shock-metamorphosed grains within them. Prior to the study of [88], only a single shock-metamorphosed grain (quartz) had been documented[96] from these layers. Using Raman microspectroscopy, Smith et al.[88] documented TiO<sub>2</sub>-II in 34 rutile grains recovered from the Carawine spherule layer (CSL), Jeerinah spherule layer (JSL), and Bee Gorge spherule layer (BGSL) in Western Australia, and Monteville spherule layer (MSL) in South Africa. Detailed geological descriptions of these four spherule layers are given in [89]. These TiO<sub>2</sub>-II-bearing grains were interpreted as shock-metamorphosed rutile grains that provide unambiguous physical evidence to further support an impact origin for the four spherule layers[88]. These grains demonstrate that TiO<sub>2</sub>-II can survive for more than 2.5 billion years.[88] The TiO<sub>2</sub>-II in these grains is apparently the first documented shock-induced high-pressure polymorph produced by Archean (>2.5 Ga) impact events.[88]

Several of the early Precambrian spherule layers in Western Australia have been correlated with spherule layers in South Africa.[89] However, correlating spherule layers is not an easy task and requires multiple lines of evidence.[97] It has

been proposed[97] that the JSL correlates with both the CSL and the MSL, and if so, these three layers would be the result of a single impact event that occurred ~2.63 Ga. Correct correlation of the early Precambrian spherule layers is especially important, since at the present time, they provide the best and virtually only record of impact events that occurred on Earth prior to ~2.4 Ga[89], and they have been used to constrain models of the impactor flux in the inner Solar System during the time period of ~3.47 to ~2.49 Ga.[90, 92, 98] Therefore, detailed characterization of the distribution of TiO<sub>2</sub>-II in the shock-metamorphosed rutile grains from the four spherule layers may provide a new approach to correlating the layers, may be useful for estimating the paleodistances of the layers from their source craters, and may provide insight into the formation of the TiO<sub>2</sub>-II.

The transformation of TiO<sub>2</sub> to TiO<sub>2</sub>-II is kinetically and thermodynamically limited.[78, 99] Moreover, the rutile/TiO<sub>2</sub>-II phase equilibrium is linear after an initial thermal activation process[99], and static high-pressure experiments estimate rutile transforms to TiO<sub>2</sub>-II at pressures of 4-12 GPa in the temperature range of 400-1500 °C. [73-75] Furthermore, shock-loading experiments suggest that rutile transforms to TiO<sub>2</sub>-II at pressures of 15-125 GPa.[100-102] In both synthetic and natural TiO<sub>2</sub>-II-bearing samples, evidence of precursory TiO<sub>2</sub> has been consistently reported.[84, 86, 101, 103, 104] Identifying naturally occurring *pure* TiO<sub>2</sub>-II and obtaining a Raman spectrum of *pure* TiO<sub>2</sub>-II have thus been elusive tasks. Here we report the means by which to discern TiO<sub>2</sub>-II using an uncontaminated Raman spectrum, and to identify and deconvolve TiO<sub>2</sub>-II and other TiO<sub>2</sub> polymorphs within complex materials both spatially and spectrally. Using Raman microspectroscopic imaging in conjunction with multivariate data analysis, including multivariate curve resolution-alternating least

squares (MCR-ALS) and principal component analysis (PCA), we demonstrate the ability to determine the spatial distribution and resolved spectra of individual chemical species and provide an estimation of the Raman spectrum of *pure* TiO<sub>2</sub>-II.

Raman microspectroscopic imaging has been applied to a myriad of research areas and can be used to collect spatially resolved molecular and chemical information.[65, 105-108] Multivariate analysis methods, including PCA, MCR-ALS, cluster analysis, neural networks, and PLS classifier, applied to Raman microspectroscopic imaging can be used to both identify the chemical species present and discern a more representative distribution of each chemical species than traditional univariate analysis methods.[50, 53-58, 65] Specifically, MCR-based methods provide a chemically meaningful additive bilinear model of pure contributions, and when used with spectroscopic imaging, resolved spatial and spectral information is produced.[61, 63, 109-112] To our knowledge, we are the first to report the use of multivariate data analysis, mainly MCR-ALS methods, applied to Raman microspectroscopic imaging measurements to determine the distribution of TiO<sub>2</sub>-II in shock-metamorphosed grains that resulted from Archean impact events.

Using MCR-ALS and Raman microspectroscopic imaging, spectral profiles and spatially-resolved chemical maps of the individual chemical species—rutile, TiO<sub>2</sub>-II, anatase, quartz, and substrate-adhesive epoxy—were generated. We discuss the ability to increase the spatial resolution of the chemical maps generated by Raman microspectroscopic imaging and MCR-ALS by limiting the spectral resolution and optimizing spectral acquisition parameters. Finally, a Raman spectrum for *pure* TiO<sub>2</sub>-II was estimated using the resolved spectra generated from MCR-ALS in order to further facilitate the identification of TiO<sub>2</sub>-II within complex materials. Using the

analytical methodology employed in this chapter, we discuss the potential use of Raman microspectroscopic imaging with multivariate methods for the broader chemical and geological communities.

## **2.3 Materials and Methods**

### **2.3.1 Sample Preparation**

All samples were carbonate-rich rocks collected from surface outcrops of the CSL, JSL, BGSL, and MSL. Details of sample location, lithology, and preparation are given in Smith et al.[88] In brief, the surface outcrop samples (~kg samples) were trimmed into smaller rock samples, rinsed with water, and dried at 60-70 °C for at least 12 hrs. Sample weights ranged from ~5-5151 g. Due to the high carbonate content in the samples, hydrochloric acid (Fisher Scientific, 12.1 N) digestion at ~60 °C was employed. After acid dissolution, the solution was equilibrated to a neutral pH by dilution, and the acid-insoluble residues were wet sieved in conjunction with ultrasonic agitation into five size fractions— <38 μm, 38-63 μm, 63-125 μm, 125-250 μm, and >250 μm. The 63-125 μm size fractions underwent heavy liquid ( $\rho = 2.96 \text{ g/cm}^3$ ) separation with 1,1,2,2-tetrabromoethane (Fisher Scientific, 99 %). The heavy mineral separates were collected on filter paper (Whatman, 11 μm pore size). The filters were rinsed with acetone (Fisher Scientific, 99%) to remove the 1,1,2,2-tetrabromoethane.

Grain mounts of selected TiO<sub>2</sub>-II-bearing grains identified by Smith et al.[88] were made. Selected grains were fixed to a glass microscope slide (Fisher Scientific, 25.4 mm diameter x 1.0 mm thick) by epoxy (Buehler). Polishing was employed using

paper strips of varying coarseness (600  $\mu\text{m}$  to 3  $\mu\text{m}$ ) and a water/detergent/glycerol solution (~70/15/15 v/v %) to not only expose the grains from the substrate-adhesive epoxy coating, but to provide a cross-sectional representation of the grain. A final polish was completed using 0.05  $\mu\text{m}$ -sized  $\text{Al}_2\text{O}_3$  powder (Excel Metallurgical, Inc., 99%) wetted with water. All samples are thus cross-sections of 63-125  $\mu\text{m}$ -sized grains.

Synthetic  $\text{TiO}_2\text{-II}$ , obtained from K. Spektor (Stockholm University), was synthesized using the procedure outlined in [78]. In brief, static-hydrothermal conditions were used to form  $\text{TiO}_2\text{-II}$  from rutile powder at a pressure of 10 GPa and a temperature of 500  $^\circ\text{C}$ .

### **2.3.2 Scanning Electron Microscopy (SEM)**

Backscattered electron (BSE) and secondary electron (SE) images were obtained for  $\text{TiO}_2\text{-II}$ -bearing grains in the uncoated polished grain mounts. These images were collected using an FEI Quanta 450 FEG scanning electron microscope operated at low vacuum and 10-30 kV.

### **2.3.3 Raman Microspectroscopic Imaging**

Raman microspectroscopic imaging was performed using a Senterra Raman spectrometer (Bruker Optics, Massachusetts, USA) coupled to a BX-51 microscope (Olympus, New York, USA). An excitation source of 532 nm was used. The laser was focused onto the sample using 20 $\times$ , 50 $\times$ , and 100 $\times$  close-working-distance objective lenses (Olympus, New York, USA) with numerical apertures of 0.40, 0.75, and 0.80, respectively. Furthermore, using the 20 $\times$ , 50 $\times$ , and 100 $\times$  objective lenses, the resulting probing area of the laser is 5  $\mu\text{m}$ , 2  $\mu\text{m}$ , and 1  $\mu\text{m}$  in diameter. The scattered light was

collected by the objective lens and dispersed by a 1200 grooves/mm grating onto a thermoelectrically-cooled charge-coupled device (CCD) detector (Bruker Optics, Massachusetts, USA) operated at a temperature of  $-65\text{ }^{\circ}\text{C}$ . The sample was kept at a constant nominal power ranging from 2 to 10 mW. Exposure times of 1 to 15 seconds were used with 3 co-averages. Background measurements were collected prior to each acquisition. For each Raman spectrum, the total collection time was  $\sim 6$  to 90 seconds. The spectral window was from  $70$  to  $1550\text{ cm}^{-1}$  and was covered under one grating position. During each Raman spectral acquisition, source wavelength and Raman shift calibration was internally performed using a neon lamp. The spectral resolution produced was  $3$  to  $5\text{ cm}^{-1}$ .

Using optimal spectral parameters, grids of Raman spectral acquisition points were selected to generate the Raman microspectroscopic maps. The shape of the spectral grids was generally rectangular and determined by the dimensions of the particular grain. The step size between Raman spectral acquisition points ranged from  $\sim 1$  to  $4\text{ }\mu\text{m}$ . Spectral grids consisting of 15-by-15 spectra, 20-by-20 spectra, 30-by-30 spectra, and 100-by-100 spectra were collected, and thus, maps were generated from spectral grids consisting of 225 to 10,000 Raman spectra. For all Raman spectral acquisitions, the  $z$  direction was held constant, and the  $x$  and  $y$  positions were controlled using a movable stage on the Raman microscope spectrometer.

The Raman spectra were collected and initial univariate data analysis methods were performed using the OPUS 7.2 program (Bruker Optics, Massachusetts, USA). Furthermore, OPUS 7.2 was used for initially estimating the identity and subsequent distribution of major chemical species (i.e.,  $\text{TiO}_2$ -II and rutile) in the sample.

### **2.3.4 Multivariate Data Analysis**

The analysis of Raman microspectroscopic imaging data is crucial for its ability to provide spatially and spectrally resolved chemical information. Traditionally, univariate methods are used to analyze spectroscopic imaging techniques, in which the scattering intensity at one particular wavenumber is used as the diagnostic for the analyte of interest. By using univariate methods, however, interference effects can significantly influence the data, and potentially useful information from the spectroscopic imaging data goes unused. Furthermore, these interference effects include background interference, fluorescence, laser power fluctuation, loss of focus, sample roughness, sample opacity, optical alignment, and overlapping Raman bands. By using multivariate analysis techniques, these interference effects can not only be addressed, but these techniques provide the additional advantages of greater sensitivity (by means of signal to noise ratio), greater selectivity, enhanced visualization of chemical distribution, and orders of magnitude data reduction when applied to spectroscopic imaging data. The two primary multivariate analysis methods employed in this chapter are principal component analysis (PCA) and multivariate curve resolution-alternating least squares (MCR-ALS).[50, 53-55, 57, 61, 113] Both PCA and MCR-ALS were performed using Matlab 7.2 (Mathworks, Massachusetts, USA). The PLS Toolbox (Eigenvector Research Incorporated, Washington, USA) was used as the graphical interface to perform both PCA and MCR-ALS, in which the PLS Toolbox is used as an add-on through Matlab.

#### **2.3.4.1 Principal Component Analysis (PCA)**

PCA is used for reducing the dimensionality of the experimental data from hundreds of spectral data points into a few orthogonal principal components (PCs).

PCA has been a primary technique used for multivariate analysis of spectroscopic imaging data. Specifically, PCA decomposes the experimental data matrix,  $D$ , as follows:

$$D = TP^T + E \quad (2.1)$$

where  $D$  is the unfolded  $M \times N$  experimental spectroscopic imaging data matrix ( $M$  is the number of pixels, and  $N$  is the number of channels),  $T$  is the  $M \times Q$  score matrix,  $P$  is the  $N \times Q$  loading matrix,  $E$  is the  $M \times N$  model residual matrix, and  $Q$  is the number of PCs. Furthermore, each orthogonal PC explains a portion of the total information contained in the experimental data; however, these PCs do not necessarily correspond to one pure chemical component, especially in cases where spectral overlap exists. For instance, if the Raman spectra of several pure components contain bands that overlap, the PCs of these respective components will most likely contain information from a mixture of chemical species (i.e., each PC will not correspond with a pure chemical component). Furthermore, the PCs explain the variance within the data: the maximum variance is captured by the first PC if the data is mean-centered prior to analysis; the second PC captures the second most variance in the data, and so forth. Overall, these PCs are created such that they are orthogonal to each other and therefore can be used for extracting useful chemical information to describe relationships amongst chemical systems. In this chapter, PCA was performed using Matlab 7.2 (Mathworks, Massachusetts, USA). The PLS Toolbox (Eigenvector Research Incorporated, Washington, USA) was used as the graphical interface to perform PCA through Matlab. For PCA, preprocessing was accomplished by normalization of the Raman spectra to unit area, and subsequent mean-centering of the data. Resulting PCA plots were visualized using Matlab.

### 2.3.4.2 Multivariate Curve Resolution-Alternating Least Squares (MCR-ALS)

MCR-ALS was applied to the Raman microspectroscopic imaging experimental data to most effectively extract useful chemical information. By generating resolved spectral and spatial information, MCR-ALS allows for the determination of the pure chemical components within a sample and the respective distribution of these components within a defined area of the sample. Furthermore, by using MCR-ALS, the instrumental response, in the form of spectroscopic imaging data, of a heterogeneous mixture of potentially unknown chemical species can be mathematically decomposed into spectral and spatial information concerning pure chemical components. Similar to PCA, the explained variance from spectroscopic imaging data is maximized using MCR-ALS; however, MCR-ALS can also provide both physical and chemical information regarding a sample. Overall, the resolved spectra of the pure chemical components are interpreted and chemically identified, and thus, the corresponding spatial distribution of the pure chemical component can be generated given its proper spectral identification.

MCR-ALS is among a wide-ranging group of multivariate self-modeling mixture analysis methods. This method, the goal of which is to resolve spatial and spectral information about a mixture, requires no prior information about the sample. Moreover, MCR-ALS resolves the experimental data matrix,  $\mathbf{D}$ , in the following fashion:

$$\mathbf{D} = \sum_i \mathbf{D}_i + \mathbf{E} \quad (2.2)$$

$$\mathbf{D} = \sum_i \mathbf{c}_i \mathbf{s}_i^T + \mathbf{E} \quad (2.3)$$

$$\mathbf{D} = \mathbf{C} \mathbf{S}^T + \mathbf{E} \quad (2.4)$$

where  $\mathbf{C}$  is the matrix of concentration profiles for each pure chemical component,  $\mathbf{S}^T$  is the matrix of the resolved spectra, and  $\mathbf{E}$  is the error matrix. Furthermore, the

number of components contributing to  $\mathbf{D}$  can be determined by PCA, singular value decomposition (SVD), based on prior knowledge of the system, or a variety of other multivariate techniques. With an initial estimation of the spectral matrix  $\mathbf{S}$ ,  $\mathbf{C}$  and  $\mathbf{S}^T$  are calculated and iteratively optimized using the ALS algorithm until convergence is achieved. ALS reaches this convergence by applying the following equations, in an alternating manner, to the updated estimates of  $\mathbf{C}$  and  $\mathbf{S}$ , which are denoted as  $\check{\mathbf{C}}$  and  $\check{\mathbf{S}}$ , respectively:

$$\check{\mathbf{S}} = \mathbf{D}^T \check{\mathbf{C}} / \check{\mathbf{C}}^T \check{\mathbf{C}} \quad (2.5)$$

$$\check{\mathbf{C}} = \mathbf{D} \check{\mathbf{S}} / \check{\mathbf{S}}^T \check{\mathbf{S}} \quad (2.6)$$

Physically meaningful constraints, such as non-negative concentrations and non-negative spectral intensity, are employed during the ALS process in order to more readily guide the resulting solutions closer to the respective true value. In our study, both the non-negative concentration constraint and the non-negative spectral intensity constraint were used, and a convergence of 0.01% was utilized. Thus,  $\check{\mathbf{C}}$  obtained from **Eq. (2.6)** was constrained by setting all negative elements to zero and the subsequently updated  $\check{\mathbf{S}}$  is obtained from **Eq. (2.5)** using the constrained  $\check{\mathbf{C}}$ . Also,  $\check{\mathbf{S}}$  obtained from **Eq. (2.5)** was constrained by setting all negative elements to zero and the subsequently updated  $\check{\mathbf{C}}$  is obtained through **Eq. (2.6)** using the constrained  $\check{\mathbf{S}}$ . MCR-ALS therefore employs non-negative concentrations and spectral intensity constraints during the process of achieving convergence to ensure that any small deviations in the initial estimations do not result in inconsistency within the results.

In the current study, the 3D spectroscopic imaging matrix (i.e., the matrix containing the x, y, and  $\text{cm}^{-1}$  information) was unfolded into the experimental data matrix,  $\mathbf{D}$ , and thus, each row of  $\mathbf{D}$  is the intensity at various wavenumbers. Prior to

ALS, the number of components was selected using initial estimations from PCA. In cases where PCA did not suffice, the number of components was selected by comparison of resolved spectra, in **S**, with Raman spectra of reference materials. Furthermore, the number of selected components was increased until the resolved spectra of the chemical components were adequately comparable to the Raman spectra of respective reference materials. Initial estimates of spectra for ALS were determined by distance criteria. The first spectrum for initialization was chosen to be furthest from the mean of the data set. Subsequent spectra were chosen to be furthest from the mean and all prior selected samples. The concentration matrix, **C**, and spectral matrix, **S**, were generated by MCR-ALS methods in Matlab with the PLS Toolbox; the final **C** matrix represents the concentration profile of each pure chemical component, in which each column corresponds to a component. The corresponding chemical maps are then reconstructed from **C** using Matlab 7.12 with the PLS Toolbox. Visualization of the chemical maps was done using OriginPro (Origin Lab v9.1 Pro, Northampton, USA), and these chemical maps are shown in the respective MCR-ALS figures. In the spectral matrix, **S**, each row contains the corresponding resolved Raman spectrum. For PCA, one spectral region was selected ( $100 - 900 \text{ cm}^{-1}$ ) and four principal components were analyzed. MCR analysis was performed using the entire spectral range ( $70 - 1550 \text{ cm}^{-1}$ ). No preprocessing was performed prior to analysis by MCR-ALS. The graphical presentations of the individual spectra were prepared using OriginPro.

## 2.4 Results and Discussion

### 2.4.1 Raman Microspectroscopy

Raman microspectroscopy was used to gain insight into the chemical species present within the TiO<sub>2</sub>-II-bearing grains recovered from the four spherule layers. Rutile (TiO<sub>2</sub>), anatase (TiO<sub>2</sub>), TiO<sub>2</sub>-II (TiO<sub>2</sub>), and quartz (SiO<sub>2</sub>) are the principal chemical species previously documented within these grains.[88] With the samples being comprised of a variety of chemical components, discerning the individual chemical species—including TiO<sub>2</sub> polymorphs—is a necessity. In addition to the three main naturally occurring polymorphs of TiO<sub>2</sub>, eight other polymorphs of titanium dioxide—three metastable synthetic forms and five high-pressure polymorphs—are known, so the ability to discern the chemical identity of these different polymorphs is a challenging task.[76, 77] Raman microspectroscopy, with the inherent ability to produce molecular signatures from polarizability and therefore crystal systems, was thus employed to determine the major chemical species present in the geological samples. Reference materials for each of the main chemical species—rutile, anatase, TiO<sub>2</sub>-II, and quartz—within these samples were obtained, and Raman spectra (**Figure 2.1**) were collected on these reference materials.

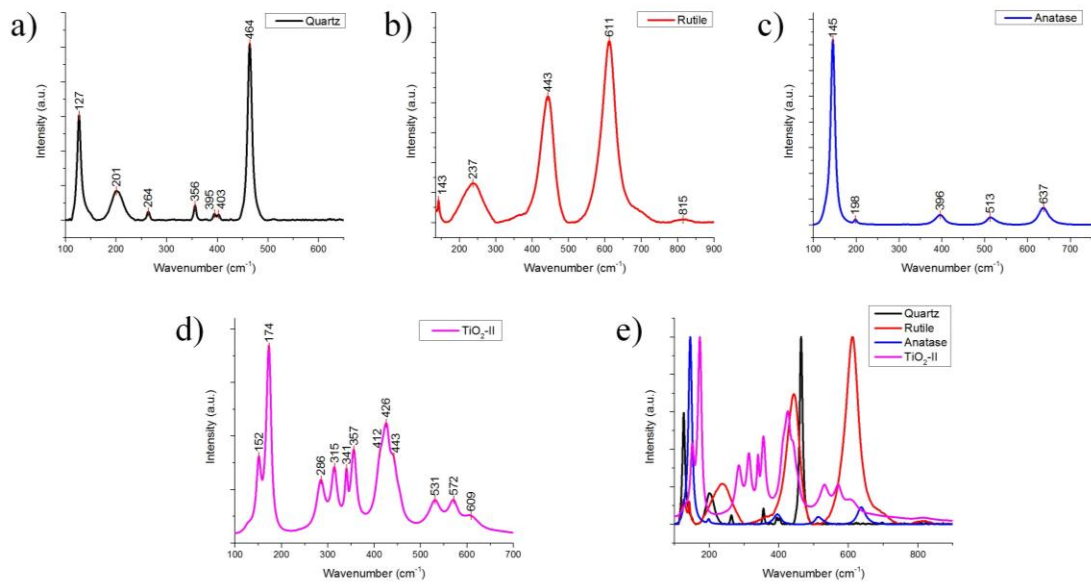


Figure 2.1: Raman spectra of quartz (a), rutile (b), anatase (c), and synthetic TiO<sub>2</sub>-II (d), with an overlay of each Raman spectrum (e). TiO<sub>2</sub>-II was synthesized from rutile powder in a static high-pressure hydrothermal environment[78] at a pressure of 10 GPa and a temperature of 500 °C.

The Raman active modes of TiO<sub>2</sub> and SiO<sub>2</sub> polymorphs have been extensively studied.[103, 104, 114-121] In order to assign the Raman active modes of each chemical species, Raman band assignments from the literature for both experimentally-determined (when available) and/or computationally-determined Raman active modes were used. These Raman band assignments (**Table 2.1**), along with the Raman spectrum of each reference material (**Figure 2.1**), are used to characterize the TiO<sub>2</sub>-II-bearing grains from the four spherule layers.

Table 2.1: Assignment of the Raman bands observed in TiO<sub>2</sub>-II-bearing grains from the four spherule layers based on literature.[114, 115, 117, 118, 121] Rutile (R), anatase (A), TiO<sub>2</sub>-II (T), and quartz (Q) are shown.

Wavenumber (cm <sup>-1</sup> )	Raman Active Mode	Chemical Origin
143	B <sub>1g</sub>	R
145	E <sub>g</sub>	A
152	B <sub>3g</sub>	T
174	A <sub>g</sub>	T
201	A <sub>1</sub>	Q
237	SOE <sup>(a)</sup>	R
264	E <sub>T</sub>	Q
286	B <sub>1g</sub>	T
315	B <sub>1g</sub>	T
341	B <sub>2g</sub>	T
356	A <sub>1</sub>	Q
357	B <sub>3g</sub>	T
395	E <sub>T</sub>	Q
396	B <sub>1g</sub>	A
403	E <sub>L</sub>	Q
412	B <sub>2g</sub>	T
426	A <sub>g</sub>	T
443	E <sub>g</sub>	R
464	A <sub>1</sub>	Q
513	A <sub>1g</sub>	A
531	A <sub>g</sub>	T
572	B <sub>1g</sub>	T
611	A <sub>1g</sub>	R
637	B <sub>1g</sub>	A
815	B <sub>2g</sub>	R

<sup>(a)</sup>SOE = Second-order effect

The primitive unit cell for rutile has 15 optical modes with a distribution of  $\Gamma = 1A_{1g} + 1A_{2g} + 1A_{2u} + 1B_{1g} + 1B_{2g} + 2B_{1u} + 1E_g + 3E_u$ . [117] Of these 15 optical modes, four modes are Raman active—B<sub>1g</sub>, B<sub>2g</sub>, E<sub>g</sub>, and A<sub>1g</sub>. [117] These active modes are consistent with the tetragonal structure and  $P4_2/mnm$  space group for rutile. [117] Thus, the observed Raman bands characteristic of rutile can be assigned to B<sub>1g</sub> (143

cm<sup>-1</sup>), second-order effect (237 cm<sup>-1</sup>), E<sub>g</sub> (443 cm<sup>-1</sup>), A<sub>1g</sub> (611 cm<sup>-1</sup>), and B<sub>2g</sub> (815 cm<sup>-1</sup>).

Although rutile and anatase are both tetragonal, anatase belongs to a different space group than rutile, giving rise to differing Raman active modes. Furthermore, anatase adopts space group *I4<sub>1</sub>/amd* and contains two TiO<sub>2</sub> formula units (six atoms) in the primitive unit cell. On the basis of factor group analysis, 15 optical modes are expected for anatase, with a distribution of  $\Gamma = 1A_{1g} + 1A_{2u} + 2B_{1g} + 1B_{2u} + 3E_g + 2E_u$ . [121, 122] The Raman active modes of anatase are A<sub>1g</sub>, B<sub>1g</sub>, and E<sub>g</sub> [123], and they are observed at the following wavenumbers—145 cm<sup>-1</sup> (E<sub>g</sub>), 396 cm<sup>-1</sup> (B<sub>1g</sub>), 513 cm<sup>-1</sup> (A<sub>1g</sub>), and 637 cm<sup>-1</sup> (B<sub>1g</sub>).

TiO<sub>2</sub>-II is isostructural with the orthorhombic  $\alpha$ -PbO<sub>2</sub> phase (space group *Pbcn*). [114] The primitive unit cell of TiO<sub>2</sub>-II contains 12 atoms and gives rise to 36 optical modes, which can be decomposed as  $\Gamma = 4B_{1u} + 3B_{2u} + 4B_{3u} + 4A_g + 5B_{1g} + 4B_{2g} + 5B_{3g} + 4A_u$  with respect to the long-wavelength optical phonon modes. [114] All of the phonon modes are nondegenerate, including four Raman active modes (A<sub>g</sub>, B<sub>1g</sub>, B<sub>2g</sub>, and B<sub>3g</sub>) that are assigned as follows—152 cm<sup>-1</sup> (B<sub>3g</sub>), 174 cm<sup>-1</sup> (A<sub>g</sub>), 286 cm<sup>-1</sup> (B<sub>1g</sub>), 315 cm<sup>-1</sup> (B<sub>1g</sub>), 341 cm<sup>-1</sup> (B<sub>2g</sub>), 357 cm<sup>-1</sup> (B<sub>3g</sub>), 412 cm<sup>-1</sup> (B<sub>2g</sub>), 426 cm<sup>-1</sup> (A<sub>g</sub>), 531 cm<sup>-1</sup> (A<sub>g</sub>), and 572 cm<sup>-1</sup> (B<sub>1g</sub>). [114] The spectral range selected for Raman measurements should ideally encompass the Raman active modes for the chemical species present. Thus, the spectral range of 70 to 1550 cm<sup>-1</sup> was used for all Raman microspectroscopy and Raman microspectroscopic imaging measurements.

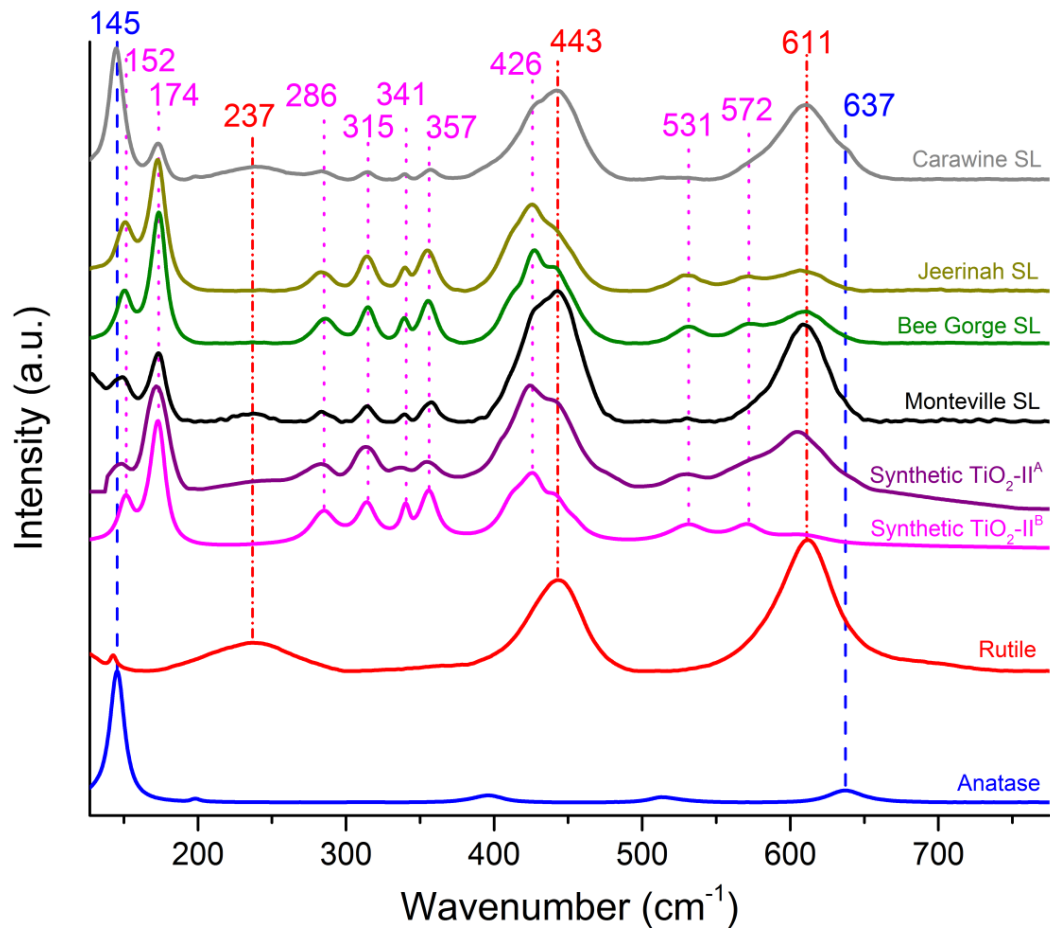


Figure 2.2: Raman spectra showing the presence of the high-pressure,  $\alpha$ - $\text{PbO}_2$ -structured polymorph  $\text{TiO}_2\text{-II}$  within four grains recovered from the Carawine spherule layer (CSL, grey), Jeerinah spherule layer (JSL, brown), Bee Gorge spherule layer (BGS�, green), and Monteville spherule layer (MSL, black). Raman spectra of anatase (blue), rutile (red), synthetic  $\text{TiO}_2\text{-II}$  formed under dry, shock-induced conditions[84, 102] (Synthetic  $\text{TiO}_2\text{-II}^{\text{A}}$ , purple), and synthetic  $\text{TiO}_2\text{-II}$  formed under hydrothermal, static conditions[78] (Synthetic  $\text{TiO}_2\text{-II}^{\text{B}}$ , pink) are also shown. Raman spectrum labeled “Synthetic  $\text{TiO}_2\text{-II}^{\text{A}}$ ” is from El Goresy et al.[84]

Raman spectra of four TiO<sub>2</sub>-II-bearing grains from the four spherule layers—Carawine spherule layer (CSL), Jeerinah spherule layer (JSL), Bee Gorge spherule layer (BGSL), and Monteville spherule layer (MSL)—show that the four grains have different relative concentrations of TiO<sub>2</sub>-II (**Figure 2.2**). The Raman spectra for the JSL and BGSL samples show more intense and distinct bands at 174 cm<sup>-1</sup>, 286 cm<sup>-1</sup>, 315 cm<sup>-1</sup>, 341 cm<sup>-1</sup>, and 357 cm<sup>-1</sup> that are characteristic of TiO<sub>2</sub>-II, relative to the respective bands in the Raman spectra for the CSL and MSL samples.

#### **2.4.2 Principal Component Analysis (PCA) and Scanning Electron Microscopy (SEM)**

The spectral features of the TiO<sub>2</sub>-II-bearing grains suggest a sample matrix comprised of TiO<sub>2</sub> polymorphs. In order to get an accurate representation of the chemical species within the grains, principal component analysis (PCA) was employed. PCA is a multivariate mathematical technique used for reducing the dimensionality of data. For Raman microspectroscopic imaging and other spectroscopic imaging techniques, high volumes of data are accumulated due to the amount of spectral acquisitions needed to compile an image. PCA is therefore well suited to reduce the dimensionality of the vast data sets accumulated from Raman microspectroscopic imaging. In this chapter, PCA is used to reduce a matrix of hundreds to thousands of data points into several orthogonal principal components.

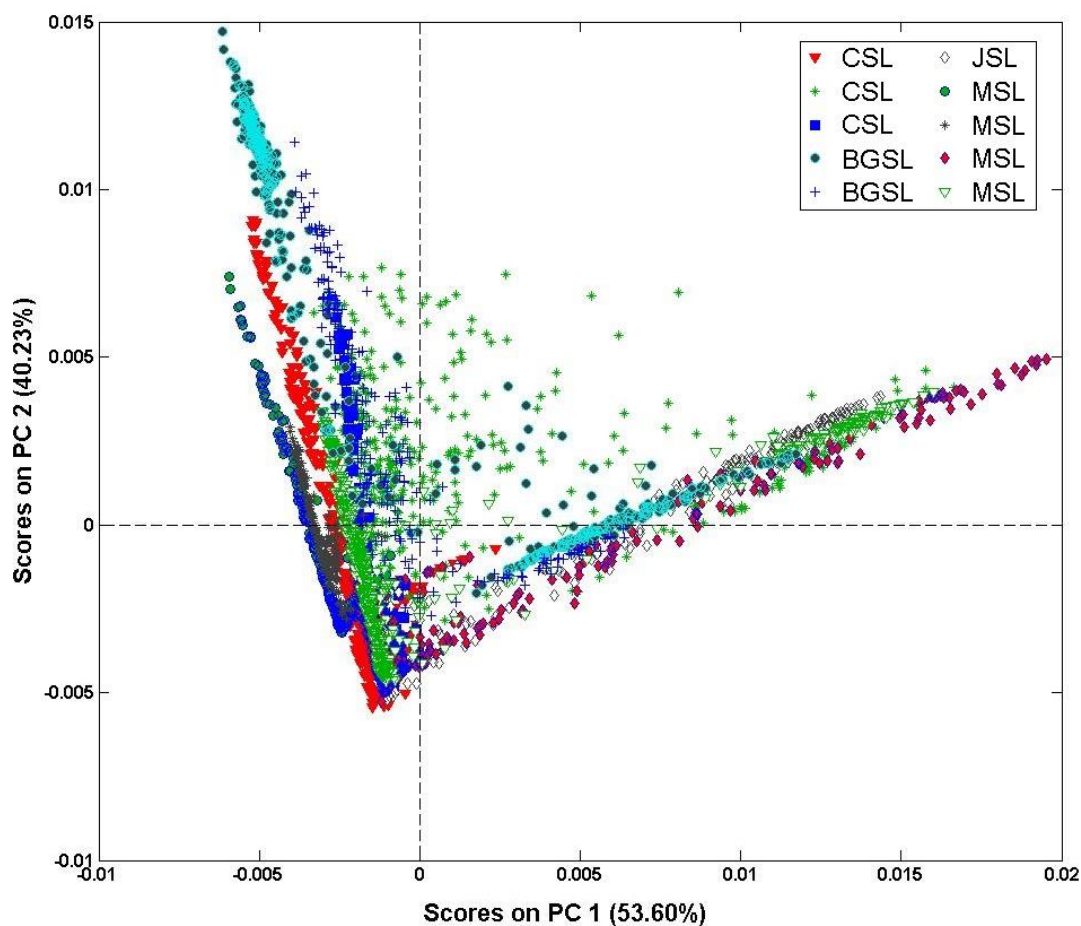


Figure 2.3: Principal component analysis (PCA) plot of the scores on the first principal component (PC 1; 53.60%) and the second principal component (PC 2; 40.23%).

PCA was used to determine the major chemical components and their relationships in samples. Furthermore, 3,650 Raman spectra collected from ten total maps—three of the CSL samples, one of the JSL sample, four of the MSL samples, and two of the BGS samples—were normalized, mean-centered, and analyzed using PCA. The resulting scores on PC1 and PC2 capture 53.60% and 40.23% of variance, respectively. Comparison of sample locations on a scores-scores plot (**Figure 2.3**)

with the appropriate Raman spectra reveals that the grains are comprised mainly of TiO<sub>2</sub>-II (**Figure 2.3**, top-left vertex), rutile (**Figure 2.3**, bottom-middle vertex), and substrate-adhesive epoxy (**Figure 2.3**, top-right vertex). The dense distribution of samples along the TiO<sub>2</sub>-II–rutile edge confirms that TiO<sub>2</sub>-II and rutile are highly co-localized within the resolution of the microscope objective. An explanation for this result would be that rutile is the direct precursor for TiO<sub>2</sub>-II, and thus, these chemical components are spatially related within the grains. The large number of samples along the substrate-adhesive epoxy–rutile edge indicates a co-localization between these two chemical components. This is due to the fact that the grains are dominated by rutile, and thus, the probability of the substrate-adhesive epoxy and rutile being spatially and spectrally related (i.e., both epoxy and rutile being observed in the chemical maps and corresponding Raman spectrum) is high. For example, if substrate-adhesive epoxy is limited to the outside portions of a grain, and rutile is a major component within that grain, epoxy and rutile will be spatially correlated on the surface of the grain.

In the scores-scores plot (**Figure 2.3**), TiO<sub>2</sub>-II and substrate-adhesive epoxy groupings are not readily connected. Therefore, TiO<sub>2</sub>-II and substrate-adhesive epoxy are much less correlated because the grains are less dominated by TiO<sub>2</sub>-II, resulting in a much lower probability that TiO<sub>2</sub>-II and substrate-adhesive epoxy are spatially associated. Finally, within the rutile grouping, multiple smaller groupings—manifested as smaller triangular groupings (**Figure 2.3**, bottom-middle vertex)—are observed. Two primary factors are responsible for this result. First, other secondary chemical species (e.g., anatase or quartz) may be present within the grains, and thus, the smaller groupings within the rutile projection may represent these additional chemical phases. The reason for these additional chemical phases being present within

the rutile grouping of the PCA plot (**Figure 2.3**) is that rutile is present within all grains; therefore, the probability of the additional chemical species being spatially associated with rutile is much higher than that of TiO<sub>2</sub>-II or substrate-adhesive epoxy. Secondly, rutile can potentially have differing chemical signatures, in the form of Raman spectra, based on its geolocation. In this case, the smaller grouping within the rutile grouping on the PCA plot could represent rutile from one geolocation (i.e., one spherule layer) versus rutile from a different geolocation. In summary, we used PCA to identify rutile, TiO<sub>2</sub>-II and substrate-adhesive epoxy as the major chemical components within the grains and to elucidate the relationships amongst these chemical components.

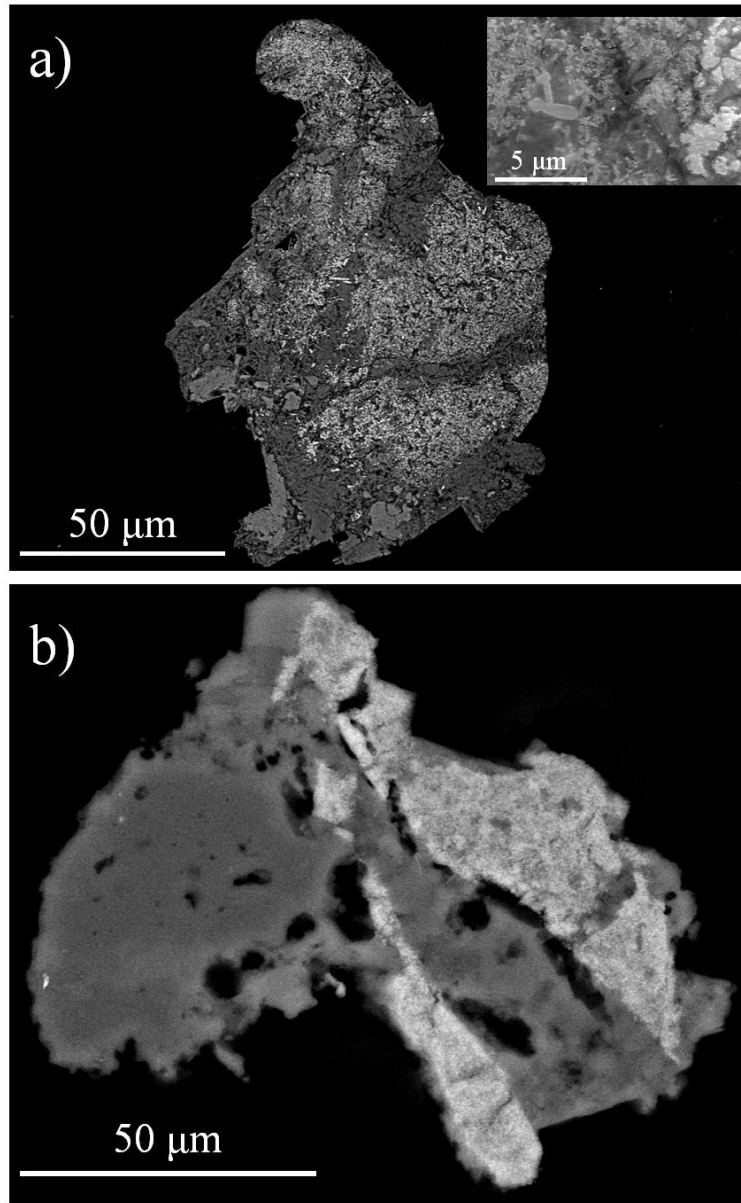


Figure 2.4: Backscattered electron (BSE) images of grains (a/b) from the Monteville spherule layer (MSL). Both grains contain polycrystalline micrometer- and submicrometer-sized particles of polydispersed sizes and shapes. Secondary electron (SE) image of the MSL grain is shown in the inset of (a).

In order to further investigate the additional chemical components of the grains, scanning electron microscopy (SEM) was employed. Backscattered-electron (BSE) images of grains from the MSL (**Figures 2.4a** and **2.4b**) display heterogeneity with respect to both the size and shape of the polycrystalline particles within them. The secondary electron (SE) image (**Figure 2.4a, inset**) displays spherically-shaped nanometer-sized particles having diameters of  $\sim 50$  nm, along with larger rod-shaped particles ranging in size from 100 nm up to 5  $\mu\text{m}$ . Moreover, the heterogeneity extends to larger particles (up to  $\sim 10$   $\mu\text{m}$  in size) that show rod, square, and spherical shapes. Since backscattered electrons result from elastic collisions with atoms, differences in the brightness of particles within a BSE image can deduce differences in the density and relative weight of the elements within the sample. The heterogeneity of the grains can thus be observed by the very bright particles accompanied by darker particles. Although the shapes and sizes of the (sub)micrometer-sized particles can be determined from BSE and SE imaging, chemical and molecular information about these particles is less easily determined, especially among materials of the same elemental composition (i.e., polymorphs of  $\text{TiO}_2$ ). Using SEM with energy-dispersive X-ray spectroscopy (EDS), for example, the spatial distribution of the titanium-bearing species can be elucidated; however, the distribution of specific  $\text{TiO}_2$  polymorphs is not readily determined using SEM-EDS. In order to determine the distribution of chemical species with the same molecular formula, chemical and/or molecular information, not elemental information, must be collected.

### 2.4.3 Multivariate Curve Resolution-Alternating Least Squares (MCR-ALS) Applied to Raman Microspectroscopic Imaging

The Raman spectra of the grains (**Figure 2.2**) from the four spherule layers contain overlapping Raman bands. Specifically, rutile and anatase display spectral overlap with respect to the  $143\text{ cm}^{-1}$  (rutile) and  $145\text{ cm}^{-1}$  (anatase) bands, and rutile, anatase,  $\text{TiO}_2\text{-II}$ , and quartz all show overlapping Raman bands in the  $350\text{ to }650\text{ cm}^{-1}$  spectral region. Due to this overlap of Raman bands, the distribution of the individual chemical components is difficult to determine using univariate methods. Furthermore, other common examples of interference for which univariate methods cannot compensate include background fluorescence, blackbody radiation, laser power fluctuations, loss of focus, sample opacity, optical alignment, sample birefringence, and samples outside the calibration set. For these reasons, multivariate methods are employed to determine the chemical components' spatial distribution and spectral profile. In this chapter, MCR-ALS applied to Raman microspectroscopic imaging was utilized for this purpose.

The chemical maps (**Figure 2.5a**) and corresponding resolved Raman spectra (**Figure 2.5b**) of a BGS<sub>L</sub> grain were generated using MCR-ALS applied to Raman microspectroscopic imaging of the probed area, outlined in green, in the optical image (**Figure 2.5a**). The mean (in black; **Figure 2.5b**) and standard deviation (+ in red, - in blue; **Figure 2.5b**) of the 400 total spectra accumulated over the sample show that  $\text{TiO}_2\text{-II}$  is the predominant chemical component. This is illustrated by the mean spectrum displaying high-intensity Raman bands at  $174\text{ cm}^{-1}$  and  $428\text{ cm}^{-1}$ , along with distinct bands at  $151\text{ cm}^{-1}$ ,  $288\text{ cm}^{-1}$ ,  $315\text{ cm}^{-1}$ ,  $340\text{ cm}^{-1}$ ,  $356\text{ cm}^{-1}$ ,  $533\text{ cm}^{-1}$ , and  $575\text{ cm}^{-1}$ , all of which are characteristic of  $\text{TiO}_2\text{-II}$ . The mean spectrum also displays bands representative of rutile ( $244\text{ cm}^{-1}$ ,  $442\text{ cm}^{-1}$ , and  $610\text{ cm}^{-1}$ ) as well as bands indicative

of substrate-adhesive epoxy ( $734\text{ cm}^{-1}$ ,  $820\text{ cm}^{-1}$ , and  $1113\text{ cm}^{-1}$ ). Using a four component MCR-ALS model, three chemically meaningful components were resolved—rutile,  $\text{TiO}_2\text{-II}$ , and substrate-adhesive epoxy. The first resolved spectrum (**Figure 2.5b**) shows major Raman bands at  $443\text{ cm}^{-1}$  and  $610\text{ cm}^{-1}$  and is thus identified as rutile. The second resolved spectrum (**Figure 2.5b**) shows Raman bands at  $151\text{ cm}^{-1}$ ,  $174\text{ cm}^{-1}$ ,  $287\text{ cm}^{-1}$ ,  $315\text{ cm}^{-1}$ ,  $340\text{ cm}^{-1}$ ,  $355\text{ cm}^{-1}$ ,  $427\text{ cm}^{-1}$ ,  $531\text{ cm}^{-1}$ , and  $570\text{ cm}^{-1}$  that are characteristic of  $\text{TiO}_2\text{-II}$ . The third resolved spectrum (**Figure 2.5b**) shows major Raman bands at  $640\text{ cm}^{-1}$ ,  $734\text{ cm}^{-1}$ ,  $820\text{ cm}^{-1}$ ,  $1113\text{ cm}^{-1}$ , and  $1185\text{ cm}^{-1}$ . These Raman bands are characteristic of substrate-adhesive epoxy that has major Raman bands at  $640\text{ cm}^{-1}$ ,  $733\text{ cm}^{-1}$ ,  $819\text{ cm}^{-1}$ ,  $1112\text{ cm}^{-1}$ , and  $1184\text{ cm}^{-1}$ . A detailed characterization of the Raman spectra and vibrational/rotational behavior of epoxy is given in Lyon et al.[124] and Chike et al.[125].

The spatial distribution of the resolved chemical species (**Figure 2.5a**) shows that for the predominant chemical components within the grain, rutile is highly concentrated towards the top of the grain, whereas  $\text{TiO}_2\text{-II}$  is more concentrated towards the bottom of the grain. Furthermore, rutile and  $\text{TiO}_2\text{-II}$  appear to be spatially complementary. This is particularly evident towards the middle of the grain, in which the localized regions of  $\text{TiO}_2\text{-II}$  are adjacent to those of rutile. The substrate-adhesive epoxy is localized to the outer portions of the grain. This shows that the cross-sectional surface of the grain is fully exposed with limited coating of epoxy.

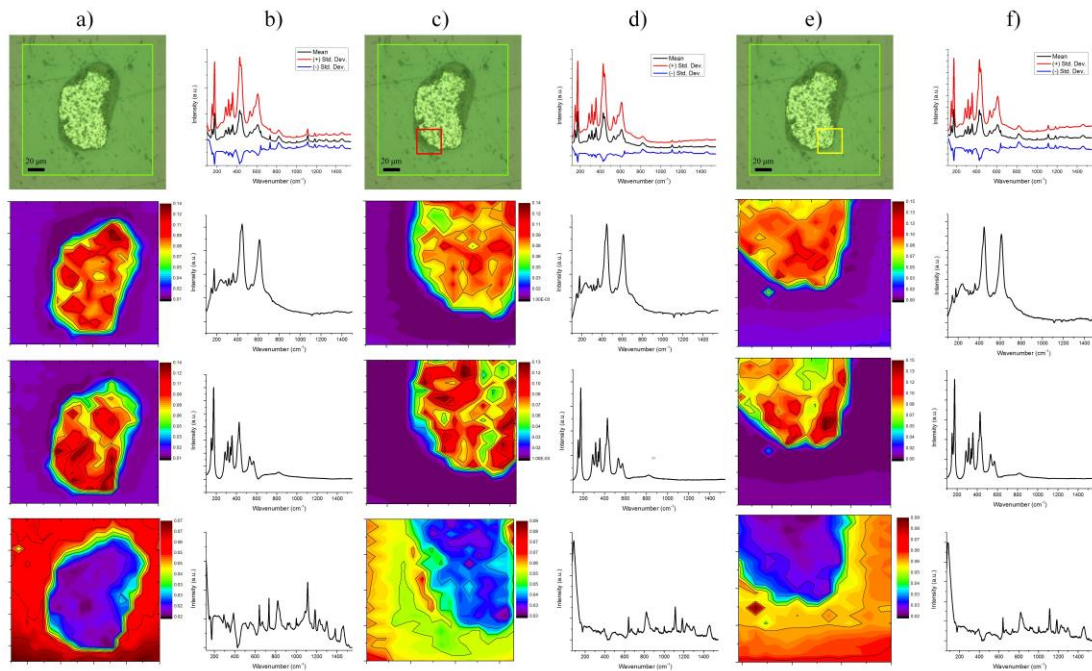


Figure 2.5: Spatially-resolved chemical maps with corresponding resolved Raman spectra for a grain from the Bee Gorge spherule layer. The optical images, with the probed area outlined in green (a), red (c), and yellow (e), and mean spectrum (black)  $\pm$  one standard deviation (+ in red, - in blue) are shown for each series of maps. Rutile, TiO<sub>2</sub>-II, and substrate-adhesive epoxy were resolved for each of the three areas outlined in green (a), red (c), and yellow (e). The maps in (a) and corresponding resolved spectra in (b) were generated using 20x magnification, whereas the maps in (c) with corresponding resolved spectra in (d) and the maps in (e) with corresponding resolved spectra in (f) were both generated using 100x magnification. Each Raman microspectroscopic imaging measurement was generated using a 20 x 20 spectral grid. The results in (a/b, c/d, and e/f) were obtained using a four component MCR-ALS model, and were generated using 532 nm excitation with 10 mW of laser power.

The chemical maps (**Figure 2.5c**) with their corresponding resolved Raman spectra (**Figure 2.5d**) were generated using MCR-ALS applied to Raman microspectroscopic imaging of the area outlined in red (**Figure 2.5c**). These results

were generated using a higher magnification, 100x, to provide a more in-depth investigation of the chemical components in a region of highly concentrated TiO<sub>2</sub>-II. The mean (in black; **Figure 2.5d**) and standard deviation (+ in red, - in blue; **Figure 2.5d**) of the collected Raman spectra show Raman bands at 151 cm<sup>-1</sup>, 175 cm<sup>-1</sup>, 288 cm<sup>-1</sup>, 316 cm<sup>-1</sup>, 340 cm<sup>-1</sup>, 357 cm<sup>-1</sup>, 428 cm<sup>-1</sup>, 532 cm<sup>-1</sup>, and 574 cm<sup>-1</sup>, which are all characteristic of TiO<sub>2</sub>-II and thus display the relatively high concentrations of TiO<sub>2</sub>-II within this region. This result is expected in light of the initial Raman microspectroscopic imaging results done at 20x magnification (**Figures 2.5a** and **2.5b**). Additionally, the mean (in black; **Figure 2.5d**) and standard deviation (+ in red, - in blue; **Figure 2.5d**) display less intense Raman bands at 241 cm<sup>-1</sup> and 443 cm<sup>-1</sup>, showing the presence of rutile within the grains and Raman bands at 640 cm<sup>-1</sup>, 820 cm<sup>-1</sup>, 1113 cm<sup>-1</sup>, and 1185 cm<sup>-1</sup>, showing the presence of epoxy within the probed area.

From MCR-ALS analysis of the Raman microspectroscopic imaging results using a four component model, three chemically meaningful components were resolved—rutile, TiO<sub>2</sub>-II, and substrate-adhesive epoxy. In the first resolved spectrum (**Figure 2.5d**), Raman bands at 237 cm<sup>-1</sup>, 446 cm<sup>-1</sup>, and 610 cm<sup>-1</sup>, characteristic of rutile, are observed. In the second resolved spectrum (**Figure 2.5d**), Raman bands occur at 151 cm<sup>-1</sup>, 175 cm<sup>-1</sup>, 288 cm<sup>-1</sup>, 316 cm<sup>-1</sup>, 340 cm<sup>-1</sup>, 356 cm<sup>-1</sup>, 413 cm<sup>-1</sup>, 428 cm<sup>-1</sup>, 532 cm<sup>-1</sup>, and 570 cm<sup>-1</sup>; these ten Raman bands are all characteristic of TiO<sub>2</sub>-II. In the third resolved spectrum (**Figure 2.5d**), Raman bands at 640 cm<sup>-1</sup>, 821 cm<sup>-1</sup>, 1113 cm<sup>-1</sup>, and 1185 cm<sup>-1</sup> show the presence of substrate-adhesive epoxy. The spatial distribution of the three resolved chemical components (**Figure 2.5c**) reveals that TiO<sub>2</sub>-II and rutile are complementary phases: TiO<sub>2</sub>-II is more localized towards the

boundaries of the grain, whereas rutile is more limited towards the interior of the grain. The chemical map of substrate-adhesive epoxy shows that epoxy is mainly limited to the exterior of the grain and along its boundary.

The chemical maps for the area outlined in yellow (**Figure 2.5e**) with their respective resolved spectra (**Figure 2.5f**) were similarly generated using 100x magnification to provide more thorough chemical information in this region of highly concentrated TiO<sub>2</sub>-II. Using a four component MCR-ALS model, rutile, TiO<sub>2</sub>-II, and substrate-adhesive epoxy were spatially (**Figure 2.5e**) and spectrally (**Figure 2.5f**) resolved. From the mean (in black; **Figure 2.5f**) and standard deviation (+ in red, - in blue; **Figure 2.5f**) of the Raman microspectroscopic imaging data within this region, rutile and TiO<sub>2</sub>-II are the predominant chemical components. This is evident by Raman bands at 150 cm<sup>-1</sup>, 175 cm<sup>-1</sup>, 288 cm<sup>-1</sup>, 316 cm<sup>-1</sup>, 340 cm<sup>-1</sup>, 357 cm<sup>-1</sup>, 429 cm<sup>-1</sup>, 533 cm<sup>-1</sup>, and 574 cm<sup>-1</sup> that are characteristic of TiO<sub>2</sub>-II and Raman bands at 240 cm<sup>-1</sup>, 443 cm<sup>-1</sup>, and 611 cm<sup>-1</sup> that are characteristic of rutile. Furthermore, the Raman bands at 640 cm<sup>-1</sup>, 819 cm<sup>-1</sup>, 1114 cm<sup>-1</sup>, and 1186 cm<sup>-1</sup> that are present in the mean spectrum show that substrate-adhesive epoxy is a primary chemical component within the probed area. For the three resolved Raman spectra (**Figure 2.5f**), the rutile component shows Raman bands at 143 cm<sup>-1</sup>, 238 cm<sup>-1</sup>, 446 cm<sup>-1</sup>, and 611 cm<sup>-1</sup>, the TiO<sub>2</sub>-II component shows Raman bands at 151 cm<sup>-1</sup>, 175 cm<sup>-1</sup>, 288 cm<sup>-1</sup>, 316 cm<sup>-1</sup>, 340 cm<sup>-1</sup>, 356 cm<sup>-1</sup>, 413 cm<sup>-1</sup>, 428 cm<sup>-1</sup>, 532 cm<sup>-1</sup>, and 571 cm<sup>-1</sup>, and the substrate-adhesive epoxy shows Raman bands at 640 cm<sup>-1</sup>, 819 cm<sup>-1</sup>, 1114 cm<sup>-1</sup>, and 1186 cm<sup>-1</sup>. Within the probed region outlined in yellow (**Figure 2.5e**), rutile is spatially distributed throughout this entire portion of the grain and it is not confined to any particular region of the grain. In contrast, TiO<sub>2</sub>-II is more highly confined to the right, boundary

corner of the grain. Rutile and  $\text{TiO}_2\text{-II}$  are also spatially distributed in a complementary fashion. The substrate-adhesive epoxy is again limited to the exterior of the grain, indicating that the grain is fully exposed. In summary, Raman microspectroscopic imaging with MCR-ALS of a grain from the BGSL using low (20x) and high (100x) magnification produced chemical maps and corresponding resolved spectra that indicate the presence of three distinct chemical species: rutile,  $\text{TiO}_2\text{-II}$ , and substrate-adhesive epoxy.

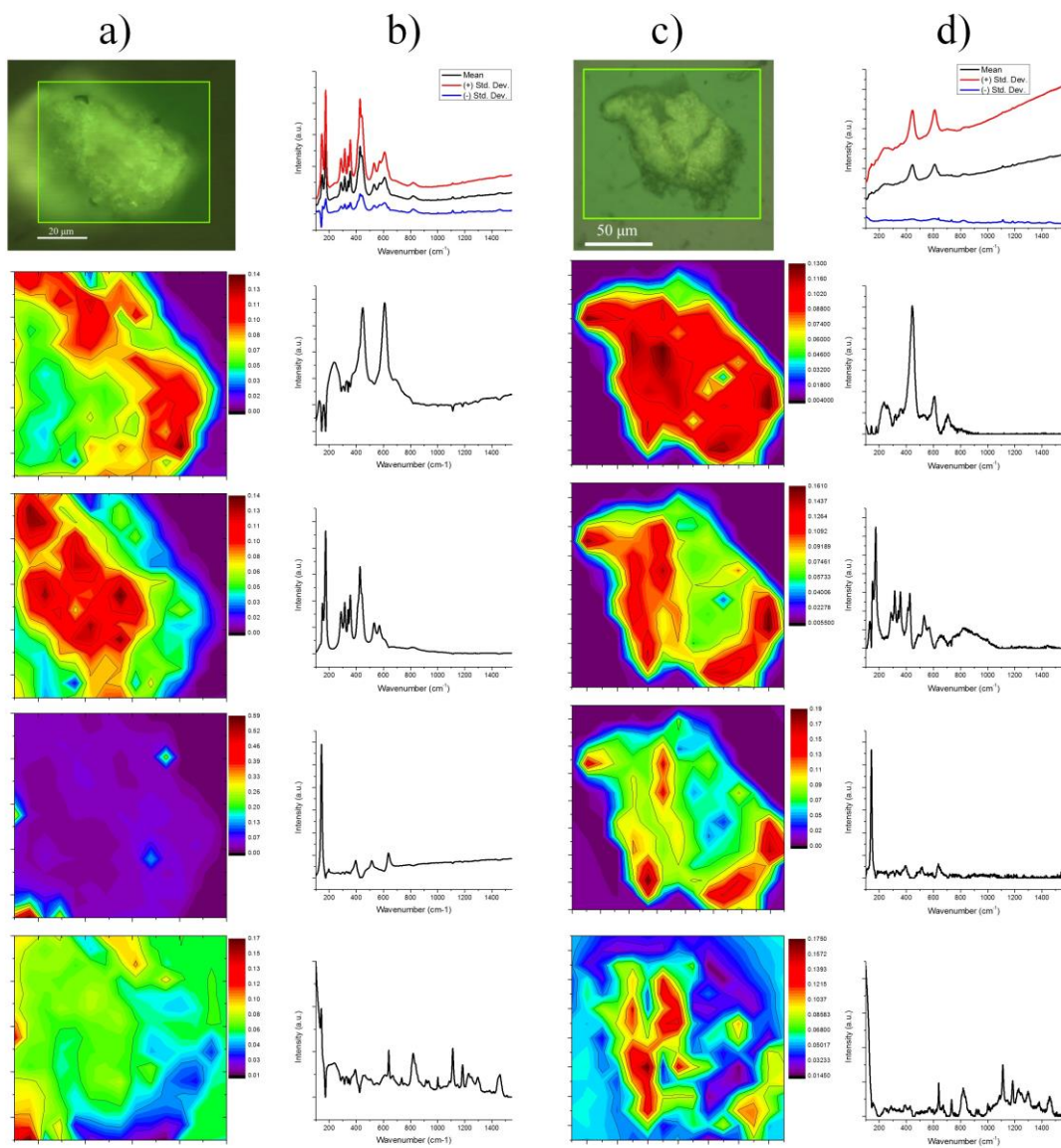


Figure 2.6: Spatially-resolved chemical maps and resolved Raman spectra generated using MCR-ALS applied to Raman microspectroscopic imaging of grains from the BGS (a/b) and MSL (c/d). The optical images, with locations of spectral grids outlined in green, and mean spectrum (black) +/- the standard deviation (+ in red, - in blue) are shown for each series of maps. Rutile, TiO<sub>2</sub>-II, anatase, and substrate-adhesive epoxy were resolved, in which the maps in (a) and corresponding resolved spectra in (b) were generated using 50x magnification, and maps in (c) with corresponding resolved spectra in (d) were generated using 20x magnification. Each of the Raman microspectroscopic imaging results was generated using a 15 x 15 spectral grid. The results in (a/b) and (c/d) were obtained using five and twelve component MCR-ALS models, respectively, and they were generated using 532 nm excitation with 5 mW of laser power.

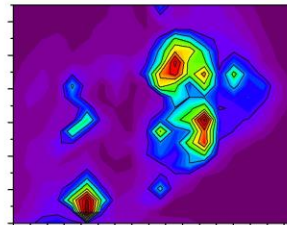
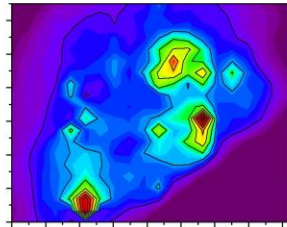
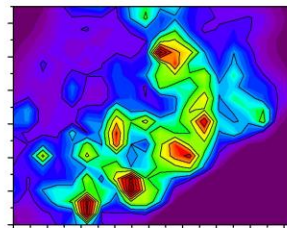
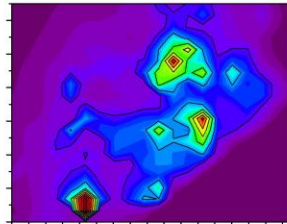
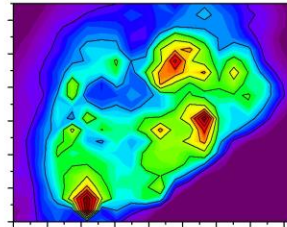
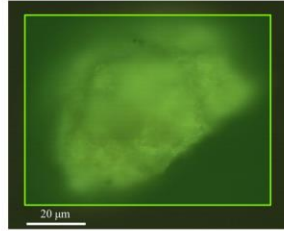
The results of Raman microspectroscopic imaging with MCR-ALS of grains from the BGS (Figures 2.6a and 2.6b) and MSL (Figures 2.6c and 2.6d) are shown. Using 50x magnification and a 15 x 15 spectral grid, chemical imaging was done of the area outlined in green in the optical image shown (Figure 2.6a). The mean (in black; Figure 2.6b) and standard deviation (+ in red, - in blue; Figure 2.6b) of the measured spectra reveal TiO<sub>2</sub>-II is the predominant phase in the probed area, as evidenced by distinct, high-intensity Raman bands at 149 cm<sup>-1</sup>, 174 cm<sup>-1</sup>, 287 cm<sup>-1</sup>, 315 cm<sup>-1</sup>, 340 cm<sup>-1</sup>, 356 cm<sup>-1</sup>, 428 cm<sup>-1</sup>, 532 cm<sup>-1</sup>, and 573 cm<sup>-1</sup>. Additional Raman bands of lower intensity are observed in the mean spectrum at 241 cm<sup>-1</sup>, 442 cm<sup>-1</sup>, and 610 cm<sup>-1</sup>, which are characteristic of rutile, as well as at 820 cm<sup>-1</sup>, 1113 cm<sup>-1</sup>, and 1186 cm<sup>-1</sup>, which are characteristic of epoxy. These Raman bands show that within the probed area (Figure 2.6a), rutile and substrate-adhesive epoxy are present, but in lower concentrations than TiO<sub>2</sub>-II. Using a five component MCR-ALS model, four chemically meaningful components—rutile, TiO<sub>2</sub>-II, anatase, and substrate-adhesive epoxy—were discerned from the resolved spectra (Figure 2.6b). The first resolved

spectrum (**Figure 2.6b**) shows Raman bands at  $237\text{ cm}^{-1}$ ,  $446\text{ cm}^{-1}$ , and  $609\text{ cm}^{-1}$  that are characteristic of rutile. The second resolved spectrum (**Figure 2.6b**) shows Raman bands at  $151\text{ cm}^{-1}$ ,  $174\text{ cm}^{-1}$ ,  $287\text{ cm}^{-1}$ ,  $315\text{ cm}^{-1}$ ,  $340\text{ cm}^{-1}$ ,  $356\text{ cm}^{-1}$ ,  $427\text{ cm}^{-1}$ ,  $532\text{ cm}^{-1}$ , and  $571\text{ cm}^{-1}$ , and these nine Raman bands are all characteristic of  $\text{TiO}_2\text{-II}$ . The third resolved spectrum (**Figure 2.6b**) shows Raman bands at  $143\text{ cm}^{-1}$ ,  $197\text{ cm}^{-1}$ ,  $396\text{ cm}^{-1}$ ,  $514\text{ cm}^{-1}$ , and  $637\text{ cm}^{-1}$  that are indicative of anatase. The fourth resolved spectrum (**Figure 2.6b**) shows Raman bands at  $640\text{ cm}^{-1}$ ,  $820\text{ cm}^{-1}$ ,  $1113\text{ cm}^{-1}$ , and  $1185\text{ cm}^{-1}$  that are characteristic of substrate-adhesive epoxy. The spatial distribution of these four chemical components (**Figure 2.6a**) shows that rutile and  $\text{TiO}_2\text{-II}$  are the predominant components within the grain, with rutile being highly concentrated in the outer portion of the grain and  $\text{TiO}_2\text{-II}$ , in contrast, being highly concentrated in and near the center of the grain. Furthermore,  $\text{TiO}_2\text{-II}$  and rutile are spatially complementary. Anatase is localized at a few small regions in the grain. The distribution of anatase suggests a secondary origin for this chemical component. The substrate-adhesive epoxy shows a distinct spatial distribution over almost the entire grain, suggesting that the grain's surface is not fully exposed.

Using 20x magnification and a 15 x 15 spectral grid, Raman microspectroscopic imaging was done of the area outlined in green in the optical image (**Figure 2.6c**). The results of the MCR-ALS applied to Raman microspectroscopic imaging of this area are shown in terms of chemical maps (**Figure 2.6c**) and corresponding resolved spectra (**Figure 2.6d**). The mean (in black; **Figure 2.6d**) and standard deviation (+ in red, - in blue; **Figure 2.6d**) of the measured Raman spectra reveal that rutile is the predominant phase in the grain, as evidenced by the most intense Raman bands occurring at  $241\text{ cm}^{-1}$ ,  $443\text{ cm}^{-1}$ , and  $610\text{ cm}^{-1}$ . Minor

Raman bands at  $176\text{ cm}^{-1}$ ,  $316\text{ cm}^{-1}$ ,  $341\text{ cm}^{-1}$ , and  $358\text{ cm}^{-1}$ , indicative of  $\text{TiO}_2\text{-II}$  and at  $820\text{ cm}^{-1}$ ,  $1113\text{ cm}^{-1}$ , and  $1185\text{ cm}^{-1}$ , indicative of substrate-adhesive epoxy are also present in the mean spectrum. Thus, the primary chemical components from the mean and standard deviation of the Raman spectra measured on this grain show the presence of rutile,  $\text{TiO}_2\text{-II}$ , and substrate-adhesive epoxy. However, using a twelve component MCR-ALS model applied to the measured Raman spectra, four chemically meaningful components were identified—rutile,  $\text{TiO}_2\text{-II}$ , anatase, and substrate-adhesive epoxy. The first resolved spectrum (**Figure 2.6d**) shows Raman bands at  $142\text{ cm}^{-1}$ ,  $243\text{ cm}^{-1}$ ,  $443\text{ cm}^{-1}$ , and  $608\text{ cm}^{-1}$  that are indicative of rutile. The second resolved spectrum (**Figure 2.6d**) shows Raman bands at  $150\text{ cm}^{-1}$ ,  $174\text{ cm}^{-1}$ ,  $287\text{ cm}^{-1}$ ,  $314\text{ cm}^{-1}$ ,  $339\text{ cm}^{-1}$ ,  $356\text{ cm}^{-1}$ ,  $411\text{ cm}^{-1}$ ,  $426\text{ cm}^{-1}$ ,  $531\text{ cm}^{-1}$ , and  $571\text{ cm}^{-1}$  that are characteristic of  $\text{TiO}_2\text{-II}$ . The third resolved spectrum (**Figure 2.6d**) shows Raman bands at  $142\text{ cm}^{-1}$ ,  $395\text{ cm}^{-1}$ ,  $516\text{ cm}^{-1}$ , and  $636\text{ cm}^{-1}$  that are indicative of anatase. The fourth resolved spectrum (**Figure 2.6d**) shows Raman bands at  $639\text{ cm}^{-1}$ ,  $820\text{ cm}^{-1}$ ,  $1112\text{ cm}^{-1}$ , and  $1185\text{ cm}^{-1}$  that are characteristic of substrate-adhesive epoxy. Regarding the spatial distribution of these chemical components (**Figure 2.6c**), rutile occurs in high concentrations at virtually all locations within the grain.  $\text{TiO}_2\text{-II}$  is concentrated towards the left and bottom margins of the grain. Anatase is more localized than the other chemical species and is spatially distributed mainly towards the bottom portion of the grain. Substrate-adhesive epoxy is present both exterior to the grain and within several parts of the grain.

a)



b)

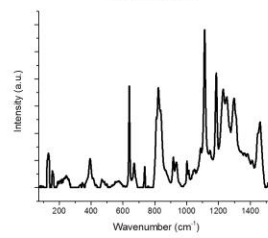
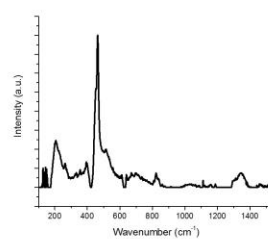
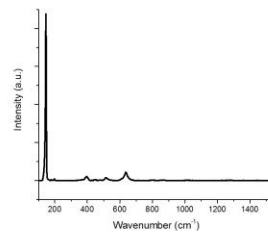
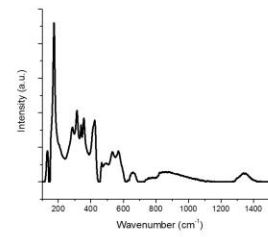
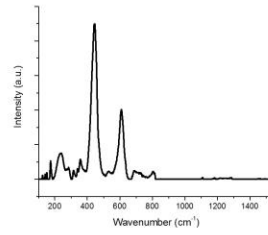
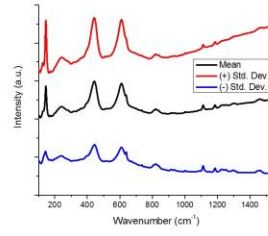


Figure 2.7: Spatially-resolved chemical maps and corresponding resolved Raman spectra were generated using MCR-ALS methods applied to Raman microspectroscopic imaging of a grain from the CSL (a/b). The optical image, with the spectral grid location outlined in green, and mean spectrum (black) +/- the standard deviation (+ in red, - in blue) are shown for the series of maps. Rutile, TiO<sub>2</sub>-II, anatase, quartz and substrate-adhesive epoxy were resolved, in which the maps in (a) and corresponding resolved spectra in (b) were generated using 50x magnification and a 20 x 20 spectral grid. The results were obtained using 532 nm excitation, 10 mW of laser power, and a twenty component MCR-ALS model.

Raman microspectroscopic imaging with MCR-ALS was also used to analyze grains from the CSL (**Figures 2.7a** and **2.7b**). Using 50x magnification and a 20 x 20 spectral grid, chemical imaging was done of the area outlined in green in the optical image (**Figure 2.7a**). The results of the MCR-ALS applied to Raman microspectroscopic imaging are shown in terms of chemical maps (**Figure 2.7a**) and corresponding resolved Raman spectra (**Figure 2.7b**). The mean and standard deviation of the measured spectra reveal Raman bands of high-intensity at 144 cm<sup>-1</sup>, 243 cm<sup>-1</sup>, 443 cm<sup>-1</sup>, and 611 cm<sup>-1</sup>. The high-intensity of the band at 144 cm<sup>-1</sup> and the minor Raman band at 513 cm<sup>-1</sup> indicate the presence of anatase. The Raman bands at 243 cm<sup>-1</sup>, 443 cm<sup>-1</sup>, and 611 cm<sup>-1</sup> show the presence of rutile. Raman bands of lower intensity at 174 cm<sup>-1</sup>, 317 cm<sup>-1</sup>, 340 cm<sup>-1</sup>, and 361 cm<sup>-1</sup> show the presence of TiO<sub>2</sub>-II within the grain, and Raman bands at 640 cm<sup>-1</sup>, 821 cm<sup>-1</sup>, 1113 cm<sup>-1</sup>, and 1186 cm<sup>-1</sup> show the presence of substrate-adhesive epoxy. Using a twenty component MCR-ALS model, five chemically meaningful components—rutile, TiO<sub>2</sub>-II, anatase, quartz and substrate-adhesive epoxy—were resolved. The first resolved spectrum (**Figure 2.7b**) shows Raman bands at 237 cm<sup>-1</sup>, 443 cm<sup>-1</sup>, and 610 cm<sup>-1</sup> that are indicative of rutile. The second resolved spectrum (**Figure 2.7b**) shows Raman bands at 174 cm<sup>-1</sup>, 286 cm<sup>-1</sup>

<sup>1</sup>, 314 cm<sup>-1</sup>, 340 cm<sup>-1</sup>, 357 cm<sup>-1</sup>, 424 cm<sup>-1</sup>, 532 cm<sup>-1</sup>, and 569 cm<sup>-1</sup> that are indicative of TiO<sub>2</sub>-II. The third resolved spectrum (**Figure 2.7b**) shows Raman bands at 145 cm<sup>-1</sup>, 197 cm<sup>-1</sup>, 395 cm<sup>-1</sup>, 514 cm<sup>-1</sup>, and 637 cm<sup>-1</sup> that are indicative of anatase. The fourth resolved spectrum (**Figure 2.7b**) shows Raman bands at 128 cm<sup>-1</sup>, 205 cm<sup>-1</sup>, 263 cm<sup>-1</sup>, 395 cm<sup>-1</sup>, and 464 cm<sup>-1</sup> that are indicative of quartz. The fifth resolved spectrum (**Figure 2.7b**) shows Raman bands at 640 cm<sup>-1</sup>, 822 cm<sup>-1</sup>, 1113 cm<sup>-1</sup>, 1186 cm<sup>-1</sup>, 1230 cm<sup>-1</sup>, 1298 cm<sup>-1</sup>, and 1462 cm<sup>-1</sup> that are indicative of substrate-adhesive epoxy. The spatial distribution of the five resolved chemical species (**Figure 2.7a**) shows that rutile and anatase are the predominant chemical components within this grain from the CSL. Rutile is distributed throughout the entirety of the grain, with high concentrations towards the bottom and upper-right portions of the grain. Anatase is distributed throughout most of the grain and has five locations of very high concentration towards the bottom-right portion of the grain. TiO<sub>2</sub>-II appears to have a lower concentration within this grain, with high concentrations complementary to rutile towards the top and middle portions of the grain. Similarly, quartz appears to have less of a presence throughout the grain and is distributed in localized areas. Finally, substrate-adhesive epoxy is distributed not only exterior to the grain but also within the grain, given that the grain is not fully exposed. Moreover, it can be seen in the optical image of the grain (**Figure 2.7a**) that portions of the grain are still covered by the substrate-adhesive epoxy.

Using 50x magnification and a 20 x 20 spectral grid, Raman microspectroscopic imaging was done of the area shown in the optical image (**Figure 2.8a**) of a grain from the MSL. The results of MCR-ALS applied to Raman microspectroscopic imaging are shown in terms of chemical maps (**Figure 2.8a**) and

corresponding resolved Raman spectra (**Figure 2.8b**). The mean and standard deviation of the measured Raman spectra show high-intensity Raman bands at 241  $\text{cm}^{-1}$ , 444  $\text{cm}^{-1}$ , and 610  $\text{cm}^{-1}$  that are indicative of rutile and at 174  $\text{cm}^{-1}$ , 285  $\text{cm}^{-1}$ , 315  $\text{cm}^{-1}$ , 340  $\text{cm}^{-1}$ , 357  $\text{cm}^{-1}$ , 429  $\text{cm}^{-1}$ , and 534  $\text{cm}^{-1}$  that are indicative of  $\text{TiO}_2$ -II. In the mean spectrum, there are Raman bands of lower intensity at 639  $\text{cm}^{-1}$ , 822  $\text{cm}^{-1}$ , 1113  $\text{cm}^{-1}$ , and 1187  $\text{cm}^{-1}$  that are characteristic of substrate-adhesive epoxy. Therefore, Raman bands for rutile,  $\text{TiO}_2$ -II, and substrate-adhesive epoxy were identified from the mean of the 400 total measured Raman spectra. Using a twenty component MCR-ALS model, five chemically meaningful components—rutile,  $\text{TiO}_2$ -II, anatase, quartz and substrate-adhesive epoxy—were resolved.

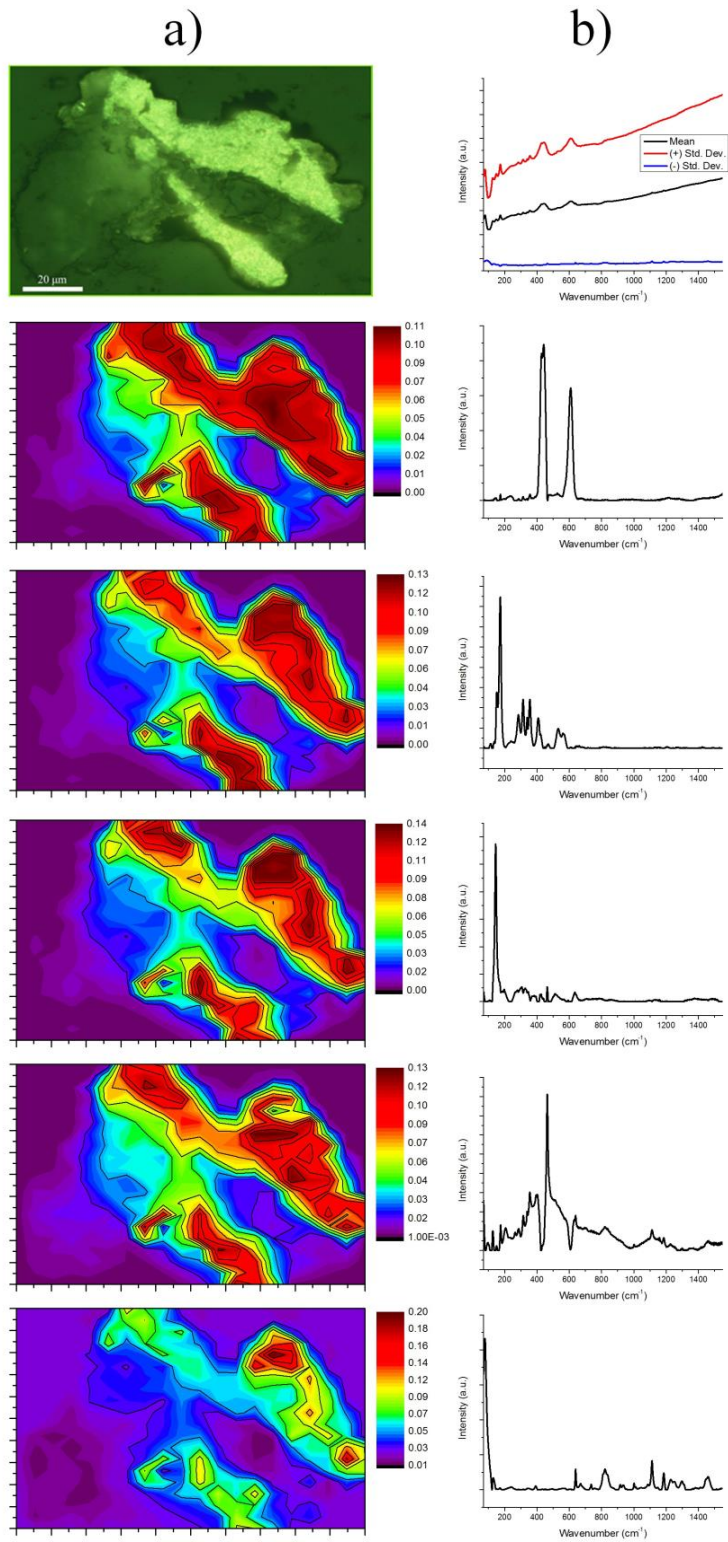


Figure 2.8: Spatially-resolved chemical maps and corresponding resolved Raman spectra were generated using MCR-ALS methods applied to Raman microspectroscopic imaging of a grain from the MSL (a/b). The optical image, with the spectral grid location outlined in green, and mean spectrum (black) +/- the standard deviation (+ in red, - in blue) are shown. Rutile, TiO<sub>2</sub>-II, anatase, quartz and substrate-adhesive epoxy were resolved, in which the maps in (a) with corresponding resolved spectra in (b) were both generated using 50x magnification. The Raman microspectroscopic imaging measurements were generated using a 20 x 20 spectral grid. The results were generated using 532 nm excitation with 5 mW of laser power, and they were obtained using a twenty component MCR-ALS model.

The first resolved spectrum (**Figure 2.8b**) shows Raman bands at 237 cm<sup>-1</sup>, 443 cm<sup>-1</sup>, and 609 cm<sup>-1</sup> that are characteristic of rutile. The second resolved spectrum (**Figure 2.8b**) shows Raman bands at 151 cm<sup>-1</sup>, 173 cm<sup>-1</sup>, 285 cm<sup>-1</sup>, 314 cm<sup>-1</sup>, 339 cm<sup>-1</sup>, 357 cm<sup>-1</sup>, 409 cm<sup>-1</sup>, 423 cm<sup>-1</sup>, 533 cm<sup>-1</sup>, and 565 cm<sup>-1</sup> that are characteristic of TiO<sub>2</sub>-II. The third resolved spectrum (**Figure 2.8b**) shows Raman bands at 144 cm<sup>-1</sup>, 197 cm<sup>-1</sup>, 514 cm<sup>-1</sup>, and 635 cm<sup>-1</sup> that are characteristic of anatase. The fourth resolved spectrum (**Figure 2.8b**) shows Raman bands at 127 cm<sup>-1</sup>, 206 cm<sup>-1</sup>, 396 cm<sup>-1</sup>, and 464 cm<sup>-1</sup> that are characteristic of quartz. The fifth resolved spectrum (**Figure 2.8b**) shows Raman bands at 640 cm<sup>-1</sup>, 821 cm<sup>-1</sup>, 1002 cm<sup>-1</sup>, 1113 cm<sup>-1</sup>, 1186 cm<sup>-1</sup>, 1229 cm<sup>-1</sup>, 1252 cm<sup>-1</sup>, 1299 cm<sup>-1</sup>, and 1461 cm<sup>-1</sup> that are characteristic of substrate-adhesive epoxy.

Regarding the spatial distribution (**Figure 2.8a**) of these identified chemical species, rutile is distributed throughout the grain in high concentration. TiO<sub>2</sub>-II, anatase, and quartz also appear to be distributed throughout large portions of the grain. The uppermost portion of the grain displays the main differences in the distribution of rutile, TiO<sub>2</sub>-II, anatase, and quartz. The locations of the highest intensities of TiO<sub>2</sub>-II and rutile appear to have a complementary distribution. In terms of high-intensity

locations, anatase is distributed similarly to TiO<sub>2</sub>-II, and quartz is distributed below the anatase and TiO<sub>2</sub>-II locations. Finally, the substrate-adhesive epoxy is distributed both exterior to the grain and within some portions on the grain, the latter distribution indicating some epoxy coating of the grain.

#### **2.4.4 Evaluation of Component Selection for MCR-ALS**

The effects of increasing the number of components used in MCR-ALS applied to Raman microspectroscopic imaging were investigated. A Monteville spherule layer (MSL) grain was used for this investigation, in which the final results of MCR-ALS applied to Raman microspectroscopic imaging of this MSL grain is shown (**Figures 2.6c** and **2.6d**). Using a four component MCR-ALS model with Raman microspectroscopic imaging applied to this MSL grain (**Figure 2.9**) that is estimated by PCA, rutile (**Figure 2.9b**) and substrate-adhesive epoxy (**Figure 2.9c**) were resolved. Furthermore, TiO<sub>2</sub>-II and anatase are both unresolved in this case. The additional two resolved spectra display initial estimates of the potential presence of TiO<sub>2</sub>-II (**Figure 2.9a**) and a component indicative of baseline fluctuations (**Figure 2.9d**). Overall, using a four component MCR-ALS model, only rutile and substrate-adhesive epoxy were spectrally resolved, whereas TiO<sub>2</sub>-II and anatase were not.

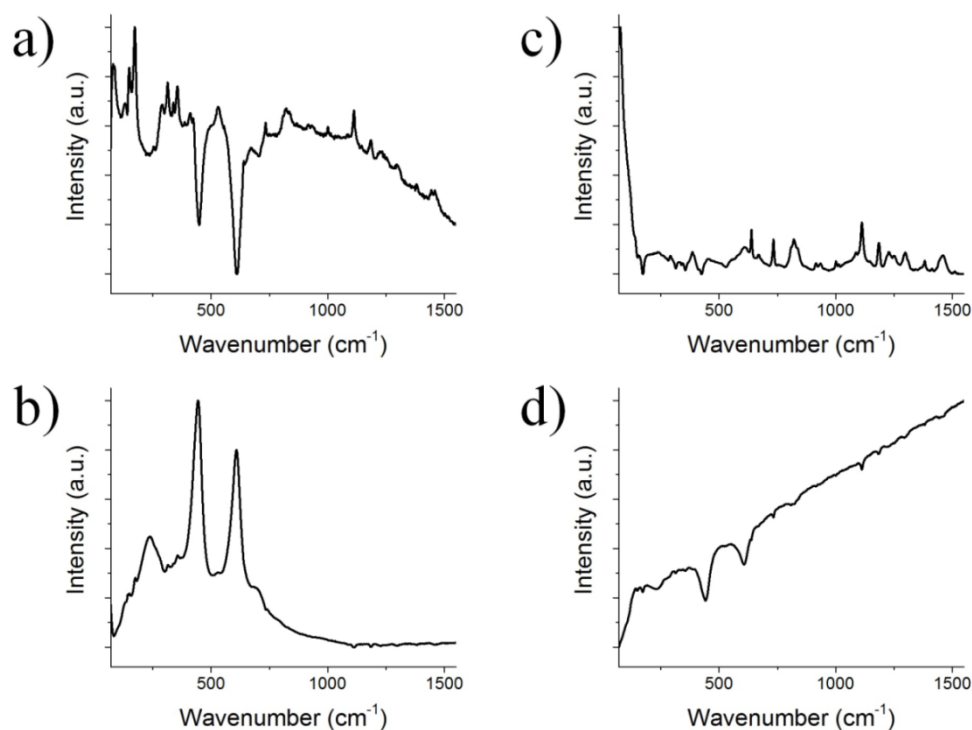


Figure 2.9: Resolved spectra resulting from MCR-ALS applied to Raman microspectroscopic imaging of a MSL grain. The MCR-ALS model was built with four components.

The resolved Raman spectra resulting from an eight component MCR-ALS model (**Figure 2.10**) show that rutile (**Figure 2.10b**), substrate-adhesive epoxy (**Figure 2.10c**), and TiO<sub>2</sub>-II (**Figure 2.10d**) can be resolved. Anatase cannot be resolved using an eight component MCR-ALS model. However, the band at 141 cm<sup>-1</sup> in the resolved Raman spectrum (**Figure 2.10e**) suggests the potential presence of anatase. Using an eight component MCR-ALS model, the additional resolved spectra are attributed to baseline and background interference (**Figure 2.10a**), fragmentation of the substrate-adhesive epoxy component into two additional components (**Figures 2.10f and 2.10g**), and fragmentation of the rutile component—specifically, the 611

$\text{cm}^{-1}$  band in the rutile Raman spectrum—into an additional component (**Figure 2.10h**). Thus, using the eight component MCR-ALS model,  $\text{TiO}_2\text{-II}$  is spectrally resolved in addition to rutile and substrate-adhesive epoxy, yet anatase is not.

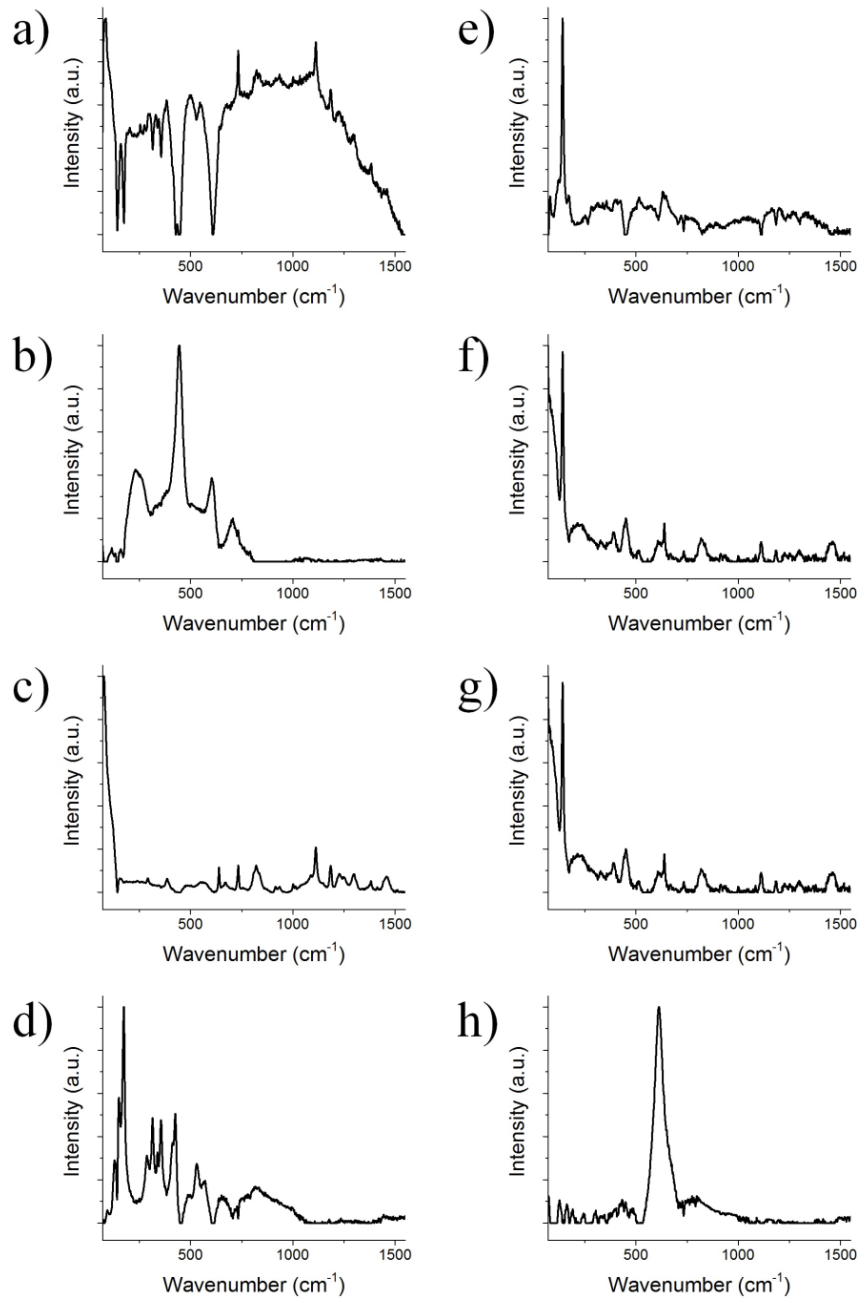


Figure 2.10: Resolved spectra resulting from MCR-ALS applied to Raman microspectroscopic imaging of a MSL grain. The MCR-ALS model was built with eight components.

MCR-ALS applied to Raman microspectroscopic imaging using a twelve component model (**Figure 2.11**) successfully shows the ability to spectrally resolve rutile (**Figure 2.11b**), substrate-adhesive epoxy (**Figure 2.11c**), TiO<sub>2</sub>-II (**Figure 2.11d**), and anatase (**Figure 2.11e**). Due to this twelve component MCR-ALS model resolving all four chemical species within this MSL grain, this was the final number of components selected. Moreover, the twelve component MCR-ALS model provides the most representative resolved Raman spectra for rutile, substrate-adhesive epoxy, TiO<sub>2</sub>-II, and anatase with respect to the Raman spectra of reference materials (**Figure 2.1**). Additional components attributed to noise and background/baseline fluctuations (**Figures 2.11g, 2.11i, 2.11j, 2.11k, and 2.11l**) are observed. As in the MCR-ALS model with eight components (**Figure 2.10**), similar fragmentation of the substrate-adhesive epoxy (**Figures 2.11a and 2.11f**) component and the rutile (**Figure 2.11h**) component is observed. Therefore, the twelve component MCR-ALS model generated the most appropriate resolved Raman spectra of the chemical species present within this MSL sample, whereas MCR-ALS models with fewer components failed to spectrally resolve and therefore properly identify all chemical species.

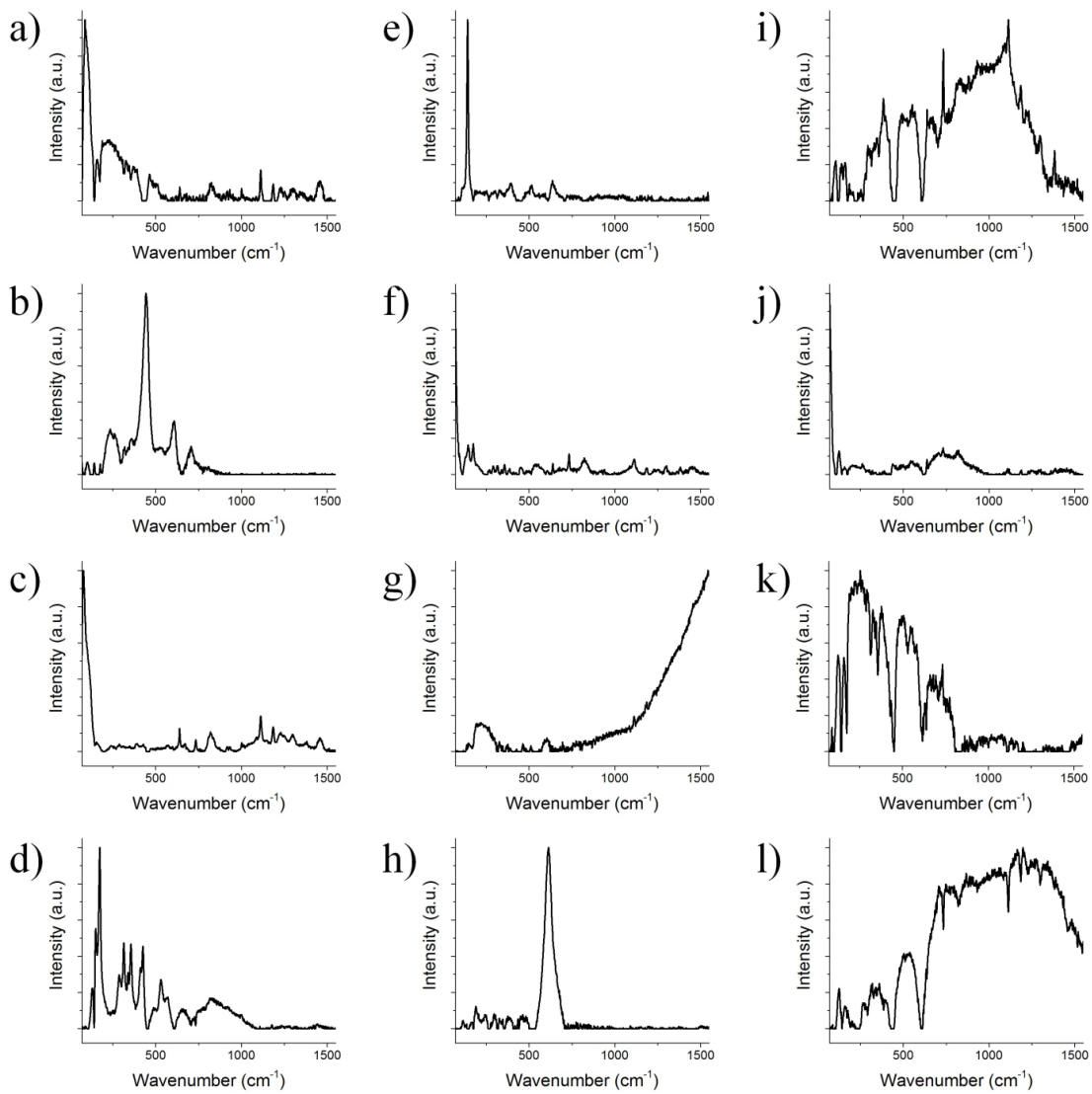


Figure 2.11: Resolved spectra resulting from MCR-ALS applied to Raman microspectroscopic imaging of a MSL grain. The MCR-ALS model was built with twelve components.

#### 2.4.5 Spatial Resolution Enhancements

For the investigation of materials using MCR-ALS applied to Raman microspectroscopic imaging, high spectral and spatial resolution are desired. However, maximizing both spectral and spatial resolution can produce expensive, lengthy analysis times. Moreover, sample defocusing, loss of signal intensity, and background fluctuations can be observed for these longer analysis times. For most of the Raman microspectroscopic maps (**Figures 2.5-2.7**), 400 total Raman spectra were measured, using a 20 x 20 spectral grid, in ~200 minutes. In order to increase the spatial resolution of the chemical maps, the total number of Raman spectra collected over the same probed area was increased to 10,000 using a 100 x 100 spectral grid. These Raman microspectroscopic maps were collected in ~167 minutes. Overall, the analysis time and cost of generating chemical maps using MCR-ALS applied to Raman microspectroscopic imaging was held essentially constant, while the spatial resolution of the chemical maps was greatly enhanced.

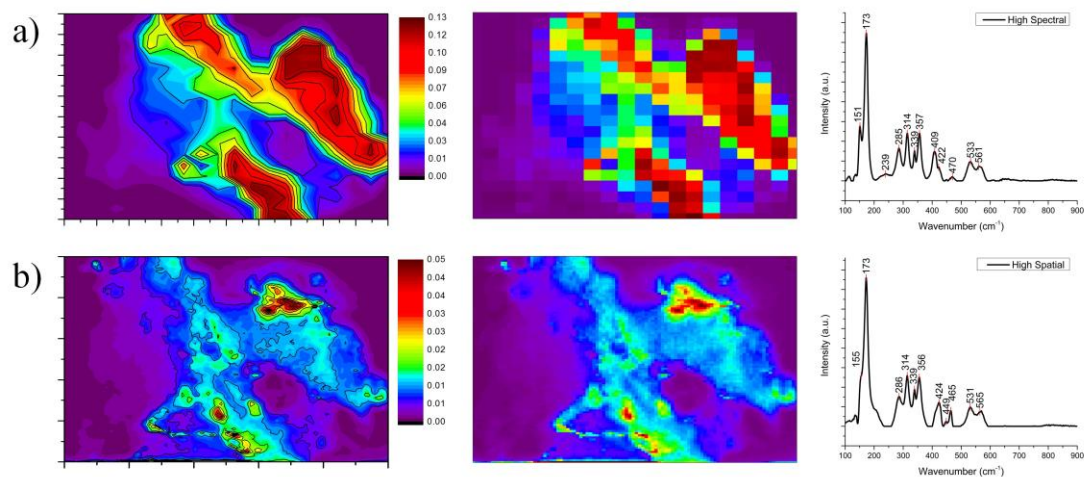


Figure 2.12: Spatially-resolved chemical maps and resulting Raman spectra of  $\text{TiO}_2\text{-II}$  generated using MCR-ALS applied to Raman microspectroscopic imaging of a grain from the MSL. The chemical maps and resolved spectrum shown in (a) were generated using 400 spectra (20 x 20 grid) obtained with 15 seconds of integration time and one co-average, termed “high spectral”. The chemical maps and resolved spectrum shown in (b) were generated using 10,000 spectra (100 x 100 grid) obtained using 1 second of integration time and no co-averages, termed “high spatial”. The results shown in (a) and (b) were both obtained using 50x magnification, 532 nm excitation, and a twenty component MCR-ALS model.

The chemical map of  $\text{TiO}_2\text{-II}$  in a grain from the MSL was used to investigate the effects of increasing the number of Raman spectra collected while simultaneously limiting spectral acquisition. Furthermore, the chemical maps and resolved spectrum (**Figure 2.12a**) generated using a matrix of 400 total Raman spectra (20 x 20 spectral grid) with integration times of 15 seconds and one co-average were termed “high spectral” resolution. The chemical maps and resolved spectrum (**Figure 2.12b**) generated using a matrix of 10,000 total Raman spectra (100 x 100 spectral grid) with

an integration time of 1 second and no co-averages were termed “high spatial” high-spatial resolution.

The distribution of TiO<sub>2</sub>-II in both the “high-spectral” and “high-spatial” Raman microspectroscopic imaging measurements is represented by both chemical contour maps and pixelated images to most appropriately exhibit differences in spatial resolution. Chemical contour maps, traditionally used with MCR-ALS applied to Raman microspectroscopic imaging, provide a useful representation of the distribution of chemical species within a sample. Furthermore, chemical contour maps produce a rendering of the distribution of chemical components with an enhanced spatial resolution. This enhanced spatial resolution is due to interpolation between respective contours within the chemical map. Therefore, in order to observe the true spatial resolution of the Raman microspectroscopic imaging with MCR-ALS measurements, pixelated images are also shown (**Figure 2.12**). Each pixel is representative of a single Raman spectrum, and thus, the “high-spectral” measurements (**Figure 2.12a**) are 20 x 20 pixels, whereas the “high-spatial” measurements (**Figure 2.12b**) are 100 x 100 pixels. This pixelated image shows the true spatial resolution of both measurements.

The “high-spectral” chemical maps (**Figure 2.12a**) show that TiO<sub>2</sub>-II is distributed throughout almost all of the grain, including the upper right and lower portions of the grain where this component is most highly concentrated. For the corresponding resolved spectrum (**Figure 2.12a**), the Raman bands at 151 cm<sup>-1</sup>, 173 cm<sup>-1</sup>, 285 cm<sup>-1</sup>, 314 cm<sup>-1</sup>, 339 cm<sup>-1</sup>, 357 cm<sup>-1</sup>, 409 cm<sup>-1</sup>, and 533 cm<sup>-1</sup> are in agreement with those of synthetic TiO<sub>2</sub>-II that occur at 152 cm<sup>-1</sup>, 174 cm<sup>-1</sup>, 286 cm<sup>-1</sup>, 315 cm<sup>-1</sup>, 341 cm<sup>-1</sup>, 357 cm<sup>-1</sup>, 412 cm<sup>-1</sup>, and 531 cm<sup>-1</sup>. These Raman spectra do show slight differences in bands assigned to TiO<sub>2</sub>-II with the resolved “high spectral” Raman

spectrum showing bands at 422  $\text{cm}^{-1}$  and 561  $\text{cm}^{-1}$ , whereas the Raman spectrum for synthetic  $\text{TiO}_2\text{-II}$  (**Figure 2.1d**) shows bands at 426  $\text{cm}^{-1}$  and 572  $\text{cm}^{-1}$ . However, the spectral shapes agree well, and thus,  $\text{TiO}_2\text{-II}$  can be identified as a chemical component using this resolved “high spectral” Raman spectrum (**Figure 2.12a**) and its distribution can be subsequently produced.

The “high-spatial” chemical maps (**Figure 2.12b**) show that  $\text{TiO}_2\text{-II}$  is distributed throughout most of the grain, including localized areas of this component in the upper-right and lower-left portions of the grain. The distribution of  $\text{TiO}_2\text{-II}$  is much more resolved in the “high-spatial” chemical maps, in which high concentrations of  $\text{TiO}_2\text{-II}$  are observed as small as  $\sim 2 \mu\text{m}$  in size. For the corresponding resolved “high spatial” Raman spectrum (**Figure 2.12b**), the Raman bands at 155  $\text{cm}^{-1}$ , 173  $\text{cm}^{-1}$ , 286  $\text{cm}^{-1}$ , 314  $\text{cm}^{-1}$ , 339  $\text{cm}^{-1}$ , 356  $\text{cm}^{-1}$ , 424  $\text{cm}^{-1}$ , and 531  $\text{cm}^{-1}$  are in agreement with those of synthetic  $\text{TiO}_2\text{-II}$  at 152  $\text{cm}^{-1}$ , 174  $\text{cm}^{-1}$ , 286  $\text{cm}^{-1}$ , 315  $\text{cm}^{-1}$ , 341  $\text{cm}^{-1}$ , 357  $\text{cm}^{-1}$ , 426  $\text{cm}^{-1}$ , and 531  $\text{cm}^{-1}$ . However, the band at 412  $\text{cm}^{-1}$  in the Raman spectrum of synthetic  $\text{TiO}_2\text{-II}$  was not resolved in the “high-spatial” Raman spectrum. Furthermore, the higher frequency  $\text{TiO}_2\text{-II}$  band occurs at 572  $\text{cm}^{-1}$  in the Raman spectrum of synthetic  $\text{TiO}_2\text{-II}$  and at 565  $\text{cm}^{-1}$  in the resolved “high-spatial” Raman spectrum. The spectral shapes of these two Raman spectra are consistent, but for the resolved “high-spatial” Raman spectrum, the 155  $\text{cm}^{-1}$  and 173  $\text{cm}^{-1}$  bands are merging and the 400-500  $\text{cm}^{-1}$  bands are less distinct than the corresponding bands in the Raman spectrum of synthetic  $\text{TiO}_2\text{-II}$ . Overall, with 25x more Raman spectra acquired over the same area of the grain using limited spectral acquisition parameters, the spatial resolution of the Raman microspectroscopic

imaging can be increased in comparable analysis times and is sufficient to identify TiO<sub>2</sub>-II.

#### 2.4.6 Estimated Raman Spectrum of Pure TiO<sub>2</sub>-II

Synthetic TiO<sub>2</sub>-II, formed under hydrothermal, static conditions[78], was investigated using two excitation wavelengths with varying laser power. Raman spectra collected using 785 nm excitation and laser powers of 1, 10, 25, 50, and 100 mW are shown (**Figure 2.13a**). At low power, the Raman spectra show 12 bands in the range of 150 cm<sup>-1</sup> to 610 cm<sup>-1</sup>. With increasing laser power, the Raman bands show the following changes: the 150 cm<sup>-1</sup> and 175 cm<sup>-1</sup> bands merge into one band centering at 168 cm<sup>-1</sup>, the bands in the 289 cm<sup>-1</sup> to 357 cm<sup>-1</sup> region broaden while changing relative intensity, the three bands in the 412 cm<sup>-1</sup> to 443 cm<sup>-1</sup> region merge into one centering at 414 cm<sup>-1</sup>, and the three bands from 534 cm<sup>-1</sup> to 610 cm<sup>-1</sup> broaden and merge to form two bands at 532 cm<sup>-1</sup> and 564 cm<sup>-1</sup>. Similarly, Raman spectra collected using 532 nm excitation and laser powers of 0.2, 2, 5, 10, and 20 mW are shown (**Figure 2.13b**). At low power, the Raman spectra show 13 bands in the range of 150 cm<sup>-1</sup> to 610 cm<sup>-1</sup>. With increasing laser power, the Raman bands show the following changes: the bands at 150 cm<sup>-1</sup> and 175 cm<sup>-1</sup> merge, the bands in the 289 cm<sup>-1</sup> to 357 cm<sup>-1</sup> region broaden while changing relative intensity—specifically, the 340 cm<sup>-1</sup> and 357 cm<sup>-1</sup> bands merge and change in relative intensity—the four bands in the 412 cm<sup>-1</sup> to 455 cm<sup>-1</sup> region form two bands at 424 cm<sup>-1</sup> and 440 cm<sup>-1</sup>, and the three bands from 534 cm<sup>-1</sup> to 610 cm<sup>-1</sup> broaden and become less distinguishable. For both excitation wavelengths, increasing the laser power causes broadening, relative intensity changes, and merging of bands within the 150 to 610 cm<sup>-1</sup> spectral range in the Raman spectra for this sample of synthetic TiO<sub>2</sub>-II. Spektor et al. demonstrated

that changes similar to these were due to heating of the  $\text{TiO}_2\text{-II}$  and they were reversible.[78]

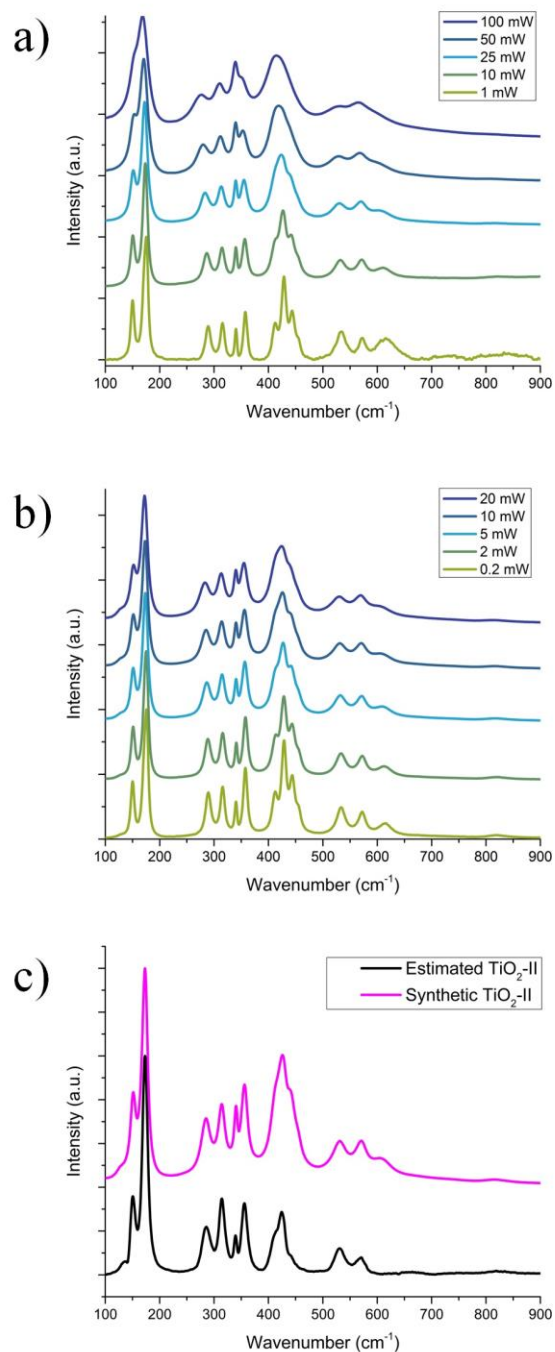


Figure 2.13: Raman spectra from synthetic TiO<sub>2</sub>-II using 785 nm excitation with a laser power of 1 to 100 mW (a) and 532 nm excitation with a laser power of 0.2 to 20 mW (b). In (c), an estimated Raman spectrum (in black) for pure TiO<sub>2</sub>-II is compared with a Raman spectrum (in pink) for synthetic TiO<sub>2</sub>-II.

The excitation wavelength and laser power used during spectral acquisition clearly affect the resulting Raman spectrum of TiO<sub>2</sub>-II (**Figures 2.13a** and **2.13b**). An estimated Raman spectrum of *pure* TiO<sub>2</sub>-II thus should be compared to the Raman spectrum of synthetic TiO<sub>2</sub>-II at an analogous excitation wavelength and laser power. A Raman spectrum for *pure* TiO<sub>2</sub>-II was estimated using the resolved Raman spectrum for the TiO<sub>2</sub>-II chemical component generated from MCR-ALS applied to Raman microspectroscopic imaging measurements. In total, resolved Raman spectra from nineteen Raman microspectroscopic imaging measurements—which produced 7,075 Raman spectra—on unique portions of six TiO<sub>2</sub>-II-bearing grains were used to generate the estimated Raman spectrum of *pure* TiO<sub>2</sub>-II. Furthermore, MCR-ALS models were built using 20 component models to ensure no other chemical species were present within the resolved Raman spectrum other than TiO<sub>2</sub>-II. Thus, nineteen resolved Raman spectra of pure TiO<sub>2</sub>-II were generated using MCR-ALS, and the average of these spectra was used to generate the Raman spectrum of *pure* TiO<sub>2</sub>-II.

The estimated Raman spectrum of *pure* TiO<sub>2</sub>-II (in black in **Figure 2.13c**) shows bands at 151 cm<sup>-1</sup>, 173 cm<sup>-1</sup>, 286 cm<sup>-1</sup>, 315 cm<sup>-1</sup>, 340 cm<sup>-1</sup>, 356 cm<sup>-1</sup>, 412 cm<sup>-1</sup>, 425 cm<sup>-1</sup>, 531 cm<sup>-1</sup>, and 571 cm<sup>-1</sup>. For comparison, a Raman spectrum of synthetic TiO<sub>2</sub>-II (in pink in **Figure 2.13c**) was collected using 532 nm excitation and a laser power of 10 mW, and this spectrum shows bands at 152 cm<sup>-1</sup>, 174 cm<sup>-1</sup>, 286 cm<sup>-1</sup>, 315 cm<sup>-1</sup>, 341 cm<sup>-1</sup>, 357 cm<sup>-1</sup>, 412 cm<sup>-1</sup>, 426 cm<sup>-1</sup>, 443 cm<sup>-1</sup>, 531 cm<sup>-1</sup>, 572 cm<sup>-1</sup>, and 609 cm<sup>-1</sup>. The spectral shape of the estimated Raman spectrum of *pure* TiO<sub>2</sub>-II is very similar to that of synthetic TiO<sub>2</sub>-II, with the most intense bands being at 173/174 cm<sup>-1</sup> and 425/426 cm<sup>-1</sup>. The Raman spectrum for synthetic TiO<sub>2</sub>-II shows bands at 443 cm<sup>-1</sup> and 609 cm<sup>-1</sup> that are not present in the estimated Raman spectrum of *pure* TiO<sub>2</sub>-II.

These two bands may be representative of rutile, the precursor phase of TiO<sub>2</sub>-II in this sample. The estimated Raman spectrum of *pure* TiO<sub>2</sub>-II generated from MCR-ALS applied to Raman microspectroscopic imaging contains ten bands in the region of 150 cm<sup>-1</sup> to 600 cm<sup>-1</sup>, and this Raman spectrum can be used to facilitate the identification of TiO<sub>2</sub>-II within complex materials.

#### **2.4.7 Geologic Importance of Characterizing the TiO<sub>2</sub>-II-Bearing Grains using MCR-ALS Applied to Raman Microspectroscopic Imaging**

The identification of chemical species within complex geological materials can be accomplished with limited sample preparation in a non-destructive, non-invasive manner using Raman microspectroscopic imaging with multivariate analysis techniques. Raman microspectroscopic imaging with MCR-ALS is an excellent tool for the discovery and characterization of fine-grained shock-metamorphosed materials. The global supply (n = 34) of documented TiO<sub>2</sub>-II-bearing grains from the CSL, JSL, BGSL, and MSL is still quite small[88], but hundreds to thousands of such grains should be recoverable from these layers using greater amounts of sample material. Detailed characterization of the distribution of chemical species in the TiO<sub>2</sub>-II-bearing grains can provide insight into the mechanisms of formation of TiO<sub>2</sub>-II. For example, in highly shock-metamorphosed gneiss clasts from impact breccia at the Ries impact structure, Germany, TiO<sub>2</sub>-II occurs along the outer margins of the rutile grains that are enclosed within biotite, and the TiO<sub>2</sub>-II is interpreted as having formed by direct phase transition from rutile during shock compression.[84] In moderately shock-metamorphosed gneiss clasts from impact breccia at the Xiuyan crater, China, some of the TiO<sub>2</sub>-II occurs as irregular layers, commonly <1.5 μm in width, along fractures and cracks within the precursor rutile grains.[86] The TiO<sub>2</sub>-II in this context may have

formed during the decompression stage at elevated shock temperatures.[86] Although the number of TiO<sub>2</sub>-II-bearing grains used in our study is limited, chemical maps for the five grains (**Figures 2.5–2.8 and 2.12**) show differences in the distribution and relative concentration of TiO<sub>2</sub>-II in these grains. For the two grains from the BGSL, TiO<sub>2</sub>-II is widely distributed in the first grain (**Figure 2.5a**), whereas TiO<sub>2</sub>-II is more highly concentrated in the interior of the second grain (**Figure 2.6a**). For the two grains from the MSL, TiO<sub>2</sub>-II is more concentrated near the margins of the first grain (**Figure 2.6c**), whereas TiO<sub>2</sub>-II occurs more widely within the second grain (**Figure 2.12**). In contrast to these four grains, in the grain from the CSL (**Figure 2.7a**), TiO<sub>2</sub>-II shows a more localized distribution and lower overall concentrations. Our results demonstrate that differences in the distribution and concentration of TiO<sub>2</sub>-II are revealed in a limited number of grains using Raman microspectroscopic imaging with MCR-ALS. Future studies of tens to hundreds of TiO<sub>2</sub>-II-bearing grains from these layers using these methods should allow a more complete characterization of the chemical species, including TiO<sub>2</sub>-II, within these grains. These results should be useful in determining the mechanism(s) of formation of the TiO<sub>2</sub>-II, as well as evaluating the potential of these grains to serve as a tool to shed light on the paleodistances of the layers from their source craters and to test the proposed correlation[97] of the CSL, JSL, and MSL.

Raman microspectroscopic imaging with MCR-ALS also provided information concerning the detection and distribution of anatase and quartz within these TiO<sub>2</sub>-II-bearing grains (**Figures 2.6 and 2.7**). In the study of TiO<sub>2</sub>-II within the Chesapeake Bay impact structure, USA, it was suggested that both rutile and anatase were precursor phases for some of the TiO<sub>2</sub>-II.[85] For our TiO<sub>2</sub>-II-bearing grains, however,

Raman microspectroscopic imaging with MCR-ALS shows that the distributions of rutile and TiO<sub>2</sub>-II are highly complementary, suggesting that rutile is the direct precursor phase for TiO<sub>2</sub>-II.

Raman microspectroscopic imaging with MCR-ALS did not detect coesite or stishovite, high-pressure polymorphs of SiO<sub>2</sub>, in these TiO<sub>2</sub>-II-bearing grains, in agreement with the results of Smith et al.[88] Our results therefore suggest that anatase and quartz are secondary phases formed after the deposition of the spherule layers.

## 2.5 Conclusions

Multivariate analysis methods, including MCR-ALS, in conjunction with Raman microspectroscopic imaging have offered unique advantages to investigating TiO<sub>2</sub>-II-bearing grains as compared to univariate analysis methods. With high spectral overlap observed in the Raman spectra of TiO<sub>2</sub> polymorphs (rutile, anatase, and TiO<sub>2</sub>-II), SiO<sub>2</sub> polymorphs (quartz), and substrate-adhesive epoxy, the determination of the individual chemical species' spatial distribution using univariate methods is a challenging task. Using MCR-ALS, however, resolved Raman spectra and spatial distributions of these chemical components were determined. Thus, MCR-ALS allowed for the resolution of chemical maps of all species present within the TiO<sub>2</sub>-II-bearing grains, whereas univariate methods cannot due to the spectral overlap. Additionally, MCR-ALS allowed for the identification of minor chemical species within the grains. MCR-ALS generated the resolved Raman spectra of minor chemical phases, including anatase and quartz, and using this resolved spectrum, proper identification of the chemical component was achieved. Subsequent to identification,

MCR-ALS also provides the spatial distribution of the minor chemical species present, allowing for accurate chemical maps to be determined. Using univariate methods, misidentification could potentially occur if the spectral overlap is significant enough, and even when identification is successful, the distribution still may be indeterminate due to this overlap. MCR-ALS also allows for the identification of chemical components embedded within low signal to noise spectra. Specifically, in the low signal to noise data we present, no reliable chemical map could be constructed using univariate methods; however, MCR-ALS resolved reasonable chemical maps and constituent spectra of quality comparable to that from high signal to noise data. Overall, MCR-ALS applied to Raman microspectroscopic imaging allowed for spatially-resolved chemical maps and resolved Raman spectra to be determined even with high spectral overlap present, and allowed for the investigation of minor chemical species within the sample.

Raman microspectroscopic imaging with MCR-ALS shows that the TiO<sub>2</sub>-II-bearing grains consist primarily of rutile and TiO<sub>2</sub>-II, confirming the results of Smith et al.[88] PCA yields a predominantly three-phase system comprised of rutile, TiO<sub>2</sub>-II, and substrate-adhesive epoxy. BSE and SE images show the grains to be heterogeneous and to consist of polydispersed, micrometer- and submicrometer-sized particles. Using MCR-ALS applied to Raman microspectroscopic imaging, we generated spectral profiles and spatially-resolved chemical maps of up to five distinct chemical species—rutile, TiO<sub>2</sub>-II, anatase, quartz, and substrate-adhesive epoxy—for these grains. The spatial resolution of the Raman microspectroscopic maps was increased in cost-effective analysis times by limiting spectral resolution and optimizing spectral acquisition. Using MCR-ALS applied to Raman

microspectroscopic imaging, we estimated a Raman spectrum for *pure* TiO<sub>2</sub>-II that can be used to facilitate the identification of TiO<sub>2</sub>-II within complex materials. This Raman spectrum contains the following ten bands in the region of 150 cm<sup>-1</sup> to 600 cm<sup>-1</sup>: 151 cm<sup>-1</sup>, 173 cm<sup>-1</sup>, 286 cm<sup>-1</sup>, 315 cm<sup>-1</sup>, 340 cm<sup>-1</sup>, 356 cm<sup>-1</sup>, 412 cm<sup>-1</sup>, 425 cm<sup>-1</sup>, 531 cm<sup>-1</sup>, and 571 cm<sup>-1</sup>. To our knowledge, this is the first report of an estimated Raman spectrum for *pure* TiO<sub>2</sub>-II. Raman microspectroscopic imaging with MCR-ALS revealed differences in the distribution of TiO<sub>2</sub>-II even within a limited number of TiO<sub>2</sub>-II-bearing grains. Using these methods, future studies of tens to hundreds of TiO<sub>2</sub>-II-bearing grains from these spherule layers should help to elucidate the formative mechanism(s) of TiO<sub>2</sub>-II in these grains and to better understand the formation of these layers. Our results suggest that rutile is the direct precursor of TiO<sub>2</sub>-II in these grains and that anatase and quartz are secondary phases. The methodology we used to investigate these TiO<sub>2</sub>-II-bearing grains should be applicable for the investigation of other high-pressure polymorphs, e.g., coesite, in shock-metamorphosed materials.

## Chapter 3

### HIGH SPECTRAL AND HIGH SPATIAL RESOLUTION RAMAN MICROSCOPIC IMAGING OF THE HIGH-PRESSURE POLYMORPH, TiO<sub>2</sub>-II: PROVIDING DATA SETS FOR MULTIVARIATE AND CHEMOMETRIC ANALYSIS

#### 3.1 Abstract

The recent identification of the high-pressure,  $\alpha$ -PbO<sub>2</sub>-structured polymorph of titanium dioxide, TiO<sub>2</sub>-II, in grains recovered from four Neoproterozoic spherule layers has provided physical evidence to further support an impact origin of these layers. Smith et al. (2017) investigated these TiO<sub>2</sub>-II-bearing grains using Raman microspectroscopic imaging with multivariate curve resolution-alternating least squares (MCR-ALS) to spatially and spectrally resolve the individual chemical species within the grains. In this chapter, we provide an analysis of high spectral and spatial resolution Raman microspectroscopic imaging data collected on the TiO<sub>2</sub>-II-bearing grains and offer a discussion of the importance of this Raman microspectroscopic imaging data to the scientific community. Moreover, in this chapter, we provide chemical maps, chemical images and Raman spectra of rutile, TiO<sub>2</sub>-II, anatase, quartz, and substrate-adhesive epoxy that were resolved using MCR-ALS applied to the Raman microspectroscopic imaging data. The results of Raman microspectroscopic imaging—collected using both high spectral resolution and high spatial resolution—

provide a myriad of opportunities for the scientific community in wide ranging applications, including the chemical imaging and chemometric disciplines.

### 3.2 Introduction

Titanium dioxide ( $\text{TiO}_2$ ) is extensively utilized in a variety of applications, ranging from photocatalysis to water splitting reactions.[67, 68, 70] Rutile, anatase, and brookite are the main natural  $\text{TiO}_2$  polymorphs, with rutile being most abundant.[71] Five high-pressure polymorphs of  $\text{TiO}_2$  exist.[76, 77] A primary focus of this chapter is the orthorhombic,  $\alpha$ - $\text{PbO}_2$ -structured high pressure polymorph, termed  $\text{TiO}_2$ -II, which has recently gained momentum due to its stability at ambient pressure and temperature.[78]

Natural  $\text{TiO}_2$ -II has been documented in both ultrahigh-pressure metamorphic[80-83] and shock-metamorphosed[84-87] materials. Recently, shock-metamorphosed grains containing rutile and  $\text{TiO}_2$ -II have been documented from four Neoproterozoic spherule layers—Carawine spherule layer (CSL), Jeerinah spherule layer (JSL), Monteville spherule layer (MSL), and Bee Gorge spherule layer (BGSL)—deposited between ~2.65 and ~2.54 billion years ago.[88] These grains, which provide unambiguous physical evidence to further support an impact origin for these layers[88], comprise the samples for this study.

Raman microspectroscopic imaging is employed in various research areas, including biological and materials sciences.[65, 105-108] Multivariate analysis methods, including MCR-ALS, applied to Raman microspectroscopic imaging can provide spatially resolved chemical images and spectra of the individual chemical species within a sample.[50, 53-55, 65] Recently, Smith et al. were the first to employ

Raman microspectroscopic imaging with MCR-ALS to determine the distribution of TiO<sub>2</sub>-II in these shock-metamorphosed grains, in which spectral profiles and spatially-resolved chemical maps of rutile, TiO<sub>2</sub>-II, anatase, quartz, and substrate-adhesive epoxy were generated at different spatial resolutions.[51]

In this chapter, we present the Raman microspectroscopic imaging data collected on the TiO<sub>2</sub>-II-bearing grains using both high spectral and high spatial resolution and the results of MCR-ALS applied to this Raman microspectroscopic imaging data on a selected grain from the MSL. We offer a detailed comparison between high spectral and high spatial resolution imaging data, and a discussion of the data's importance to the scientific community.

### **3.3 Materials and Methods**

#### **3.3.1 Sample Preparation**

Uncoated, polished grain mounts of selected TiO<sub>2</sub>-II-bearing grains identified by Smith et al.[88] were made. Moreover, surface outcrop samples (~kg-sized samples) of the four spherule layers—Carawine spherule layer (CSL), Jeerinah spherule layer (JSL), Bee Gorge spherule layer (BGSL), and Monteville spherule layer (MSL)—were trimmed, rinsed with water, and dried for at least 12 hours at 60-70 °C. Due to these samples having a high carbonate content, acid digestion with hydrochloric acid (Fisher Scientific, 12.1 N) at ~60 °C was performed. The pH of the solution was subsequently neutralized by dilution with water. The acid-insoluble residues were wet sieved and ultrasonically agitated, resulting in the collection of five size fractions: <38 μm, 38-63 μm, 63-125 μm, 125-250 μm, and >250 μm. Heavy

liquid ( $\rho = 2.96 \text{ g/cm}^3$ ) separation of the 63-125  $\mu\text{m}$  size fractions was performed with 1,1,2,2-tetrabromoethane (Fisher Scientific, 99 %), and the resulting heavy mineral separates were collected (Whatman filter paper, 11  $\mu\text{m}$  pore size) and rinsed with acetone (Fisher Scientific, 99%). Grains were subsequently fixed to a glass slide (Fisher Scientific, 25.4 mm diameter x 1.0 mm thick) using epoxy (Buehler), and polished to expose the grains. Details of locations, lithologies, and preparation are given in Smith et al.[88]

### **3.3.2 Scanning Electron Microscopy (SEM)**

Backscattered electron (BSE) images, collected using an FEI Quanta 450 FEG scanning electron microscope operated at 10-30 kV and low vacuum, were obtained for  $\text{TiO}_2$ -II-bearing grains in the polished grain mounts.

### **3.3.3 Raman Microspectroscopic Imaging**

A Senterra Raman spectrometer (Bruker Optics, Massachusetts, USA) coupled to a BX-51 microscope (Olympus, New York, USA) was used for all Raman microspectroscopic imaging measurements. A 532 nm laser excitation source was focused onto the sample using objective lenses (Olympus, New York, USA). The objective lenses, with numerical apertures (NA) listed, were 20 $\times$  (0.40 NA), 50 $\times$  (0.75 NA), and 100 $\times$  (0.80 NA) magnification, which yield a laser spot size of 5  $\mu\text{m}$ , 2  $\mu\text{m}$ , and 1  $\mu\text{m}$  in diameter, respectively. Scattered light from the sample was collected by the objective lens, dispersed by a 1200 grooves/mm grating, and detected by a charge-coupled device (CCD) detector (Bruker Optics, Massachusetts, USA) thermoelectrically-cooled to  $-65 \text{ }^\circ\text{C}$ . A constant laser power of 2 to 10 mW was used. Integration times of 1 to 15 seconds with 0 to 3 co-averages were used. Background

measurements equal to the respective integration time were acquired for each measurement. In total, the collection time for each Raman spectrum was ~6 to 90 seconds. A spectral region of 70-1550  $\text{cm}^{-1}$ , covered under one grating position, was used for all measurements. Excitation wavelength and wavenumber calibration were internally performed using a neon lamp prior to each measurement. Ultimately, the spectral resolution of each Raman spectrum was 3 to 5  $\text{cm}^{-1}$ .

Raman microspectroscopic imaging data was generated using rectangular grids with assigned size and locations for the collection of Raman spectra based on the dimensions of the grain being analyzed. The step size between collected Raman spectra within a spectral grid was ~1 to 4  $\mu\text{m}$ . Spectral grids consisting of 15 by 15 (225 total), 20 by 20 (400 total), and 100 by 100 (10,000 total) Raman spectra were generated. The lateral and horizontal motion was controlled using a motorized stage, and the height above the sample was held constant for all measurements.

Data collected using “high spectral” resolution were generated using typically 400 total Raman spectra (20 by 20 spectral grid) with 10 seconds of integration time and 3 co-averages. Using this methodology, the total analysis time is ~200 minutes. For “high spatial” resolution data, 10,000 total Raman spectra (100 by 100 spectral grid) were collected over the same area with typically 1 second of integration time and no co-averages. Using this methodology, the total analysis time is ~167 minutes. Furthermore, the “high spectral” resolution chemical maps and resolved spectra shown in this chapter were generated using 400 total Raman spectra (20 by 20 spectral grid) with integration times of 15 seconds. The “high spatial” chemical maps and resolved spectra shown in this chapter were generated using 10,000 total Raman spectra (100 by 100 spectral grid) with an integration time of 1 second and no co-averages.

### 3.3.4 Multivariate Curve Resolution-Alternating Least Squares (MCR-ALS)

MCR-ALS[53, 55, 61, 113] is used to resolve the spatial and spectral information about unique components that are imbedded in a hyperspectral image. A significant advantage of MCR-ALS is that prior information about the sample is not essential. MCR-ALS resolves an experimental data matrix,  $\mathbf{D}$ , using:

$$\mathbf{D} = \mathbf{C}\mathbf{S}^T + \mathbf{E} \quad (3.1)$$

where  $\mathbf{C}$  is the concentration profile matrix of each chemical component,  $\mathbf{S}^T$  is the resolved spectra matrix, and  $\mathbf{E}$  is the error matrix. The number of components contributing to  $\mathbf{D}$  can be determined by prior knowledge of the system, principal component analysis (PCA), or other multivariate techniques. The calculation and iterative optimization of  $\mathbf{C}$  and  $\mathbf{S}^T$  by ALS is subsequently performed after an initial estimation of  $\mathbf{S}$ . Constraints of non-negative concentrations and non-negative spectral intensity are often employed during ALS to help guide solutions to the true value. Convergence is achieved by applying Eq. (3.2) and Eq. (3.3) in an alternating fashion to the updated estimates of  $\mathbf{C}$  and  $\mathbf{S}$ , denoted as  $\check{\mathbf{C}}$  and  $\check{\mathbf{S}}$ , respectively:

$$\check{\mathbf{S}} = \mathbf{D}^T \check{\mathbf{C}} / \check{\mathbf{C}}^T \check{\mathbf{C}} \quad (3.2)$$

$$\check{\mathbf{C}} = \mathbf{D} \check{\mathbf{S}} / \check{\mathbf{S}}^T \check{\mathbf{S}} \quad (3.3)$$

In the current study, MCR-ALS is applied to the experimental data matrix,  $\mathbf{D}$ , containing the spatial and spectral information. Each row of  $\mathbf{D}$  is the intensity at various wavenumbers. The number of components was selected prior to the ALS step using initial estimations from PCA. When the model derived from these initial estimations did not suffice, the number of components was optimized by comparison of the resolved spectra in  $\mathbf{S}$  with Raman spectra of appropriate reference materials. Therefore, the number of selected components was increased until the resolved spectra

were sufficiently comparable to the Raman spectra of respective reference materials. The MCR-ALS results shown in this chapter were generated using twenty-component models. Initial estimates of spectra for ALS were determined by distance criteria, in which the first spectrum for initialization was selected to be furthest from the mean. Moreover, subsequent spectra were selected to be furthest from the mean and all prior selected samples. The constraints of non-negative concentration and non-negative spectral intensity were applied, and a 0.01% convergence was used.

All MCR-ALS results were generated in Matlab 7.12 (Mathworks) with the PLS toolbox (Eigenvector Research Inc.). The final concentration profile matrix, **C**, contains each chemical component's concentration profile, and each column in **C** thus corresponds to a component. Chemical maps are subsequently reconstructed from **C** using Matlab with the PLS Toolbox. OriginPro (Origin Lab v9.1 Pro) was used for visualization of the chemical maps, as shown in the respective MCR-ALS figures. The chemical maps are presented in terms of percent spectral contributions to investigate the relative magnitude of the chemical species within a sample. Furthermore, this percent spectral contribution is based on the chemically meaningful species within the sample. For example, if six chemically meaningful species are identified within a sample, each chemical map generated is the concentration matrix, **C**, of the respective chemical species divided by the summation of six total chemical species' concentration matrices. In the resolved spectra matrix, **S**, each row contains the resolved spectrum. The entire spectral range, 70-1550  $\text{cm}^{-1}$ , was used for MCR-ALS analysis. No preprocessing was performed prior to analysis by MCR-ALS. The graphical representations of the individual spectra were generated using OriginPro.

### 3.4 Results and Discussion

#### 3.4.1 Raman Microspectroscopy with High Spectral and High Spatial Resolution

Raman microspectroscopy was recently employed to document TiO<sub>2</sub>-II-bearing grains recovered from the CSL, JSL, BGSL, and MSL.[88] Subsequently, detailed characterization, including chemical imaging and spectroscopic probing, of the TiO<sub>2</sub>-II and the additional chemical species within these grains was performed using Raman microspectroscopic imaging with multivariate analysis methods.[51] In this chapter, Raman microspectroscopy (**Figure 3.1**) and Raman microspectroscopic imaging (**Figures 3.2** and **3.3**) were used to investigate TiO<sub>2</sub>-II-bearing grains recovered from the four spherule layers using both “high spectral” and “high spatial” resolution. Moreover, here we present the results of MCR-ALS applied to the Raman microspectroscopic imaging data of a selected grain from the MSL. This chapter thus provides the results of MCR-ALS using both “high spectral” resolution (**Figure 3.2**) and “high spatial” resolution Raman microspectroscopic imaging (**Figure 3.3**).

Raman microspectroscopy was employed on selected locations of the MSL grain in order to gain an initial estimation of the chemical species present. Backscattered electron (BSE) images (**Figure 3.1A**) show that the selected MSL grain contains polydispersed sized particles with varying shapes. Furthermore, these particles are polycrystalline, and are micrometer and sub-micrometer in size. Raman spectra (**Figure 3.1B** and **3.1C**) and their corresponding locations (**Figure 3.1A**) on the grain are displayed. For the Raman spectra collected with “high spectral” resolution (**Figure 3.1B**), rutile, TiO<sub>2</sub>-II, quartz, and substrate-adhesive epoxy are

identified. Anatase, due to the intensity of the  $145\text{ cm}^{-1}$  band (**Figure 3.1B, spectra #3**), may be present within the sample. Similarly, for the Raman spectra collected with “high spatial” resolution (**Figure 3.1C**), rutile,  $\text{TiO}_2\text{-II}$ , quartz, and substrate-adhesive epoxy are identified, and anatase is again potentially present within the sample due to the intense  $145\text{ cm}^{-1}$  Raman band.

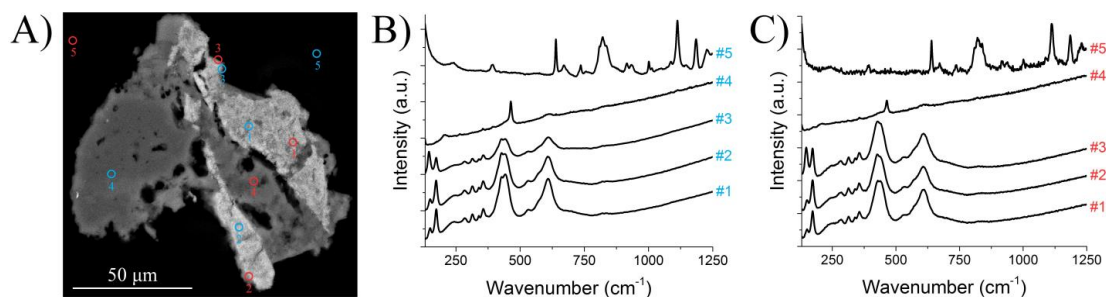


Figure 3.1: Backscattered electron (BSE) image (A) of a selected MSL grain. Raman spectra acquired with high spectral resolution (B) were collected at the corresponding numbered locations shown in blue (A). Raman spectra acquired with high spatial resolution (C) were collected at the corresponding numbered locations shown in red (A).

### 3.4.2 High Spectral Resolution Raman Microspectroscopic Imaging with Multivariate Curve Resolution-Alternating Least Squares (MCR-ALS)

MCR-ALS applied to the Raman microspectroscopic imaging data collected on the MSL grain with “high spectral” resolution (**Figure 3.2**) results in chemical maps, pixel-by-pixel chemical images, and resolved Raman spectra of rutile,  $\text{TiO}_2\text{-II}$ , anatase, quartz, and substrate-adhesive epoxy. The resolved Raman spectra generated from MCR-ALS confirm the presence of these five chemical species. Furthermore, the first resolved Raman spectrum (**Figure 3.2B**) displays bands at  $237\text{ cm}^{-1}$ ,  $443\text{ cm}^{-1}$ ,

and  $609\text{ cm}^{-1}$  that are indicative of rutile. The second resolved Raman spectrum (**Figure 3.2C**) displays bands at  $151\text{ cm}^{-1}$ ,  $173\text{ cm}^{-1}$ ,  $285\text{ cm}^{-1}$ ,  $314\text{ cm}^{-1}$ ,  $339\text{ cm}^{-1}$ ,  $357\text{ cm}^{-1}$ ,  $409\text{ cm}^{-1}$ ,  $423\text{ cm}^{-1}$ ,  $533\text{ cm}^{-1}$ , and  $565\text{ cm}^{-1}$  that are indicative of  $\text{TiO}_2\text{-II}$ . The third resolved Raman spectrum (**Figure 3.2D**) displays bands at  $144\text{ cm}^{-1}$ ,  $197\text{ cm}^{-1}$ ,  $514\text{ cm}^{-1}$ , and  $635\text{ cm}^{-1}$  that are indicative of anatase. The fourth resolved Raman spectrum (**Figure 3.2E**) displays bands at  $127\text{ cm}^{-1}$ ,  $206\text{ cm}^{-1}$ ,  $396\text{ cm}^{-1}$ , and  $464\text{ cm}^{-1}$  that are indicative of quartz. Finally, the fifth resolved Raman spectrum (**Figure 3.2F**) displays bands at  $640\text{ cm}^{-1}$ ,  $821\text{ cm}^{-1}$ ,  $1002\text{ cm}^{-1}$ ,  $1113\text{ cm}^{-1}$ ,  $1186\text{ cm}^{-1}$ ,  $1229\text{ cm}^{-1}$ ,  $1252\text{ cm}^{-1}$ ,  $1299\text{ cm}^{-1}$ , and  $1461\text{ cm}^{-1}$  that are indicative of substrate-adhesive epoxy.

The distributions of these five chemical components are also generated using the “high spectral” resolution Raman microspectroscopic imaging data with MCR-ALS. Moreover, the Raman microspectroscopic imaging data generated using “high spectral” resolution contains the 400 total Raman spectra collected within the given probed area (**Figure 3.2A**). Using a twenty component MCR-ALS model in conjunction with this “high spectral” resolution data, the distributions of rutile,  $\text{TiO}_2\text{-II}$ , anatase, quartz, and substrate-adhesive epoxy are resolved. Specifically, rutile is primarily distributed throughout the grain, and  $\text{TiO}_2\text{-II}$  is distributed in a complementary fashion to rutile. Anatase is localized in the grain, and quartz is primarily distributed on the outer portions of the grain. Finally, substrate-adhesive epoxy is located primarily outside of the grain boundaries. These distributions can be observed in both the chemical maps and the pixel-by-pixel chemical images in **Figure 3.2**.

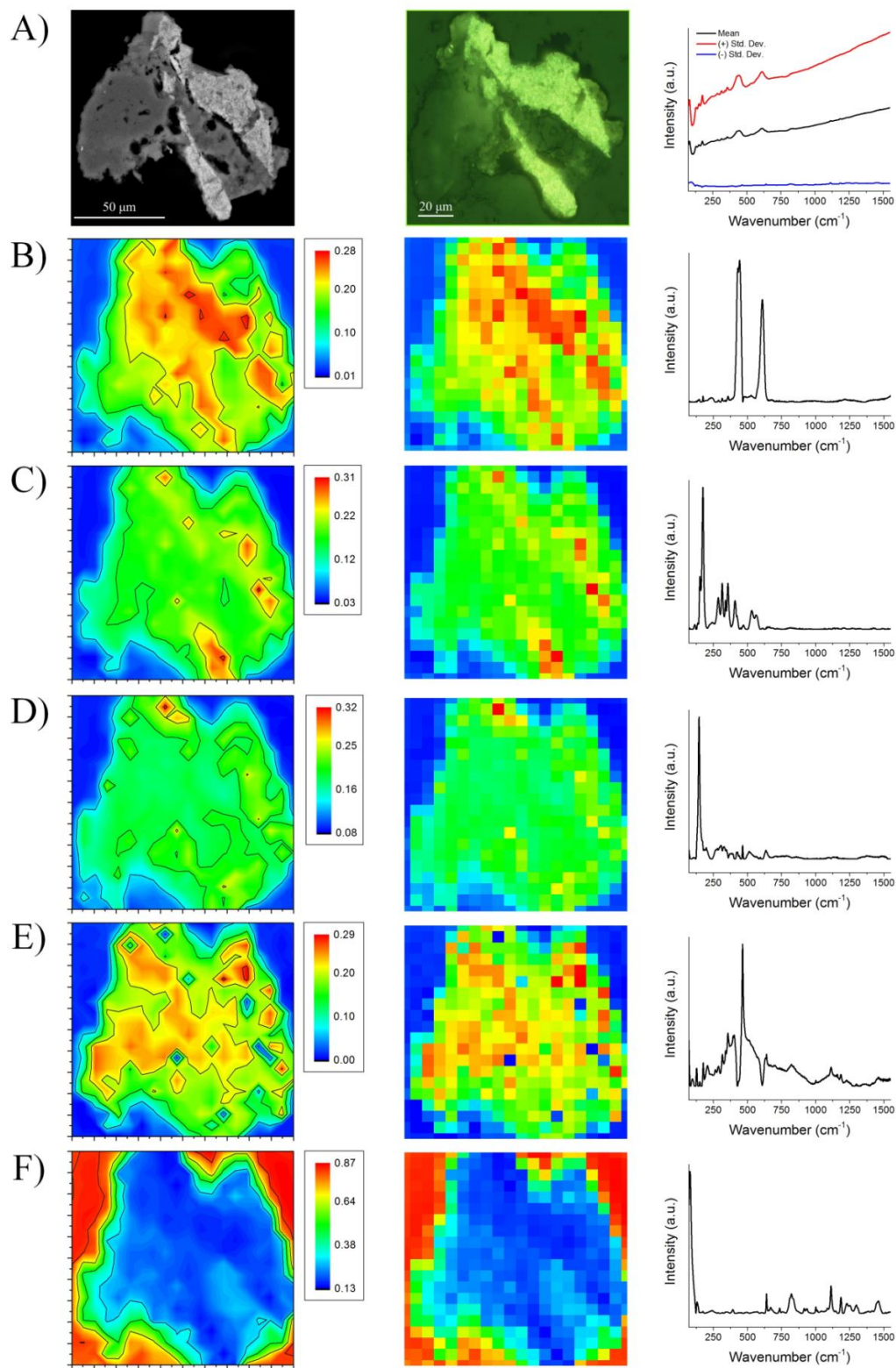


Figure 3.2: Spatially-resolved chemical maps, spatially-resolved pixel-by-pixel chemical images, and resolved Raman spectra of rutile (B), TiO<sub>2</sub>-II (C), anatase (D), quartz (E), and substrate-adhesive epoxy (F) generated using MCR-ALS applied to Raman microspectroscopic imaging. The backscattered electron (BSE) image (A), optical image (A), and mean spectrum (black, A) +/- the standard deviation (+ in red, - in blue; A) are shown. Raman microspectroscopic imaging results were generated using 532 nm excitation and a 20 by 20 spectral grid.

### 3.4.3 High Spatial Resolution Raman Microspectroscopic Imaging with MCR-ALS

MCR-ALS applied to the Raman microspectroscopic imaging data collected on the MSL grain with “high spatial” resolution (**Figure 3.3**) results in chemical maps, pixel-by-pixel chemical images, and resolved Raman spectra for rutile, TiO<sub>2</sub>-II, anatase, quartz, and substrate-adhesive epoxy. The presence of these five chemical species is confirmed by the resolved Raman spectra. Moreover, the first resolved Raman spectrum (**Figure 3.3A**) displays bands at 237 cm<sup>-1</sup>, 437 cm<sup>-1</sup>, and 605 cm<sup>-1</sup> that are indicative of rutile. The second resolved Raman spectrum (**Figure 3.3B**) displays bands at 173 cm<sup>-1</sup>, 286 cm<sup>-1</sup>, 314 cm<sup>-1</sup>, 339 cm<sup>-1</sup>, 356 cm<sup>-1</sup>, 423 cm<sup>-1</sup>, 531 cm<sup>-1</sup>, and 569 cm<sup>-1</sup> that are indicative of TiO<sub>2</sub>-II. The third resolved Raman spectrum (**Figure 3.3C**) displays bands at 146 cm<sup>-1</sup>, 199 cm<sup>-1</sup>, 401 cm<sup>-1</sup>, 513 cm<sup>-1</sup>, and 638 cm<sup>-1</sup> that are indicative of anatase. The fourth resolved Raman spectrum (**Figure 3.3D**) displays a band at 465 cm<sup>-1</sup> that is indicative of quartz. The fifth resolved Raman spectrum (**Figure 3.3E**) displays bands at 640 cm<sup>-1</sup>, 820 cm<sup>-1</sup>, 1002 cm<sup>-1</sup>, 1113 cm<sup>-1</sup>, 1185 cm<sup>-1</sup>, 1230 cm<sup>-1</sup>, 1248 cm<sup>-1</sup>, 1298 cm<sup>-1</sup>, and 1458 cm<sup>-1</sup> that are characteristic of substrate-adhesive epoxy.

The resolved spectrum for quartz (**Figure 3.3D**) also displays large, broad bands at 376 cm<sup>-1</sup> and 965 cm<sup>-1</sup> that are attributed to baseline fluctuations and

background interference effects. With the limited spectral acquisition parameters in the “high spatial” resolution measurements (i.e., 1 second integration times and no co-averages), it is more difficult to resolve the minor chemical phases. Furthermore, although the spatial resolution is increased in these “high spatial” resolution Raman microspectroscopic imaging measurements, the spectral intensity and signal-to-noise ratio can be lower, and in turn, resolving chemical species spectrally can be more difficult.

The distributions of these five chemical components are also generated using the “high spatial” resolution Raman microspectroscopic imaging data with MCR-ALS. This “high spatial” resolution Raman microspectroscopic imaging data consists of 10,000 total Raman spectra collected within the given probed area (**Figure 3.2A**). By applying a twenty component MCR-ALS model to this “high spatial” resolution Raman microspectroscopic imaging data, the distributions of rutile, TiO<sub>2</sub>-II, anatase, quartz, and substrate-adhesive epoxy are resolved. The “high spatial” resolution Raman microspectroscopic imaging data produces a more refined distribution of the chemical species present, which is especially noticeable in the pixel-by-pixel chemical images (**Figure 3.3**). Specifically, rutile is located throughout the entire grain, whereas TiO<sub>2</sub>-II is distributed in a complementary fashion to rutile throughout the grain. Anatase is highly localized towards the top of the grain. Quartz is distributed throughout most of the grain, including towards the outer-left portions of the grain. Finally, substrate-adhesive epoxy is located primarily outside of the grain boundaries. These distributions can be observed in both the chemical maps and the pixel-by-pixel chemical images in **Figure 3.3**.

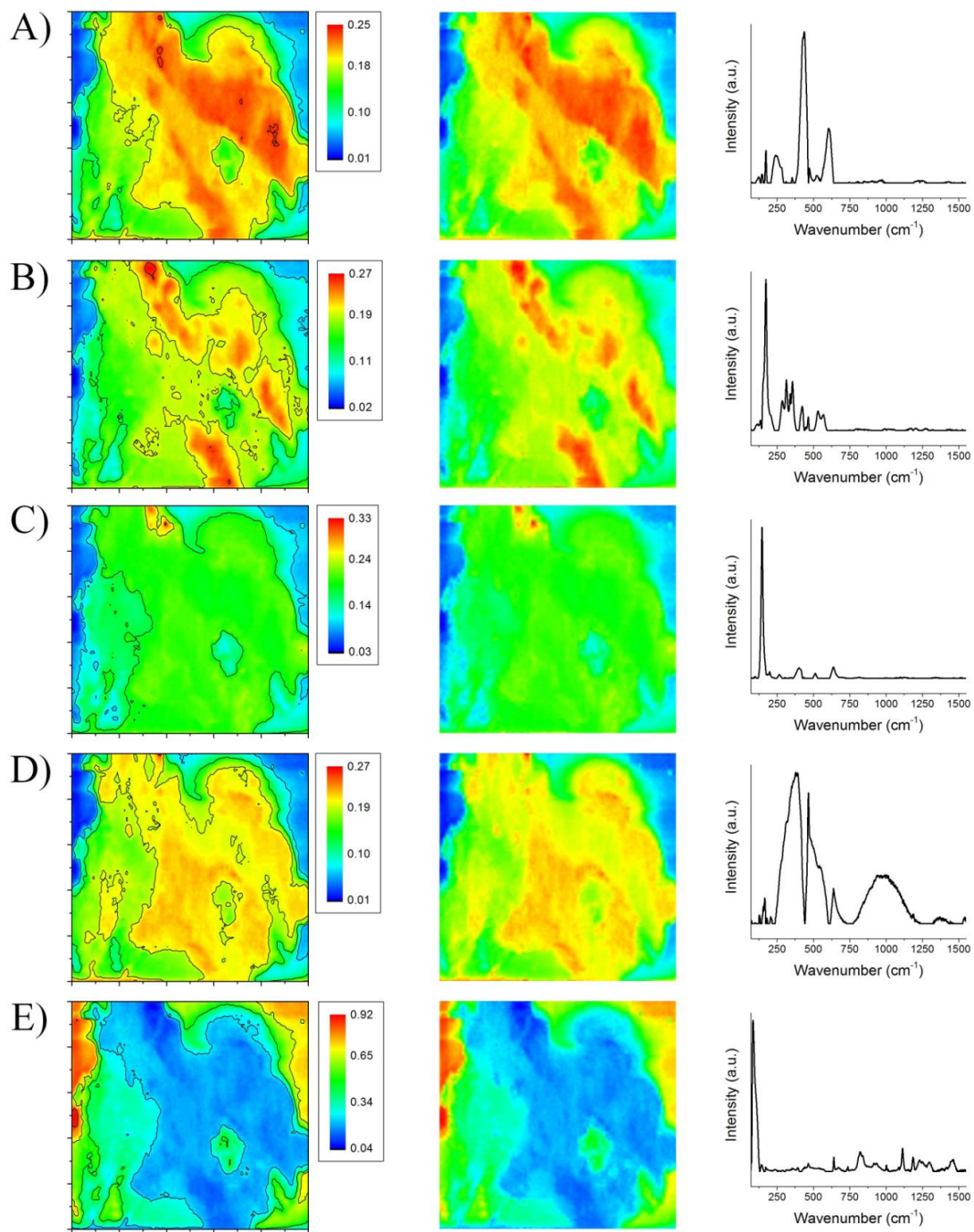


Figure 3.3: Spatially-resolved chemical maps, spatially-resolved pixel-by-pixel chemical images, and resolved Raman spectra of rutile (A), TiO<sub>2</sub>-II (B), anatase (C), quartz (D), and substrate-adhesive epoxy (E) generated using MCR-ALS applied to Raman microspectroscopic imaging. Raman microspectroscopic imaging results were generated using 532 nm excitation and a 100 by 100 spectral grid.

#### **3.4.4 Value of High Spectral and High Spatial Resolution Raman Microspectroscopic Imaging Data Sets to the Scientific Community**

In total, nineteen data sets, directly provided in Smith et al.[52], of Raman microspectroscopic imaging measurements collected on TiO<sub>2</sub>-II-bearing grains from the four spherule layers—CSL, JSL, MSL, and BGSL—were generated. Of the nineteen data sets, fifteen data sets are deemed “high spectral” resolution data and four are deemed “high spatial” resolution data. The “high spectral” resolution data are collected using typically 20 by 20 spectral grids with long integration times and co-averages. The “high spatial” resolution data are collected using 100 by 100 spectral grids with short integration times and no co-averages. Of the “high spectral” resolution data, one data set is of a CSL grain, two data sets are of a JSL grain, five data sets are of MSL grains, and seven data sets are of BGSL grains. Of the “high spatial” resolution data, one data set is of a JSL grain, two data sets are of MSL grains, and one data set is of a BGSL grain. Overall, each Raman microspectroscopic imaging data is directly available to the scientific community in Smith et al.[52]

Specifically, each data set is stored as a two-dimensional matrix. The columns of this matrix are the number of spectra collected—typically 400 total Raman spectra for the “high spectral” resolution data and 10,000 total Raman spectra for the “high spatial” resolution data—which correspond to the location of the collected Raman spectrum. The rows of this matrix are the spectral region—70 to 1550 cm<sup>-1</sup> in

increments of  $0.5 \text{ cm}^{-1}$ . These Raman microspectroscopic imaging data sets were validated by comparison of the resulting Raman spectra with corresponding Raman spectra of reference materials. Furthermore, comparison of the measured Raman spectra—including the Raman band locations and spectral shapes—resulting from Raman microspectroscopic imaging of the  $\text{TiO}_2$ -II-bearing grains with both Raman spectra of reference materials and Raman spectra from the RRUFF database project[126] provided validation of the data sets. Additionally, during Raman spectral acquisition, calibration of both the source wavelength and Raman shift are internally performed using a neon lamp. Through this internal calibration, the accuracy of the resulting Raman spectra is confirmed.

The data discussed in this chapter, which contains Raman microspectroscopic imaging results using both “high spectral” and “high spatial” resolution, offers significant value to both the chemical and broader scientific community in several ways. First, the data offers the ability to develop and test diverse algorithms for image processing, especially for multivariate analysis given the multidimensional chemical information available within the data sets. Second, the data offers a comparison between high spectral and high spatial resolution chemical imaging, and therefore, provides the ability to pursue both data fusion of these two measurements for improved imaging capabilities and image enhancements for certain regions of interest. Third, the data provides a vast resource for developing and testing multivariate analysis and chemometric methods. Specifically, with the data being comprised of three diverse  $\text{TiO}_2$  polymorphs, it can serve as a textbook data set for the classification of  $\text{TiO}_2$  polymorphs. Overall, this data provides a myriad of opportunities for the

scientific community in wide ranging applications, including the chemical imaging and multivariate analysis disciplines.

### 3.5 Conclusions

A high-pressure polymorph of titanium dioxide, termed TiO<sub>2</sub>-II, was recently identified in grains (~100 μm) recovered from four Neoproterozoic spherule layers.[88] These findings are the *first* to report a shock-induced, high-pressure polymorph formed by an Archean (>2.5 billion years old) impact event and provide unambiguous physical evidence to further support an impact origin for the spherule layers.[88] A subsequent study by Smith et al.[51] recently provided spatially and spectrally resolved chemical information of these grains and novel information regarding TiO<sub>2</sub>-II and its Raman spectrum.[51] This chapter builds off this by presenting Raman microspectroscopic imaging data of both high spectral and high spatial resolution collected on a model TiO<sub>2</sub>-II-bearing grain from one of these Neoproterozoic spherule layers—the Monteville spherule layer (MSL).

In this chapter, both Raman microspectroscopy and Raman microspectroscopic imaging were used to investigate this TiO<sub>2</sub>-II-bearing grain from the MSL. Backscattered electron (BSE) imaging of the MSL grain initially reveals a heterogeneous sample with polydispersed micron- and submicron-sized and shaped particles. Raman spectra collected with both high spectral and high spatial resolution indicate the presence of four chemical species—rutile, TiO<sub>2</sub>-II, quartz, and substrate-adhesive epoxy.

High spectral resolution Raman microspectroscopic imaging with MCR-ALS collected on this MSL grain provided chemical maps, pixel-by-pixel chemical images,

and resolved Raman spectra for five distinct chemical species—rutile, TiO<sub>2</sub>-II, anatase, quartz, and substrate-adhesive epoxy. Additionally, using high spatial resolution Raman microspectroscopic imaging with MCR-ALS, these five chemical species were also resolved, yet the resulting chemical maps and pixel-by-pixel chemical images provided a more refined spatial distribution of the chemical species. However, given the limited spectral acquisition parameters during high spatial resolution measurements, it is more difficult to spectrally resolve some minor chemical species.

Ultimately, the Raman microspectroscopic imaging data presented in this chapter, also available in Smith et al.[52], offers significant value to both the chemical and broader scientific community. The data offers the ability to develop and test diverse algorithms for image processing, including using the high spectral and high spatial resolution chemical imaging data to pursue both data fusion for improved imaging capabilities and image enhancements for certain regions of interest. The data also provides an ideal resource for developing and testing multivariate analysis and chemometric methods, such as classification of TiO<sub>2</sub> polymorphs.

## Chapter 4

### **SPATIAL AND SPECTRAL RESOLUTION OF CARBONACEOUS MATERIAL FROM HEMATITE ( $\alpha$ -Fe<sub>2</sub>O<sub>3</sub>) USING MULTIVARIATE CURVE RESOLUTION-ALTERNATING LEAST SQUARES (MCR-ALS) WITH RAMAN MICROSPECTROSCOPIC IMAGING: IMPLICATIONS FOR THE SEARCH FOR LIFE ON MARS**

#### **4.1 Abstract**

The search for evidence of extant or past life on Mars is a primary objective of both the upcoming Mars 2020 rover (NASA) and ExoMars 2020 rover (ESA/Roscosmos) missions. This search will involve the detection and identification of organic molecules and/or carbonaceous material within the Martian surface environment. For the *first* time on a mission to Mars, the scientific payload for each rover will include a Raman spectrometer, an instrument well-suited for this search. Hematite ( $\alpha$ -Fe<sub>2</sub>O<sub>3</sub>) is a widespread mineral on the Martian surface. The 2LO Raman band of hematite and the Raman D-band of carbonaceous material show spectral overlap, leading to the potential misidentification of hematite as carbonaceous material. In this chapter, we report the ability to spatially and spectrally differentiate carbonaceous material from hematite using multivariate curve resolution-alternating least squares (MCR-ALS) applied to Raman microspectroscopic imaging under both 532 nm and 785 nm excitation. A sample comprised of hematite, carbonaceous material, and substrate-adhesive epoxy in spatially distinct domains was constructed for this study. Principal component analysis (PCA) reveals that both 532 nm and 785

nm excitation produce representative three-phase systems of hematite, carbonaceous material, and substrate-adhesive epoxy in the analyzed sample. MCR-ALS with Raman microspectroscopic imaging using both 532 nm and 785 nm excitation was able to resolve hematite, carbonaceous material, and substrate-adhesive epoxy by generating spatially-resolved chemical maps and corresponding Raman spectra of these spatially distinct chemical species. Moreover, MCR-ALS applied to the combinatorial data sets of 532 nm and 785 nm excitation, which contain hematite and carbonaceous material within the same locations, was able to resolve hematite, carbonaceous material, and substrate-adhesive epoxy. Using multivariate analysis with Raman microspectroscopic imaging, 785 nm excitation more effectively resolved hematite, carbonaceous material, and substrate-adhesive epoxy as compared to 532 nm excitation. To our knowledge, this is the *first* report of multivariate analysis methods, namely MCR-ALS, with Raman microspectroscopic imaging being employed to differentiate carbonaceous material from hematite. We have therefore provided an analytical methodology useful for the search for extant or past life on the surface of Mars. Furthermore, our analytical methodology is applicable to investigating terrestrial and other extraterrestrial materials and environments, including the search for microbial life in ancient rocks on Earth.

## **4.2 Introduction**

A primary objective for the upcoming Mars 2020 rover mission of the National Aeronautics and Space Administration (NASA) and the ExoMars 2020 rover mission operated jointly by the European Space Agency (ESA) and the Russian Federal Space Agency (Roscosmos) is to search for evidence of extant or past life (fossils) on the

surface of Mars.[127-130] The search for organic molecules or carbonaceous material on the surface of Mars is a challenging task since this environment is exposed to a high flux of ultraviolet and ionizing charged particles[131-133] and can contain chemically oxidizing species, e.g., perchlorates[134]. Recently, however, the Sample Analysis at Mars instrument suite that is aboard NASA's Mars Science Laboratory Curiosity rover has definitively identified the first organic molecules on the surface of Mars.[131, 135, 136] Trace amounts of chlorobenzene (150-300 parts per billion by weight, ppbw) and C<sub>2</sub> to C<sub>4</sub> dichloroalkanes (up to 70 ppbw) were identified in powdered samples recovered from the Cumberland drill hole (~6.5 cm deep) within a mudstone interpreted as having been deposited in an ancient lake within Gale Crater.[131, 135-137] Although the carbon is believed to be indigenous to the mudstone, it is unknown whether the carbon is of Martian origin or of exogenous (e.g., meteoritic material) origin.[131] These results do show, however, that reduced material with covalent bonds can be preserved on the highly oxidizing surface of Mars[131], a discovery with significance for the upcoming rover missions to Mars.

Inclusion of a Raman spectrometer on a space mission to an extraterrestrial body in order to identify mineral phases and to search for organic molecules and carbonaceous material has been proposed.[31, 44, 138] For the first time[130], Raman spectrometers will be included in the science instrument payloads for both the Mars 2020 rover[127] and the ExoMars 2020 rover[139, 140]. The arm-mounted Scanning Habitable Environments with Raman & Luminescence for Organics & Chemicals (SHERLOC) instrument on the Mars 2020 rover will perform both Raman and fluorescence spectroscopy using a Deep Ultraviolet (248.6 nm) excitation source.[127] Raman spectra obtained by SHERLOC can detect Raman shifts  $>810\text{ cm}^{-1}$ , and this

spectral range will allow the identification of many species of organic molecules, e.g., hopanes, steranes, organic macromolecules, and mineral groups, e.g., carbonates, perchlorates, sulfates, and phyllosilicates of astrobiological interest.[127] The SHERLOC instrument is capable of detecting and classifying aromatics at a sub-parts per million (ppm) concentration, aliphatics at a <100 ppm concentration, and mineral grains <20  $\mu\text{m}$  in size.[127] The SHERLOC instrument can analyze natural surfaces, abraded surfaces, and boreholes, and it incorporates a subsystem for autofocusing and contextual imaging.[127] The SHERLOC instrument has four operational modes including autofocus and imaging, macro-mapping, micro-mapping, and point spectra.[127] In micro-mapping mode, the laser is rastered over a 1 x 1 mm area in order to collect 400 fluorescence and Raman spectra with 400 laser pulses per 50  $\mu\text{m}$  spot size.[127]

The Raman spectrometer onboard the ExoMars 2020 rover will analyze samples from drill holes that will reach a maximum depth of ~2 m.[139] A close-up imager on the rover will provide high-resolution images of the sample before the sample is crushed to a powder with a grain size of <200-250  $\mu\text{m}$ . [139] It should be noted that by crushing the sample, Raman spectral information cannot be correlated directly with detailed in situ geological textural and structural information.[139] The sample powder will be flattened, and in automatic scanning mode, the Raman spectrometer will analyze a minimum of 20 points (~50  $\mu\text{m}$  spot size) at a regularly spaced distance using a 532 nm excitation source.[139] The Raman spectrometer will be able to detect and identify a wide range of organic molecules and mineral phases.[139]

In light of the evidence documented by recent Martian rovers for surface environments on ancient Mars that were more habitable than present environments[141, 142], as well as the highly oxidizing nature of the present Martian surface, if evidence of life is found on Mars, it is more likely to be in the form of fossilized carbonaceous material.[128] The Raman spectrometers on the upcoming Martian rovers will need to be able to detect minor or trace amounts of carbonaceous material, whether of biotic or abiotic origin[128], and to clearly differentiate this component from the more abundant components in the samples. Recently, laboratory experiments have been performed on terrestrial samples containing trace-to-minor amounts of fossilized carbonaceous material to test the capabilities of the Raman spectrometer that will fly on the ExoMars 2020 rover.[128, 130, 139] Raman spectrometers used in these experiments were similar to the flight model, and they operated under conditions similar to those that will be employed on the surface of Mars.[128, 130, 139] In the first study, the Raman spectrometer analyzed a powdered sample of a 3.3 billion-year-old hydrothermally-silicified volcanic sediment (chert) from South Africa that contained carbonaceous microfossils.[139] The Raman spectrometer detected trace amounts of carbon as well as all the mineral phases in the sample that had been identified by other analytical techniques.[139] In the second study, the Raman spectrometer analyzed 21 powdered samples of shales that contained varying amounts of carbonaceous material of biotic origin.[128] Most of the samples were grey-black in color, and their total organic carbon content ranged from 0.16% to 3.42%.[128] Three samples also contained hematite ( $\alpha\text{-Fe}_2\text{O}_3$ ), giving them a red color, and their total organic carbon content ranged from 0.08% to 0.1%.[128] The Raman spectrometer readily detected the carbonaceous material in both the grey-black

and red shale samples.[128] For the red shale samples, the Raman spectra showed the presence of quartz, hematite, and carbon, the latter indicated by both the D (disordered) band at  $\sim 1350\text{ cm}^{-1}$  and the G (graphitic) band at  $\sim 1600\text{ cm}^{-1}$ . [128, 132] In the third study, Raman spectrometers using 532 nm and 785 nm excitation sources were used to analyze 12 chert samples from Western Australia that are  $\sim 3.49$  to  $3.43$  billion years old.[130] The Raman spectra for all 12 samples show bands for quartz, and the spectra for a number of the samples show bands for hematite, including the band at  $\sim 1320\text{ cm}^{-1}$ . [130] Hematite was more readily detectable using 785 nm excitation.[130] Carbonaceous material, indicated by both the D and G bands, was readily detected in all 12 samples using 785 nm excitation, but was detected in only six of the samples using 532 nm excitation.[130] Relative to the Raman spectra obtained using 532 nm excitation, Raman spectra for the carbonaceous material obtained using 785 nm excitation show reduced background levels and both the D and G bands have a much higher signal-to-noise ratio.[130] The ability of Raman spectroscopy to detect low levels of carbonaceous material in hematite-bearing rocks is of major significance for the search for life by the upcoming Martian rover missions given the following evidence for the widespread distribution of hematite on the surface of Mars.[128, 143]

Orbital spectroscopy has detected hematite at several areas on the surface of Mars.[143-145] In 1997, the Mars Pathfinder spacecraft landed at Ares Vallis, and combined elemental and visible/near-infrared (VNIR) multispectral data obtained by this mission was used to infer the presence of hematite at this site.[146] In 2004, the Mars Exploration Rovers Spirit and Opportunity landed on opposite sides of Mars at Gusev Crater and Meridiani Planum, respectively, and the rovers used Mössbauer

spectroscopy to confirm the presence of hematite in rocks and soils at both sites.[147, 148] VNIR multispectral imaging data acquired by the Opportunity rover also detected hematite at multiple locations at Meridiani Planum.[149] Since 2012, the Curiosity rover has been studying the habitability of ancient environments as recorded by sedimentary rocks in Gale Crater.[150] The Chemistry and Mineralogy (CheMin) X-ray diffraction instrument on the Curiosity rover has confirmed the presence of hematite in samples recovered from five drill holes in mudstones, one drill hole in sandstone, and in loose material scooped from an eolian dune.[137, 151-154] The drill hole samples were from depths of ~1.5 to 6.5 cm,[155] so the sample material was from below the very surficial material (0 to ~1.5 cm depth), commonly reddish in color, that was dumped around the peripheries of the drill holes.[137, 155] The CheMin instrument determined the concentration of hematite in these samples to be ~0.6 wt% to 8.4 wt% with four of the values (<1 wt%) being at, or near to, the detection limit.[137, 151-153] Therefore, both the hematite (0.7 wt%) and the organic molecules found in the Cumberland drill hole are from depths of ~1.5 to 6.5 cm.[131, 135-137] Orbital spectroscopy has detected red crystalline hematite within the uppermost stratum of a ridge, named Hematite Ridge, that extends for ~6.5 km in Gale Crater,[156] and long-distance (3-5 km) spectra obtained using laser-induced breakdown spectroscopy with the Chemistry and Camera (ChemCam) instrument on the Curiosity rover are consistent with the orbital spectral results.[153] Hematite is therefore a widespread component on the surface of Mars, and in the Cumberland drill hole in Gale Crater, its low concentration is still more than four orders of magnitude higher than that of the organic molecules.

Since it is likely that many, if not all, of the samples analyzed by the upcoming Martian rovers will show some degree of oxidation,[128, 132] and they may contain at least trace amounts of hematite, it will be necessary to detect organic molecules or carbonaceous material in the presence of hematite, and to be able to spectrally differentiate these chemical species. Differentiating carbonaceous material from hematite using Raman microspectroscopy, however, can be a challenging task. There is spectral overlap in the 1320-1350  $\text{cm}^{-1}$  range involving the Raman band at  $\sim 1318 \text{ cm}^{-1}$  (2LO mode) of hematite and the Raman band at  $\sim 1320 \text{ cm}^{-1}$  ( $A_{1g}$  mode; D-band) of carbonaceous material.[132, 157-159] This spectral overlap can lead to the Raman band at  $\sim 1318 \text{ cm}^{-1}$  of hematite being misidentified as the D-band of disordered carbonaceous material[132, 140, 158-160] that can lead to the misidentification of hematite as carbonaceous material[159, 160].

Raman microspectroscopic imaging has been utilized in a myriad of research areas, including biology and materials science, due to its ability to produce spatially-resolved molecular and chemical information.[51, 52, 106, 108] Multivariate analysis methods, including principal component analysis (PCA) and multivariate curve resolution-alternating least squares (MCR-ALS), can be used to evaluate Raman microspectroscopic imaging data, and can provide more comprehensive chemical information from this data, especially if the data contains species with spectral overlap.[50-55, 57, 61, 65, 113] Furthermore, multivariate analysis methods, namely MCR-ALS, applied to Raman microspectroscopic imaging can identify the pure, individual chemical species within complex, heterogeneous samples and determine the spatial distribution of these pure chemical species. Raman microspectroscopic imaging

and multivariate analysis methods have therefore recently gained momentum in the scientific community.[51-54, 57, 61, 113]

In this chapter, we offer the ability to detect and differentiate carbonaceous material, in the form of fossilized material, from hematite using MCR-ALS applied to Raman microspectroscopic imaging. Moreover, MCR-ALS applied to Raman microspectroscopic imaging of carbonaceous material, hematite, and substrate-adhesive epoxy produced spatially-resolved chemical maps and resolved Raman spectra for each individual chemical component. The efficacy of MCR-ALS with Raman microspectroscopic imaging for the spectral and spatial resolution of these three chemical species was evaluated using both 532 nm and 785 nm excitation. Furthermore, using combinatorial data sets, which provide experimental data in which hematite and carbonaceous material are spatially non-differentiable, MCR-ALS with Raman microspectroscopic imaging was further assessed. Using our proposed methodology, the Raman spectroscopic data collected on Martian samples by the upcoming rover missions can be analyzed to most effectively identify, differentiate, and spatially-resolve chemical components, including carbonaceous material.

### **4.3 Materials and Methods**

#### **4.3.1 Materials and Sample Preparation**

A sample of carbonaceous material in the form of a fossilized fern spore and a sample of hematite were obtained from the Department of Geological Sciences at the University of Delaware. A cross-sectional sample consisting of hematite, carbonaceous material, and substrate-adhesive epoxy was prepared. Using a porcelain

mortar and pestle, a hematite sample (~80 g) was broken into smaller pieces (~5 g) that were ground into a powder. A selected portion of the fossilized fern spore (~0.5 g) containing ample carbonaceous material atop the rock substrate was placed onto a microscope glass slide (25.4 mm diameter x 1.0 mm thick, Fisher Scientific, Hampton, New Hampshire, USA). The glass slide was used as the substrate for the cross-sectional sample. With the fossilized fern spore atop the glass substrate, the powdered hematite sample was placed directly next to the fossilized fern spore. A small portion of the fossilized fern spore was also coated in hematite to ensure the final sample would have areas with hematite and carbonaceous material on distinct portions. With hematite and carbonaceous material directly adjacent to one another, substrate-adhesive epoxy (Buehler Ltd, Lake Bluff, Illinois, USA) was used to fix these components to the glass substrate. The epoxy was allowed to harden at room temperature for ~5 hours. Initial hand polishing to expose the surface of both hematite and carbonaceous material was done using a water/detergent/glycerol solution (~70/15/15 v/v %) and paper strips ranging in coarseness from 600  $\mu\text{m}$  to 3  $\mu\text{m}$ . A final hand polish was done using  $\text{Al}_2\text{O}_3$  powder (0.05  $\mu\text{m}$ -sized, Excel Metallurgical, Inc., Springfield, Massachusetts, USA, 99%) wetted with water. The final sample consisted of a flat, cross-sectional area of hematite and carbonaceous material fixed to the underlying glass substrate using epoxy.

#### **4.3.2 Raman Microspectroscopic Imaging**

Raman microspectroscopic imaging was performed using a Senterra Raman spectrometer (Bruker Optics, Billerica, Massachusetts, USA) coupled to a BX-51 optical microscope (Olympus, Tokyo, Japan). Both 532 nm and 785 nm sources were used for excitation of the sample. The respective laser was focused onto the sample

using a 20× (0.40 numerical aperture, NA) or a 50× (0.75 NA) close-working-distance objective lens (Olympus, Tokyo, Japan), yielding a probing area of 5 μm and 2 μm in diameter, respectively. Subsequent to excitation, the scattered light was collected by the objective lens, filtered by a 50 by 1000 μm slit aperture, and dispersed by a 1200 grooves/mm grating onto a charge-coupled device (CCD) detector, which was thermoelectrically-cooled to −65 °C. The resulting spectral range, covered under two grating positions, was 70 to 2735 cm<sup>-1</sup> for 532 nm excitation and 80 to 2635 cm<sup>-1</sup> for 785 nm excitation.

During Raman microspectroscopic imaging measurements, a constant nominal power, ranging from 5 to 10 mW for 532 nm excitation and 25 to 50 mW for 785 nm excitation, was applied to the surface of the sample. For all Raman spectral acquisitions, a laser exposure time of 5 to 10 seconds with 3 co-averages was employed, and background measurements equal to the respective exposure time were collected prior to each acquisition. The total collection time for each Raman spectrum was therefore ~90 to 180 seconds. During the collection of each Raman spectrum, both Raman shift and source wavelength calibration were internally performed using a neon lamp. The resulting spectral resolution achieved was 3 to 5 cm<sup>-1</sup>.

In order to generate Raman microspectroscopic imaging data, a selected grid containing locations of Raman spectral acquisition was used. The rectangular-shaped grids were positioned on specific locations of the sample to ensure that all three chemical species would be present in the resulting Raman microspectroscopic imaging data. Specifically, the grids were positioned so that the probed area contained hematite spatially on the left, substrate-adhesive epoxy spatially in the middle, and carbonaceous material spatially on the right. The grids contained a total of 400 Raman

spectral acquisition points, in which grids of 20 by 20 spectral acquisition points with a  $\sim 5 \mu\text{m}$  step-size between acquisition points were utilized. The x and y positions were controlled using an automatic, movable stage, which resulted in the collection of Raman spectra at the defined acquisition points within each grid. The z direction was held constant during all measurements. All Raman microspectroscopic imaging measurements were performed using the OPUS 7.2 program (Bruker Optics, Billerica, Massachusetts, USA).

### **4.3.3 Multivariate Data Analysis**

In order to provide spatially and spectrally resolved information from Raman microspectroscopic imaging data, the analysis of the collected data is critical. Traditionally, this data analysis relies on univariate methods, in which the intensity or integrated intensity of a characteristic Raman band is used to represent the analyte of interest. By using univariate analysis methods, however, the data can be influenced by interference effects, such as background interference, fluorescence, fluctuations in laser power, loss of focus, sample roughness, sample opacity, and spectral overlap, and potentially useful information can go unrecovered.[50-52] Multivariate data analysis methods can address these interference effects and provide increased signal-to-noise ratio, increased selectivity, increased visualization of results, and significant data reduction.[50-52] In this chapter, the multivariate analysis methods used are principal component analysis (PCA)[50, 51, 54, 57, 161] and multivariate curve resolution-alternating least squares (MCR-ALS)[51-55, 57, 61, 65, 113, 162].

#### 4.3.3.1 Principal Component Analysis (PCA)

PCA, a multivariate analysis method commonly used with spectroscopic data, reduces the dimensionality of the experimental data. Moreover, PCA can reduce spectroscopic data from sizeable data sets, such as data sets containing hundreds of spectra, into several orthogonal principal components (PCs). PCA achieves this reduction by decomposition of the experimental data using:

$$\mathbf{D} = \mathbf{T}\mathbf{P}^T + \mathbf{E} \quad (4.1)$$

where  $\mathbf{D}$  is the experimental data matrix,  $\mathbf{T}$  is the score matrix,  $\mathbf{P}$  is the loading matrix, and  $\mathbf{E}$  is the model residual matrix. Each orthogonal PC thus explains a portion of the total information within the experimental data. These PCs, however, are not necessarily representative of pure chemical components. Moreover, if spectral overlap is present within the spectroscopic data, the PCs will most likely contain information from multiple chemical species rather than a pure chemical component. The variance within the data is explained by the PCs, and if the spectroscopic data is mean-centered prior to analysis, the first PC captures the maximum variance, the second PC captures the second most variance, etc. As such, these orthogonal PCs can provide useful chemical information extracted from the spectroscopic data, and ultimately, can determine relationships amongst the chemical species.

In this chapter, PCA was performed using Matlab 7.12 (Mathworks, Massachusetts, USA). The PLS Toolbox (Eigenvector Research Incorporated, Washington, USA) was used as the graphical interface to perform PCA through Matlab. Preprocessing of the spectroscopic data was performed by initial normalization of the Raman spectra to unit area, and subsequent mean-centering of the data. PCA was performed using the spectral ranges of 150 to 1800  $\text{cm}^{-1}$  and 120 to

1800 cm<sup>-1</sup> for 532 nm and 785 nm excitation measurements, respectively. Resulting PCA plots were visualized using Matlab.

#### 4.3.3.2 Multivariate Curve Resolution-Alternating Least Squares (MCR-ALS)

MCR-ALS, a multivariate self-modeling mixture analysis method, was applied to the Raman microspectroscopic imaging data to generate chemical maps and resolved Raman spectra of the pure chemical components within the sample. A primary advantage of MCR-ALS is that it allows spectroscopic data to be mathematically decomposed into spatial and spectral information, even if the spectroscopic data is collected on a heterogeneous sample, about which there is no prior information. The explained variance of the data is maximized using MCR-ALS in a similar fashion to PCA; however, MCR-ALS not only provides chemical information regarding the sample, but also physical information as well. Specifically, MCR-ALS resolves the experimental data matrix, **D**, by:

$$\mathbf{D} = \mathbf{CS}^T + \mathbf{E} \quad (4.2)$$

where **C** is the concentration profile matrix, **S**<sup>T</sup> is the resolved spectral matrix, and **E** is the residual error matrix. The number of components contributing to **D** can be determined by PCA, singular value decomposition, from prior knowledge of the system, or a variety of other multivariate techniques. By providing initial estimates, **C** and **S**<sup>T</sup> are calculated and iteratively optimized using the ALS algorithm until convergence is achieved. Physically meaningful constraints, such as non-negative concentrations and non-negative spectral intensities, are employed during the ALS process to guide the resulting solutions closer to the true value and to ensure that no inconsistencies caused by small deviations in the initial estimates are observed within the final results.

In this chapter, the three-dimensional Raman microspectroscopic imaging data (i.e., the matrix containing the  $x$ ,  $y$ , and  $\text{cm}^{-1}$  information) was unfolded into the experimental data matrix, **D**. Each row in **D** is the intensity at various wavenumbers. The number of components was selected prior to ALS using initial estimates from PCA. If PCA was insufficient, the number of components was selected by comparison of resolved spectra, in **S**, with Raman spectra of reference materials. The number of selected components was thus increased from the initial estimates of PCA until the resolved spectra, in **S**, were comparable to the Raman spectra of reference materials. Initial estimates of the spectral matrix for ALS were determined by distance criteria. Moreover, the first spectrum for initialization was selected to be furthest from the mean of the data set, and subsequent spectra were selected to be furthest from the mean and all prior selected spectra. The non-negative concentration constraint and the non-negative spectral intensity constraint were applied during ALS optimization, and a convergence of 0.01% was utilized. The concentration profile matrix, **C**, and spectral matrix, **S**, were generated by MCR-ALS methods in Matlab 7.12 with the Matlab toolbox by Jaumot et al.[162] and the PLS Toolbox. The final **C** matrix contains the concentration profile of each pure chemical component, in which each column corresponds to a component. The corresponding chemical maps are reconstructed from **C** using Matlab 7.12. Final chemical maps were visualized using OriginPro (Origin Lab v9.1 Pro, Northampton, Massachusetts USA). In the spectral matrix, **S**, each row contains the corresponding resolved Raman spectrum. The graphical presentations of the individual spectra were prepared using OriginPro.

MCR-ALS was performed using the spectral range of 150 to  $1800\text{ cm}^{-1}$  for 532 nm excitation and 120 to  $1800\text{ cm}^{-1}$  for 785 nm excitation. Prior to MCR-ALS

analysis, preprocessing was performed on the spectroscopic data using an asymmetric least squares baseline correction[163] to remove all variation in the Raman spectra, such as background fluctuations, that is unrelated to the chemical species. Asymmetric least squares baseline correction is an iterative method based on fitting the baseline of the data using a Whittaker smoother, and is both fast and flexible with large spectroscopic data sets.[55, 163] No other preprocessing was performed prior to MCR-ALS analysis.

#### 4.3.4 Combinatorial Data Sets

Combinatorial data sets were utilized to determine the efficiency of MCR-ALS and Raman microspectroscopic imaging to resolve hematite and carbonaceous material if both chemical species are located in the same, non-differentiable space. Combinatorial data sets were generated using the respective experimental data matrix from Raman microspectroscopic imaging measurements using both 532 nm and 785 nm excitation. A combinatorial data set is the sum of the two-dimensional experimental data matrix,  $\mathbf{D}$ , with the horizontally-flipped two-dimensional experimental data matrix,  $\mathbf{H}$ , as follows:

$$\mathbf{X} = \mathbf{D} + \mathbf{H} \quad (4.3)$$

where  $\mathbf{X}$  is the resulting combinatorial data set. In this chapter, the two-dimensional experimental data matrix,  $\mathbf{D}$ , contains spectral information about a sample with hematite, substrate-adhesive epoxy, and carbonaceous material spatially on the left, in the middle, and on the right, respectively. By horizontally-flipping  $\mathbf{D}$  to form the resulting matrix,  $\mathbf{H}$ , the spectral information within this newly formed matrix contains the opposite spatial information of  $\mathbf{D}$ . Moreover, in this chapter, this horizontally-flipped matrix,  $\mathbf{H}$ , contains spectral information with hematite now spatially located

on the right, carbonaceous material now spatially located on the left, and substrate-adhesive epoxy still spatially located at the interface of hematite and carbonaceous material. By summing these matrices as in **Eq. 4.3**, a combinatorial data set, **X**, is produced. Thus, in this chapter, the resulting matrix contains spectral information with hematite spatially located on both the left and right portions of the sample, carbonaceous material spatially located on both the left and right portions of the sample, and substrate-adhesive epoxy still spatially located at the interface of these two chemical species. A combinatorial data set, **X**, therefore can provide a challenging data set for MCR-ALS to differentiate hematite, carbonaceous material, and substrate-adhesive epoxy because hematite and carbonaceous material are now localized in the same space.

## **4.4 Results and Discussion**

### **4.4.1 Raman Spectra of Hematite and Carbonaceous Material**

Reference materials of hematite and carbonaceous material, in the form of a fossilized fern spore, were investigated using Raman microspectroscopy (**Figure 4.1**) with both 532 and 785 nm excitation. The Raman spectrum of hematite under 532 nm excitation (**Figure 4.1A**) displays primary bands at 226  $\text{cm}^{-1}$ , 245  $\text{cm}^{-1}$ , 298  $\text{cm}^{-1}$ , 411  $\text{cm}^{-1}$ , 501  $\text{cm}^{-1}$ , 613  $\text{cm}^{-1}$ , and 1317  $\text{cm}^{-1}$ . The Raman spectrum of hematite under 785 nm excitation (**Figure 4.1B**) displays primary bands at 227  $\text{cm}^{-1}$ , 246  $\text{cm}^{-1}$ , 299  $\text{cm}^{-1}$ , 412  $\text{cm}^{-1}$ , 497  $\text{cm}^{-1}$ , 613  $\text{cm}^{-1}$ , and 1321  $\text{cm}^{-1}$ . In the ~200 to 650  $\text{cm}^{-1}$  spectral range, the relative intensities of the 226  $\text{cm}^{-1}$ , 245  $\text{cm}^{-1}$ , and 298  $\text{cm}^{-1}$  bands are inversely related with respect to wavelength of excitation—532 nm excitation produces a

decreasing intensity of these Raman bands with increasing wavenumber, whereas 785 nm excitation produces an increasing intensity of these Raman bands with increasing wavenumber. The relative intensity of the Raman band at  $411\text{ cm}^{-1}$  using 532 nm excitation is much lower than that of this band when using 785 nm excitation. Using 785 nm excitation, this band, now at  $412\text{ cm}^{-1}$ , is the most intense band in the Raman spectrum. Additionally, under 532 nm excitation, the  $1317\text{ cm}^{-1}$  band is the most intense band whereas under 785 nm excitation, this band, now at  $1321\text{ cm}^{-1}$ , is one of the lower intensity bands. The Raman spectrum of hematite is thus greatly dependent upon excitation wavelength.

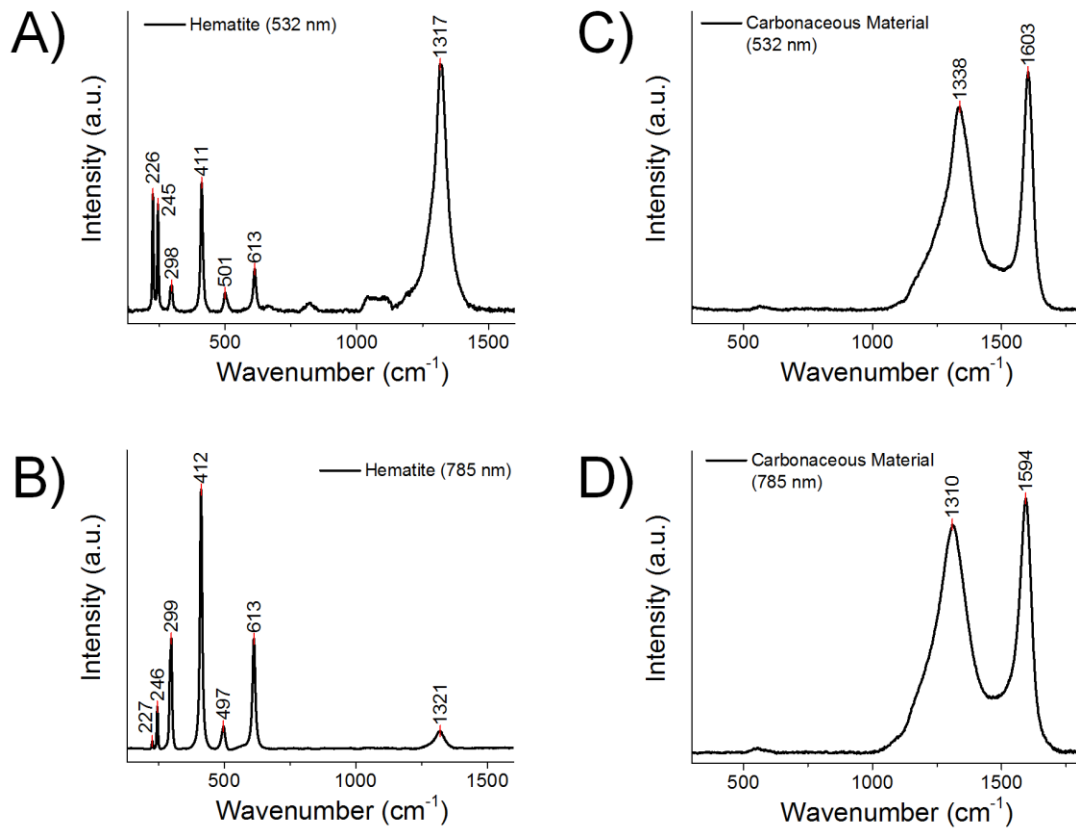


Figure 4.1: Raman spectra of hematite (A) and carbonaceous material (C) using 532 nm excitation and Raman spectra of hematite (B) and carbonaceous material (D) using 785 nm excitation.

The Raman active modes of hematite have been extensively studied.[164-168] The irreducible distribution of hematite's vibration modes are given by  $\Gamma_{\text{vib}} = 2A_{1g} + 2A_{1u} + 3A_{2g} + 2A_{2u} + 5E_g + 4E_u$ . Of these modes, the optically silent modes are the  $A_{1u}$  and the  $A_{2u}$  modes, the Raman active modes are the symmetric modes, and the infrared active modes are the antisymmetric modes.[164, 165, 168] Moreover, no modes are both Raman and infrared active due to the inversion center in the hexagonal crystal structure of hematite.[164] The observed locations of the Raman bands of

hematite using 532 nm and 785 nm excitation, with their assigned Raman active modes,[164-168] are displayed (**Table 4.1**). The Raman bands of hematite using 532 nm excitation (**Figure 4.1A**) are thus assigned as follows: 226  $\text{cm}^{-1}$  ( $A_{1g}$ ), 245  $\text{cm}^{-1}$  ( $E_g$ ), 298  $\text{cm}^{-1}$  ( $E_g$ ), 411  $\text{cm}^{-1}$  ( $E_g$ ), 501  $\text{cm}^{-1}$  ( $A_{1g}$ ), 613  $\text{cm}^{-1}$  ( $E_g$ ), and 1317  $\text{cm}^{-1}$  (2LO).[168] Similarly, the Raman bands of hematite using 785 nm excitation (**Figure 4.1B**) are 227  $\text{cm}^{-1}$  ( $A_{1g}$ ), 246  $\text{cm}^{-1}$  ( $E_g$ ), 299  $\text{cm}^{-1}$  ( $E_g$ ), 412  $\text{cm}^{-1}$  ( $E_g$ ), 497  $\text{cm}^{-1}$  ( $A_{1g}$ ), 613  $\text{cm}^{-1}$  ( $E_g$ ), and 1321  $\text{cm}^{-1}$  (2LO).[168]

Table 4.1: Assignment of the Raman bands observed in hematite (H) and carbonaceous material (CM) under 532 nm and 785 nm excitation. Band assignments are from the literature.[164-172]

Wavenumber ( $\text{cm}^{-1}$ ): 532 nm excitation	Wavenumber ( $\text{cm}^{-1}$ ): 785 nm excitation	Raman Active Mode	Chemical Origin
226	227	$A_{1g}$	H
245	246	$E_g$	H
298	299	$E_g$	H
411	412	$E_g$	H
501	497	$A_{1g}$	H
613	613	$E_g$	H
1317	1321	2LO	H
1338	1310	D-band, $A_{1g}$	CM
1603	1594	G-band, $E_{2g}$	CM

The Raman spectrum of carbonaceous material, in the form of a fossilized fern spore, under 532 nm excitation (**Figure 4.1C**) displays bands at 1338  $\text{cm}^{-1}$  and 1603  $\text{cm}^{-1}$ . The Raman spectrum of this carbonaceous material under 785 nm excitation (**Figure 4.1D**) displays bands at 1310  $\text{cm}^{-1}$  and 1594  $\text{cm}^{-1}$ . For carbonaceous material, unlike hematite, relative band intensities show little change with a change in excitation wavelength. However, using 785 nm excitation, the Raman bands for carbonaceous

material are redshifted as compared to using 532 nm excitation (cf., **Figures 4.1C** and **4.1D**).

The Raman spectra of both carbonaceous material[169-171] and fossilized material[172, 173] have been extensively studied. The Raman spectra of carbonaceous material show two distinct Raman bands—the D-band at  $\sim 1310$ - $1350\text{ cm}^{-1}$  and the G-band at  $\sim 1590$ - $1610\text{ cm}^{-1}$ . [158, 169, 170] The D-band of carbonaceous material is assigned to K-point phonons of  $A_{1g}$  symmetry, whereas the G-band of carbonaceous material is assigned to zone-center phonons of  $E_{2g}$  symmetry. [169] The Raman bands of carbonaceous material using 532 nm excitation (**Figure 4.1C**) are thus assigned as follows:  $1338\text{ cm}^{-1}$  (D-band,  $A_{1g}$  mode) and  $1603\text{ cm}^{-1}$  (G-band,  $E_{2g}$  mode). [169] The Raman bands of carbonaceous material using 785 nm excitation (**Figure 4.1D**) are  $1310\text{ cm}^{-1}$  (D-band,  $A_{1g}$  mode) and  $1594\text{ cm}^{-1}$  (G-band,  $E_{2g}$  mode). [169]

#### 4.4.2 Spectral Overlap of Chemical Species

The labeled Raman spectra of hematite and carbonaceous material collected using both 532 nm and 785 nm excitation (**Figure 4.1**) along with their Raman active modes and locations of bands (**Table 4.1**) provide the ability for a direct comparison of the Raman spectra of these two chemical species. The direct overlay of the Raman spectra of hematite and carbonaceous material (**Figure 4.2**) displays a high degree of spectral overlap. Specifically, under both 532 nm and 785 nm excitation, the spectral overlap is evident in the  $200$  to  $1700\text{ cm}^{-1}$  spectral range. In the  $200$  to  $1700\text{ cm}^{-1}$  spectral range with 532 nm excitation (**Figure 4.2A**), hematite displays Raman bands at  $226\text{ cm}^{-1}$ ,  $245\text{ cm}^{-1}$ ,  $298\text{ cm}^{-1}$ ,  $411\text{ cm}^{-1}$ ,  $501\text{ cm}^{-1}$ ,  $613\text{ cm}^{-1}$ , and  $1317\text{ cm}^{-1}$ , and carbonaceous material displays Raman bands at  $1338\text{ cm}^{-1}$  and  $1603\text{ cm}^{-1}$ . In the  $200$  to  $1700\text{ cm}^{-1}$  spectral range with 785 nm excitation (**Figure 4.2B**), hematite displays

Raman bands at  $227\text{ cm}^{-1}$ ,  $246\text{ cm}^{-1}$ ,  $299\text{ cm}^{-1}$ ,  $412\text{ cm}^{-1}$ ,  $497\text{ cm}^{-1}$ ,  $613\text{ cm}^{-1}$ , and  $1321\text{ cm}^{-1}$ , and carbonaceous material displays Raman bands at  $1310\text{ cm}^{-1}$  and  $1594\text{ cm}^{-1}$ . Spectral overlap is thus present, especially with respect to the 2LO band of hematite ( $1317\text{ cm}^{-1}$  with  $532\text{ nm}$  excitation;  $1321\text{ cm}^{-1}$  with  $785\text{ nm}$  excitation) and the D-band of carbonaceous material ( $1338\text{ cm}^{-1}$  with  $532\text{ nm}$  excitation;  $1310\text{ cm}^{-1}$  with  $785\text{ nm}$  excitation).

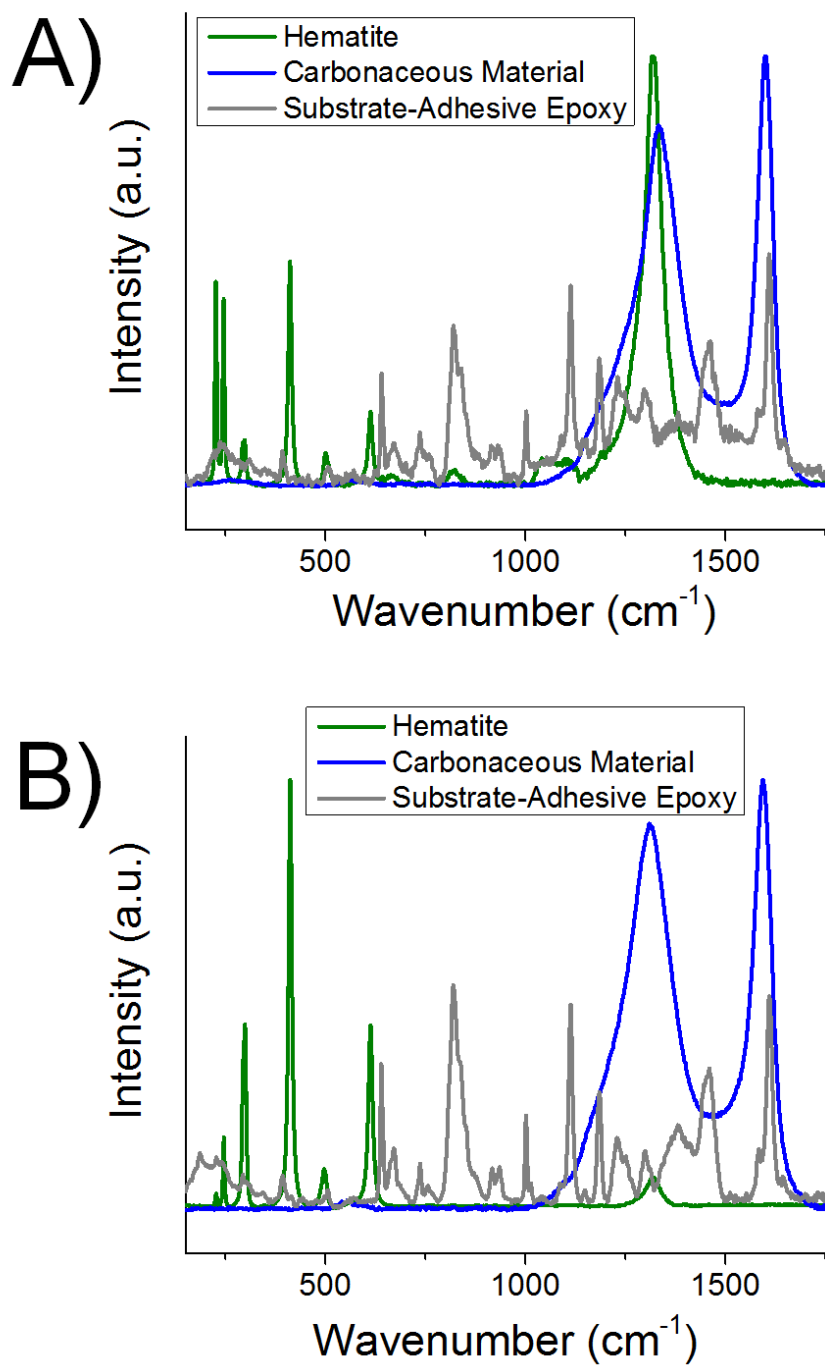


Figure 4.2: Overlay of Raman spectra (A) of hematite (green), carbonaceous material (blue), and substrate-adhesive epoxy (grey) using 532 nm excitation. Overlay of Raman spectra (B) of hematite (green), carbonaceous material (blue), and substrate-adhesive epoxy (grey) using 785 nm excitation.

The direct overlay of the Raman spectra of hematite and carbonaceous material (**Figure 4.2**) shows that the most significant spectral overlap is present in the ~1200 to 1400  $\text{cm}^{-1}$  spectral range, which is primarily used for identification of the respective chemical species. This spectral overlap has been extensively outlined in the literature[132, 140, 157-159, 174], and has been linked to potential misidentification of the two chemical species[159, 160], especially with respect to surface exploration of Mars.[132, 140, 174] Moreover, the 2LO band of hematite is significantly more intense using 532 nm excitation as opposed to 785 nm excitation, resulting in a more prominent spectral overlap of hematite and carbonaceous material when using 532 nm excitation.

When comparing the Raman spectrum of substrate-adhesive epoxy with that of hematite and carbonaceous material (**Figure 4.2**), the spectral overlap observed is even more substantial. In the 200-1700  $\text{cm}^{-1}$  spectral range with 532 nm excitation (**Figure 4.2A**), substrate-adhesive epoxy displays eleven major Raman bands at 640  $\text{cm}^{-1}$ , 671  $\text{cm}^{-1}$ , 736  $\text{cm}^{-1}$ , 820  $\text{cm}^{-1}$ , 1002  $\text{cm}^{-1}$ , 1113  $\text{cm}^{-1}$ , 1185  $\text{cm}^{-1}$ , 1230  $\text{cm}^{-1}$ , 1297  $\text{cm}^{-1}$ , 1463  $\text{cm}^{-1}$ , and 1609  $\text{cm}^{-1}$ . In the 200-1700  $\text{cm}^{-1}$  spectral range with 785 nm excitation (**Figure 4.2B**), substrate-adhesive epoxy displays major Raman bands at 640  $\text{cm}^{-1}$ , 671  $\text{cm}^{-1}$ , 737  $\text{cm}^{-1}$ , 820  $\text{cm}^{-1}$ , 1001  $\text{cm}^{-1}$ , 1113  $\text{cm}^{-1}$ , 1185  $\text{cm}^{-1}$ , 1229  $\text{cm}^{-1}$ , 1299  $\text{cm}^{-1}$ , 1460  $\text{cm}^{-1}$ , and 1610  $\text{cm}^{-1}$ . In this chapter, substrate-adhesive epoxy was used to affix the hematite and carbonaceous material to the glass substrate, and thus, it is necessary to compare the Raman spectra of substrate-adhesive epoxy with those of hematite and carbonaceous material. Furthermore, if samples of Martian origin are prepared in the laboratory, including samples cached by the Mars 2020 rover that are later returned to Earth[127], substrate-adhesive epoxy could potentially be used in

their preparation, e.g., polished thin sections and grain mounts. The Raman spectrum, Raman active modes, and Raman band assignments of substrate-adhesive epoxy have been extensively studied[124, 125] and will not be covered further in this chapter.

#### **4.4.3 Principal Component Analysis (PCA) of Raman Microspectroscopic Imaging Data**

PCA was employed to initially evaluate the potential of Raman microspectroscopic imaging for the differentiation of a three-phase mixture containing hematite, carbonaceous material, and substrate-adhesive epoxy. Raman spectra compiled from two Raman microspectroscopic imaging measurements, using both 532 nm and 785 nm excitation, collected on the hematite, carbonaceous material, and substrate-adhesive epoxy sample were investigated using PCA. Moreover, the Raman microspectroscopic imaging measurements—each containing 400 total Raman spectra—were collected and analyzed using PCA under 532 nm excitation (**Figure 4.3A**) and 785 nm excitation (**Figure 4.3B**). The scores-scores plot using 532 nm excitation (**Figure 4.3A**) captures 66.42% of the variance with the first principal component (PC1) and 14.65% of the variance with the second principal component (PC2), totaling 81.07% of the variance. The scores-scores plot using 785 nm excitation (**Figure 4.3B**) captures 80.13% of the variance with PC1 and 11.69% of the variance with PC2, totaling 91.82% of the variance.

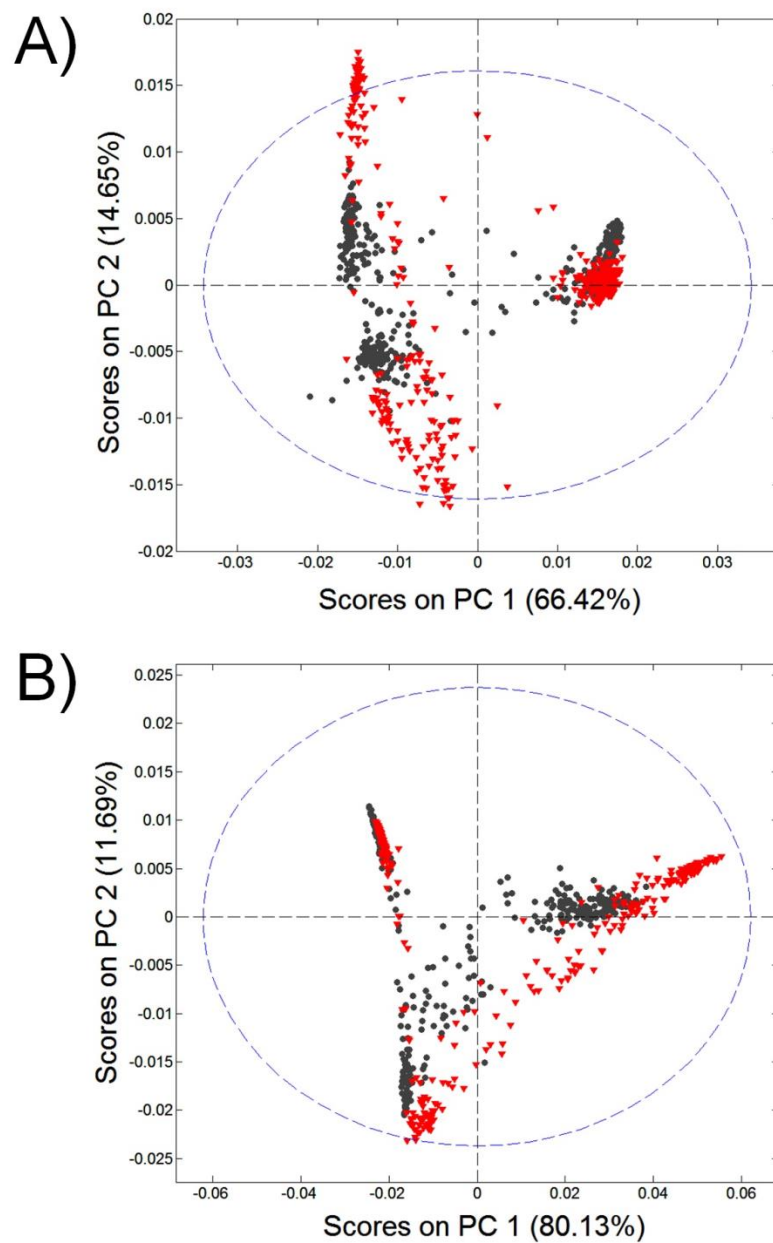


Figure 4.3: Principal component analysis (PCA) plot (A) of the scores on the first principal component (PC 1; 66.42%) and the second principal component (PC 2; 14.65%) using 532 nm excitation. PCA plot (B) of the scores on PC1 (80.13%) and PC2 (11.69%) using 785 nm excitation.

The results of PCA for both 532 nm and 785 nm excitation show separation into a three-phase system, comprised of hematite, carbonaceous material, and substrate-adhesive epoxy. The scores-scores plot using 532 nm excitation (**Figure 4.3A**), however, demonstrates the increased difficulty of Raman microspectroscopic imaging to resolve the three chemical species as compared to using 785 nm excitation. This is evident in the clear triangular separation within the scores-scores plot using 785 nm excitation (**Figure 4.3B**) as compared to the less defined, broader triangular depiction within the scores-scores plot using 532 nm excitation (**Figure 4.3A**). The more efficient separation using PCA of Raman microspectroscopic imaging data collected using 785 nm excitation as opposed to using 532 nm excitation is attributed to the increased spectral overlap between hematite, carbonaceous material, and substrate-adhesive epoxy when using 532 nm excitation. This increased spectral overlap using 532 nm excitation rather than 785 nm excitation makes it more difficult to resolve the three chemical species, as observed in the respective scores-scores plot from PCA.

#### **4.4.4 Multivariate Curve Resolution-Alternating Least Squares (MCR-ALS) Applied to Raman Microspectroscopic Imaging**

The results of Raman microspectroscopic imaging with MCR-ALS of the three-phase mixture—hematite, carbonaceous material, and substrate-adhesive epoxy—using both 532 nm (**Figure 4.4**) and 785 nm excitation (**Figure 4.5**) are shown. Specifically, MCR-ALS applied to Raman microspectroscopic imaging data collected using 532 nm excitation (**Figure 4.4**) of the hematite, carbonaceous material, and substrate-adhesive epoxy sample produced spatially-resolved chemical maps and corresponding Raman spectra of these three chemical species. The mean (in black;

**Figure 4.4A**) and standard deviation (+ in red, - in blue; **Figure 4.4A**) of the 400 total Raman spectra accumulated over the probed area (**Figure 4.4A**) demonstrate that all three chemical species are present. This result is shown by the mean Raman spectrum displaying major bands at 226  $\text{cm}^{-1}$  (hematite), 245  $\text{cm}^{-1}$  (hematite), 293  $\text{cm}^{-1}$  (hematite), 640  $\text{cm}^{-1}$  (epoxy), 669  $\text{cm}^{-1}$  (epoxy), 737  $\text{cm}^{-1}$  (epoxy), 820  $\text{cm}^{-1}$  (epoxy), 1002  $\text{cm}^{-1}$  (epoxy), 1113  $\text{cm}^{-1}$  (epoxy), 1186  $\text{cm}^{-1}$  (epoxy), 1333  $\text{cm}^{-1}$  (hematite/carbonaceous material), 1462  $\text{cm}^{-1}$  (epoxy), and 1608  $\text{cm}^{-1}$  (carbonaceous material/epoxy).

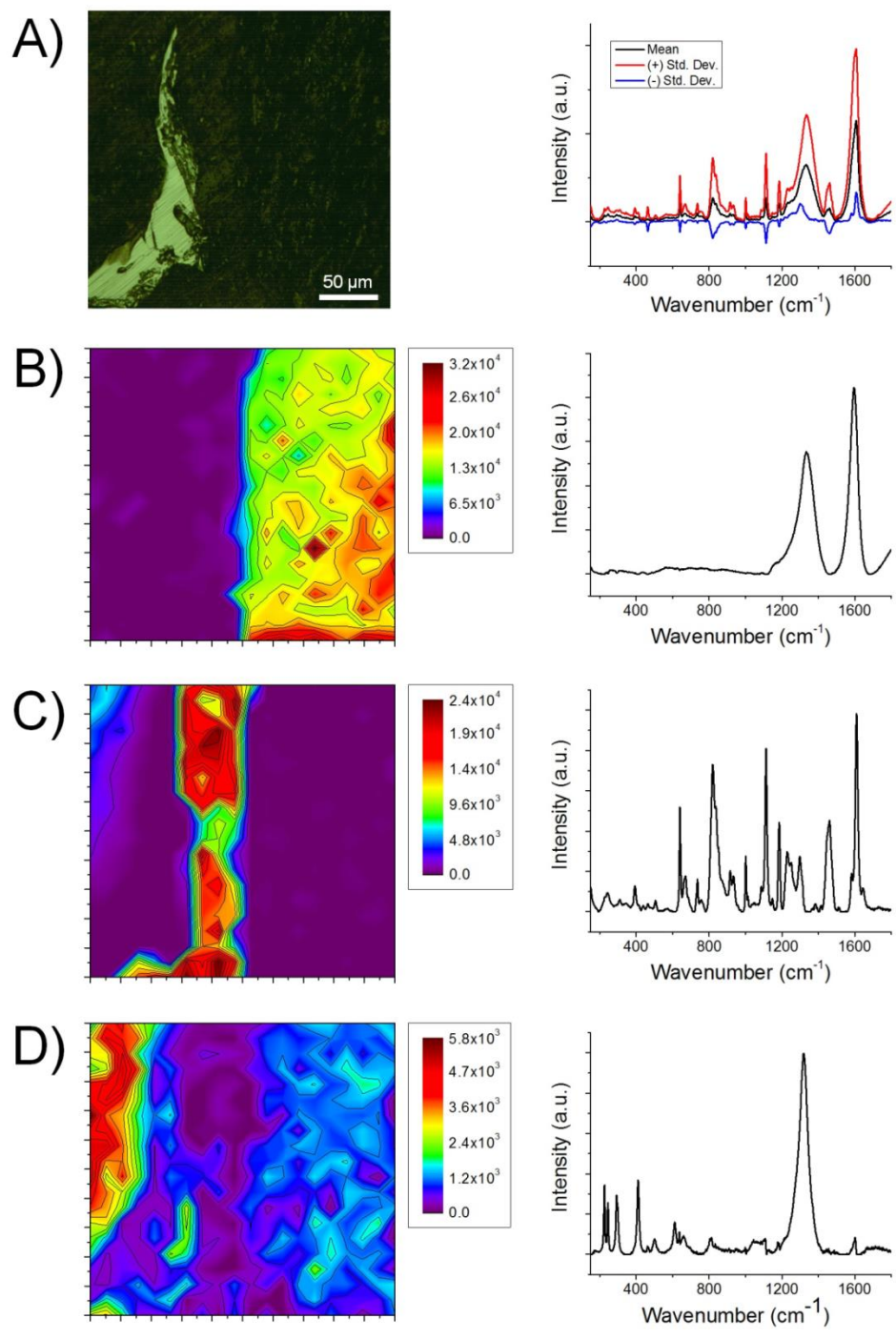


Figure 4.4: Spatially-resolved chemical maps and resolved Raman spectra of carbonaceous material (B), substrate-adhesive epoxy (C), and hematite (D) generated using MCR-ALS applied to Raman microspectroscopic imaging using 532 nm excitation. The optical image (A) and mean spectrum (black, A) +/- the standard deviation (+ in red, - in blue; A) are shown. A five-component MCR-ALS model was employed.

Using a five component MCR-ALS model, the three chemically meaningful components —hematite, carbonaceous material, and substrate-adhesive epoxy—were resolved. Specifically, the first resolved spectrum (**Figure 4.4B**) shows Raman bands at  $1334\text{ cm}^{-1}$  and  $1594\text{ cm}^{-1}$  characteristic of carbonaceous material. The second resolved spectrum (**Figure 4.4C**) shows major Raman bands at  $640\text{ cm}^{-1}$ ,  $670\text{ cm}^{-1}$ ,  $737\text{ cm}^{-1}$ ,  $820\text{ cm}^{-1}$ ,  $1002\text{ cm}^{-1}$ ,  $1113\text{ cm}^{-1}$ ,  $1185\text{ cm}^{-1}$ ,  $1229\text{ cm}^{-1}$ ,  $1298\text{ cm}^{-1}$ ,  $1462\text{ cm}^{-1}$ , and  $1610\text{ cm}^{-1}$  characteristic of substrate-adhesive epoxy. The third resolved spectrum (**Figure 4.4D**) shows major Raman bands at  $226\text{ cm}^{-1}$ ,  $245\text{ cm}^{-1}$ ,  $293\text{ cm}^{-1}$ ,  $411\text{ cm}^{-1}$ ,  $501\text{ cm}^{-1}$ ,  $612\text{ cm}^{-1}$ , and  $1319\text{ cm}^{-1}$  characteristic of hematite.

The spatial distributions of the chemical species within the probed area are in agreement with the sample design. Moreover, the spatial distribution of carbonaceous material (**Figure 4.4B**) is located in the right portion of the probed area, as expected from the corresponding optical image (**Figure 4.4A**). The spatial distribution of substrate-adhesive epoxy (**Figure 4.4C**) reveals that a small portion of the epoxy is in the center of the probed area, located at the interface of the carbonaceous material and the hematite. The spatial distribution of hematite (**Figure 4.4D**) confirms that hematite is located towards the left portion of the probed area.

MCR-ALS applied to the Raman microspectroscopic imaging data collected using 532 nm excitation is able to differentiate hematite, carbonaceous material, and

substrate-adhesive epoxy. However, the MCR-ALS results for hematite display some interference from carbonaceous material. This interference is shown in the chemical map of hematite (**Figure 4.4D**), in which a low signal for hematite is present on the right side of the probed area. Moreover, this interference is further displayed by the low intensity Raman band at  $1601\text{ cm}^{-1}$ , attributed to carbonaceous material, observed in the resolved Raman spectrum of hematite (**Figure 4.4D**).

Spatially-resolved chemical maps and their corresponding Raman spectra of hematite, carbonaceous material, and substrate-adhesive epoxy were also generated using MCR-ALS applied to Raman microspectroscopic imaging data collected using 785 nm excitation (**Figure 4.5**). The probed areas for the Raman microspectroscopic imaging measurements collected using 532 nm excitation (**Figure 4.4A**) and 785 nm excitation (**Figure 4.5A**) were specifically selected to be the same in order to most easily facilitate a direct comparison between the two sets of measurements. The mean (in black; **Figure 4.5A**) and standard deviation (+ in red, - in blue; **Figure 4.5A**) of the 400 total Raman spectra accumulated over the probed area (**Figure 4.5A**) demonstrate that all three chemical species are present. This result is shown by the mean Raman spectrum of the Raman microspectroscopic imaging data collected using 785 nm excitation displaying major Raman bands at  $226\text{ cm}^{-1}$  (hematite),  $292\text{ cm}^{-1}$  (hematite),  $411\text{ cm}^{-1}$  (hematite),  $612\text{ cm}^{-1}$  (hematite),  $1112\text{ cm}^{-1}$  (epoxy),  $1315\text{ cm}^{-1}$  (hematite/carbonaceous material), and  $1600\text{ cm}^{-1}$  (carbonaceous material/epoxy).

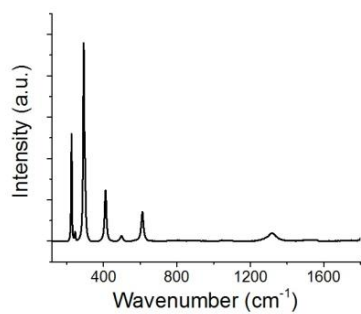
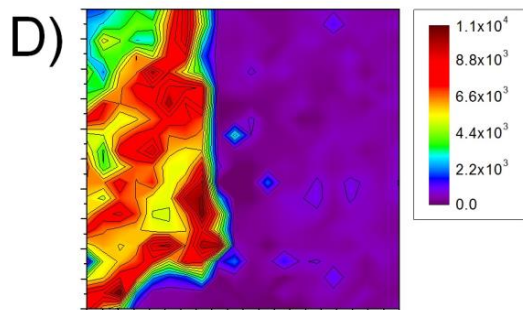
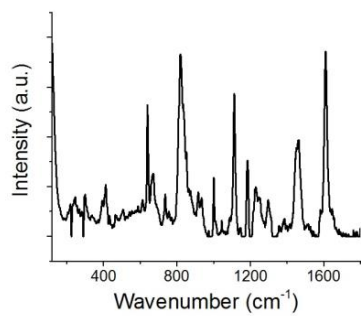
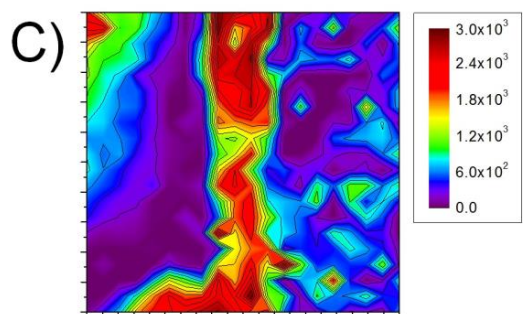
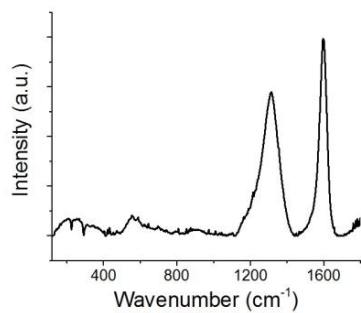
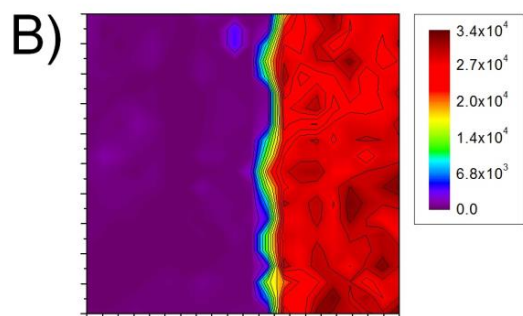
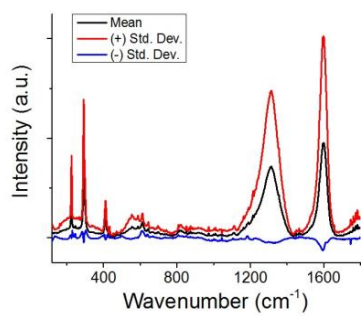
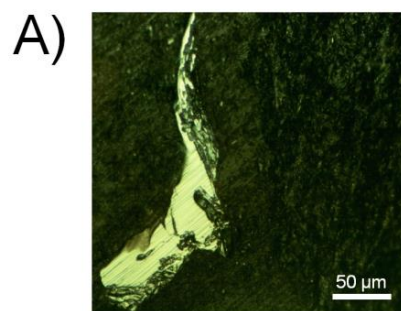


Figure 4.5: Spatially-resolved chemical maps and resolved Raman spectra of carbonaceous material (B), substrate-adhesive epoxy (C), and hematite (D) generated using MCR-ALS applied to Raman microspectroscopic imaging using 785 nm excitation. The optical image (A) and mean spectrum (black, A) +/- the standard deviation (+ in red, - in blue; A) are shown. A five-component MCR-ALS model was employed.

Using a five component MCR-ALS model, hematite, carbonaceous material, and substrate-adhesive epoxy were resolved. Specifically, the first resolved spectrum (**Figure 4.5B**) shows major Raman bands at  $1315\text{ cm}^{-1}$  and  $1596\text{ cm}^{-1}$  characteristic of carbonaceous material. The second resolved spectrum (**Figure 4.5C**) shows major Raman bands at  $640\text{ cm}^{-1}$ ,  $670\text{ cm}^{-1}$ ,  $736\text{ cm}^{-1}$ ,  $819\text{ cm}^{-1}$ ,  $1001\text{ cm}^{-1}$ ,  $1113\text{ cm}^{-1}$ ,  $1185\text{ cm}^{-1}$ ,  $1230\text{ cm}^{-1}$ ,  $1297\text{ cm}^{-1}$ ,  $1464\text{ cm}^{-1}$ , and  $1610\text{ cm}^{-1}$  characteristic of substrate-adhesive epoxy. The third resolved spectrum (**Figure 4.5D**) shows major Raman bands at  $226\text{ cm}^{-1}$ ,  $245\text{ cm}^{-1}$ ,  $292\text{ cm}^{-1}$ ,  $411\text{ cm}^{-1}$ ,  $498\text{ cm}^{-1}$ ,  $612\text{ cm}^{-1}$ , and  $1320\text{ cm}^{-1}$  characteristic of hematite.

The chemical maps generated using MCR-ALS applied to Raman microspectroscopic imaging data collected using 785 nm excitation show that the carbonaceous material (**Figure 4.5B**) is distinctly located in the right portion of the probed area. The chemical map of substrate-adhesive epoxy (**Figure 4.5C**) shows that the epoxy is mainly localized in the center of the probed area, at the interface of the carbonaceous material and the hematite, but also occurs in other minor locations throughout the probed area. The chemical map of hematite (**Figure 4.5D**) shows that the hematite is distinctly located towards the left portion of the probed area. The chemical maps thus confirm that the locations of the chemical species are as designed during sample preparation—i.e., hematite on the left, substrate-adhesive epoxy in the

middle, and carbonaceous material on the right of the probed area. Additionally, using 785 nm excitation, the resolved Raman spectrum of hematite (**Figure 4.5D**) displays no influence from carbonaceous material, and therefore, as expected, the spatial distributions of these two chemical species are distinctly located on their respective portions of the probed area.

The results of MCR-ALS applied to Raman microspectroscopic imaging data collected using both 532 nm and 785 nm excitation on a hematite, carbonaceous material, and substrate-adhesive epoxy sample demonstrate that both wavelengths of excitation are able to resolve the three chemical species. MCR-ALS with Raman microspectroscopic imaging using 785 nm excitation is more effectively able to spatially and spectrally resolve the three-phase mixture as compared to using 532 nm excitation. This result is due to the more severe spectral overlap of the chemical species using 532 nm excitation as opposed to using 785 nm excitation, as is mainly displayed in the resolved Raman spectra of hematite. The resolved Raman spectrum of hematite using 532 nm excitation (**Figure 4.4D**) is influenced by carbonaceous material—in the form of the  $1601\text{ cm}^{-1}$  Raman band—whereas the resolved Raman spectrum of hematite using 785 nm excitation (**Figure 4.5D**) displays no influence from carbonaceous material as shown by the absence of a  $1600\text{ cm}^{-1}$  band. Therefore, using the ideal sample containing hematite and carbonaceous material in separate, distinct locations within a probed area, MCR-ALS with Raman microspectroscopic imaging data collected using both 532 nm and 785 nm excitation can be employed to spatially and spectrally differentiate hematite, carbonaceous material, and substrate-adhesive epoxy.

#### **4.4.5 Multivariate Curve Resolution-Alternating Least Squares Applied to Combinatorial Data Sets**

Combinatorial data sets were employed in order to most appropriately test the efficacy of MCR-ALS in conjunction with Raman microspectroscopic imaging using both 532 nm and 785 nm excitation for the spatial and spectral resolution of hematite, carbonaceous material, and substrate-adhesive epoxy. Combinatorial data sets were generated using the experimental data from Raman microspectroscopic imaging measurements using both 532 nm and 785 nm excitation. Specifically, a combinatorial data set, which is a matrix resulting from the summation of the original two-dimensional experimental data matrix with a horizontally-flipped two-dimensional experimental data matrix, can produce data containing hematite and carbonaceous material localized in the exact same area. For example, in this chapter, a sample was designed so that hematite, carbonaceous material, and substrate-adhesive epoxy were located in distinct portions of a probed area—hematite on the left, carbonaceous material on the right, and substrate-adhesive epoxy in the middle. Thus, the original two-dimensional experimental data matrix generated from Raman microspectroscopic imaging of this sample contains spectral information on a sample with hematite spatially on the left, carbonaceous material spatially on the right, and substrate-adhesive epoxy spatially in-between hematite and carbonaceous material. By horizontally-flipping this two-dimensional experimental data matrix, a data set with spectral information on a sample of opposite spatial information is produced—the horizontally-flipped two-dimensional experimental data matrix contains spectral information with hematite now spatially located on the right, carbonaceous material now spatially located on the left, and substrate-adhesive epoxy still spatially located in-between hematite and carbonaceous material. By summing this new horizontally-

flipped two-dimensional experimental data matrix with the original two-dimensional experimental data matrix, a combinatorial data set is produced, and thus, the resulting matrix contains spectral information with hematite spatially located on both the left and right portions of the sample, carbonaceous material spatially located on both the left and right portions of the sample, and substrate-adhesive epoxy still spatially located in-between these two chemical species.

By generating combinatorial data sets using the experimental data of Raman microspectroscopic imaging using both 532 nm and 785 nm excitation, the most difficult scenario for the spatial and spectral resolution of hematite, carbonaceous material, and substrate-adhesive epoxy can be evaluated. Moreover, using combinatorial data sets, the hematite and carbonaceous material are now within the same spatial location. Thus, if MCR-ALS applied to Raman microspectroscopic imaging can resolve the pure chemical species given that hematite and carbonaceous material are located within the same pixel, this method would be an important tool for the identification of carbonaceous material in the presence of hematite on extraterrestrial bodies, especially Mars.

The results of Raman microspectroscopic imaging with MCR-ALS of the combinatorial data sets, which contain spectral and spatial information regarding the three-phase mixture in which hematite and carbonaceous material are located within the same space, are shown for 532 nm excitation (**Figure 4.6**) and 785 nm excitation (**Figure 4.7**). MCR-ALS applied to the combinatorial data set generated using 532 nm excitation (**Figure 4.6**) of the hematite, carbonaceous material, and substrate-adhesive epoxy sample produced spatially-resolved chemical maps and corresponding Raman spectra of the chemical species. The combinatorial data set was generated using the

Raman microspectroscopic imaging data collected in the probed area shown in **Figure 4.4A**.

Using a five component MCR-ALS model, hematite, carbonaceous material, and substrate-adhesive epoxy were resolved. The first resolved spectrum (**Figure 4.6A**) shows major Raman bands at  $1340\text{ cm}^{-1}$  and  $1603\text{ cm}^{-1}$  characteristic of carbonaceous material. The second resolved spectrum (**Figure 4.6B**) shows major Raman bands at  $640\text{ cm}^{-1}$ ,  $670\text{ cm}^{-1}$ ,  $737\text{ cm}^{-1}$ ,  $820\text{ cm}^{-1}$ ,  $1002\text{ cm}^{-1}$ ,  $1113\text{ cm}^{-1}$ ,  $1185\text{ cm}^{-1}$ ,  $1229\text{ cm}^{-1}$ ,  $1299\text{ cm}^{-1}$ ,  $1462\text{ cm}^{-1}$ , and  $1609\text{ cm}^{-1}$  characteristic of substrate-adhesive epoxy. The third resolved spectrum (**Figure 4.6C**) shows major Raman bands at  $226\text{ cm}^{-1}$ ,  $245\text{ cm}^{-1}$ ,  $292\text{ cm}^{-1}$ ,  $411\text{ cm}^{-1}$ ,  $612\text{ cm}^{-1}$ , and  $1319\text{ cm}^{-1}$  characteristic of hematite.

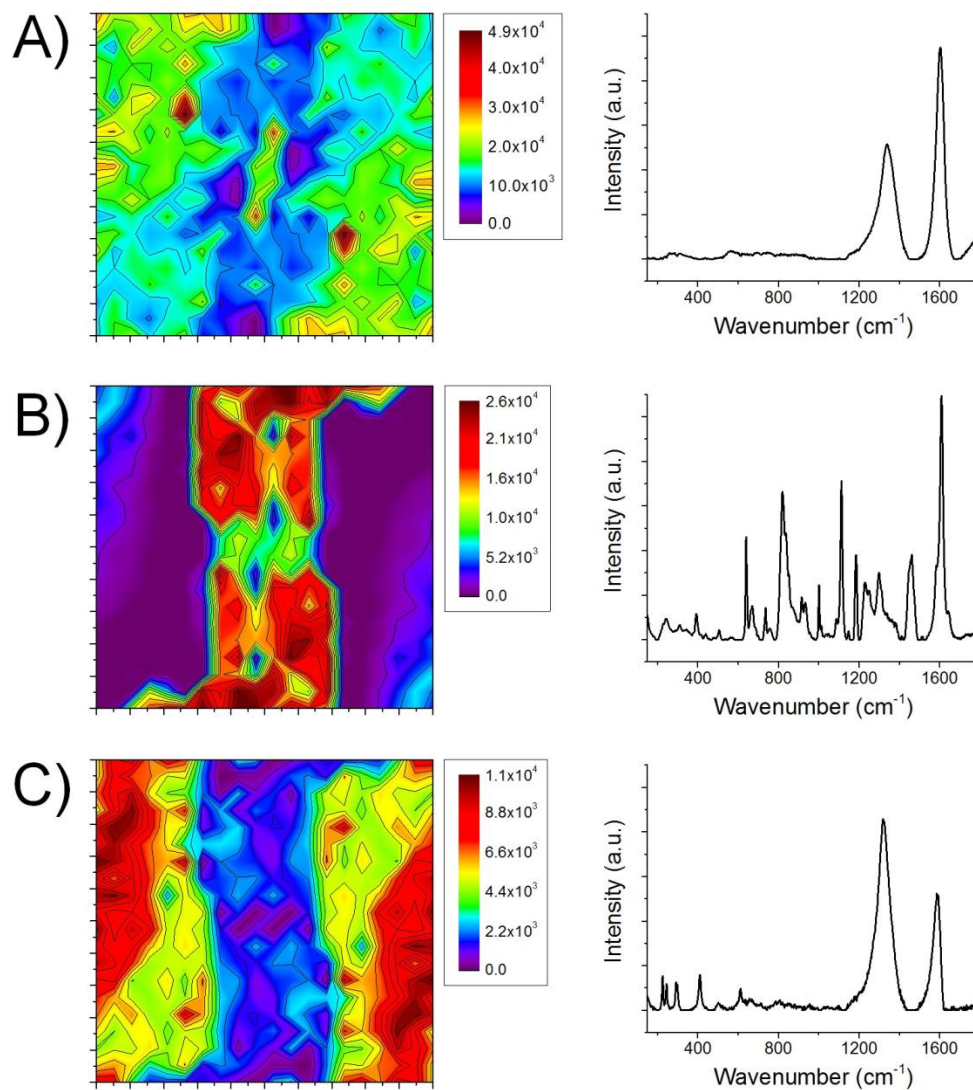


Figure 4.6: Spatially-resolved chemical maps and resolved Raman spectra of carbonaceous material (A), substrate-adhesive epoxy (B), and hematite (C) generated using MCR-ALS applied to the 532 nm excitation combinatorial data set. A five-component MCR-ALS model was employed.

The spatial distribution of the chemical species, generated using MCR-ALS applied to the combinatorial data set collected at 532 nm excitation, is consistent with the results obtained on the original experimental data. Specifically, the spatial distribution of carbonaceous material (**Figure 4.6A**) is located on both the right and left portions of the probed area as expected given the original experimental data (**Figure 4.4B**). The spatial distribution of substrate-adhesive epoxy (**Figure 4.6B**) shows that the epoxy is localized in the center of the probed area, and this distribution is in agreement with the spatial distribution observed using the original experimental data (**Figure 4.4C**). The spatial distribution of hematite (**Figure 4.6C**) shows that hematite is localized on both the right and left portions of the probed area in agreement with the original experimental data (**Figure 4.4D**).

Similar to the chemical map of hematite from the original experimental data (**Figure 4.4D**), the distribution of hematite from the combinatorial data set using 532 nm excitation (**Figure 4.6C**) displays some influence from carbonaceous material. This is observed in the resolved Raman spectrum of hematite (**Figure 4.6C**), in which the Raman band at  $1603\text{ cm}^{-1}$ , characteristic of carbonaceous material, is present. The intensity of this band at  $1603\text{ cm}^{-1}$  is higher in the results obtained from the combinatorial data set (**Figure 4.6C**) as compared to those observed in the original experimental data (**Figure 4.4D**). As it appears that carbonaceous material is influencing the resolved Raman spectrum of hematite more when using the combinatorial data set, the difficulty of resolving hematite and carbonaceous material using 532 nm excitation is greater if these two chemical species are located in the same spatial region. Overall, the chemical maps generated from MCR-ALS applied to the 532 nm excitation combinatorial data set (**Figure 4.6**) display that hematite and

carbonaceous material can be resolved even if these two chemical species are located in the same spatial region, and these chemical maps are in agreement with those generated using the original experimental data (**Figure 4.4**).

Spatially-resolved chemical maps and corresponding resolved Raman spectra of hematite, carbonaceous material, and substrate-adhesive epoxy were generated using MCR-ALS applied to the combinatorial data set collected at 785 nm excitation (**Figure 4.7**). Specifically, the Raman microspectroscopic imaging data within the previously probed area (**Figure 4.5A**), collected using 785 nm excitation, was used to produce this combinatorial data set. Hematite, carbonaceous material, and substrate-adhesive epoxy were spatially and spectrally resolved using a five component MCR-ALS model applied to this combinatorial data set. The first resolved spectrum (**Figure 4.7A**) shows major Raman bands at  $1316\text{ cm}^{-1}$  and  $1600\text{ cm}^{-1}$  characteristic of carbonaceous material. The second resolved spectrum (**Figure 4.7B**) shows major Raman bands at  $640\text{ cm}^{-1}$ ,  $670\text{ cm}^{-1}$ ,  $736\text{ cm}^{-1}$ ,  $819\text{ cm}^{-1}$ ,  $1001\text{ cm}^{-1}$ ,  $1113\text{ cm}^{-1}$ ,  $1185\text{ cm}^{-1}$ ,  $1231\text{ cm}^{-1}$ ,  $1298\text{ cm}^{-1}$ ,  $1461\text{ cm}^{-1}$ , and  $1609\text{ cm}^{-1}$  characteristic of substrate-adhesive epoxy. The third resolved spectrum (**Figure 4.7C**) shows major Raman bands at  $226\text{ cm}^{-1}$ ,  $245\text{ cm}^{-1}$ ,  $292\text{ cm}^{-1}$ ,  $410\text{ cm}^{-1}$ ,  $498\text{ cm}^{-1}$ ,  $611\text{ cm}^{-1}$ , and  $1311\text{ cm}^{-1}$  characteristic of hematite.

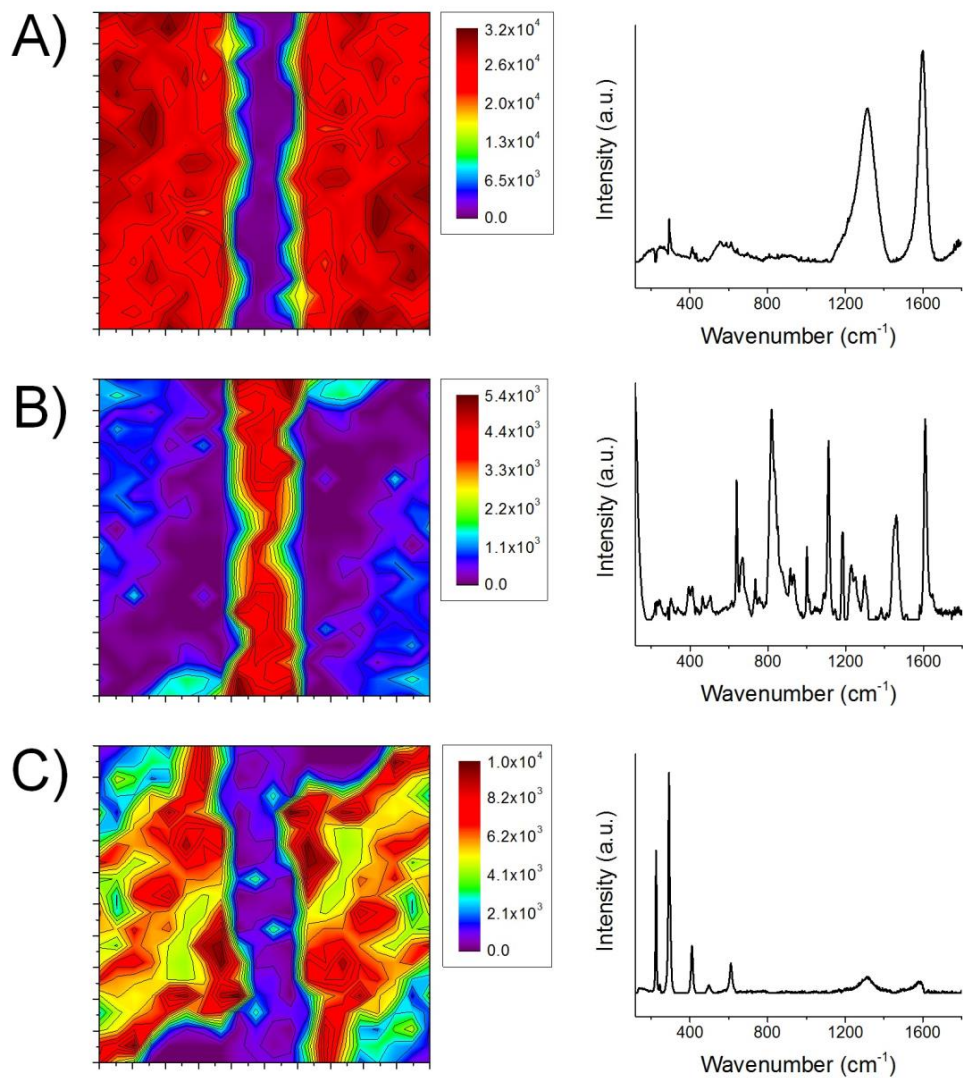


Figure 4.7: Spatially-resolved chemical maps and resolved Raman spectra of carbonaceous material (A), substrate-adhesive epoxy (B), and hematite (C) generated using MCR-ALS applied to the 785 nm excitation combinatorial data set. A five-component MCR-ALS model was employed.

The chemical maps (**Figure 4.7**) generated using MCR-ALS applied to the combinatorial data set collected with 785 nm excitation are consistent with the results obtained using the original experimental data (**Figure 4.5**). The chemical map of the carbonaceous material (**Figure 4.7A**) shows it to be distinctly located, in agreement with the original experimental data (**Figure 4.5B**), on both the right and left portions of the probed area, and to have a high intensity in both portions of the probed area. The chemical map of substrate-adhesive epoxy (**Figure 4.7B**) shows that epoxy is distributed primarily throughout the center of the probed area, between the hematite and carbonaceous material, and this result agrees with that of the original experimental data (**Figure 4.5C**). The chemical map of hematite (**Figure 4.7C**) shows that the hematite is located on both the right and left portions of the probed area, and this result agrees with that of the original experimental data (**Figure 4.5D**).

Using MCR-ALS applied to the combinatorial data set collected using 785 nm excitation, hematite, carbonaceous material, and substrate-adhesive epoxy were spatially and spectrally differentiated. Moreover, the spatial distributions of hematite, carbonaceous material, and substrate-adhesive epoxy (**Figure 4.7**) resulting from MCR-ALS applied to the combinatorial data set acquired using 785 nm excitation are highly consistent with those of the original experimental data (**Figure 4.5**). However, using the combinatorial data set with 785 nm excitation, the resolved Raman spectrum of hematite (**Figure 4.7C**) is influenced by carbonaceous material as evidenced by the band at  $1589\text{ cm}^{-1}$ . Furthermore, given that this  $1589\text{ cm}^{-1}$  band, characteristic of carbonaceous material, is observed in the resolved Raman spectrum of hematite using the combinatorial data set and not observed in the resolved Raman spectrum using the original experimental data (**Figure 4.5D**), it is more challenging to differentiate

hematite and carbonaceous material using MCR-ALS applied to Raman microspectroscopic imaging data if these two chemical species are localized in the same area.

The results obtained by applying MCR-ALS to combinatorial data sets collected using both 532 nm (**Figure 4.6**) and 785 nm (**Figure 4.7**) excitation show that Raman microspectroscopic imaging in conjunction with multivariate analysis methods can be used to spatially and spectrally resolve hematite, carbonaceous material, and substrate-adhesive epoxy even when hematite and carbonaceous material are located within the same area. However, using both 532 nm and 785 nm excitation, the results using MCR-ALS applied to the respective combinatorial data set reveal the difficulty in resolving carbonaceous material from hematite. This is evidenced by bands characteristic of carbonaceous material— $1603\text{ cm}^{-1}$  for 532 nm excitation (**Figure 4.6C**) and  $1589\text{ cm}^{-1}$  for 785 nm excitation (**Figure 4.7C**)—being present within the resolved Raman spectra of hematite. This band, which displays a much higher intensity in the resolved Raman spectrum of hematite using 532 nm excitation (**Figure 4.6C**) than it does using 785 nm excitation (**Figure 4.7C**), illustrates the greater difficulty in differentiating hematite from carbonaceous material using 532 nm excitation as compared to using 785 nm excitation if these two chemical species are located in the same spatial region. For carbonaceous material, hematite, and substrate-adhesive epoxy, the chemical maps generated using MCR-ALS applied to the combinatorial data set collected at 785 nm excitation (**Figure 4.7**) display much more distinct distributions of the three chemical species as compared to those collected at 532 nm excitation (**Figure 4.6**). These results demonstrate the effectiveness of 785 nm excitation for the resolution of hematite from carbonaceous material if these two

chemical species are located in the same spatial region. This increased effectiveness of 785 nm excitation as opposed to that of 532 nm excitation for the resolution of these three chemical species can be attributed to the much greater spectral overlap of the three chemical species that is observed using 532 nm excitation rather than 785 nm excitation. Overall, combinatorial data sets produced using both 532 nm (**Figure 4.6**) and 785 nm (**Figure 4.7**) excitation, which allow for hematite and carbonaceous material to be localized in the exact same spatial region, revealed that MCR-ALS in conjunction with Raman microspectroscopic imaging can be employed for the resolution of hematite, carbonaceous material, and substrate-adhesive epoxy, in which the differentiation of these three chemical species is more efficient using 785 nm excitation as opposed to using 532 nm excitation.

#### **4.4.6 Implications for Planetary Science, Geochemistry, and Geology**

This chapter provides an analytical methodology to help solve the basic problem of distinguishing carbonaceous material from hematite ( $\alpha\text{-Fe}_2\text{O}_3$ ) that has been encountered in Raman spectroscopic analysis of various geologic samples.[132, 140, 158-160, 174] Our results are timely in that both the upcoming Mars 2020 rover and ExoMars 2020 rover missions to Mars will search for evidence of extant or past life, and will, for the first time, conduct Raman spectroscopy on the surface of Mars.[127, 139] Given the widespread distribution of hematite on the Martian surface[137, 143-149, 151-154, 156] and the recent discovery that trace amounts of organic molecules and hematite are present in the same samples from a drill hole within Gale Crater on Mars [131, 135-137], it is likely that any organic molecules and/or carbonaceous material detected in Martian samples by the upcoming rover missions will occur in the presence of hematite.[132] It will therefore be crucial to

robustly distinguish carbonaceous material from hematite in Raman spectra obtained by the upcoming rover missions to Mars, and the analytical methodology proposed here should help to solve this problem. The Mars 2020 rover mission will cache samples for a possible future return to Earth[127], and our results should help mission scientists in their selection of those samples.

Our results have an increased importance for these upcoming Mars missions given the excitation wavelengths of 248.6 nm and 532 nm used by the Raman spectrometers onboard the Mars 2020 rover[127] and the ExoMars 2020 rover[139], respectively. The wavenumbers displayed in the Raman spectra collected by the SHERLOC instrument onboard the Mars 2020 rover will be  $>810\text{ cm}^{-1}$ . [127] These Raman spectra, therefore, will not include several bands for hematite present in the  $200\text{ to }700\text{ cm}^{-1}$  spectral region (**Figures 4.1A** and **4.1B**) that are key to identifying this phase.[158] In the Raman spectra collected by the SHERLOC instrument, therefore, the 2LO band of hematite will have an increased importance for the identification of this phase, so our results have important implications for robustly distinguishing hematite from carbonaceous material in these Raman spectra. In addition, as with 532 nm excitation (**Figure 4.1A**), under 248 nm excitation, the 2LO band of hematite is again a broad high-intensity band[175] that will have spectral overlap with the D-band for carbonaceous material. As regards Raman spectra collected by the ExoMars 2020 rover mission using 532 nm excitation, our analytical methodology can resolve carbonaceous material from hematite that are located in the same spatial region, but it is more difficult to resolve the two chemical species using 532 nm excitation as opposed to using 785 nm excitation. Our analytical methodology

used to distinguish carbonaceous material from hematite will, therefore, be especially useful for the upcoming rover missions in their search for extant or past life on Mars.

In addition to Mars, our proposed analytical methodology for distinguishing carbonaceous material from hematite should be applicable to a wide variety of studies involving extraterrestrial bodies or materials containing carbonaceous material and hematite, especially when these components have a close spatial association. For example, Raman spectroscopy has been used to document both micron-sized magnetite-hematite grains[176] and carbonaceous material containing both the D- and G-bands in micron-sized fragments[177] from different grains returned by the Stardust mission from comet 81P/Wild 2. Most of the magnetite-hematite grains are believed to be indigenous to the comet as opposed to being artifacts of capture or analysis.[176] Raman spectroscopy has also been used to document hematite and organic carbon on a micron-scale in a stratospheric dust particle (10  $\mu\text{m}$  x 9  $\mu\text{m}$  in size) of putative extraterrestrial origin.[178]

For geological studies, the problem of distinguishing carbonaceous material from hematite is especially acute in the search for evidence of microbial fossils in ancient geologic samples. The spectral overlap of the 2LO band of hematite and the D-band of carbonaceous material has contributed to the misidentification of hematite as carbonaceous microfossils in 3.5-billion-year-old cherts.[158-160] Our proposed analytical methodology used to distinguish carbonaceous material from hematite, therefore, should help researchers who are engaged in the difficult task of searching for evidence of early life on Earth. Furthermore, our results should have applications for studies on redbeds and banded iron formations (BIFs) that comprise two major types of iron-bearing sedimentary rocks. For example, a recent study of Early Permian

redbed mudstones in Texas, USA, containing well-preserved plant macrofossils shows that the rocks contain hematite and minor amounts (~0.08-0.27 wt%) of total organic carbon.[179] Raman spectroscopy on a polished thin section of a sample from the Vichadero BIF, Uruguay, shows that carbonaceous material and hematite locally have an intimate spatial association on a micron-scale.[180] It is clear, therefore, that our proposed analytical methodology to distinguish carbonaceous material from hematite will have applicability to a host of studies involving both terrestrial and extraterrestrial samples and environments.

#### 4.5 Conclusions

The search for extant or past life on Mars in the form of organic molecules or carbonaceous material will be a primary objective of both the upcoming Mars 2020 rover and ExoMars 2020 rover missions. For the *first* time, Raman spectroscopy and Raman microspectroscopic imaging will be conducted on the surface of Mars. Hematite ( $\alpha$ -Fe<sub>2</sub>O<sub>3</sub>) is a widespread mineral on the Martian surface. As the 2LO Raman band of hematite and the Raman D-band of carbonaceous material show spectral overlap, a detailed analytical methodology for both the collection and analysis of Raman spectroscopic data is needed to robustly differentiate carbonaceous material from hematite in samples on the surface of Mars. Moreover, the differentiation of carbonaceous material from hematite is a challenging task using univariate analysis due to the high spectral overlap of these components that is observed using both 532 nm and 785 nm excitation. In this chapter, we have shown the ability of multivariate analysis, in the form of multivariate curve resolution-alternating least squares (MCR-ALS), in conjunction with Raman microspectroscopic imaging, to identify and

differentiate, both spatially and spectrally, carbonaceous material from hematite. Our measured Raman spectra of hematite and carbonaceous material display increased spectral overlap using 532 nm excitation as compared to using 785 nm excitation. This result is evidenced by 2LO band of hematite being more intense under 532 nm excitation as compared to under 785 nm excitation. A sample comprised of hematite, carbonaceous material, and substrate-adhesive epoxy in spatially distinct domains was prepared for this investigation. On this sample, using both 532 nm and 785 nm excitation, spatially-resolved chemical maps and corresponding Raman spectra of the individual chemical species—hematite, carbonaceous material, and substrate-adhesive epoxy—were generated using MCR-ALS with Raman microspectroscopic imaging. Furthermore, Raman microspectroscopic imaging with MCR-ALS using both 532 nm and 785 nm excitation was able to differentiate hematite and carbonaceous material when these species were in spatially distinct domains. Principal component analysis (PCA) applied to the Raman microspectroscopic imaging data demonstrated that both 532 nm and 785 nm excitation produced three-phase systems comprised of hematite, carbonaceous material, and substrate-adhesive epoxy, in which 785 nm excitation provided a more refined differentiation of the three chemical species. MCR-ALS applied to the Raman microspectroscopic imaging data confirmed this result: 785 nm excitation better resolved hematite, carbonaceous material, and substrate-adhesive epoxy. Combinatorial data sets were also used to analyze experimental data with hematite and carbonaceous material within the same, non-differentiable space. MCR-ALS applied to combinatorial data sets using both 532 nm and 785 nm excitation was able to resolve carbonaceous material from hematite that are located in the same spatial region, and again, 785 nm excitation was better able to differentiate hematite,

carbonaceous material, and substrate-adhesive epoxy. Using multivariate analysis methods, including PCA and MCR-ALS, with Raman microspectroscopic imaging, 785 nm excitation was more effective at resolving hematite, carbonaceous material, and substrate-adhesive epoxy as compared to 532 nm excitation. This result can be attributed to the increased spectral overlap of the 2LO band of hematite with the D-band of carbonaceous material using 532 nm excitation as compared to using 785 nm excitation. To our knowledge, this is the *first* time multivariate analysis methods with Raman microspectroscopic imaging have been employed to differentiate carbonaceous material from hematite. We have therefore provided an analytical methodology, including both data collection and analysis, which should prove useful in the upcoming rover missions that will search for extant or past life on the surface of Mars. In addition to Mars, our proposed analytical methodology for differentiating carbonaceous material from hematite should be useful for a wide range of studies of both terrestrial and extraterrestrial materials and environments, including the daunting task of finding evidence of microbial life in ancient rocks on Earth.

## Chapter 5

### **MULTIVARIATE CURVE RESOLUTION-ALTERNATING LEAST SQUARES (MCR-ALS) WITH RAMAN MICROSPECTROSCOPIC IMAGING APPLIED TO LUNAR METEORITES**

#### **5.1 Abstract**

Lunar meteorites provide a more random sampling of the Moon's surface than do the returned lunar samples, and they provide valuable information to help estimate the chemical composition of the lunar crust, the lunar mantle, and the bulk Moon. As of July 2014, ~96 lunar meteorites had been documented and 10 of these are unbrecciated mare basalts. Using multivariate curve resolution-alternating least squares (MCR-ALS) with Raman microspectroscopic imaging, portions of two polished thin sections of two paired, unbrecciated, mare-basalt lunar meteorites that had been collected from the LaPaz Icefield (LAP) of Antarctica—LAP 02205 and LAP 04841—were investigated. Polarized light microscopy displays that both meteorites are heterogeneous and consist of polydispersed sized and shaped particles of varying chemical composition. For two distinct probed areas within each meteorite, the individual chemical species were elucidated using MCR-ALS applied to Raman microspectroscopic imaging. Spatially-resolved chemical images and corresponding resolved Raman spectra of these chemical species were generated using MCR-ALS in conjunction with Raman microspectroscopic imaging. For LAP 02205, MCR-ALS with Raman microspectroscopic imaging spatially and spectrally resolved clinopyroxene, ilmenite, substrate-adhesive epoxy, and diamond-polish within the

probed areas. Similarly, for LAP 04841, spatially-resolved chemical images with corresponding resolved Raman spectra of clinopyroxene, troilite, a high-temperature polymorph of anorthite, substrate-adhesive epoxy, and diamond-polish were generated using MCR-ALS with Raman microspectroscopic imaging. In both LAP 02205 and LAP 04841, substrate-adhesive epoxy and diamond-polish were more readily observed within fractures/veinlet features. Spectrally-diverse clinopyroxenes were resolved in LAP 04841 using MCR-ALS with Raman microspectroscopic imaging. Factors that allow these resolved clinopyroxenes to be differentiated include crystal orientation, spatially-distinct chemical zoning of pyroxene crystals, and/or chemical and molecular composition. The minerals we identified using our analytical methodology—clinopyroxene, anorthite, ilmenite, and troilite—are consistent with the results of previous studies of the two meteorites using electron microprobe analysis. To our knowledge, this is the *first* report of MCR-ALS with Raman microspectroscopic imaging used for the investigation of both lunar and other types of meteorites. We have demonstrated the use of multivariate analysis methods, namely MCR-ALS, with Raman microspectroscopic imaging to investigate heterogeneous lunar meteorites. Our analytical methodology can be used to elucidate the chemical, molecular, and structural characteristics of phases in a host of complex, heterogeneous geological, geochemical, and extraterrestrial materials.

## 5.2 Introduction

Raman spectroscopy has been proposed as a tool for the *in situ* detection, identification, and characterization of various materials, e.g., minerals, glasses, and organic molecules, on the surfaces of extraterrestrial bodies including Mars and the

Moon.[30, 31, 44, 138, 181] The upcoming Mars 2020[127] and ExoMars 2020[129, 139] rover missions to Mars that are being developed by the National Aeronautics and Space Administration (NASA)[127] and the European Space Agency (ESA)/Russian Federal Space Agency (Roscosmos)[139], respectively, will use Raman spectrometers, for the *first* time[130], to investigate the surface materials of an extraterrestrial body.[127, 139] As for lunar materials, Raman spectroscopy and Raman microspectroscopic imaging have been shown to readily identify and determine the spatial distribution of mineral phases in both Apollo lunar samples[30, 44, 181-183] and lunar meteorites found on Earth[44, 182].

Lunar meteorites provide a more random sampling of the Moon's surface than the samples returned to Earth by the Apollo and Luna missions.[184] Lunar meteorites provide valuable information that is used to help estimate the chemical composition of both the lunar crust and the bulk Moon, as well as to help constrain the Mg/(Mg + Fe) ratio of the lunar mantle.[184, 185] Furthermore, the chemical, molecular, and structural characteristics of the mineral phases within lunar samples are used to elucidate the petrogenesis of their host rocks.[182, 184, 186-190] From the discovery of the first lunar meteorite in 1979 until June 2005, ~36 lunar meteorites had been identified, analyzed, and described, and ~86% of them had been found in Antarctica and the deserts of northern Africa and Oman.[184] Lunar meteorites continued to be discovered so that by July 2014, ~96 lunar meteorites had been documented.[191] Most of these meteorites are different types of breccias with only 10 (~10%) of them being unbrecciated mare basalts.[191] In this chapter, we investigated two unbrecciated mare-basalt meteorites, and we now provide some basic background on the minerals in these rocks that we analyzed.

The common silicate minerals pyroxene, plagioclase feldspar, and olivine together comprise >90 vol.% of many lunar rocks, including mare basalts.[181, 184, 190] These phases are readily distinguished from each other using Raman spectroscopy since their major Raman bands do not overlap.[30, 44, 181] Ilmenite is a common oxide mineral ( $\leq 5$  vol.%) and troilite is a common, but minor, sulfide mineral in lunar samples.[184, 190] Olivine was not analyzed in this chapter, so we do not discuss it here.

Pyroxenes comprise an important rock-forming group of minerals,[182] and pyroxene is the most abundant phase in mare basalts.[190] Pyroxenes crystallize in either the orthorhombic (orthopyroxene) or monoclinic (clinopyroxene) crystal systems, and they have a wide range of chemical compositions.[192] For this chapter, we need only consider those pyroxenes that have the general formula  $(\text{Mg,Fe}^{2+},\text{Ca})_2\text{Si}_2\text{O}_6$  and are plotted on the pyroxene quadrilateral.[192, 193] The pyroxene quadrilateral is an isosceles trapezoid with the left and right vertices of the lower base being the end member compositions  $\text{Mg}_2\text{Si}_2\text{O}_6$  (enstatite, En) and  $(\text{Fe}^{2+})_2\text{Si}_2\text{O}_6$  (ferrosilite, Fs), respectively, and the left and right vertices of the upper base being the end member compositions  $\text{CaMgSi}_2\text{O}_6$  (diopside, Di) and  $\text{CaFe}^{2+}\text{Si}_2\text{O}_6$  (hedenbergite, Hd), respectively.[192, 193] The  $\text{Ca}_2\text{Si}_2\text{O}_6$  (wollastonite, Wo) component of the chemical compositions of pyroxenes plotted on the pyroxene quadrilateral ranges from  $\text{Wo}_0$  along the lower base (En-Fs series) to  $\text{Wo}_{50}$  along the upper base (Di-Hd series).[192] Pyroxenes of the En-Fs series are orthopyroxenes with space group *Pbca* that may contain up to five molecular percent of the wollastonite component.[192] Clinopyroxenes have a higher molecular percentage of the wollastonite component than do orthopyroxenes, and they have a variety of names

based on their chemical compositions.[192, 193] We here consider the clinopyroxene varieties pigeonite and augite. Pigeonite— $(\text{Mg,Fe}^{2+},\text{Ca})_2\text{Si}_2\text{O}_6$ —refers to a low-Ca clinopyroxene having a wollastonite component with values of  $\text{Wo}_{5-20}$ .[192] Low-temperature pigeonite has space group  $P2_1/c$ , and upon heating, high-temperature pigeonite has space group  $C2/c$ .[192] Augite— $(\text{Ca,Mg,Fe}^{2+})_2\text{Si}_2\text{O}_6$ —refers to clinopyroxenes having a wollastonite component with values of  $\text{Wo}_{20-45}$ .[192] Augite and the clinopyroxenes of the Di-Hd series have space group  $C2/c$ .[192] With increasing Fe content, pigeonite and augite have been referred to as ferropigeonite and ferroaugite, respectively[193], although these terms are now considered obsolete.[192] The mineral pyroxferroite ( $\sim\text{Ca}_{1/7}\text{Fe}_{6/7}\text{SiO}_3$ ) is a triclinic pyroxenoid with space group  $P\bar{1}$  and it would plot along or close to the Di-Fs leg of the pyroxene quadrilateral corresponding to compositions with very high Fe contents (molecular  $\text{Mg}/(\text{Mg} + \text{Fe})$  ratios of  $\sim 0.05$ .[181, 182, 190, 193] In lunar mare basalts, orthopyroxene is rare or absent, augite and pigeonite are typical pyroxenes that commonly coexist, and pyroxferroite may form during late-stage rapid crystallization of Fe-enriched melt.[190]

Feldspar-group minerals are common rock-forming minerals in the crust of terrestrial bodies, e.g., Earth, Mars, and the Moon, and they include the plagioclase and alkali feldspar series of minerals.[194] Plagioclase feldspar commonly consists of a solid solution of  $\text{CaAl}_2\text{Si}_2\text{O}_8$  (anorthite, An) and  $\text{NaAlSi}_3\text{O}_8$  (albite, Ab), and alkali feldspars commonly have a composition of  $\text{NaAlSi}_3\text{O}_8$  to  $\text{KAlSi}_3\text{O}_8$ .[194] The plagioclase and alkali feldspar series both have members that have different structural states.[194] For many lunar rocks, calcic plagioclase is the major feldspar mineral

with compositions typically ranging from  $\sim\text{An}_{65}$  to  $\text{An}_{98}$ , and alkali feldspar is commonly a minor mineral.[181]

Ilmenite ( $\text{FeTiO}_3$ ) is an abundant oxide mineral in lunar samples, especially in lunar mare basalts. Ilmenite in lunar mare basalts contains up to  $\sim 6$  wt.% MgO.[190] The distribution of Mg between ilmenite and coexisting silicate minerals may provide information on the crystallization sequence of minerals from a melt. Ilmenite may be associated with other Fe- and/or Ti-bearing minerals, and these various mineral associations can provide information on oxygen fugacities and temperatures during the formation of these phases.[195, 196] Troilite ( $\text{FeS}$ ) commonly occurs as a late-stage crystallization product in mare basalts, and its presence is consistent with the highly-reducing, low-oxygen characteristics of lunar magmas and post-crystallization lunar environment.[190]

In this chapter, we investigated two polished thin sections of two lunar meteorites that had been found in the LaPaz Icefield (LAP) of Antarctica. Lunar meteorite LAP 02205 was found during the 2002 Antarctic Search for Meteorites (ANSMET) field season[184, 193] and lunar meteorite LAP 04841 was found during the 2004 ANSMET field season[197]. LAP 02205 and LAP 04841 are both unbrecciated mare basalts[184, 193, 197], so they represent a relatively rare type of lunar meteorite [191]. When collected, LAP 02205 had a mass[184] of 1226 g making it the largest known mare-basalt meteorite[193], and LAP 04841 had a mass of 60 g.[197] LAP 04841 is most likely paired with LAP 02205[197], meaning that the two rocks were most likely part of the same meteoroid prior to atmospheric entry.

Mineralogy and mineral chemistry clearly indicate a lunar origin for LAP 02205[193, 198-200] and LAP 04841[197]. Modal mineralogy, texture, and mineral

chemistry have been well-characterized for LAP 02205[193, 198-200] and LAP 04841[197]. LAP 02205 and LAP 04841 are unbrecciated, coarse-grained, holocrystalline basalts, and according to the scheme of Neal and Taylor[186], the meteorites are classified as low-titanium (Ti) mare basalts.[193, 197] Pyroxene ranges from 43.9 to 56.9 modal percent in LAP 02205[193, 198] and it comprises 56.2 modal percent of LAP 04841[197]. Plagioclase feldspar ranges from 33.1 to 45.3 modal percent in LAP 02205[193, 198] and it comprises 31.9 modal percent of LAP 04841[197] Pyroxene and plagioclase feldspar together comprise ~90 and ~88 modal percent of LAP 02205[193, 198] and LAP 04841[197], respectively. Electron microprobe analysis of LAP 02205 and LAP 04841 shows that most of the pyroxene grains are chemically zoned (core to rim) with pigeonite (relatively high Mg) in the core transitioning to augite, ferropigeonite and ferroaugite (ferroproxene), and finally to very Fe-rich rims, some of which have compositions of pyroxferroite.[193, 197-200] Electron microprobe analysis of plagioclase feldspar grains show compositional variation from An<sub>81</sub> to An<sub>91</sub> for both LAP 02205[199] and LAP 04841[197]. For LAP 02205, electron microprobe analysis shows that plagioclase feldspar is zoned from cores of An<sub>90</sub> composition to rims of An<sub>85</sub> composition.[198] Ilmenite is by far the major oxide mineral ranging from 2.74 to 3.7 modal percent in LAP 02205[193, 198, 199] and comprising 3.34 modal percent of LAP 04841[197]. Electron microprobe analysis shows low contents of MgO in ilmenite, up to 0.24 wt.% for LAP 02205[193, 198, 199], and up to 0.13 wt.% for LAP 04841[197]. Troilite comprises up to 1.4 modal percent in LAP 02205[193, 198] and occurs in trace amounts in LAP 04841[197]. Lunar meteorites LAP 02205 and LAP 04841 both show several types of shock-metamorphic effects.[193, 197-199] The level of shock metamorphism in LAP

02205 and LAP 04841 is quite variable, even on the scale of a thin section[197], so estimates of shock pressures show a wide range from ~10 GPa up to ~50 GPa, with localized shock pressures perhaps exceeding 60 GPa[197-199].

Given these chemical species of interest within lunar meteorites, Raman microspectroscopic imaging can be employed for the investigation of extraterrestrial materials[44] for planetary science applications as well as in a variety of other disciplines, ranging from pharmaceuticals to material sciences[49, 106, 201-205]. Raman microspectroscopic imaging is primarily employed in order to collect spatially-resolved chemical information about a sample. By providing multidimensional analytical information, Raman microspectroscopic imaging can spatially and spectrally characterize materials with unique advantages, including high specificity, molecular fingerprinting ability, low sensitivity to water, and high sampling versatility with limited preparation.[5, 40, 49] Furthermore, Raman microspectroscopic imaging centers on the ability to collect Raman spectra at defined locations within a sample, and thus, hundreds to millions of independent, spatially-resolved spectra can be accumulated using this technique.[5, 40] These extensive data sets ultimately allow for the visualization of chemical, molecular, and structural information about a sample.

The analysis of Raman microspectroscopic imaging data subsequent to its collection is essential for the ability of this technique to provide spatially-resolved chemical and molecular information. The analysis of Raman microspectroscopic imaging data is traditionally performed using univariate methods, in which “heat” or intensity maps are generated based on the integration or amplitude of a characteristic Raman band of a known analyte of interest. By using univariate methods, however, interference effects can significantly impact the data and its analysis.[50-52]

Moreover, if a sample is a mixture of chemical species containing either a potentially unknown composition or overlapping spectral features, univariate methods can provide a limited analysis that could ultimately allow for critical chemical information to go unnoticed and unused.[50-52] Additionally, other interference effects commonly observed in Raman microspectroscopic imaging data that univariate methods frequently fail to overcome are background interference, fluorescence, laser power fluctuation, loss of focus, sample roughness, sample opacity, and optical alignment.[50-52] Multivariate and chemometric analysis methods, however, can address these interference effects, and provide increased sensitivity, increased selectivity, enhanced visualization, and significant data reduction when used in conjunction with Raman microspectroscopic imaging.[50-52] Thus, multivariate analysis methods applied to Raman microspectroscopic imaging data can be used to both identify the chemical species present within an unknown sample and discern a representative distribution of the individual, pure chemical species.[50, 53-55]

A variety of multivariate methods have been used to analyze Raman microspectroscopic imaging data, including multivariate curve resolution-alternating least squares (MCR-ALS), principal component analysis (PCA), cluster analysis, neural networks, partial least squares (PLS), and direct classical least squares (DCLS).[50, 56-58] Specifically, MCR-ALS has recently gained momentum due to its ability to provide spatially- and spectrally-resolved chemical information from Raman microspectroscopic imaging data using a simple, additive bilinear model of pure contributions.[55, 61, 65] Unlike other multivariate analysis methods, the results of MCR-ALS applied to Raman microspectroscopic imaging data can be evaluated by both spectroscopists and chemometricians.[55, 61] By using the straightforward MCR-

ALS algorithm with Raman microspectroscopic imaging, spatially-resolved chemical images and corresponding resolved Raman spectra of the individual, pure chemical species within a complex, unknown sample can be generated.

In this chapter, we present the results of an initial investigation of lunar meteorites LAP 02205 and LAP 04841 that was accomplished using Raman microspectroscopic imaging in conjunction with MCR-ALS. Spatially-resolved chemical images and corresponding resolved Raman spectra of the individual chemical species within distinct areas of both lunar meteorites were generated using MCR-ALS with Raman microspectroscopic imaging. Polarized light microscopy was employed to initially determine the heterogeneity of the lunar meteorites with respect to particle size, shape, and composition. MCR-ALS with Raman microspectroscopic imaging was subsequently utilized to elucidate the chemical properties of distinct areas within both LAP 02205 and LAP 04841. To the best of our knowledge, this is the *first* report of MCR-ALS with Raman microspectroscopic imaging applied to lunar or other types of meteorites. Overall, we demonstrate and evaluate the effectiveness of multivariate analysis methods with microspectroscopic chemical imaging to investigate mineralogically heterogeneous meteorites.

### **5.3 Materials and Methods**

#### **5.3.1 Materials and Sample Preparation**

Polished thin sections LAP 02205,51 and LAP 04841,18 from the two lunar meteorites LAP 02205 and LAP 04841, respectively, were kindly provided by the Meteorite Working Group (MWG) and the NASA Johnson Space Center. Polished

thin sections LAP 02205,51 and LAP 04841,18 have surface areas of  $\sim 0.45 \text{ cm}^2$  and  $\sim 1.35 \text{ cm}^2$ , respectively. The samples are flat, cross-sectional representations of the given meteorite, in which the surface of the meteorite was fully exposed and the total sample depth was  $\sim 30\text{-}40 \text{ }\mu\text{m}$ . All sample preparation was performed by the MWG at the NASA Johnson Space Center. In brief, a portion of the meteorite is mounted in epoxy and polished to produce a flat surface. This flat, polished surface is subsequently fixed to a glass substrate using epoxy. The meteorite sample is then cut to a thickness of  $\sim 100 \text{ }\mu\text{m}$  such that the newly prepared surface is parallel to the glass substrate. The meteorite is then polished to a final thickness of  $\sim 30\text{-}40 \text{ }\mu\text{m}$  and has a flat, polished upper surface. Overall, the polished thin section contains a cross-sectional representation of the lunar meteorite, in which the meteorite is fixed to a glass substrate with epoxy.

### **5.3.2 Polarized Light Microscopy**

A SZM1500 stereomicroscope (Nikon) was used for the collection of all polarized light images. Both plane polarized and cross polarized optical images were collected. A magnification ranging from  $0.75\times$  to  $11.25\times$  was utilized for polarized light microscopy measurements.

### **5.3.3 Raman Microspectroscopic Imaging**

A Senterra Raman spectrometer (Bruker Optics) coupled to a BX-51 optical microscope (Olympus) was used for all Raman microspectroscopic imaging measurements. Both 532 nm and 785 nm excitation sources were used for Raman microspectroscopic imaging measurements. For the respective excitation source, the laser was focused onto the sample using a  $20\times$  (0.40 numerical aperture, NA) or a  $50\times$

(0.75 NA) close-working-distance objective lens (Olympus). The laser spot size resulting from 20× and 50× magnification was  $\sim 5 \mu\text{m}$  and  $\sim 2 \mu\text{m}$  in diameter, respectively. After excitation of the sample, scattered light was collected by the objective lens, filtered by a 50 x 1000  $\mu\text{m}$  slit aperture, and dispersed by a 1200 grooves/mm grating onto a thermoelectrically-cooled charge-coupled device (CCD) detector held at a temperature of  $-65 \text{ }^\circ\text{C}$ . For 532 and 785 nm excitations, the spectral ranges were 70 to 1550  $\text{cm}^{-1}$  and 80 to 1525  $\text{cm}^{-1}$ , respectively. These spectral ranges were both covered under one grating position.

A constant nominal power of either 5 or 10 mW was used for 532 nm excitation Raman microspectroscopic imaging measurements, and a constant nominal power of either 25 or 50 mW was used for 785 nm excitation Raman microspectroscopic imaging measurements. This laser power was applied to the sample's surface for all Raman microspectroscopic imaging measurements. Integration times of 5 to 10 seconds with 3 co-averages were employed for Raman microspectroscopic imaging measurements. During Raman microspectroscopic imaging, a background measurement was collected prior to each Raman spectral acquisition, in which the background measurement contained an integration time equal to that of the respective Raman spectral acquisition. A total collection time of 30 to 60 seconds was utilized for each Raman spectral acquisition. Raman shift and source wavelength calibration were internally performed using a neon lamp. A spectral resolution of 3 to 5  $\text{cm}^{-1}$  was achieved for all Raman microspectroscopic imaging measurements.

A grid containing the selected locations of Raman spectral acquisition was generated for Raman microspectroscopic imaging measurements. These grids, which

were rectangular in shape, were positioned on specific locations of interest of the respective lunar meteorite sample. Moreover, the grids were generated in a 20 by 20 spectral arrangement with a step-size between spectra of  $\sim 5 \mu\text{m}$ . Thus, each grid contained a total of 400 Raman spectral acquisition points. An automated sample stage was utilized to controllably define specific x and y positions on the sample to collect Raman spectra. The height, or z direction, of the sample stage was held constant during Raman microspectroscopic imaging measurements. The OPUS 7.2 program (Bruker Optics) was used for the collection of all Raman microspectroscopic imaging data.

#### 5.3.4 Multivariate Curve Resolution-Alternating Least Squares (MCR-ALS)

The analysis of Raman microspectroscopic imaging data was performed using the multivariate self-modeling mixture analysis method of MCR-ALS. Using MCR-ALS in conjunction with Raman microspectroscopic imaging allows for the generation of spatially-resolved chemical images and corresponding resolved Raman spectra of the individual chemical species within a given sample area. Furthermore, MCR-ALS provides a unique advantage due to its ability to spatially and spectrally resolve chemical information about a heterogeneous, unknown sample. Mathematically, MCR-ALS decomposes the experimental data matrix,  $\mathbf{D}$ , as follows:

$$\mathbf{D} = \mathbf{C}\mathbf{S}^T + \mathbf{E} \quad (5.1)$$

where  $\mathbf{C}$  is the concentration profile matrix,  $\mathbf{S}^T$  is the resolved spectral matrix, and  $\mathbf{E}$  is the residual error matrix. Using a variety of multivariate techniques, including principal component analysis (PCA), or prior knowledge of the chemical species, the number of components contributing to  $\mathbf{D}$  can be determined. After providing an initial estimation, the calculation and iterative optimization of  $\mathbf{C}$  and  $\mathbf{S}^T$  are accomplished

using ALS until convergence is reached. During the ALS calculation, constraints of physically meaningful origin can be applied to readily guide the solution. With Raman microspectroscopic imaging, these constraints are typically the non-negative concentrations and non-negative spectral intensities due to the fact that the concentration of a particular chemical species within each pixel and the intensity of the scattered radiation should not be negative.

In this chapter, the Raman microspectroscopic imaging data, which initially contained a three-dimensional matrix consisting of spatial information (x and y) and spectral information ( $\text{cm}^{-1}$ ) was unfolded into a two-dimensional experimental data matrix,  $\mathbf{D}$ . Furthermore, each row in  $\mathbf{D}$  is the intensity at various wavenumbers. The number of components was selected prior to ALS using initial estimates from PCA, or by comparison of resolved Raman spectra, in  $\mathbf{S}^T$ , with Raman spectra of reference materials. An initial estimation of  $\mathbf{S}^T$  was determined prior to ALS using distance criteria, in which the first Raman spectrum for initialization was selected to be furthest from the mean, and subsequent Raman spectra were selected to be furthest from the mean and all prior selected Raman spectra. The physically meaningful constraints of non-negative concentration and non-negative spectral intensity were both employed during ALS. A convergence of 0.01% was achieved for all MCR-ALS models. MCR-ALS methods were utilized in Matlab 7.12 (MathWorks) with the Matlab toolbox by Jaumot et al.[162] and the PLS Toolbox (Eigenvector Research) to generate both the concentration profile matrix,  $\mathbf{C}$ , and the resolved spectral matrix,  $\mathbf{S}^T$ . The final concentration profile matrix,  $\mathbf{C}$ , was reconstructed in Matlab 7.12 to form chemical images for each respective resolved component. These chemical images were subsequently visualized using OriginPro (Origin Lab v9.1 Pro). The final spectral

matrix,  $\mathbf{S}^T$ , contains the resolved Raman spectrum for each chemical species. These resolved Raman spectra were visualized using OriginPro.

MCR-ALS was performed using the spectral range of 200 to 1550  $\text{cm}^{-1}$  for 532 nm excitation and 200 to 1525  $\text{cm}^{-1}$  for 785 nm excitation. Prior to MCR-ALS analysis, preprocessing was performed on the Raman microspectroscopic imaging data using an asymmetric least squares baseline correction[163] to remove all variation in the Raman spectra unrelated to chemical species. Moreover, the asymmetric least squares baseline correction is an iterative method based on fitting the spectral baseline using a Whittaker smoother, and is both fast and flexible with the large data sets generated from Raman microspectroscopic imaging.[55, 163] No other preprocessing was performed prior to MCR-ALS analysis.

## 5.4 Results and Discussion

### 5.4.1 Polarized Light Microscopy of Lunar Meteorites LAP 02205 and LAP 04841

An initial investigation of polished thin sections LAP 02205,51 and LAP 04841,18 using polarized light microscopy was performed. Plane polarized images of LAP 02205 and LAP 04841 (**Figures 5.1a** and **5.1c**, respectively) and cross polarized images of LAP 02205 and LAP 04841 (**Figures 5.1b** and **5.1d**, respectively) display the mineral heterogeneity of these lunar meteorites. The polarized light images of LAP 02205 (**Figures 5.1a** and **5.1b**) show features within the meteorite consistent with previous studies.[193] For example, the high modal abundance of pyroxene (56.9%) and plagioclase feldspar (33.1%) within LAP 02205[193] was observed in the polarized light images. Polarized light images of LAP 02205 (**Figures 5.1a** and **5.1b**)

also provided insight into the structural and chemical variation amongst these abundant chemical species, including an initial differentiation of pyroxene, plagioclase feldspar, and ilmenite within LAP 02205. Moreover, polarized light images of LAP 02205 (**Figures 5.1a** and **5.1b**) display that this sample contains polydispersed micrometer-sized particles of various shapes. Specifically, pyroxenes within LAP 02205 are  $\sim 100$  to  $1000 \mu\text{m}$  in size and show diverse shapes, including rectangular-, oval-, and circular-shaped crystals. Due to the contrasting nature of plane polarized and cross polarized images, the chemical and structural heterogeneity of the major chemical species was observed for LAP 02205.

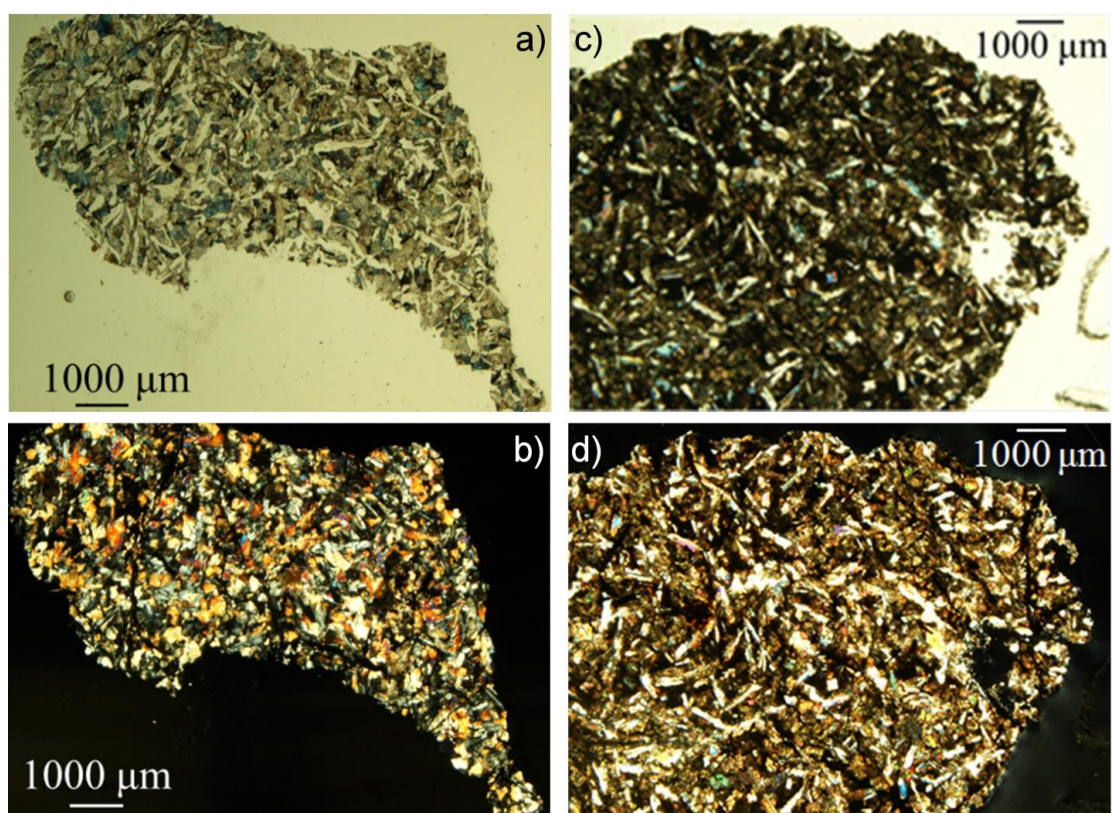


Figure 5.1: Polarized light microscopy images of LAP 02205 (a/b) and LAP 04841 (c/d).

Similarly, as shown by the polarized light images (**Figures 5.1c and 5.1d**), LAP 04841 displays a high degree of heterogeneity. Again, the polarized light images of LAP 04841 (**Figures 5.1c and 5.1d**) display features within the meteorite consistent with previous studies.[197] Specifically, the high modal abundance of both pyroxene (56.2%) and plagioclase feldspar (31.9%) within LAP 04841[197], similar to the respective abundance of these phases in LAP 02205[193], was observed using polarized light microscopy. As with LAP 02205, LAP 04841 displays polydispersed micrometer-sized particles of various shapes, including pyroxenes ranging in size from ~100 to 1000  $\mu\text{m}$  and having rectangular and elongated shapes. The polarized light images of LAP 04841 (**Figures 5.1c and 5.1d**) display the general heterogeneity and complexity of the chemical species within this lunar meteorite. Overall, using polarized light microscopy, both lunar meteorites—LAP 02205 and LAP 04841—display high heterogeneity and are comprised of polydispersed, micrometer-sized particles of various shapes and diverse chemical properties.

#### **5.4.2 Multivariate Curve Resolution-Alternating Least Squares (MCR-ALS) with Raman Microspectroscopic Imaging of Lunar Meteorite LAP 02205**

The modal abundances of the varying chemical species within lunar meteorite LAP 02205 show that undifferentiated pyroxene (56.9%) and plagioclase feldspar/maskelynite (33.1%) comprise most of this sample.[193] Maskelynite is a shock-induced diaplectic glass formed from plagioclase feldspar[197], and in LAP 02205, the plagioclase feldspar shows only partial conversion to maskelynite.[193] Raman spectroscopy has previously been employed for the characterization of pyroxenes, including distinguishing the three general structural types of quadrilateral pyroxenes, i.e., orthorhombic (orthopyroxene), monoclinic (clinopyroxene), and

triclinic (pyroxenoid).[30, 44, 181, 182, 206, 207] A detailed discussion of using Raman spectroscopy, including detailed interpretation of Raman spectra, relative intensities, Raman spectral patterns, and Raman band locations, for the characterization of the structural types and chemical compositions of the quadrilateral pyroxenes is given in Wang et al.[182]. We present some of the key results needed for the identification and differentiation of quadrilateral pyroxenes using Raman microspectroscopic imaging in the following discussion.

A key spectral region within the Raman spectra of pyroxenes is  $\sim 200$  to  $1100\text{ cm}^{-1}$ . Specifically, in the  $600\text{-}800\text{ cm}^{-1}$  spectral region, Raman spectra for orthorhombic pyroxenes show two bands (a doublet) near  $\sim 670\text{ cm}^{-1}$ . [182] Similar results have also been reported [30, 181, 206, 207] that show this doublet to commonly consist of Raman bands near  $\sim 660\text{ cm}^{-1}$  and  $\sim 678/683\text{ cm}^{-1}$ . Within this same spectral region ( $600\text{-}800\text{ cm}^{-1}$ ), clinopyroxenes (monoclinic) with space group  $C2/c$ , in contrast to orthopyroxenes, have only a single major Raman band near  $\sim 670\text{ cm}^{-1}$  [182], and again, similar results have been reported extensively in the literature. [30, 181, 206, 207] Like the monoclinic pyroxenes, Raman spectra for triclinic pyroxenoids have a single major band in the  $600\text{-}800\text{ cm}^{-1}$  spectral region, but this band commonly occurs at frequencies somewhat lower than  $\sim 660\text{ cm}^{-1}$ . [182] Furthermore, other Raman band positions for the triclinic pyroxenoids are shifted to lower wavenumbers as compared to those for clinopyroxenes and orthopyroxenes, such that the band positions for pyroxferroite are  $\sim 10\text{-}20\text{ cm}^{-1}$  lower than those for augite. [182] For the quadrilateral pyroxenes, only the major cations  $\text{Mg}^{2+}$ ,  $\text{Fe}^{2+}$ , and  $\text{Ca}^{2+}$  have a significant effect on the Raman band positions. [182] For the Raman spectra of quadrilateral pyroxenes, the most useful bands for estimating cation ratios appear to be those that occur near  $\sim 1000$

$\text{cm}^{-1}$ ,  $\sim 670 \text{ cm}^{-1}$ , and  $\sim 325 \text{ cm}^{-1}$ . [182] The positions of these Raman bands shift to higher frequencies with an increase in molar ratio of  $\text{Mg}^{2+}$ . [182] A similar pattern in the shift of frequencies of Raman band positions as a function of the molar ratio of  $\text{Mg}^{2+}$  was reported for several bands in both orthopyroxenes and clinopyroxenes. [206, 207] These shifts in Raman band positions appear to be more sensitive for orthopyroxenes as compared to clinopyroxenes. [206, 207]

The vibrational modes of pyroxenes, including Raman active vibrational modes, producing these key spectral features have been extensively studied. [182, 208-210] In this chapter, monoclinic pyroxenes, termed clinopyroxenes, will be the primary focus. Per factor group analysis, monoclinic pyroxenes of the space group  $C2/c$  display 57 optical vibrational modes, in which 30 are Raman active. [182] Of these 30 Raman active modes, typically 3 to 10 Raman bands are observed for most naturally occurring monoclinic pyroxenes. [30, 181, 182] Specifically, these major Raman bands detected within monoclinic pyroxenes are as follows: the symmetric stretching mode of the Si-O bond containing nonbridging oxygen within  $[\text{SiO}_4]^{4-}$  subunits at  $\sim 1000 \text{ cm}^{-1}$  ( $A_g$ ), the symmetric stretching mode of Si-O-Si bonds containing bridging oxygen at  $\sim 670 \text{ cm}^{-1}$  ( $A_g$ ), and crystal lattice modes resulting from translational motion of the cations in the lower wavenumber spectral region ( $\sim 300\text{-}400 \text{ cm}^{-1}$ ). [182] It is clear, therefore, that Raman spectroscopy provides a valuable tool for investigating the nature of pyroxenes, including those in lunar samples. [30, 44, 181, 182]

In addition to pyroxenes, ilmenite ( $\text{FeTiO}_3$ ) has a modal abundance of 3.3% within LAP 02205. [193] Ilmenite contains a hexagonal close-packed oxygen framework with Fe and Ti cations ordered among the two-thirds-filled octahedral

sites, and has ten predicted Raman active vibrational modes— $5A_g + 5E_g$ . [211, 212] Moreover, the major bands observed in the Raman spectrum of ilmenite are assigned as follows— $226\text{ cm}^{-1}$  ( $A_g$ ),  $370\text{ cm}^{-1}$  ( $A_g$ ), and  $679\text{ cm}^{-1}$  ( $A_g$ ). Moreover, the intense Raman band at  $679\text{ cm}^{-1}$  corresponds to the symmetric stretching vibration of  $\text{Ti}^{4+}\text{O}_6$  octahedra. [211] Given that the Raman spectra and Raman active modes of both pyroxene [30, 181, 182, 206, 207] and ilmenite [211, 212] have been reported, Raman microspectroscopic imaging can provide a valuable tool for investigating the nature of both pyroxenes and ilmenite in lunar samples. [44] Additionally, given the importance of both chemical species within lunar meteorites, distinct probing areas of LAP 02205 that contain pyroxene and ilmenite were investigated using Raman microspectroscopic imaging with multivariate curve resolution-alternating least squares (MCR-ALS).

Spatially-resolved chemical images (**Figures 5.2b, 5.2c, and 5.2d**) and corresponding resolved Raman spectra (**Figures 5.2b, 5.2c, and 5.2d**) of a probed area (**Figure 5.2a**) of LAP 02205 were generated using MCR-ALS applied to Raman microspectroscopic imaging. The mean (in black; **Figure 5.2a**) and standard deviation (+ in red, - in blue; **Figure 5.2a**) of the 400 total Raman spectra accumulated over the probed area (**Figure 5.2a**) show the presence of pyroxene, substrate-adhesive epoxy, and diamond-polish. This is illustrated by the mean spectrum displaying major Raman bands at  $393\text{ cm}^{-1}$ ,  $665\text{ cm}^{-1}$ , and  $1002\text{ cm}^{-1}$  characteristic of pyroxene, major Raman bands at  $640\text{ cm}^{-1}$ ,  $823\text{ cm}^{-1}$ ,  $1002\text{ cm}^{-1}$ ,  $1113\text{ cm}^{-1}$ ,  $1186\text{ cm}^{-1}$ , and  $1462\text{ cm}^{-1}$  characteristic of substrate-adhesive epoxy, and a major Raman band at  $1332\text{ cm}^{-1}$  characteristic of diamond-polish. Using a five component MCR-ALS model, three chemically meaningful components were resolved—diamond-polish, monoclinic-structured pyroxene (clinopyroxene), and substrate-adhesive epoxy. The first resolved

Raman spectrum (**Figure 5.2b**) shows a major Raman band at  $1333\text{ cm}^{-1}$  indicative of diamond-polish. Detailed descriptions of the Raman spectra of diamond and diamond-polish are given in Solin et al.[213] and Nasdala et al.[214], respectively. In brief, diamond displays a major Raman band at  $\sim 1332\text{ cm}^{-1}$  within the spectral region covered in this chapter, and this band corresponds to the overlap of three zone-center phonons—one longitudinal and two transverse optical modes—of  $F_{2g}$  symmetry.[213, 214] The second resolved Raman spectrum (**Figure 5.2c**) shows major Raman bands at  $324\text{ cm}^{-1}$ ,  $389\text{ cm}^{-1}$ ,  $532\text{ cm}^{-1}$ ,  $661\text{ cm}^{-1}$ ,  $995\text{ cm}^{-1}$ , and  $1007\text{ cm}^{-1}$  indicative of clinopyroxene. The third resolved Raman spectrum (**Figure 5.2d**) shows major Raman bands at  $640\text{ cm}^{-1}$ ,  $822\text{ cm}^{-1}$ ,  $1003\text{ cm}^{-1}$ ,  $1113\text{ cm}^{-1}$ ,  $1185\text{ cm}^{-1}$ ,  $1298\text{ cm}^{-1}$ , and  $1462\text{ cm}^{-1}$  characteristic of substrate-adhesive epoxy. Moreover, these seven major Raman bands closely match those reported for epoxy.[124, 125] A more detailed description and interpretation of Raman spectra for epoxy, including Raman active modes, is given in Chike et al.[125] and Lyon et al.[124].

The distributions of these resolved chemical species, in the form of spatially-resolved chemical images (**Figures 5.2b, 5.2c, and 5.2d**), were generated using MCR-ALS with Raman microspectroscopic imaging. Specifically, diamond-polish is localized (**Figure 5.2b**) within the fracture/veinlet feature within the probed area. This fracture/veinlet feature appears dark in the optical image (**Figure 5.2a**). The distribution of clinopyroxene (**Figure 5.2c**) displays that clinopyroxene is the predominant chemical species within the probed area, as clinopyroxene is spatially distributed throughout this entire area except for the fracture/veinlet feature. The spatial distribution of substrate-adhesive epoxy (**Figure 5.2d**) shows that the substrate-

adhesive epoxy is located throughout the entire probed area, with high concentrations within the fracture/veinlet feature as well as along the right portion of the probed area.

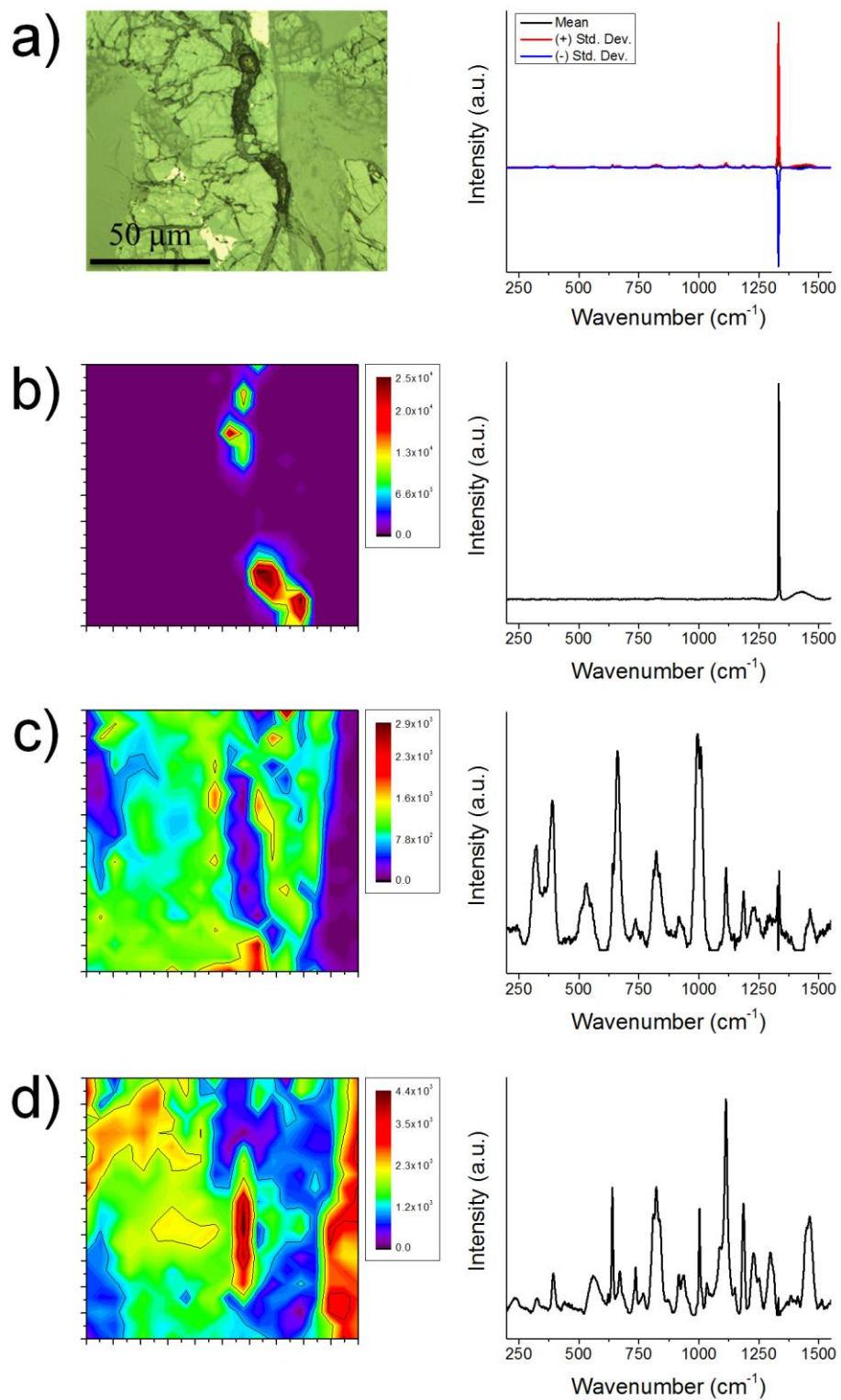


Figure 5.2: Results of MCR-ALS applied to Raman microspectroscopic imaging using 532 nm excitation of LAP 02205. Spatially-resolved chemical images and corresponding resolved Raman spectra of diamond-polish (b), pyroxene (c), and substrate-adhesive epoxy (d) are shown. The optical image (a) and mean spectrum (black, a) +/- the standard deviation (+ in red, - in blue; a) are shown. A five-component MCR-ALS model was employed.

Another location within LAP 02205 was analyzed using Raman microspectroscopic imaging with multivariate analysis methods (**Figure 5.3**). The resulting spatially-resolved chemical images (**Figures 5.3b, 5.3c, and 5.3d**) and corresponding resolved Raman spectra (**Figures 5.3b, 5.3c, and 5.3d**) were generated from MCR-ALS applied to Raman microspectroscopic imaging of the probed area displayed in the optical image (**Figure 5.3a**). The mean (in black; **Figure 5.3a**) and standard deviation (+ in red, - in blue; **Figure 5.3a**) of the 400 total Raman spectra collected over this probed area demonstrate that ilmenite, pyroxene, and substrate-adhesive epoxy are present. Specifically, the mean spectrum of the Raman microspectroscopic imaging data displays primary bands with corresponding chemical species as follows: 226  $\text{cm}^{-1}$  (ilmenite), 370  $\text{cm}^{-1}$  (ilmenite), 678  $\text{cm}^{-1}$  (ilmenite), 822  $\text{cm}^{-1}$  (substrate-adhesive epoxy), 992  $\text{cm}^{-1}$  (pyroxene), 1112  $\text{cm}^{-1}$  (substrate-adhesive epoxy), 1185  $\text{cm}^{-1}$  (substrate-adhesive epoxy) and 1378  $\text{cm}^{-1}$  (epoxy/substrate-adhesive epoxy). Using a three component MCR-ALS model, three chemically meaningful components were resolved—ilmenite, clinopyroxene, and substrate-adhesive epoxy. The first resolved Raman spectrum (**Figure 5.3b**) shows major Raman bands at 226  $\text{cm}^{-1}$ , 370  $\text{cm}^{-1}$ , and 679  $\text{cm}^{-1}$  characteristic of ilmenite. The second resolved Raman spectrum (**Figure 5.3c**) shows major Raman bands at 318  $\text{cm}^{-1}$ , 354  $\text{cm}^{-1}$ , 387  $\text{cm}^{-1}$ , 536  $\text{cm}^{-1}$ , 663  $\text{cm}^{-1}$ , and 993  $\text{cm}^{-1}$  characteristic of

clinopyroxene. The third resolved Raman spectrum (**Figure 5.3d**) shows major Raman bands at  $640\text{ cm}^{-1}$ ,  $822\text{ cm}^{-1}$ ,  $1113\text{ cm}^{-1}$ ,  $1185\text{ cm}^{-1}$ , and  $1225\text{ cm}^{-1}$  characteristic of substrate-adhesive epoxy. Furthermore, the resolved Raman spectrum of substrate-adhesive epoxy (**Figure 5.3d**) also displays a high-intensity, broad Raman band at  $1378\text{ cm}^{-1}$  characteristic of the glass substrate.

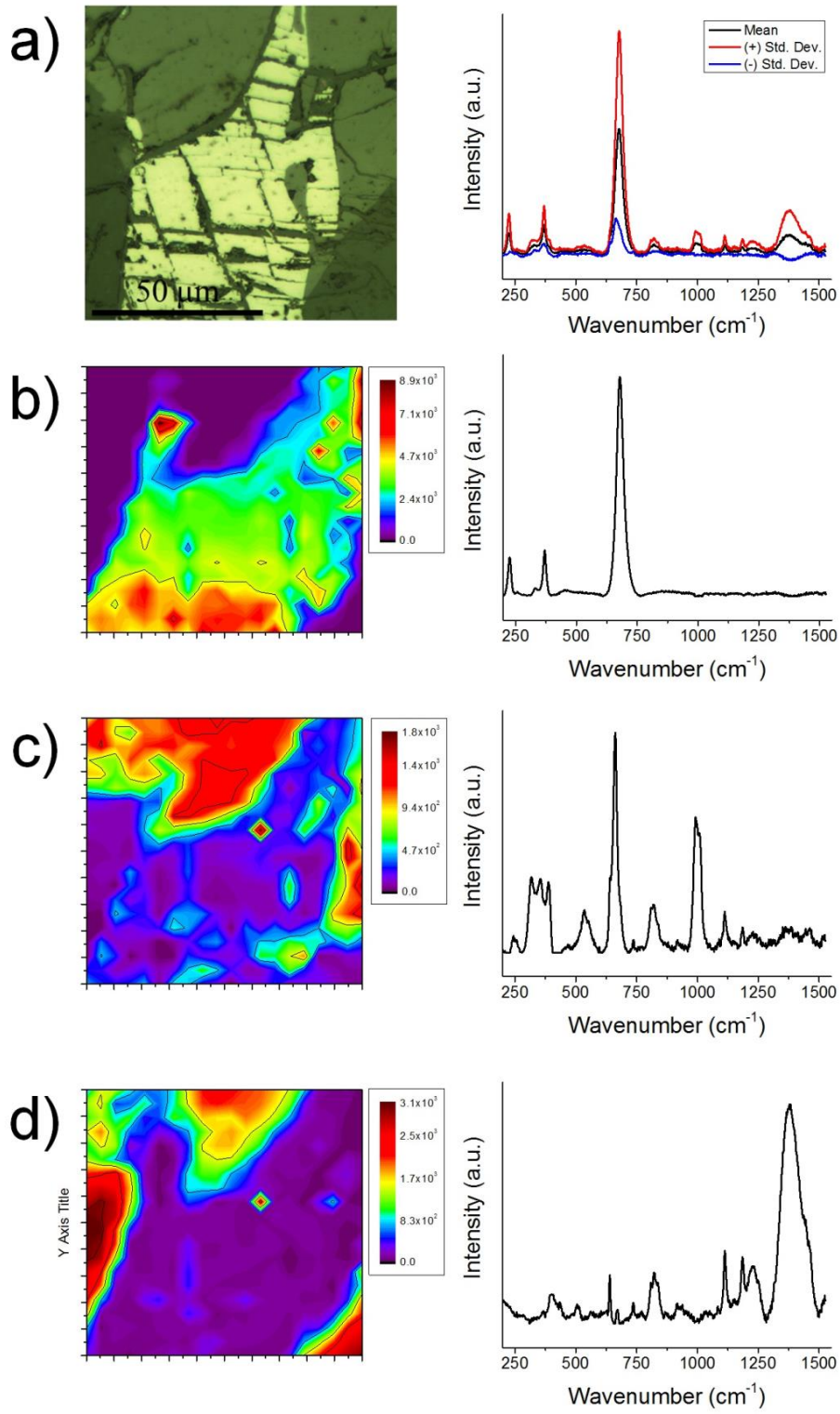


Figure 5.3: Results of MCR-ALS applied to Raman microspectroscopic imaging using 785 nm excitation of LAP 02205. Spatially-resolved chemical images and corresponding resolved Raman spectra of ilmenite (b), pyroxene (c), and substrate-adhesive epoxy (d) are shown. The optical image (a) and mean spectrum (black, a) +/- the standard deviation (+ in red, - in blue; a) are shown. A three-component MCR-ALS model was employed.

The spatial distributions of the resolved chemical species (**Figures 5.3b, 5.3c, and 5.3d**) were also generated using MCR-ALS applied to Raman microspectroscopic imaging of the probed area shown in the optical image (**Figure 5.3A**). The distribution of ilmenite (**Figure 5.3b**) shows that this chemical species occupies a large amount of the probed area, with a higher concentration towards the lower portion of this area. The distribution of clinopyroxene (**Figure 5.3c**) shows that clinopyroxene is located towards the top and right portions of the probed area in fashion complementary to that of ilmenite. The spatial distribution of substrate-adhesive epoxy (**Figure 5.3d**), which is also influenced by glass (1378  $\text{cm}^{-1}$  band in the resolved Raman spectrum of **Figure 5.3d**), shows that the substrate-adhesive epoxy is located towards the top-left and bottom-right portions of the probed area in a similar fashion to that of clinopyroxene.

#### **5.4.3 Multivariate Curve Resolution-Alternating Least Squares (MCR-ALS) with Raman Microspectroscopic Imaging of Lunar Meteorite LAP 04841**

The modal abundances of the varying chemical species within lunar meteorite LAP 04841 show that undifferentiated pyroxene (56.2%) and plagioclase feldspar/maskelynite (31.9%) comprise most of this sample.[197] These values are quite similar to their respective values in LAP 02205.[193] In addition to pyroxenes[182, 206, 207], Raman spectroscopy can also readily characterize plagioclase feldspars[194], including distinguishing calcic plagioclase feldspar from

alkali feldspars in lunar samples.[30, 44, 181] Moreover, a Raman spectroscopic study of natural feldspar-group minerals having a wide range of compositions, crystal structures, and degrees of cation disorder concluded that ten types of feldspars can be classified using this technique alone, but that the cation compositions of the various feldspar phases could not be quantitatively determined using Raman band positions.[194]

The Raman active modes of plagioclase feldspar, including anorthite ( $\text{CaAl}_2\text{Si}_2\text{O}_8$ ), have been extensively investigated.[194, 209] Anorthite is a member of the plagioclase feldspar mineral group and belongs to the triclinic space group  $P\bar{1}$  at low temperatures.[209] Upon heating, anorthite can form high-temperature polymorphs, and specifically, it can transform to a high-temperature polymorph with a body-centered structure and a space group of  $I\bar{1}$ . [194] From factor-group analysis, 156  $A_g$  (Raman active) and 156  $A_u$  (infrared active) optical modes are predicted for anorthite.[209] Of these 156 predicted Raman active optical modes, anorthite typically displays only seven well-resolved Raman bands in the  $\sim 200$  to  $1550 \text{ cm}^{-1}$  spectral region[194], with the strongest Raman band being at  $\sim 505 \text{ cm}^{-1}$ . [194, 209] This band, which is characteristic of the plagioclase feldspar structure, is attributed to motion of the oxygen (O) atom along a line bisecting the T-O-T angle, where T represents either a Si or Al atom.[209, 215]

In LAP 04841, in contrast to the abundant pyroxene and plagioclase feldspar, troilite (FeS) has a modal abundance of  $<0.07\%$ . [197] In meteorites, troilite is the most common and abundant sulfide phase.[216] Troilite belongs to the  $P6_3/mmc$  space group and contains a NiAs-type structure with both the Fe and S atoms in a six-fold coordination.[216] Using Raman spectroscopy, Fe-rich sulfides, including troilite, are

difficult to identify and characterize.[216] Specifically, the Raman spectrum of troilite typically displays a low signal-to-noise ratio, and can be characterized by low-signal Raman bands within lower wavenumber regions, including bands at 160  $\text{cm}^{-1}$ , 290  $\text{cm}^{-1}$ , and 335  $\text{cm}^{-1}$ .[216] Moreover, a sample from the RRUFF database project documented to be troilite by electron microprobe analysis displays Raman spectra with very low signal-to-noise ratios and primary Raman bands at  $\sim 720 \text{ cm}^{-1}$  and  $\sim 840 \text{ cm}^{-1}$ .[126] The variation in the spectral location of these Raman bands is high due to the intense noise observed in the Raman spectra of troilite.

We here present the results of our investigation of pyroxenes, plagioclase feldspar (e.g., anorthite) and troilite in two probed areas of LAP 04841 using Raman microspectroscopic imaging in conjunction with MCR-ALS. Specifically, spatially-resolved chemical images (**Figures 5.4b, 5.4c, 5.4d, 5.4e, and 5.4f**) and corresponding resolved Raman spectra (**Figures 5.4b, 5.4c, 5.4d, 5.4e, and 5.4f**) of a probed area of LAP 04841, shown in the optical image (**Figure 5.4a**), were generated using MCR-ALS applied to Raman microspectroscopic imaging. The mean (in black; **Figure 5.4a**) and standard deviation (+ in red, - in blue; **Figure 5.4a**) of the 400 total Raman spectra accumulated over the probed area (**Figure 5.4a**) show the presence of pyroxene and substrate-adhesive epoxy. The mean Raman spectrum has major Raman bands at 327  $\text{cm}^{-1}$ , 394  $\text{cm}^{-1}$ , 667  $\text{cm}^{-1}$ , and 1010  $\text{cm}^{-1}$  characteristic of pyroxene and major Raman bands at 640  $\text{cm}^{-1}$ , 822  $\text{cm}^{-1}$ , 1113  $\text{cm}^{-1}$ , 1186  $\text{cm}^{-1}$ , and 1462  $\text{cm}^{-1}$  characteristic of substrate-adhesive epoxy. Using a five component MCR-ALS model, five chemically meaningful components were resolved—three clinopyroxenes, troilite, and substrate-adhesive epoxy. The first resolved Raman spectrum (**Figure 5.4b**) shows major Raman bands at 329  $\text{cm}^{-1}$ , 398  $\text{cm}^{-1}$ , 670  $\text{cm}^{-1}$ , and 1000  $\text{cm}^{-1}$  indicative of

clinopyroxene. The second resolved Raman spectrum (**Figure 5.4c**) shows major Raman bands at  $324\text{ cm}^{-1}$ ,  $360\text{ cm}^{-1}$ ,  $394\text{ cm}^{-1}$ ,  $666\text{ cm}^{-1}$ , and  $1010\text{ cm}^{-1}$  indicative of clinopyroxene. The third resolved Raman spectrum (**Figure 5.4d**) shows major Raman bands at  $320\text{ cm}^{-1}$ ,  $664\text{ cm}^{-1}$ , and  $1006\text{ cm}^{-1}$  indicative of clinopyroxene. The fourth resolved Raman spectrum (**Figure 5.4e**) shows major Raman bands at  $311\text{ cm}^{-1}$ ,  $345\text{ cm}^{-1}$ ,  $750\text{ cm}^{-1}$ , and  $823\text{ cm}^{-1}$ . On the basis of the presence of the lower wavenumber bands, the overall low signal-to-noise ratio of the spectrum, and comparison with the Raman spectra of troilite from the RRUFF database project[126], this resolved Raman spectrum (**Figure 5.4e**) is interpreted as that of troilite. The fifth resolved Raman spectrum (**Figure 5.4f**) shows major Raman bands at  $640\text{ cm}^{-1}$ ,  $823\text{ cm}^{-1}$ ,  $1113\text{ cm}^{-1}$ ,  $1186\text{ cm}^{-1}$ ,  $1228\text{ cm}^{-1}$ ,  $1299\text{ cm}^{-1}$ , and  $1463\text{ cm}^{-1}$  characteristic of substrate-adhesive epoxy.

The spatially-resolved chemical images (**Figures 5.4b, 5.4c, 5.4d, 5.4e, and 5.4f**) generated from MCR-ALS applied to Raman microspectroscopic imaging of the probed area (**Figure 5.4a**) of LAP 04841 highlight the distribution of the resolved chemical species. The distribution of the three clinopyroxenes (**Figures 5.4b, 5.4c, and 5.4d**) show that clinopyroxene is the dominant chemical species in this probed area of LAP 04841 and that the clinopyroxenes are distributed in a complementary fashion. Specifically, the first clinopyroxene (**Figure 5.4b**) is distributed primarily towards the bottom and center portions of the probed area. The second clinopyroxene (**Figure 5.4c**) is distributed towards the center and right portions of the probed area. The third clinopyroxene (**Figure 5.4d**) is distributed towards the left and bottom portions of the probed area in a more localized fashion than the other resolved clinopyroxenes. The three clinopyroxenes are thus distributed in a complementary

fashion with high concentrations towards the center of the probed area. The distribution of troilite (**Figure 5.4e**) is highly localized and it primarily occurs towards the left region of the probed area. This result is consistent with the very low modal abundance of troilite within LAP 04841.[197] The distribution of substrate-adhesive epoxy (**Figure 5.4f**) shows that this chemical species is prevalent throughout most of the probed area with higher concentrations towards the right portion of this area.

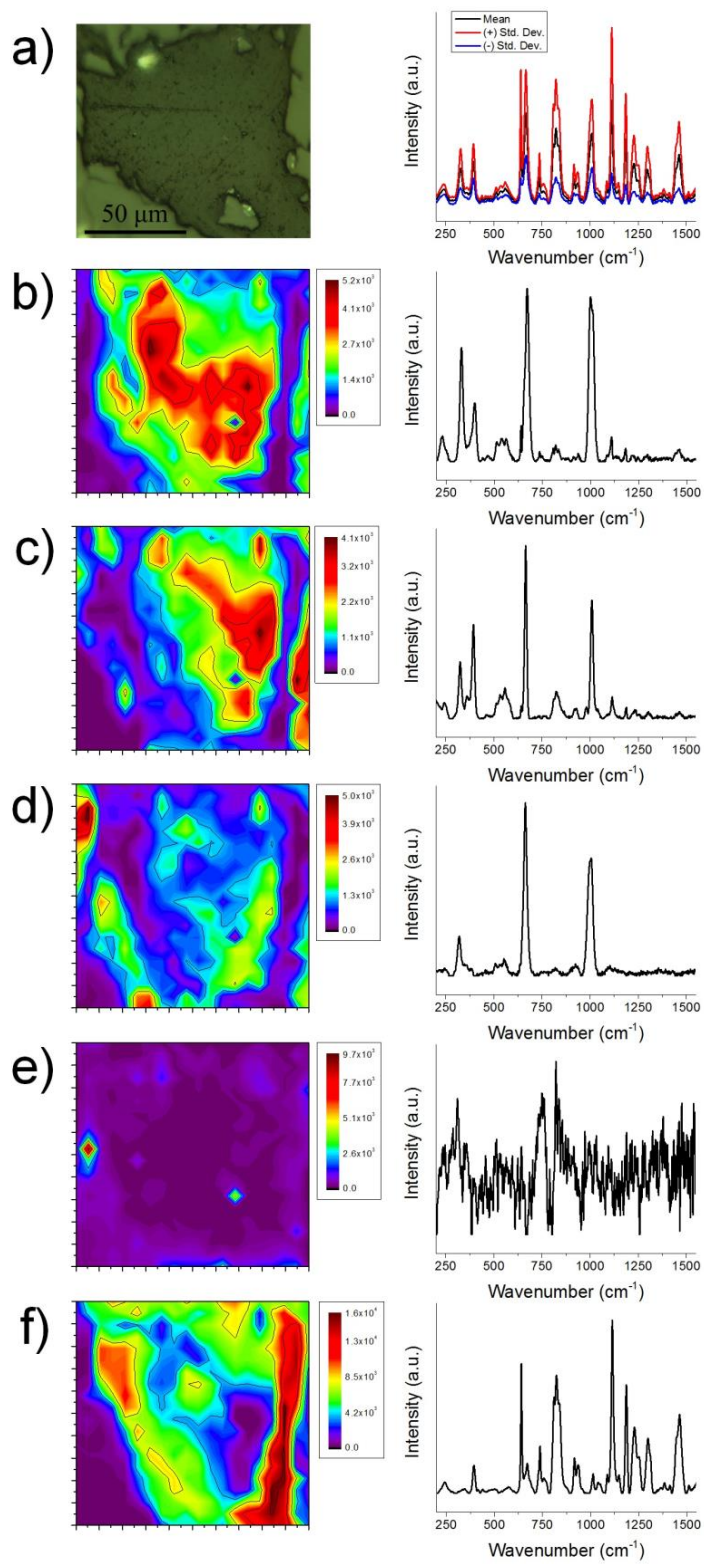


Figure 5.4: Results of MCR-ALS applied to Raman microspectroscopic imaging using 532 nm excitation of LAP 04841. Spatially-resolved chemical images and corresponding resolved Raman spectra of pyroxene (b), pyroxene (c), pyroxene (d), troilite (e), and substrate-adhesive epoxy (f). The optical image (a) and mean spectrum (black, a) +/- the standard deviation (+ in red, - in blue; a) are shown. A five-component MCR-ALS model was employed.

Spatially-resolved chemical images (**Figures 5.5b, 5.5c, 5.5d, 5.5e, 5.5f, and 5.5g**) and corresponding resolved Raman spectra (**Figures 5.5b, 5.5c, 5.5d, 5.5e, 5.5f, and 5.5g**) were produced from utilizing MCR-ALS with Raman microspectroscopic imaging of a second probed area of LAP 04841, shown in the optical image (**Figure 5.5a**). The mean (in black; **Figure 5.5a**) and standard deviation (+ in red, - in blue; **Figure 5.5a**) of the 400 total Raman spectra accumulated over this probed area demonstrate the presence of pyroxene, substrate-adhesive epoxy, and diamond-polish. The mean Raman spectrum shows the following primary Raman bands and their assigned chemical species are in parentheses—325  $\text{cm}^{-1}$  (pyroxene), 392  $\text{cm}^{-1}$  (pyroxene), 533  $\text{cm}^{-1}$  (pyroxene), 644  $\text{cm}^{-1}$  (pyroxene), 822  $\text{cm}^{-1}$  (substrate-adhesive epoxy), 1001  $\text{cm}^{-1}$  (pyroxene/substrate-adhesive epoxy), 1113  $\text{cm}^{-1}$  (substrate-adhesive epoxy), 1186  $\text{cm}^{-1}$  (substrate-adhesive epoxy) and 1331  $\text{cm}^{-1}$  (diamond-polish). Using a six component MCR-ALS model, six chemically meaningful components were resolved—diamond-polish, three clinopyroxenes, substrate-adhesive epoxy, and a high-temperature polymorph of anorthite. The first resolved Raman spectrum (**Figure 5.5b**) shows a major Raman band at 1331  $\text{cm}^{-1}$  characteristic of diamond-polish. The second resolved Raman spectrum (**Figure 5.5c**) shows major Raman bands at 324  $\text{cm}^{-1}$ , 392  $\text{cm}^{-1}$ , 533  $\text{cm}^{-1}$ , 555  $\text{cm}^{-1}$ , 666  $\text{cm}^{-1}$ , and 1009  $\text{cm}^{-1}$  characteristic of clinopyroxene. The third resolved Raman spectrum (**Figure 5.5d**) shows major Raman

bands at 640  $\text{cm}^{-1}$ , 822  $\text{cm}^{-1}$ , 1113  $\text{cm}^{-1}$ , 1187  $\text{cm}^{-1}$ , 1228  $\text{cm}^{-1}$ , and 1464  $\text{cm}^{-1}$  characteristic of substrate-adhesive epoxy. The fourth resolved Raman spectrum (**Figure 5.5e**) shows major Raman bands at 325  $\text{cm}^{-1}$ , 397  $\text{cm}^{-1}$ , 539  $\text{cm}^{-1}$ , 666  $\text{cm}^{-1}$ , and 996  $\text{cm}^{-1}$  characteristic of clinopyroxene. The fifth resolved Raman spectrum (**Figure 5.5f**) shows major Raman bands at 312  $\text{cm}^{-1}$ , 350  $\text{cm}^{-1}$ , 384  $\text{cm}^{-1}$ , 659  $\text{cm}^{-1}$ , 992  $\text{cm}^{-1}$ , and 1006  $\text{cm}^{-1}$  characteristic of clinopyroxene. The sixth resolved Raman spectrum (**Figure 5.5g**) shows major Raman bands at 287  $\text{cm}^{-1}$ , 404  $\text{cm}^{-1}$ , 486  $\text{cm}^{-1}$ , 506  $\text{cm}^{-1}$ , and 562  $\text{cm}^{-1}$ , characteristic of a high-temperature polymorph of anorthite. This high-temperature polymorph of anorthite has a body-centered crystal structure with  $I\bar{1}$  symmetry and exhibits primary bands in its Raman spectrum at 286  $\text{cm}^{-1}$ , 405  $\text{cm}^{-1}$ , 485  $\text{cm}^{-1}$ , 505  $\text{cm}^{-1}$ , and 564  $\text{cm}^{-1}$ . [194] Furthermore, under equilibrium conditions, this high-temperature polymorph of anorthite forms above  $\sim 240$   $^{\circ}\text{C}$  and retains a high degree of long-range Al-Si order up to the melting temperature of  $\sim 1557$   $^{\circ}\text{C}$  [217]. Electron microprobe analysis shows the plagioclase feldspar in LAP 04841 to have a composition of  $\text{An}_{81-91}$ , [197] similar to that ( $\text{An}_{79}$ ) of the sample of the high-temperature polymorph of anorthite with  $I\bar{1}$  symmetry whose Raman spectrum is previously reported [194]. For LAP 04841, an initial eruption temperature of the basaltic melt, whose crystallization formed this lunar meteorite, was estimated to be 1217  $^{\circ}\text{C}$ . [197] Given this measured anorthite composition and estimated eruption temperature, our identification of the high-temperature polymorph of anorthite having a body-centered crystal structure with  $I\bar{1}$  symmetry in LAP 04841 is consistent with the proposed temperature-composition diagrams for polymorphs of calcic plagioclase. [218]

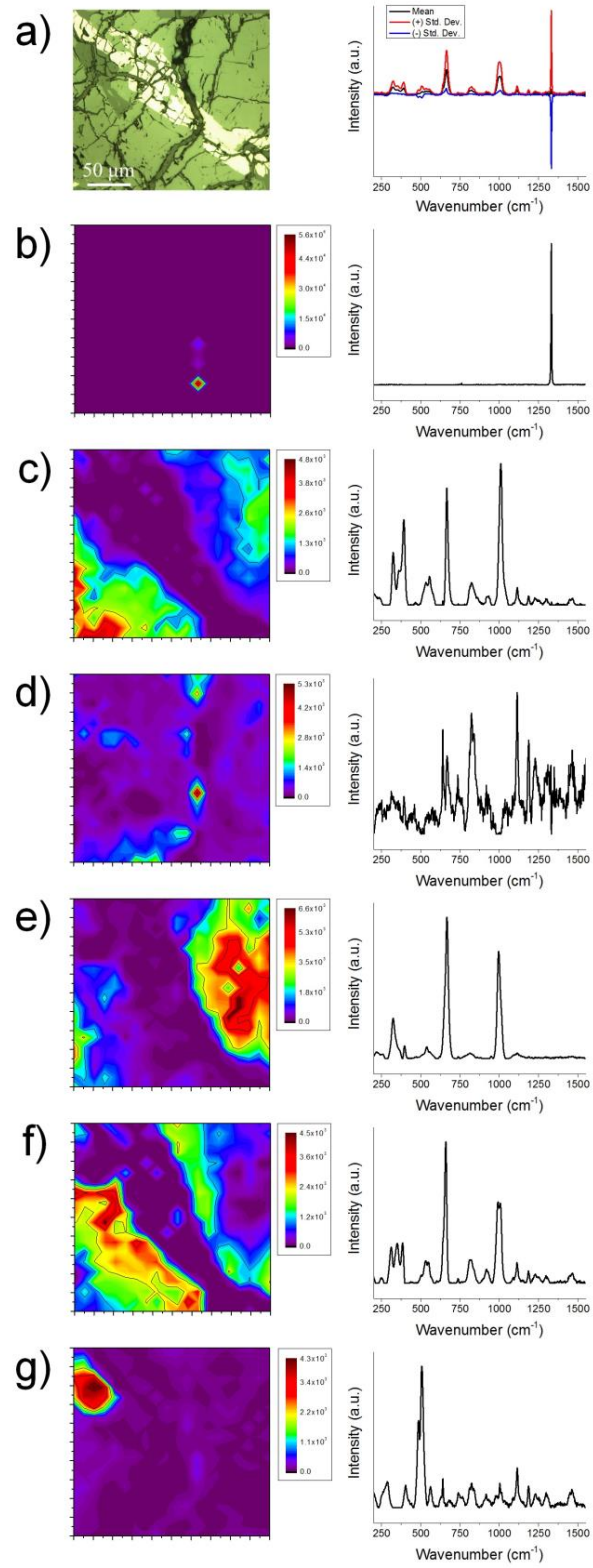


Figure 5.5: Results of MCR-ALS applied to Raman microspectroscopic imaging using 532 nm excitation of LAP 04841. Spatially-resolved chemical images and corresponding resolved Raman spectra of diamond-polish (b), pyroxene (c), substrate-adhesive epoxy (d), pyroxene (e), pyroxene (f) and high-temperature polymorphic anorthite (g). The optical image (a) and mean spectrum (black, a) +/- the standard deviation (+ in red, - in blue; a) are shown. A six-component MCR-ALS model was employed.

The spatial distribution of these six resolved chemical species (**Figures 5.5b, 5.5c, 5.5d, 5.5e, 5.5f, and 5.5g**) in the probed area of LAP 04841 (**Figure 5.5a**) was generated using MCR-ALS with Raman microspectroscopic imaging. The optical image of this probed area (**Figure 5.5a**) displays numerous fractures/veinlets, including a prominent fracture/veinlet feature in the center of the area. The spatial distribution of diamond-polish (**Figure 5.5b**) and substrate-adhesive epoxy (**Figure 5.5d**) demonstrate that both of these chemical species, which are employed during sample preparation, are primarily located within this prominent fracture/veinlet feature. Specifically, the spatially-resolved chemical image of diamond (**Figure 5.5b**) demonstrates that diamond is highly localized, including within this fracture/veinlet feature. The spatially-resolved chemical image of substrate-adhesive epoxy (**Figure 5.5d**) demonstrates that epoxy is also localized throughout the probed area, and again, is primarily located within this fracture/veinlet feature. The spatially-resolved chemical images of clinopyroxene (**Figures 5.5c, 5.5e, and 5.5f**) demonstrate that all three resolved clinopyroxenes are distributed in a complementary fashion. The distribution of the first resolved clinopyroxene (**Figure 5.5c**) shows that this clinopyroxene is primarily located towards the bottom-left and top-right portions of the probed area. The distribution of the second resolved clinopyroxene (**Figure 5.5e**) shows that this clinopyroxene is primarily located towards the top-right portion of the

probed area, with minor localizations on the bottom-left portion of the probed area. The distribution of the third resolved clinopyroxene (**Figure 5.5f**) shows that this pyroxene is located primarily towards the bottom-left portion of the probed area, including minor localizations towards the top-right portion of the probed area that are complementary to the second resolved clinopyroxene (**Figure 5.5e**). Finally, the spatially-resolved chemical image of the high-temperature polymorph of anorthite (**Figure 5.5g**) shows that this chemical species is highly localized towards the top-left portion of the probed area and displays an oval-shaped distribution.

In both probed areas (**Figures 5.4a** and **5.5a**) of LAP 04841, multiple chemical species were resolved using MCR-ALS with Raman microspectroscopic imaging, including three spectrally-diverse clinopyroxenes within each area. The clinopyroxenes are identified as such by comparing their resolved Raman spectra that were generated using MCR-ALS applied to Raman microspectroscopic imaging data with Raman spectra from the literature.[30, 44, 181, 182, 206, 207] All the resolved Raman spectra identified as monoclinic pyroxene (clinopyroxene) display several key spectral features. First, the resolved Raman spectra of clinopyroxenes do not display two distinct Raman bands (a doublet) at  $\sim 670\text{ cm}^{-1}$  that are characteristic of orthorhombic pyroxenes (orthopyroxenes)[182]. Second, the resolved Raman spectra of the clinopyroxenes show a single major Raman band near  $\sim 670\text{ cm}^{-1}$  that is characteristic of clinopyroxene.[182] Third, this major Raman band is not observed to be significantly ( $\sim 10\text{-}20\text{ cm}^{-1}$ ) redshifted to lower frequencies as is characteristic of triclinic pyroxenoids.[182] Moreover, the other major Raman bands within the resolved Raman spectra of the clinopyroxenes do not display significant redshifting, as would be expected for Raman spectra of triclinic pyroxenoids.[182] Therefore, the

pyroxenes in both probed areas within LAP 04841 all appear to be clinopyroxenes, but their resolved Raman spectra show distinct differences in their spectral features. These differences include the band location and relative intensity of the high-intensity Raman bands at  $\sim 667\text{ cm}^{-1}$  and  $\sim 1000\text{ cm}^{-1}$  as well as with the number of bands and their relative intensities in the lower wavenumber spectral range of  $\sim 230\text{ cm}^{-1}$  to  $400\text{ cm}^{-1}$ . In this lower wavenumber spectral range, there can be three Raman bands at  $312\text{ cm}^{-1}$ ,  $350\text{ cm}^{-1}$ , and  $384\text{ cm}^{-1}$  (**Figure 5.5f**), two moderate-intensity Raman bands at  $\sim 324\text{ cm}^{-1}$  and  $\sim 392\text{ cm}^{-1}$  (**Figures 5.4b, 5.4c, and 5.5c**), or a single, moderate-intensity Raman band at  $\sim 325\text{ cm}^{-1}$  (**Figures 5.4d and 5.5e**). Furthermore, these bands show differences in relative intensities. Therefore, for both probed areas of LAP 04841, the three resolved clinopyroxenes display differences in their spectral features that include the locations and relative intensities of the high-intensity Raman bands at  $\sim 667\text{ cm}^{-1}$  and  $\sim 1000\text{ cm}^{-1}$  as well as the number of Raman bands that are present in the  $\sim 230\text{ cm}^{-1}$  to  $400\text{ cm}^{-1}$  spectral range and the relative intensities of these latter bands.

We now discuss the factors that may be responsible for the differences in the spectral features of the resolved Raman spectra of the clinopyroxenes that were observed in our samples. The crystal orientation of a chemical species, including pyroxene[30], relative to the direction of the excitation laser beam is known to affect Raman band intensities and spectral patterns. In the study by Haskin et al.[30], a single grain of orthopyroxene was oriented in three different positions relative to the direction of excitation, and marked changes in the Raman spectral patterns and relative intensities of the Raman bands, including those in the  $\sim 300$  to  $400\text{ cm}^{-1}$  spectral region, were observed. Moreover, Wang et al.[182] noted that with a high ( $3\text{-}4\text{ cm}^{-1}$ )

resolution spectrometer, such as was used in our study, the major Raman band at  $\sim 1000\text{ cm}^{-1}$  for monoclinic pyroxenes may appear as two overlapping bands at  $\sim 1000\text{ cm}^{-1}$  and  $\sim 1010\text{ cm}^{-1}$ , and that the relative intensity of these two bands depends on crystal orientation. A second possible factor concerns chemical zonation within clinopyroxene crystals. Strong compositional zoning of pyroxene crystals in lunar samples has been documented previously using Raman spectroscopy, including zoning from orthopyroxene to pigeonite to Fe-augite over distances of a few micrometers within a polished thin section of an Apollo 14 impact-melt rock.[30] Moreover, a single pyroxene grain of  $\sim 500\text{ }\mu\text{m}$  in size within that same sample was previously determined to be zoned (core-to-rim) from orthopyroxene to pigeonite to pyroxferroite.[181] Electron microprobe analysis of LAP 02205 and LAP 04841 shows that most of the pyroxene grains are chemically zoned with pigeonite (relatively high Mg) cores transitioning to augite, Fe-rich pyroxene (ferropyroxene), and finally to very Fe-rich rims, some having compositions of pyroxferroite.[193, 197-200] We speculate that for the second probed area in LAP 04841 (**Figure 5.5a**), the differences in the spectral features of the resolved Raman spectra of the clinopyroxenes (**Figures 5.5c, 5.5e, and 5.5f**) may reflect chemical zonation of the clinopyroxenes. As observed in the spatially-resolved chemical images, the resolved Raman spectrum for the clinopyroxenes near their margins (**Figure 5.5f**) is distinctly different than the resolved Raman spectra (**Figures 5.5c and 5.5e**) for the more interior portions of the clinopyroxene crystals. Finally, a third possible factor involves the chemical composition of the pyroxenes. Previous studies[193, 197] on both LAP 02205 and LAP 04841 have highlighted that the pyroxene within both lunar meteorites is primarily the monoclinic-structured pyroxene (clinopyroxene) and specifically, augite,

pigeonite, and Fe-rich clinopyroxene. For example, the modal abundances of pyroxene varieties within LAP 02205 are as follows—29.0% augite, 12.0% pigeonite, and 15.9% Fe-pyroxene.[193] This variation of the chemical composition of augite, pigeonite, and Fe-rich clinopyroxenes can therefore be a potential factor in the resolution of the spectrally diverse clinopyroxenes.

## 5.5 Conclusions

The chemical, molecular, and structural information of the chemical species within lunar meteorites can help to reveal the petrogenesis of these rocks as well as to provide important constraints on the chemical composition of the Moon's crust and mantle. In this chapter, using chemical imaging with chemometric analysis, we investigated two polished thin sections of two paired, unbrecciated, mare-basalt lunar meteorites—LAP 02205 and LAP 04841—that had been collected from the LaPaz Icefield (LAP) of Antarctica. Initial investigation of LAP 02205 and LAP 04841 using polarized light microscopy showed these samples to be heterogeneous and comprised of polydispersed sized and shaped particles of varying chemical composition. Using multivariate curve resolution-alternating least squares (MCR-ALS) applied to Raman microspectroscopic imaging, two distinct areas in each of the meteorites were analyzed to elucidate their respective chemical properties. Using MCR-ALS with Raman microspectroscopic imaging, spatially-resolved chemical images and corresponding resolved Raman spectra of diamond-polish, clinopyroxene, and substrate-adhesive epoxy were generated on the first probed area of LAP 02205. Similarly, using MCR-ALS with Raman microspectroscopic imaging, the second probed area of LAP 02205 yielded the spatial and spectral resolution of ilmenite,

clinopyroxene, and substrate-adhesive epoxy. For the first probed area of LAP 04841, MCR-ALS with Raman microspectroscopic imaging generated spatially-resolved chemical images and resolved Raman spectra of three spectrally distinct clinopyroxene phases, as well as troilite and substrate-adhesive epoxy. A second probed area of LAP 04841 analyzed by MCR-ALS with Raman microspectroscopic imaging produced the spatial and spectral resolution of six individual chemical species—diamond-polish, three spectrally distinct clinopyroxene phases, substrate-adhesive epoxy, and a high-temperature, body-centered-structured ( $I\bar{1}$  space group) polymorph of anorthite. The minerals we resolved in our samples of LAP 02205 and LAP 04841—clinopyroxene, ilmenite, troilite, and anorthite—are consistent with the results of previous studies of these lunar meteorites using electron microprobe analysis. Substrate-adhesive epoxy and diamond-polish, introduced into the meteorites during sample preparation, were more readily observed within the fracture/veinlet features of both meteorites. In the four probed areas of LAP 02205 and LAP 04841 that we investigated using MCR-ALS with Raman microspectroscopic imaging, no orthopyroxene or triclinic pyroxenoids were resolved. Moreover, the resolution of the spectrally diverse clinopyroxene phases within LAP 04841 can be attributed to chemical zoning of pyroxenes, which is commonly observed in lunar meteorites, crystal orientation of the pyroxenes, and chemical composition of clinopyroxenes, e.g., pigeonite, augite, and Fe-rich clinopyroxenes. Overall, using MCR-ALS applied to Raman microspectroscopic imaging, we generated spatially-resolved chemical images and corresponding resolved Raman spectra of individual chemical species in diverse probed areas of lunar meteorites LAP 02205 and LAP 04841, and our results are consistent with those of previous studies using electron microprobe analysis. To the

best of our knowledge, this is the *first* report of MCR-ALS used in conjunction with Raman microspectroscopic imaging as applied to lunar or other meteorites. We therefore demonstrate the use of multivariate analysis methods with Raman microspectroscopic imaging to investigate complex, heterogeneous meteorites. This analytical methodology can be used in conjunction with other analytical techniques, e.g., electron microprobe analysis, to elucidate the chemical, molecular, and structural characteristics of phases within a host of geological, geochemical, and extraterrestrial materials (e.g., meteorites and samples returned by spacecraft).

## Chapter 6

### CONCLUSIONS AND FUTURE DIRECTIONS

In this dissertation, the development, application, and evaluation of innovative analytical methodology utilizing Raman microspectroscopic imaging with multivariate analysis methods was performed. This dissertation thus focuses on both the collection and analysis of chemical data resulting from Raman microspectroscopic imaging. Furthermore, by combining both Raman microspectroscopic imaging and multivariate analysis methods, the chemical properties of complex, heterogeneous materials were elucidated and fundamentally investigated. Specifically, this dissertation encompasses three primary studies. First, the high-pressure,  $\alpha$ -PbO<sub>2</sub>-structured polymorph of titanium dioxide, termed TiO<sub>2</sub>-II, was investigated for applications in geological sciences, geochemistry, and solar system modeling. Second, the search for life on Mars was enhanced by demonstrating the effectiveness of Raman microspectroscopic imaging with multivariate analysis methods to spatially and spectrally resolve chemical species relevant to Martian exploration and discovery. This study ultimately has implications not only in analytical chemistry, but in planetary science, geology, and astrobiology. Third, lunar meteorites, directly provided by the NASA Johnson Space Center, were fundamentally investigated using Raman microspectroscopic imaging with multivariate analysis methods. The results of this investigation are of significant interest for further application in meteoritics, cosmochemistry, planetary science, and solar system exploration and discovery. This dissertation has therefore aimed to advance analytical chemistry in innovative ways that are beneficial to the

scientific community at large, including developing and applying analytical methodology to fundamentally study complex, diverse materials.

### **6.1 Conclusions of the Investigation of the High-Pressure, $\alpha$ -PbO<sub>2</sub>-Structured Polymorph of Titanium Dioxide, TiO<sub>2</sub>-II**

In this dissertation, the high-pressure,  $\alpha$ -PbO<sub>2</sub>-structured polymorph of titanium dioxide (TiO<sub>2</sub>-II), recently identified in micrometer-sized grains recovered from four Neoproterozoic spherule layers deposited between ~2.65 and ~2.54 billion years ago[88], was investigated using a variety of analytical techniques. This discovery of TiO<sub>2</sub>-II, accomplished using Raman microspectroscopy, provides physical evidence to further support an impact origin of these spherule layers. In this dissertation, Raman microspectroscopic imaging with multivariate analysis, namely multivariate curve resolution-alternating least squares (MCR-ALS) and principal component analysis (PCA), were utilized to provide a detailed characterization of these TiO<sub>2</sub>-II-bearing grains. Moreover, PCA applied to Raman microspectroscopic imaging data initially determined the TiO<sub>2</sub>-II-bearing grains were displaying a representative three-phase chemical system comprised of rutile, TiO<sub>2</sub>-II, and substrate-adhesive epoxy. Backscattered electron (BSE) and secondary electron (SE) imaging revealed the grains to be heterogeneous, complex samples consisting of polydispersed micrometer- and submicrometer-sized particles. By employing MCR-ALS with Raman microspectroscopic imaging, spatially-resolved chemical maps and corresponding resolved Raman spectra of up to five distinct chemical species—rutile, TiO<sub>2</sub>-II, anatase, quartz, and substrate-adhesive epoxy—were resolved within the grains. Moreover, the results of MCR-ALS with Raman microspectroscopic imaging suggest that rutile is the direct precursor of TiO<sub>2</sub>-II in these grains, and anatase and

quartz are secondary phases. This finding is in agreement with previous studies.[88] Additionally, using a unique, cost-effective strategy, the spatial resolution of the chemical images resulting from Raman microspectroscopic imaging with MCR-ALS was greatly increased. This was accomplished in a comparable analysis time to traditional measurements by limiting spectral acquisition parameters during Raman microspectroscopic imaging. Finally, the Raman spectrum of *pure* TiO<sub>2</sub>-II was estimated, for the *first* time, using the resolved Raman spectra generated by MCR-ALS.

Throughout this investigation of the TiO<sub>2</sub>-II-bearing grains, unique advantages of utilizing multivariate analysis methods with Raman microspectroscopic imaging were observed. The high spectral overlap between the chemical species within these grains—TiO<sub>2</sub> polymorphs (rutile, anatase, and TiO<sub>2</sub>-II), SiO<sub>2</sub> polymorphs (quartz), and substrate-adhesive epoxy—ensures that univariate analysis methods cannot be employed with Raman microspectroscopic imaging. Multivariate analysis methods, especially MCR-ALS, were able to overcome this spectral overlap and ultimately produced spatially-resolved chemical maps and resolved Raman spectra for the individual chemical species within these grains. Multivariate analysis methods also were able to identify and resolve minor chemical species within the grains. Specifically, MCR-ALS successfully resolved both anatase and quartz within the grains, demonstrating the ability of this analytical methodology to discern minor chemical species within complex samples. Finally, MCR-ALS allowed for the spatial and spectral resolution of chemical species within low signal-to-noise Raman spectra. Overall, MCR-ALS applied to Raman microspectroscopic imaging was able to successfully investigate and fundamentally study complex, heterogeneous TiO<sub>2</sub>-II-

bearing grains and offer unique advantages over traditional univariate analysis methods.

## **6.2 Conclusions of High Spectral and High Spatial Resolution Raman Microspectroscopic Imaging Data and its Analysis by Multivariate Methods**

An investigation of Raman microspectroscopic imaging data of both high spectral and high spatial resolution collected on TiO<sub>2</sub>-II-bearing grains was offered in chapter three of this dissertation. Specifically, a Monteville spherule layer (MSL) grain was initially analyzed using BSE imaging, revealing this grain contains polydispersed micron- and submicron-sized and shaped particles. Raman microspectroscopy, using both high spectral and high spatial resolution, was subsequently utilized to investigate diverse locations on this MSL grain. Resulting Raman spectra collected with both high spectral and high spatial resolution indicate the presence of four chemical species—rutile, TiO<sub>2</sub>-II, quartz, and substrate-adhesive epoxy. By using MCR-ALS—a multivariate analysis method—with Raman microspectroscopic imaging, chemical maps, pixel-by-pixel chemical images, and resolved Raman spectra of the individual chemical species within this MSL grain were generated. Moreover, high spectral resolution Raman microspectroscopic imaging with MCR-ALS spatially and spectrally resolved five distinct chemical species—rutile, TiO<sub>2</sub>-II, anatase, quartz, and substrate-adhesive epoxy—within this MSL grain. Similarly, high spatial resolution Raman microspectroscopic imaging with MCR-ALS also resolved these five chemical species. However, the resulting chemical maps and pixel-by-pixel chemical images displayed a drastically increased spatial resolution and therefore, a superior spatial distribution for each chemical species. A disadvantage of using high spatial resolution Raman microspectroscopic imaging measurements was

an increased difficulty for the spectral resolution of the minor chemical species. This is due to the limited spectral acquisition parameters used during high spatial resolution measurements, which produce lower signal-to-noise data as compared to the high spectral resolution measurements. Overall, both high spectral and high spatial resolution Raman microspectroscopic imaging measurements were utilized with MCR-ALS to investigate a TiO<sub>2</sub>-II-bearing grain from the MSL, in which both analytical methodologies were evaluated.

The Raman microspectroscopic imaging data presented in this dissertation, also available in Smith et al.[52], offers significant value to both the chemical and broader scientific community. The data offers the ability to develop and test diverse algorithms for image processing. For example, high spectral and high spatial resolution spectroscopic imaging data can be used for data fusion, and specifically, for improving imaging capabilities as well as for image enhancements for certain regions of interest. The Raman microspectroscopic imaging data of high spectral and high spatial resolution also provides a textbook data set for developing and testing multivariate analysis and chemometric methods. For example, the classification of TiO<sub>2</sub> polymorphs using multivariate analysis methods can be explored using this data. Overall, the data generated using high spectral and high spatial resolution Raman microspectroscopic imaging measurements can be employed for advanced data analysis for a variety of applications.

### **6.3 Conclusions of the Spatial and Spectral Resolution of Carbonaceous Material from Hematite ( $\alpha$ -Fe<sub>2</sub>O<sub>3</sub>) using Raman Microspectroscopic Imaging and Multivariate Analysis**

In this dissertation, the ability of multivariate analysis with Raman microspectroscopic imaging to spatially and spectrally resolve a mixture of carbonaceous material, hematite, and substrate-adhesive epoxy was demonstrated. Given that two rover missions to Mars are being planned by both the National Aeronautics and Space Administration (NASA) and the European Space Agency (ESA) jointly with the Russian Federal Space Agency (Roscosmos) for the year 2020, the development and application of this innovative analytical methodology is both urgent and essential. Specifically, the primary objective of both rover missions is the search for extant or past life. For this search, Raman microspectroscopy and Raman microspectroscopic imaging will be directly employed on the rover missions. This will be the *first* time that a Raman spectrometer is used in a rover or planetary mission.

Hematite ( $\alpha$ -Fe<sub>2</sub>O<sub>3</sub>) is an abundant chemical species on the surface of Mars. Using Raman spectroscopy, it is difficult to differentiate carbonaceous material from hematite. This difficulty has even led to the misidentification of hematite as carbonaceous material in terrestrial samples previously.[158-160] Misidentification can occur because the 2LO Raman band of hematite and the Raman D-band of carbonaceous material displaying high spectral overlap. As such, an analytical methodology that can solve this challenging task is needed. In this dissertation, an analytical methodology has been developed and applied to robustly identify, differentiate, and resolve carbonaceous material from hematite using Raman microspectroscopic imaging with MCR-ALS.

Using Raman microspectroscopy with 532 nm and 785 nm excitation, hematite and carbonaceous material were initially evaluated. In both cases, the Raman spectra

of hematite and carbonaceous material displayed spectral overlap, in which increased spectral overlap was observed using 532 nm excitation as compared to using 785 nm excitation. In order to investigate the spatial and spectral resolution of carbonaceous material from hematite, a sample comprised of hematite, carbonaceous material, and substrate-adhesive epoxy in spatially distinct domains was prepared. Principal component analysis was employed to initially assess the ability of Raman microspectroscopic imaging using 532 nm and 785 nm excitation to differentiate carbonaceous material from hematite. The results of PCA demonstrated that both 532 nm and 785 nm excitation were able to produce representative three-phase systems of hematite, carbonaceous material, and substrate-adhesive epoxy. Spatially-resolved chemical maps and corresponding resolved Raman spectra of the individual chemical species—hematite, carbonaceous material, and substrate-adhesive epoxy—were generated by MCR-ALS with Raman microspectroscopic imaging using both 532 nm and 785 nm excitation. Therefore, Raman microspectroscopic imaging with MCR-ALS was able to spatially and spectrally differentiate hematite and carbonaceous material when these species were in spatially distinct domains.

The ability of MCR-ALS with Raman microspectroscopic imaging for the differentiation of carbonaceous material from hematite was further evaluated by employing combinatorial data sets. Combinatorial data sets were used because they contain experimental data with hematite and carbonaceous material within the same, non-differentiable space. MCR-ALS applied to these combinatorial data sets of 532 nm and 785 nm excitation successfully resolved carbonaceous material from hematite, even though these two chemical species were located in the same spatial region. When hematite and carbonaceous material are in spatially distinct domains and when

hematite and carbonaceous material are within the same spatial domain, 785 nm excitation better resolved the mixture containing hematite, carbonaceous material, and substrate-adhesive epoxy. This result is attributed to the presence of increased spectral overlap of the 2LO band of hematite with the D-band of carbonaceous material using 532 nm excitation as compared to using 785 nm excitation.

To our knowledge, this is the *first* report of multivariate analysis methods with Raman microspectroscopic imaging being utilized for the identification, differentiation, and resolution of carbonaceous material from hematite. In this dissertation, we have thus provided an analytical methodology, including both collection and analysis of chemical data, that can directly enhance the search for extant or past life on Mars during the 2020 rover missions. In addition to Mars, this analytical methodology should prove useful for terrestrial and other extraterrestrial materials and environments, including finding evidence of microbial life in ancient rocks on Earth.

#### **6.4 Conclusions of the Investigation of Lunar Meteorites Using Raman Microspectroscopic Imaging and Multivariate Analysis**

Investigating lunar meteorites to determine the chemical properties of the species within the meteorites can provide valuable information related to the petrogenesis of the meteorites as well as the composition of the Moon's crust and mantle. In this dissertation, two paired, unbrecciated mare-basalt lunar meteorites collected from the LaPaz Icefield (LAP) of Antarctica—LAP 02205 and LAP 04841—were investigated using multivariate analysis with Raman microspectroscopic imaging. These lunar meteorites were prepared by the meteorite working group (MWG) at the NASA Johnson Space Center as polished thin sections. Initially,

polarized light microscopy determined that both LAP 02205 and LAP 04841 were heterogeneous samples comprised of polydispersed sized and shaped particles of varying chemical composition. Using MCR-ALS with Raman microspectroscopic imaging, two distinct areas in each of the lunar meteorites were analyzed to elucidate their respective chemical properties. Spatially-resolved chemical images and corresponding resolved Raman spectra of diamond-polish, clinopyroxene, and substrate-adhesive epoxy were generated on the first probed area of LAP 02205 by MCR-ALS with Raman microspectroscopic imaging. Similarly, using MCR-ALS with Raman microspectroscopic imaging, the second probed area of LAP 02205 yielded spatially-resolved chemical images and corresponding resolved Raman spectra of ilmenite, clinopyroxene, and substrate-adhesive epoxy. For the first probed area of LAP 04841, MCR-ALS with Raman microspectroscopic imaging produced spatially-resolved chemical images and resolved Raman spectra of three spectrally distinct clinopyroxene phases, troilite, and substrate-adhesive epoxy. A second probed area of LAP 04841 analyzed by MCR-ALS with Raman microspectroscopic imaging generated spatially-resolved chemical images and resolved Raman spectra of six individual chemical species—diamond-polish, three spectrally distinct clinopyroxene phases, substrate-adhesive epoxy, and a high-temperature, body-centered-structured ( $I\bar{1}$  space group) polymorph of anorthite.

The chemical species resolved in LAP 02205 and LAP 04841—clinopyroxene, ilmenite, troilite, and anorthite—are consistent with the results of previous studies[193, 197] of both samples using electron microprobe analysis. Substrate-adhesive epoxy and diamond-polish, introduced into the meteorites during sample preparation, were more readily observed within the fracture/veinlet features of LAP

02205 and LAP 04841. In the four probed areas of the lunar meteorites that we investigated using MCR-ALS with Raman microspectroscopic imaging, orthopyroxene and triclinic pyroxenoids were not identified. The resolution of the spectrally diverse clinopyroxenes within LAP 04841 can be attributed to chemical zoning of pyroxenes, which is commonly observed in lunar meteorites, crystal orientation of the pyroxenes, and chemical composition of clinopyroxenes, e.g., pigeonite, augite, and Fe-rich clinopyroxenes.

Overall, using MCR-ALS applied to Raman microspectroscopic imaging, spatially-resolved chemical images and corresponding resolved Raman spectra of individual chemical species within distinct areas of the lunar meteorites LAP 02205 and LAP 04841 were produced. The results displayed in this dissertation are consistent with those of previous studies[193, 197] using electron microprobe analysis. To the best of our knowledge, this is the *first* report of MCR-ALS and Raman microspectroscopic imaging being applied to lunar or other meteorites. Therefore, this dissertation has demonstrated the use of multivariate analysis methods with Raman microspectroscopic imaging to investigate complex, heterogeneous extraterrestrial meteorites. This analytical methodology can be used in conjunction with more traditional analytical techniques, e.g., electron microprobe analysis, to elucidate the chemical, molecular, and structural characteristics of chemical species within a variety of geological, geochemical, and extraterrestrial materials.

## **6.5 Future Directions**

There are a variety of future directions for the research presented throughout this dissertation. Moreover, this dissertation has demonstrated the ability of

multivariate analysis and Raman microspectroscopic imaging to spatially and spectrally resolve the individual, pure chemical species within complex, heterogeneous materials. Given its efficacy, this analytical methodology can be employed in a variety of different future applications, ranging from *in situ* investigation of biological or protein crystallization processes to utilization on planetary rover missions for biomarker detection. In this chapter, the future directions will be tailored to the previous studies presented in this dissertation and will focus on the most prevalent future directions.

A natural future direction focusing on the results obtained during the TiO<sub>2</sub>-II investigation entails analyzing tens to hundreds of TiO<sub>2</sub>-II-bearing grains from the spherule layers using Raman microspectroscopic imaging with MCR-ALS. This future direction would allow for a more complete characterization of the chemical species, especially TiO<sub>2</sub>-II, within these grains. The results of this future direction coupled with the results of this dissertation should be useful for determining the mechanism(s) of formation of the TiO<sub>2</sub>-II, evaluating the potential of these grains to serve as a tool for determining paleodistances of the layers from their source craters, and testing the proposed correlation of the spherule layers. Another future application of this dissertation is to use Raman microspectroscopic imaging with multivariate analysis for the identification of other high-pressure polymorphs within complex geological samples. In this dissertation, Raman microspectroscopic imaging and multivariate analysis have spatially and spectrally resolved a high-pressure polymorph, a direct precursor to this polymorph, and secondary phases coupled with these chemical species. This analytical methodology can therefore be used to search for other polymorphs within geological materials, including high-pressure polymorphs of SiO<sub>2</sub>

(coesite or stishovite), as well as determining precursors or secondary phases within materials containing the respective polymorphs. Moreover, this analytical methodology could also be employed to detect low concentration or minor polymorphic species (i.e., high-pressure polymorphs) within samples. Overall, Raman microspectroscopic imaging with multivariate analysis methods can be utilized in future studies for the robust detection and investigation of complex, heterogeneous geological samples, especially samples containing high-pressure polymorphs.

An additional future direction of this dissertation is to develop a novel component determination strategy for MCR-ALS. In this dissertation, the effects of increasing the number of components used in MCR-ALS during the analysis of Raman microspectroscopic imaging data were investigated. During this investigation, the appropriate number of components for MCR-ALS was determined by comparing the resolved Raman spectra from MCR-ALS with Raman spectra of reference materials. The initial findings of this study demonstrated that in some cases, the major chemical species within a sample were better resolved by MCR-ALS with lower numbers of components (i.e., the number of components predicted by PCA), whereas more minor chemical species were better resolved by MCR-ALS with an increased number of components. Therefore, a future direction of this dissertation will be a comprehensive study of this method for component determination during MCR-ALS. Moreover, this future study will include comparison of the resolved Raman spectra from MCR-ALS with the Raman spectra of reference materials from a variety of sources, including Raman spectra from the RRUFF database project[126] as well as Raman spectra collected on the Raman microscope used for the study. This future direction would include determining the most effective component selection strategy

for various chemical systems, and ultimately, this study can offer a novel, quantitative approach for determining the appropriate number of components for MCR-ALS.

Future directions of this dissertation also involve utilizing the Raman microspectroscopic imaging data for developing and testing novel chemometric analysis methods. Using the Raman microspectroscopic imaging data collected with both high spectral and high spatial resolution, future work developing and testing algorithms for image processing can be pursued. This data also allows for future studies in data fusion, including improving imaging capabilities and enhancing certain regions of interest within images. Overall, this data can provide a valid resource for future studies developing and evaluating multivariate and chemometric analysis methods.

Additionally, a future direction of this dissertation is to further replicate the instrumental and experimental conditions for collecting Raman microspectroscopic imaging data on a planetary rover mission. This future study would entail collecting Raman microspectroscopic imaging data on Raman spectrometers that mimic instruments used on planetary rover missions. Using an instrumental design similar to rover-based Raman spectrometers, the exact collection parameters for Raman spectral acquisition being proposed by NASA and ESA/Roscosmos can be used to generate Raman microspectroscopic imaging data. Subsequent analysis of this more representative data by MCR-ALS can further validate this analytical methodology for the search for life on Mars in the upcoming rover missions. Similarly, another future direction is use Raman microspectroscopic imaging with MCR-ALS for the resolution of carbonaceous material from a true simulated martian environment. Instead of using only hematite as the abundant chemical species on the surface of Mars, preparing an

exact replica of Martian sediment and resolving carbonaceous material from this replica would further validate this analytical methodology for use on the upcoming rover missions to Mars. Other related future directions are to employ MCR-ALS with Raman microspectroscopic imaging for identification of carbonaceous material within terrestrial and other extraterrestrial materials. These future studies could involve resolving carbonaceous material from hematite within comets or stratospheric dust particles. In addition, this analytical methodology could be applied to searching for evidence of ancient microbial life on Earth, such as investigating redbeds and banded iron formations known to contain both organic carbon and hematite.

Finally, the remaining future directions of this dissertation involve advancing the investigation of lunar meteorites using Raman microspectroscopic imaging with MCR-ALS. A future study providing more in-depth analysis of certain regions of interest within the lunar meteorites can certainly be pursued. Probing interesting areas of lunar meteorites, such as shock-melt veins, using Raman microspectroscopic imaging can be accomplished. During the study presented in this dissertation, fracture/veinlet features of the lunar meteorites frequently contained high concentrations of substrate-adhesive epoxy and diamond-polish, introduced to the meteorites during sample preparation. A future study that increases the magnification, the integration times, and the co-averages of Raman spectral acquisition could allow for the resolution of the chemical species within these areas that are inherent to the meteorites. Other future directions of this dissertation involve investigating not only lunar meteorites, but also martian and asteroidal meteorites. The MWG within the NASA Johnson space center can directly provide martian and asteroidal meteorites for analysis. Given the accessibility of extraterrestrial meteorites, a comprehensive study

of these samples using Raman microspectroscopic imaging with multivariate analysis, especially MCR-ALS, can be performed. Overall, the future directions outlined in this dissertation can help propel Raman microspectroscopic imaging with multivariate analysis to the forefront of the scientific community as an effective analytical methodology for the investigation of complex materials, especially materials of geological and planetary importance.

## REFERENCES

1. C.V. Raman, K.S. Krishnan, A New Type of Secondary Radiation, *Nature*, 121 (1928) 501-502.
2. T. Dieing, O. Hollricher, J. Toporski, *Confocal Raman Microscopy*, Springer, Berlin, 2010.
3. Z. Movasaghi, S. Rehman, I.U. Rehman, Raman Spectroscopy of Biological Tissues, *Applied Spectroscopy Reviews*, 42 (2007) 493-541.
4. R. Petry, M. Schmitt, J. Popp, Raman Spectroscopy - A Prospective Tool in the Life Sciences, *Chemphyschem*, 4 (2003) 14-30.
5. L. Opilik, T. Schmid, R. Zenobi, Modern Raman Imaging: Vibrational Spectroscopy on the Micrometer and Nanometer Scales, in: R.G. Cooks, J.E. Pemberton (Eds.) *Annual Review of Analytical Chemistry*, Vol 6, Annual Reviews, Palo Alto, 2013, pp. 379-398.
6. S.D. Rassat, E.J. Davis, Temperature-Measurement of Single Levitated Microparticles using Stokes and Anti-Stokes-Raman Intensity Ratios, *Applied Spectroscopy*, 48 (1994) 1498-1505.
7. G.T. Went, S.T. Oyama, A.T. Bell, Laser Raman Spectroscopy of Supported Vanadium-Oxide Catalysts, *Journal of Physical Chemistry*, 94 (1990) 4240-4246.
8. M.A. Vuurman, I.E. Wachs, In Situ Raman Spectroscopy of Alumina-Supported Metal-Oxide Catalysts, *Journal of Physical Chemistry*, 96 (1992) 5008-5016.
9. S. Piscanec, M. Cantoro, A.C. Ferrari, J.A. Zapien, Y. Lifshitz, S.T. Lee, S. Hofmann, J. Robertson, Raman Spectroscopy of Silicon Nanowires, *Physical Review B*, 68 (2003) 4.
10. A.C. Ferrari, Raman Spectroscopy of Graphene and Graphite: Disorder, Electron-Phonon Coupling, Doping and Nonadiabatic Effects, *Solid State Communications*, 143 (2007) 47-57.

11. M.S. Dresselhaus, G. Dresselhaus, R. Saito, A. Jorio, Raman Spectroscopy of Carbon Nanotubes, *Physics Reports-Review Section of Physics Letters*, 409 (2005) 47-99.
12. J.L. Yu, W.B. Lu, J.P. Smith, K.S. Booksh, L.H. Meng, Y.D. Huang, Q.W. Li, J.H. Byun, Y. Oh, Y.S. Yan, T.W. Chou, A High Performance Stretchable Asymmetric Fiber-Shaped Supercapacitor with a Core-Sheath Helical Structure, *Advanced Energy Materials*, 7 (2017) 8.
13. T. De Beer, A. Burggraeve, M. Fonteyne, L. Saelens, J.P. Remon, C. Vervaet, Near Infrared and Raman Spectroscopy for the In-Process Monitoring of Pharmaceutical Production Processes, *International Journal of Pharmaceutics*, 417 (2011) 32-47.
14. T. Vankeirsbilck, A. Vercauteren, W. Baeyens, G. Van der Weken, F. Verpoort, G. Vergote, J.P. Remon, Applications of Raman Spectroscopy in Pharmaceutical Analysis, *Trends in Analytical Chemistry*, 21 (2002) 869-877.
15. C.J. Strachan, T. Rades, K.C. Gordon, J. Rantanen, Raman Spectroscopy for Quantitative Analysis of Pharmaceutical Solids, *Journal of Pharmacy and Pharmacology*, 59 (2007) 179-192.
16. S. Keren, C. Zavaleta, Z. Cheng, A. de la Zerda, O. Gheysens, S.S. Gambhir, Noninvasive Molecular Imaging of Small Living Subjects using Raman Spectroscopy, *Proceedings of the National Academy of Sciences of the United States of America*, 105 (2008) 5844-5849.
17. M.G. Shim, L. Song, N.E. Marcon, B.C. Wilson, In Vivo Near-Infrared Raman Spectroscopy: Demonstration of Feasibility during Clinical Gastrointestinal Endoscopy, *Photochemistry and Photobiology*, 72 (2000) 146-150.
18. Y.W.C. Cao, R.C. Jin, C.A. Mirkin, Nanoparticles with Raman Spectroscopic Fingerprints for DNA and RNA Detection, *Science*, 297 (2002) 1536-1540.
19. Z.W. Huang, A. McWilliams, H. Lui, D.I. McLean, S. Lam, H.S. Zeng, Near-Infrared Raman Spectroscopy for Optical Diagnosis of Lung Cancer, *International Journal of Cancer*, 107 (2003) 1047-1052.

20. A.S. Haka, K.E. Shafer-Peltier, M. Fitzmaurice, J. Crowe, R.R. Dasari, M.S. Feld, Diagnosing Breast Cancer by Using Raman Spectroscopy, *Proceedings of the National Academy of Sciences of the United States of America*, 102 (2005) 12371-12376.
21. I. DeWolf, Micro-Raman Spectroscopy to Study Local Mechanical Stress in Silicon Integrated Circuits, *Semiconductor Science and Technology*, 11 (1996) 139-154.
22. O. Lourie, H.D. Wagner, Evaluation of Young's Modulus of Carbon Nanotubes by Micro-Raman Spectroscopy, *Journal of Materials Research*, 13 (1998) 2418-2422.
23. J.L. Yu, W.B. Lu, S.P. Pei, K. Gong, L.Y. Wang, L.H. Meng, Y.D. Huang, J.P. Smith, K.S. Booksh, Q.W. Li, J.H. Byun, Y. Oh, Y.S. Yan, T.W. Chou, Omnidirectionally Stretchable High-Performance Supercapacitor Based on Isotropic Buckled Carbon Nanotube Films, *ACS Nano*, 10 (2016) 5204-5211.
24. R. Kizil, J. Irudayaraj, K. Seetharaman, Characterization of Irradiated Starches by using FT-Raman and FTIR Spectroscopy, *Journal of Agricultural and Food Chemistry*, 50 (2002) 3912-3918.
25. E.C.Y. LiChan, The Applications of Raman Spectroscopy in Food Science, *Trends in Food Science & Technology*, 7 (1996) 361-370.
26. R. Sparkes, N. Hovius, A. Galy, R.V. Kumar, J.T. Liu, Automated Analysis of Carbon in Powdered Geological and Environmental Samples by Raman Spectroscopy, *Applied Spectroscopy*, 67 (2013) 779-788.
27. M.L. Frezzotti, F. Tecce, A. Casagli, Raman Spectroscopy for Fluid Inclusion Analysis, *Journal of Geochemical Exploration*, 112 (2012) 1-20.
28. D.W. Li, W.L. Zhai, Y.T. Li, Y.T. Long, Recent Progress in Surface Enhanced Raman Spectroscopy for the Detection of Environmental Pollutants, *Microchimica Acta*, 181 (2014) 23-43.
29. R.A. Halvorson, P.J. Vikesland, Surface-Enhanced Raman Spectroscopy (SERS) for Environmental Analyses, *Environmental Science & Technology*, 44 (2010) 7749-7755.

30. L.A. Haskin, A. Wang, K.M. Rockow, B.L. Jolliff, R.L. Korotev, K.M. Viskupic, Raman Spectroscopy for Mineral Identification and Quantification for In Situ Planetary Surface Analysis: A Point Count Method, *Journal of Geophysical Research-Planets*, 102 (1997) 19293-19306.
31. S.M. Angel, N.R. Gomer, S.K. Sharma, C. McKay, Remote Raman Spectroscopy for Planetary Exploration: A Review, *Applied Spectroscopy*, 66 (2012) 137-150.
32. M. Votteler, D.A.C. Berrio, M. Pudlas, H. Walles, U.A. Stock, K. Schenke-Layland, Raman Spectroscopy for the Non-Contact and Non-Destructive Monitoring of Collagen Damage within Tissues, *Journal of Biophotonics*, 5 (2012) 47-56.
33. K. Kneipp, H. Kneipp, I. Itzkan, R.R. Dasari, M.S. Feld, Ultrasensitive Chemical Analysis by Raman Spectroscopy, *Chemical Reviews*, 99 (1999) 2957.
34. J.F. Lin, M. Santoro, V.V. Struzhkin, H.K. Mao, R.J. Hemley, In Situ High Pressure-Temperature Raman Spectroscopy Technique with Laser-Heated Diamond Anvil Cells, *Review of Scientific Instruments*, 75 (2004) 3302-3306.
35. H.J. Butler, L. Ashton, B. Bird, G. Cinque, K. Curtis, J. Dorney, K. Esmonde-White, N.J. Fullwood, B. Gardner, P.L. Martin-Hirsch, M.J. Walsh, M.R. McAinsh, N. Stone, F.L. Martin, Using Raman Spectroscopy to Characterize Biological Materials, *Nature Protocols*, 11 (2016) 664-687.
36. R.L. Frost, D.A. Henry, M.L. Weier, W. Martens, Raman Spectroscopy of Three Polymorphs of  $\text{BiVO}_4$ : Clinobisvanite, Dreyerite and Pucherite, with Comparisons to  $(\text{VO}_4)^{3-}$  Bearing Minerals: Namibite, Pottsite and Schumacherite, *Journal of Raman Spectroscopy*, 37 (2006) 722-732.
37. A. Dandeu, B. Humbert, C. Carteret, H. Muhr, E. Plasari, J.M. Bossoutrot, Raman Spectroscopy - A Powerful Tool for the Quantitative Determination of the Composition of Polymorph Mixtures: Application to  $\text{CaCO}_3$  Polymorph Mixtures, *Chemical Engineering & Technology*, 29 (2006) 221-225.
38. R.J. Swain, M.M. Stevens, Raman Microspectroscopy for Non-Invasive Biochemical Analysis of Single Cells, *Biochemical Society Transactions*, 35 (2007) 544-549.

39. S. Schlucker, M.D. Schaeberle, S.W. Huffman, I.W. Levin, Raman Microspectroscopy: A Comparison of Point, Line, and Wide-Field Imaging Methodologies, *Analytical Chemistry*, 75 (2003) 4312-4318.
40. S. Stewart, R.J. Priore, M.P. Nelson, P.J. Treado, Raman Imaging, in: R.G. Cooks, E.S. Yeung (Eds.) *Annual Review of Analytical Chemistry*, Vol 5, Annual Reviews, Palo Alto, 2012, pp. 337-360.
41. K. Meister, J. Niesel, U. Schatzschneider, N. Metzler-Nolte, D.A. Schmidt, M. Havenith, Label-Free Imaging of Metal-Carbonyl Complexes in Live Cells by Raman Microspectroscopy, *Angewandte Chemie-International Edition*, 49 (2010) 3310-3312.
42. Z.H. Ni, Y.Y. Wang, T. Yu, Z.X. Shen, Raman Spectroscopy and Imaging of Graphene, *Nano Research*, 1 (2008) 273-291.
43. E. Gaufres, N.Y.W. Tang, F. Lapointe, J. Cabana, M.A. Nadon, N. Cottenye, F. Raymond, T. Szkopek, R. Martel, Giant Raman Scattering from J-Aggregated Dyes Inside Carbon Nanotubes for Multispectral Imaging, *Nature Photonics*, 8 (2014) 73-79.
44. A. Wang, R.L. Korotev, B.L. Jolliff, Z.C. Ling, Raman Imaging of Extraterrestrial Materials, *Planetary and Space Science*, 112 (2015) 23-34.
45. S.F. El-Mashtoly, H.K. Yosef, D. Petersen, L. Mavarani, A. Maghnouj, S. Hahn, C. Kotting, K. Gerwert, Label-Free Raman Spectroscopic Imaging Monitors the Integral Physiologically Relevant Drug Responses in Cancer Cells, *Analytical Chemistry*, 87 (2015) 7297-7304.
46. J.W. Kang, P.T.C. So, R.R. Dasari, D.K. Lim, High Resolution Live Cell Raman Imaging Using Subcellular Organelle-Targeting SERS-Sensitive Gold Nanoparticles with Highly Narrow Intra-Nanogap, *Nano Letters*, 15 (2015) 1766-1772.
47. C.L. Zavaleta, B.R. Smith, I. Walton, W. Doering, G. Davis, B. Shojaei, M.J. Natan, S.S. Gambhir, Multiplexed Imaging of Surface Enhanced Raman Scattering Nanotags in Living Mice using Noninvasive Raman Spectroscopy, *Proceedings of the National Academy of Sciences of the United States of America*, 106 (2009) 13511-13516.
48. S.F. El-Mashtoly, D. Petersen, H.K. Yosef, A. Mosig, A. Reinacher-Schick, C. Kotting, K. Gerwert, Label-Free Imaging of Drug Distribution and Metabolism in Colon Cancer Cells by Raman Microscopy, *Analyst*, 139 (2014) 1155-1161.

49. C. Gendrin, Y. Roggo, C. Collet, Pharmaceutical Applications of Vibrational Chemical Imaging and Chemometrics: A Review, *Journal of Pharmaceutical and Biomedical Analysis*, 48 (2008) 533-553.
50. C.M. Stellman, K.S. Booksh, A.R. Muroski, M.P. Nelson, M.L. Myrick, Principal Component Mapping Applied to Raman Microspectroscopy of Fiber-Reinforced Polymer Composites, *Science and Engineering of Composite Materials*, 7 (1998) 51-80.
51. J.P. Smith, F.C. Smith, J. Ottaway, A.E. Krull-Davatzes, B.M. Simonson, B.P. Glass, K.S. Booksh, Raman Microspectroscopic Mapping with Multivariate Curve Resolution-Alternating Least Squares (MCR-ALS) Applied to the High-Pressure Polymorph of Titanium Dioxide, TiO<sub>2</sub>-II, *Applied Spectroscopy*, (2017). DOI: 10.1177/0003702816687573
52. J.P. Smith, F.C. Smith, A.E. Krull-Davatzes, B.M. Simonson, B.P. Glass, K.S. Booksh, Raman Microspectroscopic Mapping with Multivariate Curve Resolution-Alternating Least Squares (MCR-ALS) of the High-Pressure,  $\alpha$ -PbO<sub>2</sub>-Structured Polymorph of Titanium Dioxide, TiO<sub>2</sub>-II, *Chemical Data Collections*, 9-10 (2017) 35-43.
53. M. Ando, H.O. Hamaguchi, Molecular Component Distribution Imaging of Living Cells by Multivariate Curve Resolution Analysis of Space-Resolved Raman Spectra, *Journal of Biomedical Optics*, 19 (2014) 1-6.
54. B. Vajna, G. Patyi, Z. Nagy, A. Bodis, A. Farkas, G. Marosi, Comparison of Chemometric Methods in the Analysis of Pharmaceuticals with Hyperspectral Raman Imaging, *Journal of Raman Spectroscopy*, 42 (2011) 1977-1986.
55. J. Felten, H. Hall, J. Jaumot, R. Tauler, A. de Juan, A. Gorzsas, Vibrational Spectroscopic Image Analysis of Biological Material using Multivariate Curve Resolution-Alternating Least Squares (MCR-ALS), *Nature Protocols*, 10 (2015) 217-240.
56. P. Robert, D. Bertrand, M.F. Devaux, A. Sire, Identification of Chemical Constituents by Multivariate Near-Infrared Spectral Imaging, *Analytical Chemistry*, 64 (1992) 664-667.
57. L. Zhang, M.J. Henson, S.S. Sekulic, Multivariate Data Analysis for Raman Imaging of a Model Pharmaceutical Tablet, *Analytica Chimica Acta*, 545 (2005) 262-278.

58. P.Q. Yu, Application of Cluster Analysis (CLA) in Feed Chemical Imaging to Accurately Reveal Structural-Chemical Features of Feeds and Plants within Cellular Dimension, *Journal of Agricultural and Food Chemistry*, 53 (2005) 2872-2880.
59. W.H. Lawton, E.A. Sylvestre, Self Modeling Curve Resolution, *Technometrics*, 13 (1971) 617-.
60. M. Maeder, A.D. Zuberbuehler, The Resolution of Overlapping Chromatographic Peaks by Evolving Factor-Analysis, *Analytica Chimica Acta*, 181 (1986) 287-291.
61. A. de Juan, J. Jaumot, R.A. Tauler, Multivariate Curve Resolution (MCR). Solving the Mixture Analysis Problem, *Analytical Methods*, 6 (2014) 4964-4976.
62. X. Zhang, R. Tauler, Application of Multivariate Curve Resolution Alternating Least Squares (MCR-ALS) to Remote Sensing Hyperspectral Imaging, *Analytica Chimica Acta*, 762 (2013) 25-38.
63. S. Piqueras, L. Duponchel, R. Tauler, A. de Juana, Monitoring Polymorphic Transformations by using In Situ Raman Hyperspectral Imaging and Image Multiset Analysis, *Analytica Chimica Acta*, 819 (2014) 15-25.
64. S. Piqueras, L. Duponchel, M. Offroy, F. Jamme, R. Tauler, A. de Juan, Chemometric Strategies To Unmix Information and Increase the Spatial Description of Hyperspectral Images: A Single-Cell Case Study, *Analytical Chemistry*, 85 (2013) 6303-6311.
65. X. Zhang, A. de Juan, R. Tauler, Multivariate Curve Resolution Applied to Hyperspectral Imaging Analysis of Chocolate Samples, *Applied Spectroscopy*, 69 (2015) 993-1003.
66. M.B. Mamian-Lopez, R.J. Poppi, SERS Hyperspectral Imaging Assisted by MCR-ALS for Studying Polymeric Microfilms Loaded with Paracetamol, *Microchemical Journal*, 123 (2015) 243-251.
67. M. Pelaez, N.T. Nolan, S.C. Pillai, M.K. Seery, P. Falaras, A.G. Kontos, P.S.M. Dunlop, J.W.J. Hamilton, J.A. Byrne, K. O'Shea, M.H. Entezari, D.D. Dionysiou, A Review on the Visible Light Active Titanium Dioxide Photocatalysts for Environmental Applications, *Applied Catalysis B-Environmental*, 125 (2012) 331-349.

68. S.U.M. Khan, M. Al-Shahry, W.B. Ingler, Efficient Photochemical Water Splitting by a Chemically Modified n-TiO<sub>2</sub>, *Science*, 297 (2002) 2243-2245.
69. S. Farrokhpay, A Review of Polymeric Dispersant Stabilisation of Titania Pigment, *Advances in Colloid and Interface Science*, 151 (2009) 24-32.
70. K. Nakata, A. Fujishima, TiO<sub>2</sub> Photocatalysis: Design and Applications, *Journal of Photochemistry and Photobiology C-Photochemistry Reviews*, 13 (2012) 169-189.
71. G. Meinhold, Rutile and its Applications in Earth Sciences, *Earth-Science Reviews*, 102 (2010) 1-28.
72. S.J. Smith, R. Stevens, S.F. Liu, G.S. Li, A. Navrotsky, J. Boerio-Goates, B.F. Woodfield, Heat Capacities and Thermodynamic Functions of TiO<sub>2</sub> Anatase and Rutile: Analysis of Phase Stability, *American Mineralogist*, 94 (2009) 236-243.
73. A.C. Withers, E.J. Essene, Y.X. Zhang, Rutile/TiO<sub>2</sub>II Phase Equilibria, *Contributions to Mineralogy and Petrology*, 145 (2003) 199-204.
74. W.J. Yong, E. Dachs, A. Benisek, R.A. Secco, Heat Capacity and Entropy of Rutile and TiO<sub>2</sub>II: Thermodynamic Calculation of Rutile-TiO<sub>2</sub>II Transition Boundary, *Physics of the Earth and Planetary Interiors*, 226 (2014) 39-47.
75. J.S. Olsen, L. Gerward, J.Z. Jiang, On the Rutile/alpha-PbO<sub>2</sub>-type Phase Boundary of TiO<sub>2</sub>, *Journal of Physics and Chemistry of Solids*, 60 (1999) 229-233.
76. T. Zhu, S.P. Gao, The Stability, Electronic Structure, and Optical Property of TiO<sub>2</sub> Polymorphs, *Journal of Physical Chemistry C*, 118 (2014) 11385-11396.
77. Y.C. Lan, Y.L. Lu, Z.F. Ren, Mini Review on Photocatalysis of Titanium Dioxide Nanoparticles and their Solar Applications, *Nano Energy*, 2 (2013) 1031-1045.
78. K. Spektor, D.T. Tran, K. Leinenweber, U. Haussermann, Transformation of Rutile to TiO<sub>2</sub>-II in a High Pressure Hydrothermal Environment, *Journal of Solid State Chemistry*, 206 (2013) 209-216.

79. C. Shang, W.N. Zhao, Z.P. Liu, Searching for New TiO<sub>2</sub> Crystal Phases with Better Photoactivity, *Journal of Physics-Condensed Matter*, 27 (2015) 8.
80. S.L. Hwang, P.Y. Shen, H.T. Chu, T.F. Yui, Nanometer-size alpha-PbO<sub>2</sub>-type TiO<sub>2</sub> in Garnet: A Thermobarometer for Ultrahigh-Pressure Metamorphism, *Science*, 288 (2000) 321-324.
81. X.L. Wu, D.W. Meng, Y.J. Han, Alpha-PbO<sub>2</sub>-type Nanophase of TiO<sub>2</sub> from Coesite-Bearing Eclogite in the Dabie Mountains, China, *American Mineralogist*, 90 (2005) 1458-1461.
82. R. Wirth, F. Kaminsky, S. Matsyuk, A. Schreiber, Unusual Micro- and Nano-Inclusions in Diamonds from the Juina Area, Brazil, *Earth and Planetary Science Letters*, 286 (2009) 292-303.
83. L.F. Dobrzhinetskaya, R. Wirth, J.S. Yang, I.D. Hutcheon, P.K. Weber, H.W. Green, High-Pressure Highly Reduced Nitrides and Oxides from Chromitite of a Tibetan Ophiolite, *Proceedings of the National Academy of Sciences of the United States of America*, 106 (2009) 19233-19238.
84. A. El Goresy, M. Chen, P. Gillet, L. Dubrovinsky, G. Graup, R. Ahuja, A Natural Shock-Induced Dense Polymorph of Rutile with alpha-PbO<sub>2</sub> Structure in the Suvite from the Ries Crater in Germany, *Earth and Planetary Science Letters*, 192 (2001) 485-495.
85. J.C. Jackson, J.W. Horton, I.M. Chou, H.E. Belkin, A Shock-Induced Polymorph of Anatase and Rutile from the Chesapeake Bay Impact Structure, Virginia, USA, *American Mineralogist*, 91 (2006) 604-608.
86. M. Chen, X.P. Gu, X.D. Xie, F. Yin, High-Pressure Polymorph of TiO<sub>2</sub>-II from the Xiuyan Crater of China, *Chinese Science Bulletin*, 58 (2013) 4655-4662.
87. B.P. Glass, M. Fries, Micro-Raman Spectroscopic Study of Fine-Grained, Shock-Metamorphosed Rock Fragments from the Australasian Microtektite Layer, *Meteoritics & Planetary Science*, 43 (2008) 1487-1496.
88. F.C. Smith, B.P. Glass, B.M. Simonson, J.P. Smith, A.E. Krull-Davatzes, K.S. Booksh, Shock-Metamorphosed Rutile Grains Containing the High-Pressure Polymorph TiO<sub>2</sub>-II in Four Neoproterozoic Spherule Layers, *Geology*, 44 (2016) 775-778.

89. B.P. Glass, B.M. Simonson, *Distal Impact Ejecta Layers: A Record of Large Impacts in Sedimentary Deposits*, Springer, Berlin, Germany, 2013.
90. D.R. Lowe, G.R. Byerly, F.T. Kyte, Recently Discovered 3.42-3.23 Ga Impact Layers, Barberton Belt, South Africa: 3.8 Ga Detrital Zircons, Archean Impact History, and Tectonic Implications, *Geology*, 42 (2014) 747-750.
91. D.R. Lowe, G.R. Byerly, F.T. Kyte, A. Shukolyukov, F. Asaro, A. Krull, Spherule Beds 3.47-3.24 Billion Years Old in the Barberton Greenstone Belt, South Africa: A Record of Large Meteorite Impacts and their Influence on Early Crustal and Biological Evolution, *Astrobiology*, 3 (2003) 7-48.
92. B.C. Johnson, H.J. Melosh, Impact Spherules as a Record of an Ancient Heavy Bombardment of Earth, *Nature*, 485 (2012) 75-77.
93. F.T. Kyte, A. Shukolyukov, G.W. Lugmair, D.R. Lowe, G.R. Byerly, Early Archean Spherule Beds: Chromium Isotopes Confirm Origin through Multiple Impacts of Projectiles of Carbonaceous Chondrite Type, *Geology*, 31 (2003) 283-286.
94. B.M. Simonson, I. McDonald, A. Shukolyukov, C. Koeberl, W.U. Reimold, G.W. Lugmair, Geochemistry of 2.63-2.49 Ga Impact Spherule Layers and Implications for Stratigraphic Correlations and Impact Processes, *Precambrian Research*, 175 (2009) 51-76.
95. S. Goderis, B.M. Simonson, I. McDonald, S.W. Hassler, A. Izmer, J. Belza, H. Terryn, F. Vanhaecke, P. Claeys, Ni-rich Spinels and Platinum Group Element Nuggets Condensed from a Late Archean Impact Vapour Cloud, *Earth and Planetary Science Letters*, 376 (2013) 87-98.
96. B. Rasmussen, C. Koeberl, Iridium Anomalies and Shocked Quartz in a Late Archean Spherule Layer from the Pilbara Craton: New Evidence for a Major Asteroid Impact at 2.63 Ga, *Geology*, 32 (2004) 1029-1032.
97. B.M. Simonson, D.Y. Sumner, N.J. Beukes, S. Johnson, J. Gutzmer, Correlating Multiple Neoproterozoic-Paleoproterozoic Impact Spherule Layers between South Africa and Western Australia, *Precambrian Research*, 169 (2009) 100-111.

98. W.F. Bottke, D. Vokrouhlicky, D. Minton, D. Nesvorny, A. Morbidelli, R. Brasser, B. Simonson, H.F. Levison, An Archaean Heavy Bombardment from a Destabilized Extension of the Asteroid Belt, *Nature*, 485 (2012) 78-81.
99. Y. Al-Khatatbeh, K.K.M. Lee, B. Kiefer, High-Pressure Behavior of TiO<sub>2</sub> as Determined by Experiment and Theory, *Physical Review B*, 79 (2009) 9.
100. R.G. McQueen, J.C. Jamieson, S.P. Marsh, Shock-Wave Compression and X-ray Studies of Titanium Dioxide, *Science*, 155 (1967) 1401.
101. K. Kusaba, M. Kikuchi, K. Fukuoka, Y. Syono, Anisotropic Phase-Transition of Rutile under Shock Compression, *Physics and Chemistry of Minerals*, 15 (1988) 238-245.
102. R.K. Linde, P.S. Decarli, Polymorphic Behavior of Titania under Dynamic Loading, *Journal of Chemical Physics*, 50 (1969) 319.
103. J.F. Mammone, S.K. Sharma, M. Nicol, Raman Study of Rutile (TiO<sub>2</sub>) at High-Pressures, *Solid State Communications*, 34 (1980) 799-802.
104. J.F. Mammone, M. Nicol, S.K. Sharma, Raman Spectra of TiO<sub>2</sub>-II, TiO<sub>2</sub>-III, SnO<sub>2</sub>, and GeO<sub>2</sub> at High-Pressure, *Journal of Physics and Chemistry of Solids*, 42 (1981) 379-384.
105. S. Koljenovic, T.C.B. Schut, J.P. van Meerbeeck, A. Maat, S.A. Burgers, P.E. Zondervan, J.M. Kros, G.J. Puppels, Raman Microspectroscopic Mapping Studies of Human Bronchial Tissue, *Journal of Biomedical Optics*, 9 (2004) 1187-1197.
106. P. Xu, J.M. Kang, J.W. Suhr, J.P. Smith, K.S. Booksh, B.Q. Wei, J.Y. Yu, F.X. Li, J.H. Byun, Y.S. Oh, T.W. Chou, Spatial Strain Variation of Graphene Films for Stretchable Electrodes, *Carbon*, 93 (2015) 620-624.
107. M. Lopez-Lopez, M.A.F. de la Ossa, C. Garcia-Ruiz, Fast Analysis of Complete Macroscopic Gunshot Residues on Substrates Using Raman Imaging, *Applied Spectroscopy*, 69 (2015) 889-893.
108. J. Nallala, O. Piot, M.D. Diebold, C. Gobinet, O. Bouche, M. Manfait, G.D. Sockalingum, Infrared and Raman Imaging for Characterizing Complex Biological Materials: A Comparative Morpho-Spectroscopic Study of Colon Tissue, *Applied Spectroscopy*, 68 (2014) 57-68.

109. M. Offroy, M. Moreau, S. Sobanska, P. Milanfar, L. Duponchel, Pushing Back the Limits of Raman Imaging by Coupling Super-Resolution and Chemometrics for Aerosols Characterization, *Scientific Reports*, 5 (2015) 14.
110. C.D.L. Albuquerque, R.J. Poppi, Detection of Malathion in Food Peels by Surface-Enhanced Raman Imaging Spectroscopy and Multivariate Curve Resolution, *Analytica Chimica Acta*, 879 (2015) 24-33.
111. C.K. Huang, M. Ando, H. Hamaguchi, S. Shigeto, Disentangling Dynamic Changes of Multiple Cellular Components during the Yeast Cell Cycle by in Vivo Multivariate Raman Imaging, *Analytical Chemistry*, 84 (2012) 5661-5668.
112. T.W. Bocklitz, S.X. Guo, O. Ryabchykov, N. Vogler, J. Popp, Raman Based Molecular Imaging and Analytics: A Magic Bullet for Biomedical Applications!?, *Analytical Chemistry*, 88 (2016) 133-151.
113. H. Motegi, Y. Tsuboi, A. Saga, T. Kagami, M. Inoue, H. Toki, O. Minowa, T. Noda, J. Kikuchi, Identification of Reliable Components in Multivariate Curve Resolution-Alternating Least Squares (MCR-ALS): A Data-Driven Approach across Metabolic Processes, *Scientific Reports*, 5 (2015) 12.
114. Y.Q. Cai, C. Zhang, Y.P. Feng, Dielectric Properties and Lattice Dynamics of alpha-PbO<sub>2</sub>-type TiO<sub>2</sub>: The Role of Soft Phonon Modes in Pressure-Induced Phase Transition to Baddeleyite-type TiO<sub>2</sub>, *Physical Review B*, 84 (2011) 8.
115. M. Landmann, E. Rauls, W.G. Schmidt, The Electronic Structure and Optical Response of Rutile, Anatase and Brookite TiO<sub>2</sub>, *Journal of Physics-Condensed Matter*, 24 (2012) 6.
116. T.I. Dyuzheva, L.M. Lityagina, N.A. Bendeliani, Hydrothermal Crystal Growth of the High-Pressure Phases of alpha-PbO<sub>2</sub> and TiO<sub>2</sub>II, *Journal of Alloys and Compounds*, 377 (2004) 17-20.
117. I. Lukacevic, S.K. Gupta, P.K. Jha, D. Kirin, Lattice Dynamics and Raman Spectrum of Rutile TiO<sub>2</sub>: The Role of Soft Phonon Modes in Pressure Induced Phase Transition, *Materials Chemistry and Physics*, 137 (2012) 282-289.
118. P. Umari, A. Pasquarello, A. Dal Corso, Raman Scattering Intensities in alpha-Quartz: A First-principles Investigation, *Physical Review B*, 63 (2001) 9.

119. R.S. Krishnan, Raman Spectrum of Quartz, *Nature*, 155 (1945) 452-452.
120. D.T. Cromer, K. Herrington, The Structures of Anatase and Rutile, *Journal of the American Chemical Society*, 77 (1955) 4708-4709.
121. M. Giarola, A. Sanson, F. Monti, G. Mariotto, M. Bettinelli, A. Speghini, G. Salviulo, Vibrational Dynamics of Anatase TiO<sub>2</sub>: Polarized Raman Spectroscopy and Ab Initio Calculations, *Physical Review B*, 81 (2010) 7.
122. T. Ohsaka, F. Izumi, Y. Fujiki, Raman Spectrum of Anatase, TiO<sub>2</sub>, *Journal of Raman Spectroscopy*, 7 (1978) 321-324.
123. F. Tian, Y.P. Zhang, J. Zhang, C.X. Pan, Raman Spectroscopy: A New Approach to Measure the Percentage of Anatase TiO<sub>2</sub> Exposed (001) Facets, *Journal of Physical Chemistry C*, 116 (2012) 7515-7519.
124. R.E. Lyon, K.E. Chike, S.M. Angel, In Situ Cure Monitoring of Epoxy Resins using Fiber-Optic Raman Spectroscopy, *Journal of Applied Polymer Science*, 53 (1994) 1805-1812.
125. K.E. Chike, M.L. Myrick, R.E. Lyon, S.M. Angel, Raman and Near-Infrared Studies of an Epoxy-Resin, *Applied Spectroscopy*, 47 (1993) 1631-1635.
126. B. Lafuente, R.T. Downs, H. Yang, N. Stone, The Power of Databases: The RRUFF Project, in: T. Armbruster, R.M. Danisi (Eds.) *Highlights in Mineralogical Crystallography*, De Gruyter, Berlin, Germany, 2015, pp. 1-30.
127. L. Beegle, R. Bhartia, M. White, L. DeFlores, W. Abbey, Y.H. Wu, B. Cameron, J. Moore, M. Fries, A. Burton, K.S. Edgett, M.A. Ravine, W. Hug, R. Reid, T. Nelson, S. Clegg, R. Wiens, S. Asher, P. Sobron, SHERLOC: Scanning Habitable Environments with Raman & Luminescence for Organics & Chemicals, 2015 IEEE Aerospace Conference, 10 (2015) 1-11.
128. I.B. Hutchinson, J. Parnell, H.G.M. Edwards, J. Jehlicka, C.P. Marshall, L.V. Harris, R. Ingley, Potential for Analysis of Carbonaceous Matter on Mars using Raman Spectroscopy, *Planetary and Space Science*, 103 (2014) 184-190.
129. E. Gibney, Mars Rover Goes Ahead Despite Crash of Test Craft, *Nature*, 540 (2016) 177-178.

130. L.V. Harris, I.B. Hutchinson, R. Ingley, C.P. Marshall, A.O. Marshall, H.G.M. Edwards, Selection of Portable Spectrometers for Planetary Exploration: A Comparison of 532 nm and 785 nm Raman Spectroscopy of Reduced Carbon in Archean Cherts, *Astrobiology*, 15 (2015) 420-429.
131. C. Freissinet, D.P. Glavin, P.R. Mahaffy, K.E. Miller, J.L. Eigenbrode, R.E. Summons, A.E. Brunner, A. Buch, C. Szopa, P.D. Archer, H.B. Franz, S.K. Atreya, W.B. Brinckerhoff, M. Cabane, P. Coll, P.G. Conrad, D.J. Des Marais, J.P. Dworkin, A.G. Fairen, P. Francois, J.P. Grotzinger, S. Kashyap, I.L. ten Kate, L.A. Leshin, C.A. Malespin, M.G. Martin, F.J. Martin-Torres, A.C. McAdam, D.W. Ming, R. Navarro-Gonzalez, A.A. Pavlov, B.D. Prats, S.W. Squyres, A. Steele, J.C. Stern, D.Y. Sumner, B. Sutter, M.P. Zorzano, M.S.L.S. Team, Organic Molecules in the Sheepbed Mudstone, Gale Crater, Mars, *Journal of Geophysical Research-Planets*, 120 (2015) 495-514.
132. C. Brolly, J. Parnell, S. Bowden, Raman Spectroscopy: Caution when Interpreting Organic Carbon from Oxidising Environments, *Planetary and Space Science*, 121 (2016) 53-59.
133. L.R. Dartnell, K. Page, S.E. Jorge-Villar, G. Wright, T. Munshi, I.J. Scowen, J.M. Ward, H.G.M. Edwards, Destruction of Raman Biosignatures by Ionising Radiation and the Implications for Life Detection on Mars, *Analytical and Bioanalytical Chemistry*, 403 (2012) 131-144.
134. P.D. Archer, H.B. Franz, B. Sutter, R.D. Arevalo, P. Coll, J.L. Eigenbrode, D.P. Glavin, J.J. Jones, L.A. Leshin, P.R. Mahaffy, A.C. McAdam, C.P. McKay, D.W. Ming, R.V. Morris, R. Navarro-Gonzalez, P.B. Nilés, A. Pavlov, S.W. Squyres, J.C. Stern, A. Steele, J.J. Wray, Abundances and Implications of Volatile-Bearing Species from Evolved Gas Analysis of the Rocknest Aeolian Deposit, Gale Crater, Mars, *Journal of Geophysical Research-Planets*, 119 (2014) 237-254.

135. D.W. Ming, P.D. Archer, D.P. Glavin, J.L. Eigenbrode, H.B. Franz, B. Sutter, A.E. Brunner, J.C. Stern, C. Freissinet, A.C. McAdam, P.R. Mahaffy, M. Cabane, P. Coll, J.L. Campbell, S.K. Atreya, P.B. Nilés, J.F. Bell, D.L. Bish, W.B. Brinckerhoff, A. Buch, P.G. Conrad, D.J. Des Marais, B.L. Ehlmann, A.G. Fairen, K. Farley, G.J. Flesch, P. Francois, R. Gellert, J.A. Grant, J.P. Grotzinger, S. Gupta, K.E. Herkenhoff, J.A. Hurowitz, L.A. Leshin, K.W. Lewis, S.M. McLennan, K.E. Miller, J. Moersch, R.V. Morris, R. Navarro-Gonzalez, A.A. Pavlov, G.M. Perrett, I. Pradler, S.W. Squyres, R.E. Summons, A. Steele, E.M. Stolper, D.Y. Sumner, C. Szopa, S. Teinturier, M.G. Trainer, A.H. Treiman, D.T. Vaniman, A.R. Vasavada, C.R. Webster, J.J. Wray, R.A. Yingst, M.S.L.S. Team, Volatile and Organic Compositions of Sedimentary Rocks in Yellowknife Bay, Gale Crater, Mars, *Science*, 343 (2014) 9.
136. K.E. Miller, B. Kotrc, R.E. Summons, I. Belmahdi, A. Buch, J.L. Eigenbrode, C. Freissinet, D.P. Glavin, C. Szopa, Evaluation of the Tenax Trap in the Sample Analysis at Mars Instrument Suite on the Curiosity Rover as a Potential Hydrocarbon Source for Chlorinated Organics Detected in Gale Crater, *Journal of Geophysical Research-Planets*, 120 (2015) 1446-1459.
137. D.T. Vaniman, D.L. Bish, D.W. Ming, T.F. Bristow, R.V. Morris, D.F. Blake, S.J. Chipera, S.M. Morrison, A.H. Treiman, E.B. Rampe, M. Rice, C.N. Achilles, J.P. Grotzinger, S.M. McLennan, J. Williams, J.F. Bell, H.E. Newsom, R.T. Downs, S. Maurice, P. Sarrazin, A.S. Yen, J.M. Morookian, J.D. Farmer, K. Stack, R.E. Milliken, B.L. Ehlmann, D.Y. Sumner, G. Berger, J.A. Crisp, J.A. Hurowitz, R. Anderson, D.J. Des Marais, E.M. Stolper, K.S. Edgett, S. Gupta, N. Spanovich, M.S.L.S. Team, Mineralogy of a Mudstone at Yellowknife Bay, Gale Crater, Mars, *Science*, 343 (2014) 8.
138. A. Ellery, D. Wynn-Williams, Why Raman Spectroscopy on Mars? A Case of the Right Tool for the Right Job, *Astrobiology*, 3 (2003) 565-579.
139. G. Lopez-Reyes, F. Rull, G. Venegas, F. Westall, F. Foucher, N. Bost, A. Sanz, A. Catala-Espi, A. Vegas, I. Hermosilla, A. Sansano, J. Medina, Analysis of the Scientific Capabilities of the ExoMars Raman Laser Spectrometer Instrument, *European Journal of Mineralogy*, 25 (2013) 721-733.
140. H.G.M. Edwards, I.B. Hutchinson, R. Ingley, J. Parnell, P. Vitek, J. Jehlicka, Raman Spectroscopic Analysis of Geological and Biogeological Specimens of Relevance to the ExoMars Mission, *Astrobiology*, 13 (2013) 543-549.

141. S.W. Squyres, J.P. Grotzinger, R.E. Arvidson, J.F. Bell, W. Calvin, P.R. Christensen, B.C. Clark, J.A. Crisp, W.H. Farrand, K.E. Herkenhoff, J.R. Johnson, G. Klingelhofer, A.H. Knoll, S.M. McLennan, H.Y. McSween, R.V. Morris, J.W. Rice, R. Rieder, L.A. Soderblom, In Situ Evidence for an Ancient Aqueous Environment at Meridiani Planum, Mars, *Science*, 306 (2004) 1709-1714.
142. J.P. Grotzinger, D.Y. Sumner, L.C. Kah, K. Stack, S. Gupta, L. Edgar, D. Rubin, K. Lewis, J. Schieber, N. Mangold, R. Milliken, P.G. Conrad, D. DesMarais, J. Farmer, K. Siebach, F. Calef, J. Hurowitz, S.M. McLennan, D. Ming, D. Vaniman, J. Crisp, A. Vasavada, K.S. Edgett, M. Malin, D. Blake, R. Gellert, P. Mahaffy, R.C. Wiens, S. Maurice, J.A. Grant, S. Wilson, R.C. Anderson, L. Beegle, R. Arvidson, B. Hallet, R.S. Sletten, M. Rice, J. Bell, J. Griffes, B. Ehlmann, R.B. Anderson, T.F. Bristow, W.E. Dietrich, G. Dromart, J. Eigenbrode, A. Fraeman, C. Hardgrove, K. Herkenhoff, L. Jandura, G. Kocurek, S. Lee, L.A. Leshin, R. Leveille, D. Limonadi, J. Maki, S. McCloskey, M. Meyer, M. Minitti, H. Newsom, D. Oehler, A. Okon, M. Palucis, T. Parker, S. Rowland, M. Schmidt, S. Squyres, A. Steele, E. Stolper, R. Summons, A. Treiman, R. Williams, A. Yingst, M.S.L.S. Team, A Habitable Fluvio-Lacustrine Environment at Yellowknife Bay, Gale Crater, Mars, *Science*, 343 (2014) 14.
143. R.V. Morris, D.C. Golden, J.F. Bell, Low-Temperature Reflectivity Spectra of Red Hematite and the Color of Mars, *Journal of Geophysical Research-Planets*, 102 (1997) 9125-9133.
144. R.E. Milliken, J.P. Grotzinger, B.J. Thomson, Paleoclimate of Mars as Captured by the Stratigraphic Record in Gale Crater, *Geophysical Research Letters*, 37 (2010) 6.
145. A.D. Rogers, V.E. Hamilton, Compositional Provinces of Mars from Statistical Analyses of TES, GRS, OMEGA and CRISM Data, *Journal of Geophysical Research-Planets*, 120 (2015) 62-91.
146. R.V. Morris, D.C. Golden, J.F. Bell, T.D. Shelfer, A.C. Scheinost, N.W. Hinman, G. Furniss, S.A. Mertzman, J.L. Bishop, D.W. Ming, C.C. Allen, D.T. Britt, Mineralogy, Composition, and Alteration of Mars Pathfinder Rocks and Soils: Evidence from Multispectral, Elemental, and Magnetic Data on Terrestrial Analogue, SNC Meteorite, and Pathfinder Samples, *Journal of Geophysical Research-Planets*, 105 (2000) 1757-1817.

147. R.V. Morris, G. Klingelhofer, C. Schroder, D.S. Rodionov, A. Yen, D.W. Ming, P.A. de Souza, T. Wdowiak, I. Fleischer, R. Gellert, B. Bernhardt, U. Bonnes, B.A. Cohen, E.N. Evlanov, J. Foh, P. Gutlich, E. Kankeleit, T. McCoy, D.W. Mittlefehldt, F. Renz, M.E. Schmidt, B. Zubkov, S.W. Squyres, R.E. Arvidson, Mossbauer Mineralogy of Rock, Soil, and Dust at Meridiani Planum, Mars: Opportunity's Journey across Sulfate-Rich Outcrop, Basaltic Sand and Dust, and Hematite Lag Deposits, *Journal of Geophysical Research-Planets*, 111 (2006) 27.
148. R.V. Morris, G. Klingelhofer, C. Schroder, I. Fleischer, D.W. Ming, A.S. Yen, R. Gellert, R.E. Arvidson, D.S. Rodionov, L.S. Crumpler, B.C. Clark, B.A. Cohen, T.J. McCoy, D.W. Mittlefehldt, M.E. Schmidt, P.A. de Souza, S.W. Squyres, Iron Mineralogy and Aqueous Alteration from Husband Hill through Home Plate at Gusev Crater, Mars: Results from the Mossbauer Instrument on the Spirit Mars Exploration Rover, *Journal of Geophysical Research-Planets*, 113 (2008) 43.
149. W.H. Farrand, J.R. Johnson, M.S. Rice, A. Wang, J.F. Bell, VNIR Multispectral Observations of Aqueous Alteration Materials by the Pancams on the Spirit and Opportunity Mars Exploration Rovers, *American Mineralogist*, 101 (2016) 2005-2019.
150. J.P. Grotzinger, S. Gupta, M.C. Malin, D.M. Rubin, J. Schieber, K. Siebach, D.Y. Sumner, K.M. Stack, A.R. Vasavada, R.E. Arvidson, F. Calef, L. Edgar, W.F. Fischer, J.A. Grant, J. Griffes, L.C. Kah, M.P. Lamb, K.W. Lewis, N. Mangold, M.E. Minitti, M. Palucis, M. Rice, R.M.E. Williams, R.A. Yingst, D. Blake, D. Blaney, P. Conrad, J. Crisp, W.E. Dietrich, G. Dromart, K.S. Edgett, R.C. Ewing, R. Gellert, J.A. Hurowitz, G. Kocurek, P. Mahaffy, M.J. McBride, S.M. McLennan, M. Mischna, D. Ming, R. Milliken, H. Newsom, D. Oehler, T.J. Parker, D. Vaniman, R.C. Wiens, S.A. Wilson, Deposition, Exhumation, and Paleoclimate of an Ancient Lake Deposit, Gale Crater, Mars, *Science*, 350 (2015) 13.
151. D.L. Bish, D.F. Blake, D.T. Vaniman, S.J. Chipera, R.V. Morris, D.W. Ming, A.H. Treiman, P. Sarrazin, S.M. Morrison, R.T. Downs, C.N. Achilles, A.S. Yen, T.F. Bristow, J.A. Crisp, J.M. Morookian, J.D. Farmer, E.B. Rampe, E.M. Stolper, N. Spanovich, M.S.L.S. Team, X-ray Diffraction Results from Mars Science Laboratory: Mineralogy of Rocknest at Gale Crater, *Science*, 341 (2013) 5.

152. A.H. Treiman, D.L. Bish, D.T. Vaniman, S.J. Chipera, D.F. Blake, D.W. Ming, R.V. Morris, T.F. Bristow, S.M. Morrison, M.B. Baker, E.B. Rampe, R.T. Downs, J. Filiberto, A.F. Glazner, R. Gellert, L.M. Thompson, M.E. Schmidt, L. Le Deit, R.C. Wiens, A.C. McAdam, C.N. Achilles, K.S. Edgett, J.D. Farmer, K.V. Fendrich, J.P. Grotzinger, S. Gupta, J.M. Morookian, M.E. Newcombe, M.S. Rice, J.G. Spray, E.M. Stolper, D.Y. Sumner, A.R. Vasavada, A.S. Yen, Mineralogy, Provenance, and Diagenesis of a Potassic Basaltic Sandstone on Mars: CheMin X-ray Diffraction of the Windjana Sample (Kimberley Area, Gale Crater), *Journal of Geophysical Research-Planets*, 121 (2016) 75-106.
153. J.R. Johnson, J.F. Bell, S. Bender, D. Blaney, E. Cloutis, B. Ehliaviann, A. Fraeman, O. Gasnault, K. Kinch, S. Le Mouelic, S. Maurice, E. Rampe, D. Vaniman, R.C. Wiens, Constraints on Iron Sulfate and Iron Oxide Mineralogy from ChemCam Visible/Near-Infrared Reflectance Spectroscopy of Mt. Sharp Basal Units, Gale Crater, Mars, *American Mineralogist*, 101 (2016) 1501-1514.
154. M. Nachon, N. Mangold, O. Forni, L.C. Kah, A. Cousin, R.C. Wiens, R. Anderson, D. Blaney, J.G. Blank, F. Calef, S.M. Clegg, C. Fabre, M.R. Fisk, O. Gasnault, J.P. Grotzinger, R. Kronyak, N.L. Lanza, J. Lasue, L. Le Deit, S. Le Mouelic, S. Maurice, P.Y. Meslin, D.Z. Oehler, V. Payre, W. Rabin, S. Schroder, K. Stack, D. Sumner, Chemistry of Diagenetic Features Analyzed by ChemCam at Pahrump Hills, Gale Crater, Mars, *Icarus*, 281 (2017) 121-136.
155. R.C. Anderson, L. Jandura, A.B. Okon, D. Sunshine, C. Roumeliotis, L.W. Beegle, J. Hurowitz, B. Kennedy, D. Limonadi, S. McCloskey, M. Robinson, C. Seybold, K. Brown, Collecting Samples in Gale Crater, Mars; an Overview of the Mars Science Laboratory Sample Acquisition, Sample Processing and Handling System, *Space Science Reviews*, 170 (2012) 57-75.
156. A.A. Fraeman, R.E. Arvidson, J.G. Catalano, J.P. Grotzinger, R.V. Morris, S.L. Murchie, K.M. Stack, D.C. Humm, J.A. McGovern, F.P. Seelos, K.D. Seelos, C.E. Viviano, A Hematite-Bearing Layer in Gale Crater, Mars: Mapping and Implications for Past Aqueous Conditions, *Geology*, 41 (2013) 1103-1106.
157. L. Zajickova, P. Synek, O. Jasek, M. Elias, B. David, J. Bursik, N. Pizurova, R. Hanzlikova, L. Lazar, Synthesis of Carbon nNanotubes and Iron Oxide Nanoparticles in MW Plasma Torch with Fe(CO)<sub>5</sub> in Gas Feed, *Applied Surface Science*, 255 (2009) 5421-5424.

158. C.P. Marshall, A.O. Marshall, Hematite and Carbonaceous Materials in Geological Samples: A Cautionary Tale, *Spectrochimica Acta Part a-Molecular and Biomolecular Spectroscopy*, 80 (2011) 133-137.
159. C.P. Marshall, A.O. Marshall, Raman Hyperspectral Imaging of Microfossils: Potential Pitfalls, *Astrobiology*, 13 (2013) 920-931.
160. C.P. Marshall, J.R. Emry, A.O. Marshall, Haematite Pseudomicrofossils Present in the 3.5-Billion-Year-Old Apex Chert, *Nature Geoscience*, 4 (2011) 240-243.
161. C.A. Drumm, M.D. Morris, Microscopic Raman Line-Imaging With Principal Component Analysis, *Applied Spectroscopy*, 49 (1995) 1331-1337.
162. J. Jaumot, R. Gargallo, A. de Juan, R. Tauler, A Graphical User-Friendly Interface for MCR-ALS: A New Tool for Multivariate Curve Resolution in Matlab, *Chemometrics and Intelligent Laboratory Systems*, 76 (2005) 101-110.
163. P.H.C. Eilers, Parametric Time Warping, *Analytical Chemistry*, 76 (2004) 404-411.
164. A.M. Jubb, H.C. Allen, Vibrational Spectroscopic Characterization of Hematite, Maghemite, and Magnetite Thin Films Produced by Vapor Deposition, *ACS Applied Materials & Interfaces*, 2 (2010) 2804-2812.
165. I.V. Chernyshova, M.F. Hochella, A.S. Madden, Size-Dependent Structural Transformations of Hematite Nanoparticles. 1. Phase transition, *Physical Chemistry Chemical Physics*, 9 (2007) 1736-1750.
166. D.L.A. deFaria, S.V. Silva, M.T. deOliveira, Raman Microspectroscopy of Some Iron Oxides and Oxyhydroxides, *Journal of Raman Spectroscopy*, 28 (1997) 873-878.
167. M. Hanesch, Raman Spectroscopy of Iron Oxides and (Oxy)Hydroxides at Low Laser Power and Possible Applications in Environmental Magnetic Studies, *Geophysical Journal International*, 177 (2009) 941-948.
168. I. Chamritski, G. Burns, Infrared- and Raman-Active Phonons of Magnetite, Maghemite, and Hematite: A Computer Simulation and Spectroscopic Study, *Journal of Physical Chemistry B*, 109 (2005) 4965-4968.

169. A.C. Ferrari, J. Robertson, Interpretation of Raman Spectra of Disordered and Amorphous Carbon, *Physical Review B*, 61 (2000) 14095-14107.
170. A. Sadezky, H. Muckenhuber, H. Grothe, R. Niessner, U. Poschl, Raman Micro-Spectroscopy of Soot and Related Carbonaceous Materials: Spectral Analysis and Structural Information, *Carbon*, 43 (2005) 1731-1742.
171. F. Tuinstra, J.L. Koenig, Raman Spectrum of Graphite, *Journal of Chemical Physics*, 53 (1970) 1126-1130.
172. C.P. Marshall, H.G.M. Edwards, J. Jehlicka, Understanding the Application of Raman Spectroscopy to the Detection of Traces of Life, *Astrobiology*, 10 (2010) 229-243.
173. D.M. Bower, A. Steele, M.D. Fries, L. Kater, Micro Raman Spectroscopy of Carbonaceous Material in Microfossils and Meteorites: Improving a Method for Life Detection, *Astrobiology*, 13 (2013) 103-113.
174. L.V. Harris, M. McHugh, I.B. Hutchinson, R. Ingley, C. Malherbe, J. Parnell, A.O. Marshall, H.G.M. Edwards, Avoiding Misidentification of Bands in Planetary Raman Spectra, *Journal of Raman Spectroscopy*, 46 (2015) 863-872.
175. S. Acquaviva, P. Baraldi, E. D'Anna, M.L. De Giorgi, A. Della Patria, L. Giotta, S. Omarini, R. Piccolo, Yellow Pigments in Painting: Characterisation and UV Laser-Induced Modifications, *Journal of Raman Spectroscopy*, 40 (2009) 1664-1667.
176. J.C. Bridges, M.J. Burchell, H.C. Changela, N.J. Foster, J.A. Creighton, J.D. Carpenter, S.J. Gurman, I.A. Franchi, H. Busemann, Iron Oxides in Comet 81P/Wild 2, *Meteoritics & Planetary Science*, 45 (2010) 55-72.
177. B. Wopenka, Raman Spectroscopic Investigation of Two Grains from Comet 81P/Wild 2: Information that can be Obtained beyond the Presence of sp<sup>2</sup>-Bonded Carbon, *Meteoritics & Planetary Science*, 47 (2012) 565-584.
178. G.M. Muñoz Caro, F.J.M. Rietmeijer, V. Souza-Egipsy, M.P. Valles-Gonzalez, A Potentially New Type of Nonchondritic Interplanetary Dust Particle with Hematite, Organic Carbon, Amorphous Na,Ca-Aluminosilicate, and FeO-Spheres, *Meteoritics & Planetary Science*, 47 (2012) 248-261.

179. S.S.T. Simon, M.R. Gibling, W.A. DiMichele, D.S. Chaney, C.V. Looy, N.J. Tabor, An Abandoned-Channel Fill with Exquisitely Preserved Plants in Redbeds of the Clear Fork Formation, Texas, USA: An Early Permian Water-Dependent Habitat on the Arid Plains of Pangea, *Journal of Sedimentary Research*, 86 (2016) 944-964.
180. D. Papineau, B.T. De Gregorio, R.M. Stroud, A. Steele, E. Pecoits, K. Konhauser, J.H. Wang, M.L. Fogel, Ancient Graphite in the Eoarchean Quartz-Pyroxene Rocks from Akilia in Southern West Greenland II: Isotopic and Chemical Compositions and Comparison with Paleoproterozoic Banded Iron Formations, *Geochimica Et Cosmochimica Acta*, 74 (2010) 5884-5905.
181. A. Wang, B.L. Jolliff, L.A. Haskin, Raman Spectroscopy as a Method for Mineral Identification on Lunar Robotic Exploration Missions, *Journal of Geophysical Research-Planets*, 100 (1995) 21189-21199.
182. A. Wang, B.L. Jolliff, L.A. Haskin, K.E. Kuebler, K.M. Viskupic, Characterization and Comparison of Structural and Compositional Features of Planetary Quadrilateral Pyroxenes by Raman Spectroscopy, *American Mineralogist*, 86 (2001) 790-806.
183. A. Steele, F.M. McCubbin, M. Fries, M. Glamoclija, L. Kater, H. Nekvasil, Graphite in an Apollo 17 Impact Melt Breccia, *Science*, 329 (2010) 51.
184. R.L. Korotev, Lunar Geochemistry as told by Lunar Meteorites, *Chemie Der Erde-Geochemistry*, 65 (2005) 297-346.
185. P.H. Warren, New Lunar Meteorites: Implications for Composition of the Global Lunar Surface, Lunar Crust, and the Bulk Moon, *Meteoritics & Planetary Science*, 40 (2005) 477-506.
186. C.R. Neal, L.A. Taylor, Petrogenesis of Mare Basalts - A Record of Lunar Volcanism, *Geochimica Et Cosmochimica Acta*, 56 (1992) 2177-2211.
187. J.J. Papike, Pyroxene as a Recorder of Cumulate Formational Processes in Asteroids, Moon, Mars, Earth: Reading the Record with the Ion Microprobe, *American Mineralogist*, 81 (1996) 525-544.
188. C.K. Shearer, J.J. Papike, Magmatic Evolution of the Moon, *American Mineralogist*, 84 (1999) 1469-1494.

189. I.S. McCallum, J.M. Schwartz, Lunar Mg Suite: Thermobarometry and Petrogenesis of Parental Magmas, *Journal of Geophysical Research-Planets*, 106 (2001) 27969-27983.
190. J.J. Papike, F.N. Hodges, A.E. Bence, M. Cameron, J.M. Rhodes, Mare Basalts: Crystal Chemistry, Mineralogy, and Petrology, *Reviews of Geophysics and Space Physics*, 14 (1976) 475-540.
191. A. Calzada-Diaz, K.H. Joy, I.A. Crawford, T.A. Nordheim, Constraining the Source Regions of Lunar Meteorites using Orbital Geochemical Data, *Meteoritics & Planetary Science*, 50 (2015) 214-228.
192. N. Morimoto, J. Fabries, A.K. Ferguson, I.V. Ginzburg, M. Ross, F.A. Seifert, J. Zussman, K. Aoki, G. Gottardi, Nomenclature of Pyroxenes, *Mineralogy and Petrology*, 39 (1988) 55-76.
193. M. Anand, L.A. Taylor, C. Floss, C.R. Neal, K. Terada, S. Tanikawa, Petrology and Geochemistry of LaPaz Icefield 02205: A New Unique Low-Ti Mare-Basalt Meteorite, *Geochimica Et Cosmochimica Acta*, 70 (2006) 246-264.
194. J.J. Freeman, A. Wang, K.E. Kuebler, B.L. Jolliff, L.A. Haskin, Characterization of Natural Feldspars by Raman Spectroscopy for Future Planetary Exploration, *The Canadian Mineralogist*, 46 (2008) 1477-1500.
195. S.E. Haggerty, Subsolidus Reduction of Lunar Spinel, *Nature-Physical Science*, 234 (1971) 113-117.
196. L.A. Taylor, R.J. Williams, R.H. McCallister, Stability Relations of Ilmenite and Ulvöspinel in the Fe-Ti-O System and Application of These Data to Lunar Mineral Assemblages, *Earth and Planetary Science Letters*, 16 (1972) 282-288.
197. E. Hill, L.A. Taylor, C. Floss, Y. Liu, Lunar Meteorite LaPaz Icefield 04841: Petrology, Texture, and Impact-Shock Effects of a Low-Ti Mare Basalt, *Meteoritics & Planetary Science*, 44 (2009) 87-94.
198. K. Righter, S.J. Collins, A.D. Brandon, Mineralogy and Petrology of the LaPaz Icefield Lunar Mare Basaltic Meteorites, *Meteoritics & Planetary Science*, 40 (2005) 1703-1722.

199. K.H. Joy, I.A. Crawford, H. Downes, S.S. Russell, A.T. Kearsley, A Petrological, Mineralogical, and Chemical Analysis of the Lunar Mare Basalt Meteorite LaPaz Icefield 02205, 02224, and 02226, *Meteoritics & Planetary Science*, 41 (2006) 1003-1025.
200. J.M.D. Day, L.A. Taylor, C. Floss, A.D. Patchen, D.W. Schnare, D.G. Pearson, Comparative Petrology, Geochemistry, and Petrogenesis of Evolved, Low-Ti Lunar Mare Basalt Meteorites from the LaPaz Icefield, Antarctica, *Geochimica Et Cosmochimica Acta*, 70 (2006) 1581-1600.
201. J.V. Jokerst, A.J. Cole, D. Van de Sompel, S.S. Gambhir, Gold Nanorods for Ovarian Cancer Detection with Photoacoustic Imaging and Resection Guidance via Raman Imaging in Living Mice, *ACS Nano*, 6 (2012) 10366-10377.
202. H. Yamakoshi, K. Dodo, A. Palonpon, J. Ando, K. Fujita, S. Kawata, M. Sodeoka, Alkyne-Tag Raman Imaging for Visualization of Mobile Small Molecules in Live Cells, *Journal of the American Chemical Society*, 134 (2012) 20681-20689.
203. H. Abramczyk, B. Brozek-Pluska, Raman Imaging in Biochemical and Biomedical Applications. Diagnosis and Treatment of Breast Cancer, *Chemical Reviews*, 113 (2013) 5766-5781.
204. X. Ma, Q.Y. Qu, Y.Y. Zhao, Z. Luo, K.W. Ng, Y.L. Zhao, Graphene Oxide Wrapped Gold Nanoparticles for Intracellular Raman Imaging and Drug Delivery, *Journal of Materials Chemistry B*, 1 (2013) 6495-6500.
205. Z.L. Song, Z. Chen, X. Bian, L.Y. Zhou, D. Ding, H. Liang, Y.X. Zou, S.S. Wang, L. Chen, C. Yang, X.B. Zhang, W.H. Tan, Alkyne-Functionalized Superstable Graphitic Silver Nanoparticles for Raman Imaging, *Journal of the American Chemical Society*, 136 (2014) 13558-13561.
206. T.P. Mernagh, D.M. Hoatson, Raman Spectroscopic Study of Pyroxene Structures from the Munni Munni Layered Intrusion, Western Australia, *Journal of Raman Spectroscopy*, 28 (1997) 647-658.
207. E. Huang, C.H. Chen, T. Huang, E.H. Lin, J.A. Xu, Raman Spectroscopic Characteristics of Mg-Fe-Ca Pyroxenes, *American Mineralogist*, 85 (2000) 473-479.
208. S.K. Sharma, B. Simons, Raman Study of Crystalline Polymorphs and Glasses of Spodumene Composition Quenched from Various Pressures, *American Mineralogist*, 66 (1981) 118-126.

209. S.K. Sharma, B. Simons, H.S. Yoder, Raman Study of Anorthite, Calcium Tschermak's Pyroxene, and Gehlenite in Crystalline and Glassy States, *American Mineralogist*, 68 (1983) 1113-1125.
210. S. Ghose, N. Choudhury, S.L. Chaplot, C.P. Chowdhury, S.K. Sharma, Lattice Dynamics and Raman Spectroscopy of Protoenstatite  $Mg_2Si_2O_6$ , *Physics and Chemistry of Minerals*, 20 (1994) 469-477.
211. A. Wang, K.E. Kuebler, B.L. Jolliff, L.A. Haskin, Raman Spectroscopy of Fe-Ti-Cr-Oxides, Case Study: Martian Meteorite EETA79001, *American Mineralogist*, 89 (2004) 665-680.
212. N.L. Ross, P. McMillan, The Raman Spectrum of  $MgSiO_3$  Ilmenite, *American Mineralogist*, 69 (1984) 719-721.
213. S.A. Solin, A.K. Ramdas, Raman Spectrum of Diamond, *Physical Review B*, 1 (1970) 1687-1698.
214. L. Nasdala, S. Steger, C. Reissner, Raman Study of Diamond-Based Abrasives, and Possible Artefacts in Detecting UHP Microdiamond, *Lithos*, 265 (2016) 317-327.
215. F.L. Galeener, Band Limits and the Vibrational Spectra of Tetrahedral Glasses, *Physical Review B*, 19 (1979) 4292-4297.
216. C. Avril, V. Malavergne, R. Caracas, B. Zanda, B. Reynard, E. Charon, E. Bobocioiu, F. Brunet, S. Borensztajn, S. Pont, M. Tarrida, F. Guyot, Raman Spectroscopic Properties and Raman Identification of CaS-MgS-MnS-FeS-Cr<sub>2</sub>FeS<sub>4</sub> Sulfides in Meteorites and Reduced Sulfur-Rich Systems, *Meteoritics & Planetary Science*, 48 (2013) 1415-1426.
217. M.A. Carpenter, Mechanisms and Kinetics of Al-Si Ordering in Anorthite: I. Incommensurate Structure and Domain Coarsening, *American Mineralogist*, 76 (1991) 1110-1119.
218. T.L. Grove, J.M. Ferry, F.S. Spear, Phase Transitions and Decomposition Relations in Calcic Plagioclase, *American Mineralogist*, 68 (1983) 41-59.

## Appendix A

### REPRINT PERMISSIONS

Sections of Chapter 2 are modified and/or reprinted with permission from SAGE Publishing for the following publication:

Joseph P. Smith, Frank C. Smith, Joshua Ottaway, Alexandra E. Krull-Davatzes, Bruce M. Simonson, Billy P. Glass, and Karl S. Booksh. “Raman Microspectroscopic Mapping with Multivariate Curve Resolution–Alternating Least Squares (MCR-ALS) Applied to the High-Pressure Polymorph of Titanium Dioxide, TiO<sub>2</sub>-II”. *Applied Spectroscopy*. 2017. DOI: 10.1177/0003702816687573  
Copyright 2017, SAGE Publishing.

Sections of Chapter 3 are modified and/or reprinted with permission from Elsevier for the following publication:

Joseph P. Smith, Frank C. Smith, Alexandra E. Krull-Davatzes, Bruce M. Simonson, Billy P. Glass, and Karl S. Booksh. “Raman microspectroscopic mapping with multivariate curve resolution-alternating least squares (MCR-ALS) of the high-pressure,  $\alpha$ -PbO<sub>2</sub>-structured polymorph of titanium dioxide, TiO<sub>2</sub>-II”. *Chemical Data Collections*. 2017. 9-10. 35-43. DOI: 10.1016/j.cdc.2017.02.005  
Copyright 2017, Elsevier.

Sections of Chapters 4 and 5 are manuscripts either under review or in submission and should be published prior to the final publication of this dissertation.

The specific terms and conditions with respect to reprint permission from Elsevier are displayed within Appendix A of this dissertation.

ELSEVIER LICENSE  
TERMS AND CONDITIONS

This Agreement between Joseph P Smith ("You") and Elsevier ("Elsevier") consists of your license details and the terms and conditions provided by Elsevier and Copyright Clearance Center.

License Number 4097150612480

License date Apr 27, 2017

Licensed Content Publisher Elsevier

Licensed Content Publication Chemical Data Collections

Licensed Content Title Raman microspectroscopic mapping with multivariate curve Resolution-alternating least squares (MCR-ALS) of the high-pressure,  $\alpha$ -PbO<sub>2</sub>-structured polymorph of titanium dioxide, TiO<sub>2</sub>-II

Licensed Content Author Joseph P. Smith, Frank C. Smith, Alexandra E. Krull-Davatzes, Bruce M. Simonson, Billy P. Glass, Karl S. Booksh

Licensed Content Date August 2017

Licensed Content Volume 9

Licensed Content Issue n/a

Licensed Content Pages 9

Start Page 35

End Page 43

Type of Use reuse in a thesis/dissertation

Portion full article

Format both print and electronic

Are you the author of this Elsevier article? Yes

Will you be translating? No

Order reference number

Title of your thesis/dissertation Raman Microspectroscopic Imaging and Multivariate Analysis to Investigate the Chemical Properties of Novel Geological and Planetary Materials

Expected completion date May 2017

Estimated size (number of pages) 242

Elsevier VAT number GB 494 6272 12

Requestor Location Joseph P Smith 004 Lammot du Pont Lab Newark, DE 19716

United States

Attn: Joseph P Smith

Publisher Tax ID 980397604

Total 0.00 USD

## INTRODUCTION

1. The publisher for this copyrighted material is Elsevier. By clicking "accept" in connection with completing this licensing transaction, you agree that the following terms and conditions apply to this transaction (along with the Billing and Payment terms and conditions established by Copyright Clearance Center, Inc. ("CCC"), at the time that you opened your Rightslink account and that are available at any time at <http://myaccount.copyright.com>).

## GENERAL TERMS

2. Elsevier hereby grants you permission to reproduce the aforementioned material subject to the terms and conditions indicated.

3. Acknowledgement: If any part of the material to be used (for example, figures) has appeared in our publication with credit or acknowledgement to another source, permission must also be sought from that source. If such permission is not obtained then that material may not be included in your publication/copies. Suitable acknowledgement to the source must be made, either as a footnote or in a reference list at the end of your publication, as follows: "Reprinted from Publication title, Vol /edition number, Author(s), Title of article / title of chapter, Pages No., Copyright (Year), with permission from Elsevier [OR APPLICABLE SOCIETY COPYRIGHT OWNER]." Also Lancet special credit " Reprinted from The Lancet, Vol. number, Author(s), Title of article, Pages No., Copyright (Year), with permission from Elsevier."

4. Reproduction of this material is confined to the purpose and/or media for which permission is hereby given.

5. Altering/Modifying Material: Not Permitted. However figures and illustrations may be altered/adapted minimally to serve your work. Any other abbreviations, additions, deletions and/or any other alterations shall be made only with prior written authorization of Elsevier Ltd. (Please contact Elsevier at [permissions@elsevier.com](mailto:permissions@elsevier.com)). No modifications can be made to any Lancet figures/tables and they must be reproduced in full.

6. If the permission fee for the requested use of our material is waived in this instance, please be advised that your future requests for Elsevier materials may attract a fee.

7. **Reservation of Rights:** Publisher reserves all rights not specifically granted in the combination of (i) the license details provided by you and accepted in the course of this licensing transaction, (ii) these terms and conditions and (iii) CCC's Billing and Payment terms and conditions.

8. **License Contingent Upon Payment:** While you may exercise the rights licensed immediately upon issuance of the license at the end of the licensing process for the transaction, provided that you have disclosed complete and accurate details of your proposed use, no license is finally effective unless and until full payment is received from you (either by publisher or by CCC) as provided in CCC's Billing and Payment terms and conditions. If full payment is not received on a timely basis, then any license preliminarily granted shall be deemed automatically revoked and shall be void as if never granted. Further, in the event that you breach any of these terms and conditions or any of CCC's Billing and Payment terms and conditions, the license is automatically revoked and shall be void as if never granted. Use of materials as described in a revoked license, as well as any use of the materials beyond the scope of an unrevoked license, may constitute copyright infringement and publisher reserves the right to take any and all action to protect its copyright in the materials.

9. **Warranties:** Publisher makes no representations or warranties with respect to the licensed material.

10. **Indemnity:** You hereby indemnify and agree to hold harmless publisher and CCC, and their respective officers, directors, employees and agents, from and

against any and all claims arising out of your use of the licensed material other than as specifically authorized pursuant to this license.

11. No Transfer of License: This license is personal to you and may not be sublicensed, assigned, or transferred by you to any other person without publisher's written permission.

12. No Amendment Except in Writing: This license may not be amended except in a writing signed by both parties (or, in the case of publisher, by CCC on publisher's behalf).

13. Objection to Contrary Terms: Publisher hereby objects to any terms contained in any purchase order, acknowledgment, check endorsement or other writing prepared by you, which terms are inconsistent with these terms and conditions or CCC's Billing and Payment terms and conditions. These terms and conditions, together with CCC's Billing and Payment terms and conditions (which are incorporated herein), comprise the entire agreement between you and publisher (and CCC) concerning this licensing transaction. In the event of any conflict between your obligations established by these terms and conditions and those established by CCC's Billing and Payment terms and conditions, these terms and conditions shall control.

14. Revocation: Elsevier or Copyright Clearance Center may deny the permissions described in this License at their sole discretion, for any reason or no reason, with a full refund payable to you. Notice of such denial will be made using the contact information provided by you. Failure to receive such notice will not alter or invalidate the denial. In no event will Elsevier or Copyright Clearance Center be responsible or liable for any costs, expenses or damage incurred by you as a result of a

denial of your permission request, other than a refund of the amount(s) paid by you to Elsevier and/or Copyright Clearance Center for denied permissions.

#### LIMITED LICENSE

The following terms and conditions apply only to specific license types:

15. Translation: This permission is granted for nonexclusive world English rights only unless your license was granted for translation rights. If you licensed translation rights you may only translate this content into the languages you requested. A professional translator must perform all translations and reproduce the content word for word preserving the integrity of the article.

16. Posting licensed content on any Website: The following terms and conditions apply as follows: Licensing material from an Elsevier journal: All content posted to the web site must maintain the copyright information line on the bottom of each image; A hypertext must be included to the Homepage of the journal from which you are licensing at <http://www.sciencedirect.com/science/journal/xxxxx> or the Elsevier homepage for books at <http://www.elsevier.com>; Central Storage: This license does not include permission for a scanned version of the material to be stored in a central repository such as that provided by Heron/XanEdu. Licensing material from an Elsevier book: A hypertext link must be included to the Elsevier homepage at <http://www.elsevier.com> . All content posted to the web site must maintain the copyright information line on the bottom of each image. Posting licensed content on Electronic reserve: In addition to the above the following clauses are applicable: The web site must be password protected and made available only to bona fide students

registered on a relevant course. This permission is granted for 1 year only. You may obtain a new license for future website posting.

17. For journal authors: the following clauses are applicable in addition to the above: Preprints: A preprint is an author's own write-up of research results and analysis, it has not been peer reviewed, nor has it had any other value added to it by a publisher (such as formatting, copyright, technical enhancement etc.). Authors can share their preprints anywhere at any time. Preprints should not be added to or enhanced in any way in order to appear more like, or to substitute for, the final versions of articles however authors can update their preprints on arXiv or RePEc with their Accepted Author Manuscript (see below). If accepted for publication, we encourage authors to link from the preprint to their formal publication via its DOI. Millions of researchers have access to the formal publications on ScienceDirect, and so links will help users to find, access, cite and use the best available version. Please note that Cell Press, The Lancet and some society-owned have different preprint policies. Information on these policies is available on the journal homepage. Accepted Author Manuscripts: An accepted author manuscript is the manuscript of an article that has been accepted for publication and which typically includes author-incorporated changes suggested during submission, peer review and editorauthor communications. Authors can share their accepted author manuscript: immediately via their noncommercial person homepage or blog by updating a preprint in arXiv or RePEc with the accepted manuscript via their research institute or institutional repository for internal institutional uses or as part of an invitation only research collaboration workgroup directly by providing copies to their students or to research collaborators for their personal use for private scholarly sharing as part of an invitation

only work group on commercial sites with which Elsevier has an agreement. After the embargo period via noncommercial hosting platforms such as their institutional repository via commercial sites with which Elsevier has an agreement In all cases accepted manuscripts should: link to the formal publication via its DOI bear a CCBYNCND license this is easy to do if aggregated with other manuscripts, for example in a repository or other site, be shared in alignment with our hosting policy not be added to or enhanced in any way to appear more like, or to substitute for, the published journal article. Published journal article (JPA): A published journal article (PJA) is the definitive final record of published research that appears or will appear in the journal and embodies all value-adding publishing activities including peer review coordination, copyediting, formatting, (if relevant) pagination and online enrichment. Policies for sharing publishing journal articles differ for subscription and gold open access articles: Subscription Articles: If you are an author, please share a link to your article rather than the fulltext. Millions of researchers have access to the formal publications on ScienceDirect, and so links will help your users to find, access, cite, and use the best available version. Theses and dissertations which contain embedded PJAs as part of the formal submission can be posted publicly by the awarding institution with DOI links back to the formal publications on ScienceDirect. If you are affiliated with a library that subscribes to ScienceDirect you have additional private sharing rights for others' research accessed under that agreement. This includes use for classroom teaching and internal training at the institution (including use in course packs and courseware programs), and inclusion of the article for grant funding purposes. Gold Open Access Articles: May be shared according to the authorselected enduser license and should contain a CrossMark logo, the end user license, and a DOI

link to the formal publication on ScienceDirect. Please refer to Elsevier's posting policy for further information.

18. For book authors the following clauses are applicable in addition to the above: Authors are permitted to place a brief summary of their work online only. You are not allowed to download and post the published electronic version of your chapter, nor may you scan the printed edition to create an electronic version. Posting to a repository: Authors are permitted to post a summary of their chapter only in their institution's repository.

19. Thesis/Dissertation: If your license is for use in a thesis/dissertation your thesis may be submitted to your institution in either print or electronic form. Should your thesis be published commercially, please reapply for permission. These requirements include permission for the Library and Archives of Canada to supply single copies, on demand, of the complete thesis and include permission for Proquest/UMI to supply single copies, on demand, of the complete thesis. Should your thesis be published commercially, please reapply for permission. Theses and dissertations which contain embedded PJAs as part of the formal submission can be posted publicly by the awarding institution with DOI links back to the formal publications on ScienceDirect.

## ELSEVIER OPEN ACCESS TERMS AND CONDITIONS

You can publish open access with Elsevier in hundreds of open access journals or in nearly 2000 established subscription journals that support open access publishing. Permitted third party reuse of these open access articles is defined by the

author's choice of Creative Commons user license. See our open access license policy for more information.

Terms & Conditions applicable to all Open Access articles published with Elsevier: Any reuse of the article must not represent the author as endorsing the adaptation of the article nor should the article be modified in such a way as to damage the author's honour or reputation. If any changes have been made, such changes must be clearly indicated. The author(s) must be appropriately credited and we ask that you include the end user license and a DOI link to the formal publication on ScienceDirect. If any part of the material to be used (for example, figures) has appeared in our publication with credit or acknowledgement to another source it is the responsibility of the user to ensure their reuse complies with the terms and conditions determined by the rights holder.

Additional Terms & Conditions applicable to each Creative Commons user license: CC BY: The CCBY license allows users to copy, to create extracts, abstracts and new works from the Article, to alter and revise the Article and to make commercial use of the Article (including reuse and/or resale of the Article by commercial entities), provided the user gives appropriate credit (with a link to the formal publication through the relevant DOI), provides a link to the license, indicates if changes were made and the licensor is not represented as endorsing the use made of the work. The full details of the license are available at <http://creativecommons.org/licenses/by/4.0>.

CC BY NC SA: The CC BYNCSA license allows users to copy, to create extracts, abstracts and new works from the Article, to alter and revise the Article, provided this is not done for commercial purposes, and that the user gives appropriate

credit (with a link to the formal publication through the relevant DOI), provides a link to the license, indicates if changes were made and the licensor is not represented as endorsing the use made of the work. Further, any new works must be made available on the same conditions. The full details of the license are available at <http://creativecommons.org/licenses/byncsa/4.0>.

CC BY NC ND: The CC BYNCND license allows users to copy and distribute the Article, provided this is not done for commercial purposes and further does not permit distribution of the Article if it is changed or edited in any way, and provided the user gives appropriate credit (with a link to the formal publication through the relevant DOI), provides a link to the license, and that the licensor is not represented as endorsing the use made of the work. The full details of the license are available at <http://creativecommons.org/licenses/byncnd/4.0>.

Any commercial reuse of Open Access articles published with a CC BY NC SA or CC BY NC ND license requires permission from Elsevier and will be subject to a fee. Commercial reuse includes: Associating advertising with the full text of the Article; Charging fees for document delivery or access; Article aggregation; Systematic distribution via email lists or share buttons; Posting or linking by commercial companies for use by customers of those companies.

20. Other Conditions: v1.9 Questions: [customercare@copyright.com](mailto:customercare@copyright.com) or +18552393415 (toll free in the US) or +19786462777.